In memory of Natalia Yakovlevna Puchkova

Effect of superconducting transition on the low-temperature jumplike deformation of metals and alloys (Review)

V. V. Pustovalov*

B. Verkin Institute for Low Temperature Physics and Engineering, National Academy of Sciences of Ukraine, pr. Lenina 47, 61164 Kharkov, Ukraine

The available experimental data on the effect of the superconducting transition on the low-temperature jumplike deformation of metals and alloys are examined. Different hypotheses as to the mechanism for this effect are stated and compared with experiment. The experimental and theoretical papers on the low-temperature jumplike deformation are discussed, and conjectures as to the mechanism for the effect are set forth. © *2000 American Institute of Physics.*
[S1063-777X(00)00106-7]

INTRODUCTION

As the temperature is lowered, the plastic deformation of the majority of metals, alloys, and ionic crystals becomes macroscopically unstable, and jumps in the flow stress, amounting to 10–15% of the stress level, appear on the work-hardening curve.[1,2] The experimental data accumulated over more than forty years reveal some characteristic regularities in the low-temperature jumplike deformation (LJD) on such a scale. This type of jumplike (also called steplike, but perhaps more aptly called jumpy) deformation is not a consequence of processes of deformation twinning, deformation polymorphism, or crack formation, which are also accompanied by jumps in the stress; the LJD arises at a definite low temperature (below 20–30 K) for each material, and as the temperature is lowered further the amplitude and frequency of the jumps increase, and the onset of the LJD is shifted toward the yield point (Fig. 1). In very pure metals the LJD is not observed even at the lowest measurement temperatures (0.5 K), and in impure crystals and alloys the jumplike deformation is enhanced as the concentrations of the impurities and dopants are increased. Often the jumplike deformation on the work-hardening curve begins with isolated jumps separated by segments of stable deformation.

Because its nature is unclear, the LJD has been the subject of many experimental and theoretical studies (the majority of which are mentioned in the reviews[1,2]). Over the course of these studies, several hypotheses have been advanced as to the nature of the LJD. There are two main hypotheses: one of them, which we call the thermal hypothesis, assumes that the cause of the low-temperature jumps is a thermomechanical instability, i.e., the onset of brief local overheatings, which lead to a sharp drop in the flow stress. Such overheatings can arise at low temperatures on account of the localization of the deformation, an increase in the flow stress, and a lowering of the thermophysical characteristics (specific heat, thermal conductivity). The main argument in favor of this interpretation is apparently the detection of a temperature spike at the jump. This hypothesis, which is comparatively easy to formalize, has been used as the basis for a large number of detailed theoretical studies, in which the investigators have determined the criteria of instability, the existence region, and the dependence of the stress σ_{cr} and strain ε_{cr} at the onset of the LJD on the temperature and size of the sample. Let us cite the first papers published by the various authors.[3–9] It should be emphasized that the hypothesis of a thermomechanical instability can be realized only in
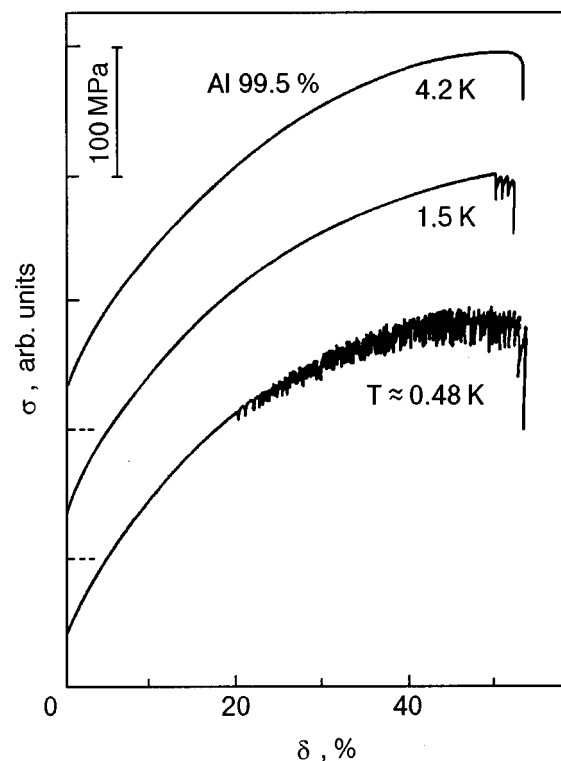

FIG. 1. Tension curves of 99.5% pure polycrystalline aluminum in the normal state. For clarity the curves have been shifted by 100 MPa. The strain rate was $1 \times 10^{-4} \, \text{s}^{-1}$.

the case when the plastic deformation is a thermally activated process.

The second hypothesis, which was proposed in Ref. 10, might be called the dislocation hypothesis. It assumes that in the deformation process the cross slip, which is hindered at low temperatures, is accompanied by the formation of dislocation pileups, the breakaway of which at high local stresses is synchronized in time and, integrated together, leads to a macroscopic jump in the stress. The hypothesis of Ref. 10 is supported by considerable indirect experimental evidence (the sensitivity of the LJD to the structure, impurities, and orientation and the presence of LJD in the case of a positive temperature sensitivity of the stress). The existence of dislocation pileups has been confirmed by direct electron-microscope observations. Unfortunately, this hypothesis has not been the subject of theoretical investigations.

To facilitate progress in elucidating the nature and specific mechanisms of the LJD it would be desirable to do some new experiments which would permit making controlled changes in a single sample subjected to deformation. From this standpoint superconductors are attractive in that they undergo fundamental changes at the transition temperature—one can strain the same sample in different electronic states. The superconducting transition can be made to occur during straining, including during jumplike deformation. In this case the flow stress changes by a fraction of one percent on account of the decrease in the electron drag on the dislocations, but the thermal conductivity of the sample decreases (or sometimes increases) very substantially. Finding out how the superconducting transition influences the LJD, if at all, will lend preference to one of the hypotheses. For some time this transparent idea could not be implemented because of technical difficulties: in superconductors with relatively high T_c (e.g., in lead and its alloys) the jumplike deformation arises, as a rule, near ~ 1 K. In materials in which the jumplike deformation is well developed at 4.2 K (e.g., in aluminum and its alloys) T_c is extremely low (~ 1 K). The creation of a new straining technique[11] has made it possible to broaden the interval of measurements to 0.4 K.

By now there is a sufficient amount of experimental material that one can systematize the data and understand the general regularities in the influence of the superconducting transition on the LJD. We shall see that the result is always qualitatively the same: in the superconducting state the macroscopic jumplike deformation is either absent or substantially less developed than in the normal state. An analysis of the observed regularities and a comparison with the existing hypotheses is the subject of this review article.

1. FIRST EXPERIMENTS

The question of the influence of the superconducting transition on the jumplike deformation was first raised, we believe, in Ref. 4, for single crystals of niobium. The experiment consisted in the straining of several samples of the same purity and close to the same orientations of the axes of tension, at temperatures below T_c. Some of the samples were strained entirely in the normal state (the samples were immersed in a magnetic field above the critical field H_c of the superconducting transition), and others in the supercon-
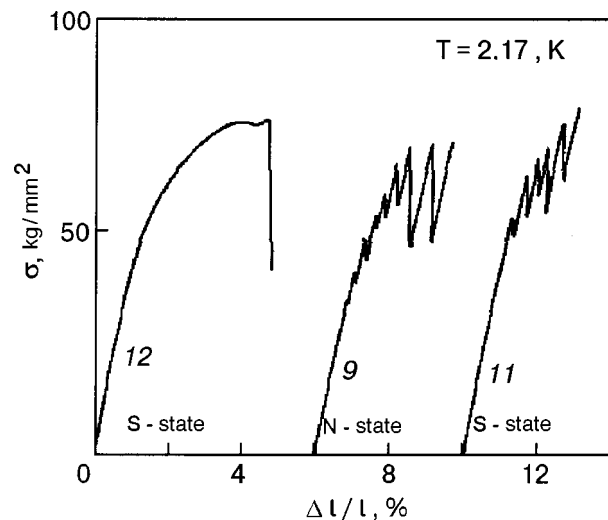

FIG. 2. Tension curves of niobium single crystals with nearly the same orientations of the axes of tension in different states; $T = 2.17$ K, $\dot{\varepsilon} < 10^{-4}$ s^{-1} (Ref. 4).

ducting state. At 2.17 K the shape of the tension curves differed noticeably (see Fig. 2), and the curves with a jumplike deformation had different values of the shear stress τ_c at the start of the jumplike deformation. In the N state the stress jumps started earlier ($\tau_{cN} = 165$ MPa) than in the S state ($\tau_{cS} = 208$ MPa). When the same samples were found in the S state the jumplike deformation was not observed at all. The result obtained at 4.2 K turned out to be less definite, since the difference was not large. The authors stated (no graphs or numbers were given) that at 4.2 K the value of τ_{cS} was slightly lower than τ_{cN}, i.e., the effect was the opposite. The reliability of the conclusions was lowered by the fact that the experiments were done on different samples, which differed in the orientations of the axes of tension. In measurements on the same samples but with a change of state in the course of the straining, more definite results were obtained in Ref. 12, for lead and its alloys. In the normal state at tensions near the failure the strain occurred in jumps (Fig. 3). The superconducting transition leads either to vanishing of the jumps or to a substantial decrease in their amplitudes [Fig. 3b]. However, in the investigated temperature interval (down to 1.65 K) the jumplike deformation was not always observed, and it often took place beyond the boundary of uniform elongation.

Another of the first papers was Ref. 13, in which a microscopic jumplike deformation was observed, with an amplitude of the jumps that was $\sim 0.01\%$ of the flow stress τ. The effect of the superconducting transition turned out to be opposite to that which arose under conditions of macroscopic jumplike deformation. This result is analyzed in Sec. 4, and it is shown that the observed regularities are evidence that these are a different kind of jump. Thus for elucidating the effect of the superconducting transition on the jumplike deformation, one generally needs systematic detailed studies for $T < 1$ K.

2. EXPERIMENTAL TECHNIQUE

The objects of study were superconductors in which a well-developed jumplike deformation was observed at helium temperatures. The investigated materials included pure
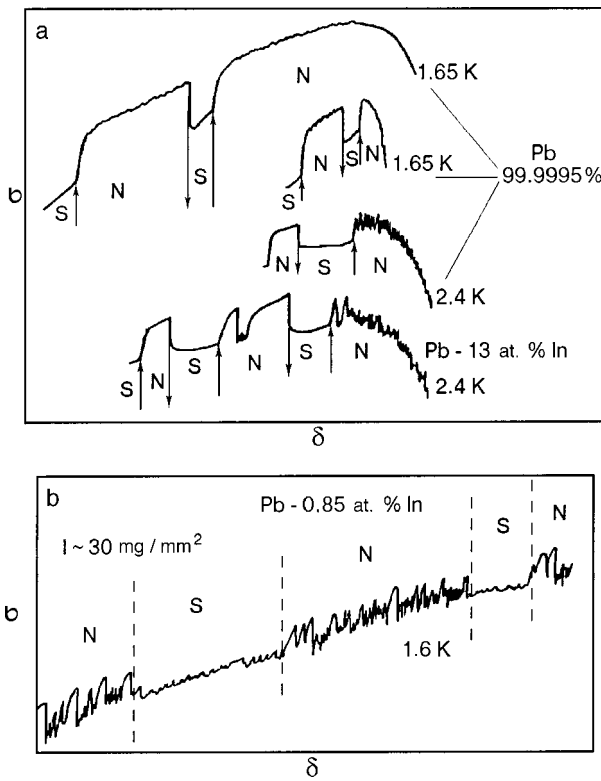
FIG. 3. Portions of the tension curves for high-purity lead (99.9995% Pb) and the alloys Pb–13 at.% In (a) and Pb–0.85 at.% In (b) with multiple *SN* and *NS* transitions; $\dot{\varepsilon} = 7 \times 10^{-4}$ s^{-1}, $T = 1.6$–4.2 K (Ref. 12).

metals (Al, Pb, In), alloys (In–Pb, Pb–In, Al–Mg, Al–Mn, Al–Li, and Sn–Cd), and a composite superconductor Nb–Cu. Both single-crystal and polycrystalline samples were studied under conditions of tension and compression with a constant strain rate $\dot{\varepsilon} = 10^{-4}$–$10^{-5}$ s^{-1}. The majority of the experiments were done in the interval 4.2–0.5 K on a specially built apparatus[11] with a three-step system of cooling with the use of liquid nitrogen, ^{4}He, and ^{3}He. A detailed description of the apparatus and the experimental procedure can be found in Ref. 14. The normal state of the sample below T_c was brought about by applying a magnetic field above the critical value, and the transition of the sample from the S to the N state and back during the course of the straining was brought about by switching the magnetic field on and off.

3. EXPERIMENTAL RESULTS

3.1. Pure metals

One of the most convenient metals for investigating the LJD is aluminum, which was the first object of detailed study of the effect of the superconducting transition on the LJD. Figure 4 shows a portion of the work-hardening curve of 99.5% pure polycrystalline aluminum in a medium of liquid He-3 at $T = 0.5$ K and an enlargement of an element of this curve. The notations N and $\uparrow$ correspond to the times when the magnetic field $H \geqslant H_c$ is switched on, and S and $\downarrow$ to when it was switched off. It is seen that initially a jumplike deformation arises only in the normal state, and the jumps vanish completely upon the transition to the superconducting state; the increase in the flow stress due to the transition of
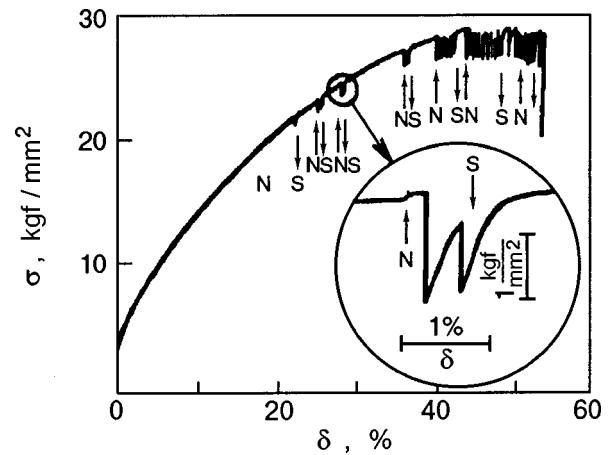

FIG. 4. Curve of tension of 99.5% pure polycrystalline aluminum with multiple changes of state ($\uparrow$ indicates the times at which a magnetic field $H > H_c$ was switched on, and $\downarrow$ the times at which it was switched off), $\dot{\varepsilon} = 1.1 \times 10^{-4}$ s^{-1}, $T = 0.5$ K (Ref. 15).

the sample to the normal state, $\Delta \sigma_{NS}$, is much smaller than the drop in the load at the jump, and a repeated breakdown of the load can occur at a lower stress than in the superconducting state prior to the onset of the jumplike deformation. The jumps in the superconducting state appeared at stresses near the ultimate strength of the sample, the breakdown of the load occurred at stresses larger than at the onset of the jumps in the normal state. This sensitivity of the character of the plastic flow to the electronic state was also observed in single-crystal aluminum (Fig. 5). The dependence of the character of the plastic flow on the electronic state of the sample shows up very clearly in experiments on the deformation of the same samples at the same temperature but in different states. Fig. 6 also shows data of this kind for 99.5% pure polycrystalline aluminum, at 0.8 K in the normal ($\times$) and superconducting ($\bigcirc$) states. One notices two features: a) the number of jumps in the N state is much greater than the number in the S state; b) the work-hardening curve in the N state lies somewhat lower than the curve in the S state. The latter feature is apparently not due to the presence of absence of jumplike deformation but is due (as special studies showed) to a large coefficient of work hardening in the superconducting states. From the curves obtained at different temperatures, the temperature dependence of the number of jumps n in the N and S states was determined (Fig. 7). As
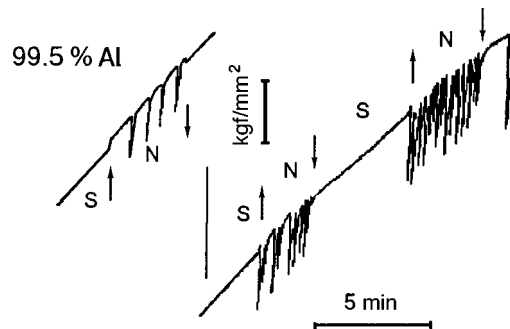

FIG. 5. Portions of the tension curve of 99.5% pure aluminum single crystals with multiple *SN* and *NS* transitions ($\uparrow$ indicates the times of transition to the N state, and $\downarrow$ the transitions to the S states); $\dot{\varepsilon} = 1.1 \times 10^{-4}$ s^{-1}, $T = 0.5$ K.
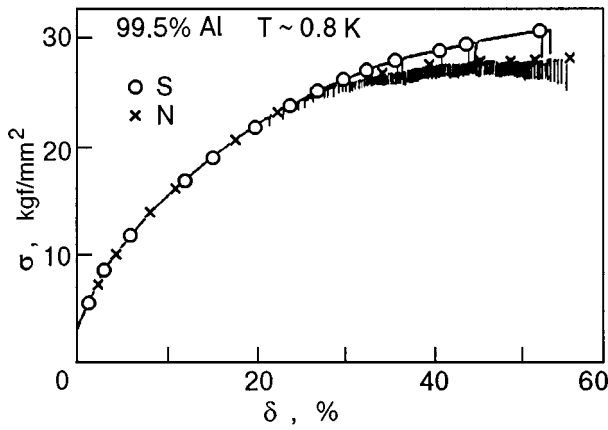
FIG. 6. Tension curves of 99.5% pure polycrystalline aluminum, obtained for straining entirely in the N ($\times$) or S ($\bigcirc$) state; $T = 0.8$ K (Ref. 15).

FIG. 8. Portions of the tension curves for $T = 0.5$ K (a) and compression curves (Ref. 17) at $T = 0.48$ K (b) for 99.9997% pure polycrystalline lead in the region of the onset of the jumplike deformation, with multiple NS and SN transitions, $\dot{\varepsilon} = 10^{-4}$ s^{-1}.

the temperature is lowered, the number of jumps in the N state increases sharply, while the number of jumps in the S state is almost an order of magnitude smaller and depends very weakly on temperature. We note in passing that changing the cooling medium (replacing the He-4 by He-3, which differs strongly in its thermal properties) had practically no effect on the number of jumps.

Studies done on lead[12,13,17] down to 0.5 K revealed the presence of jumplike deformation on two scales. The macroscopic jumplike deformation, which increases monotonically as the temperature is lowered, turned out to be extremely sensitive to the electronic state of the sample (Fig. 8). In highly pure (99.997%) polycrystalline lead the appearance of macroscopic jumps was observed below 1 K. As in aluminum, the LJD arises only in the N state. As the strain increases, the amplitude of the jumps increases and reaches $\Delta\sigma_{NS}$ in order of magnitude, whereas the jumps in Al are always considerably larger than $\Delta\sigma_{NS}$ (see Fig. 4). The amplitude of the load jumps in lead is an order of magnitude smaller (in absolute value) than in aluminum. Special experiments showed that the sensitivity of the LJD of lead to the electronic state does not depend on the type of stress (tension or compression) and is independent of the strain rate in the investigated interval $1 \times 10^{-5} - 1 \times 10^{-4}$ s^{-1}. The micro-
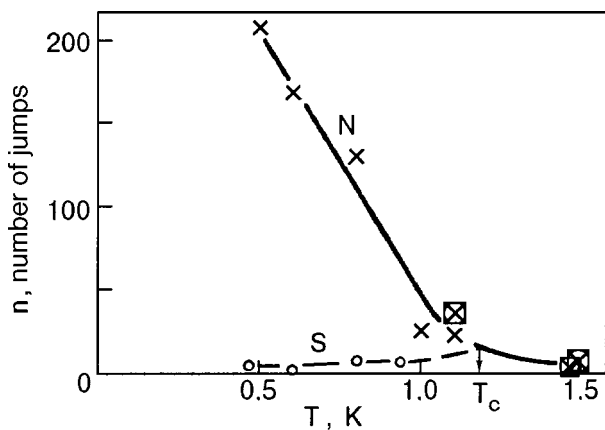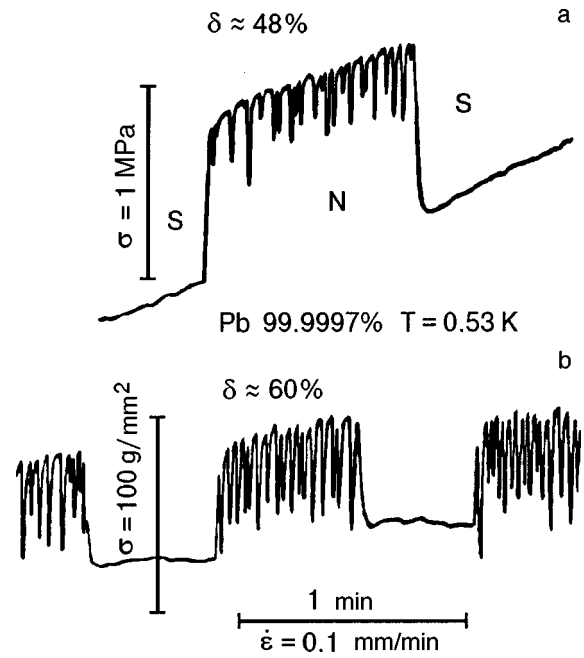
scopic jumplike deformation, its regularities, and a discussion of the possible mechanisms are the subject of Sec. 4.

Indium single crystals have also been investigated in detail.[18] The axis of compression was chosen midway between the [100] and [110] directions to eliminate deformation twinning. At $T < 1.7$ K and $\varepsilon > 30\%$ the deformation is jumplike. The character of the LJD depends on the degree of strain and the electronic state of the sample. The first jumps appear in the N state (Fig. 9). Their frequency increases as the strain increases. At a certain degree of strain, individual jumps begin to appear in the S state as well. These are distinguished by large segments of monotonic deformation (not shown in the figure). At a certain stage the deformation is jumplike in both the N and S states, but the amplitude of the

FIG. 7. Temperature dependence of the number of jumps in the N ($\times$, $\boxtimes$) and S ($\bigcirc$) states; $\times$, $\bigcirc$—experiments in liquid He-3; $\boxtimes$—in liquid He-4 (Ref. 15).

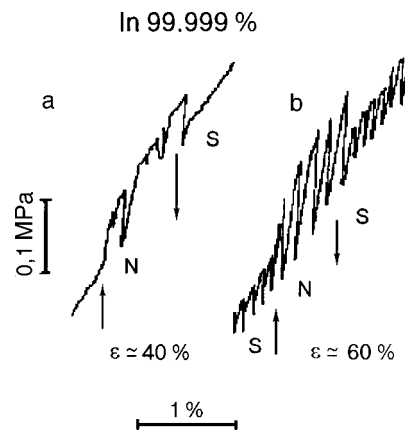FIG. 9. Portions of the compression curve for 99.999% pure indium single crystals in the region of the start of the jumplike deformation (a) and in the region of intense jumplike deformation (b); $\uparrow$ indicates the times at which the magnetic field was switched on (N state), and $\downarrow$ the times at which it was switched off (S state); $\dot{\varepsilon} = 2 \times 10^{-5}$ s^{-1}, $T = 0.48$ K (Ref. 18).
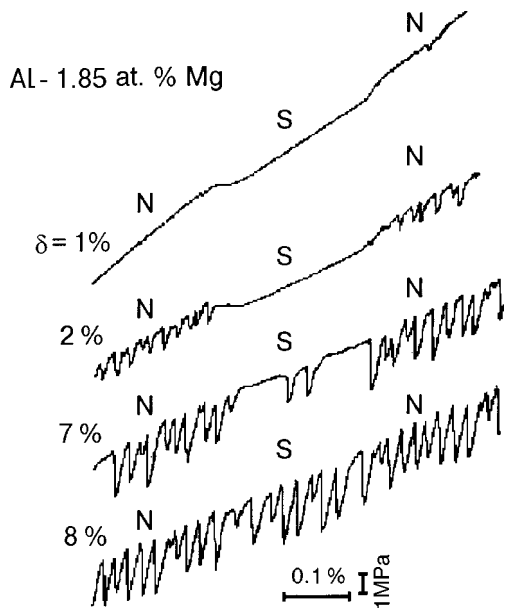
FIG. 10. Portions of the tension curve for polycrystalline Al–1.85 at.% Mg when the electronic state of the sample was changed in the course of the straining; $\dot{\varepsilon} = 1.1 \times 10^{-4}$ s^{-1}, $T = 0.48$ K (Ref. 19).

TABLE I. Parameters of the jumplike deformation of polycrystalline aluminum alloys in the normal and superconducting states.

Alloy	T, K	σ_c, MPa	ε_c, %	n
	4.2	366	37.8	9
	2.5	256	17.0	118
Al-1.4 at. % Mg				
	0.5 (*N*-state)	185	9.2	430
	4.2 (*S*-state)	252	10.4	333
	4.2	366	26.6	19
	2.5	261	12.8	192
Al-1.85 at. % Mg				
	0.5 (*N*-state)	164	4.0	456
	4.2 (*S*-state)	200	8.1	322
	4.2	–	–	–
	2.5	290	9.7	25
Al-1.23 at. % Mg				
	0.5 (*N*-state)	172	2.8	303
	4.2 (*S*-state)	200	4.0	245

Note: σ_C is the stress at which the jumplike deformation begins (the first jump); ε_c is the strain at the start of the jumplike deformation (first jump); n is the total number of jumps.

jumps in the *N* state is approximately 2.5 times larger. The lower level of the load jump does not depend on the state of the sample.

3.2. Alloys

The first measurements were made on alloys of aluminum with magnesium (Al–1.4 at.% Mg; Al–1.85 at.% Mg) and manganese (Al–1.23 at.% Mn).[19] At low temperatures these alloys exhibit a well-developed jumplike deformation, which for $T < 1$ K is occurs togetherr with superconductivity. Figure 10 shows parts of the tension curve of polycrystalline samples of the alloy Al–1.85 at.% Mg, corresponding to different degrees of strain, with the state of the sample changed repeatedly in the process. It is clearly seen that at the start of the straining the jumps arises only in the *N* state, and the jumps vanish completely when the sample is put into the *S* state. As the strain increases, the jumps begin to appear in the *S* state as well. Their amplitude and frequency increase with increasing strain, after a certain stage reaching the value and frequency observed in the *N* state. Typically the amplitude of the first jumps in the *S* state is considerably greater (8.9 MPa, Al–1.4 at.% Mg) than the amplitude of the first jumps in the *N* states. The results of a study of these alloys at relatively small strains turn out to be qualitatively similar to those for experiments with pure metals, and at large strains the sensitivity to the *NS* transition vanishes; this is different from the typical behavior for pure metals. This difference is apparently due to heating of the sample to T_c in the case of alloys, in which the flow stresses are substantially larger, and at the comparatively low cooling power of the apparatus, ~ 3 mW,[14] can lead to overheating. If it is assumed that up to 90% of the energy expended on plastic deformation is released in the form of heat, then in an Al sample with dimensions of $15 \times 3 \times 1$ mm at a strain rate of 10^{-4} s^{-1} near the yield stress, 16 MPa, the rate of heat release is 0.2 mW, and at the ultimate strength, equal to 290 MPa, it is almost 4.5

mW. In polycrystalline samples of the alloy Al–1.8 at.% Mg the rate of heat release increases to 1.1 and 5.1 mW, respectively, starting to exceed the cooling capacity of the apparatus. Because of this growth of the heat release and the thermal spikes, at the time of the jumps there can be a very slight heating (0.5–0.6 K) which is nevertheless capable of causing a transition of the sample to the normal state. The dependence of the character of the plastic flow on the electronic state is clearly seen in experiments on the same sample at the same temperature but in different states (see Table I). At 0.5 K in the alloy Al–1.4 at.% Mg one observes 430 jumps in the *N* state and 333 jumps in the *S* state; in Al–1.8 at.% Mg there are 453 jumps in the *N* state and 322 in the *S* state, and in Al–1.23 at.% Mn there are 303 and 245 jumps, respectively. The stresses and strains at the first jump show similar differences. At the same time, the maximum homogeneous strain remains practically the same.

A detailed investigation of the LJD was done in quenched polycrystalline samples of the binary alloys Al–Li at 3.8, 7.0, and 10.4 at.% Li. The dimensions of the parts subjected to tensile straining were $15 \times 3.0 \times 0.8$ mm, and the average grain size was 0.6 mm. The low-temperature jumplike deformation arises in the interval 10–4.2 K. Its main regularities are as follows. With increasing Li concentration it begins at lower strains, and the frequency and amplitude of the jumps increase. For example, at 4.2 K the jumps in the alloy Al–3.8 at.% Li begin after a 35% strain, in Al–7.0 at.% Li they begin after 25% strain, and in Al–10.4 at.% Li they begin after a 21% strain. Lowering the temperature has an analogous effect: in the alloy Al–3.8 at.% Li at a temperature of 4.2 K the jumps begin after a 35% strain, at 2.2 K they begin after a 16% strain, and at 0.5 K they begin after a 10% strain. At a fixed temperature and impurity concentration the amplitude and frequency of the jumps increase gradually with increasing strain, and the intervals between jumps become shorter. Figure 11 shows the dependence of the amplitude $\delta\sigma$ of the jump on the degree of strain ε in the alloy Al–3.8 at.% Li at several temperatures. As the tem-
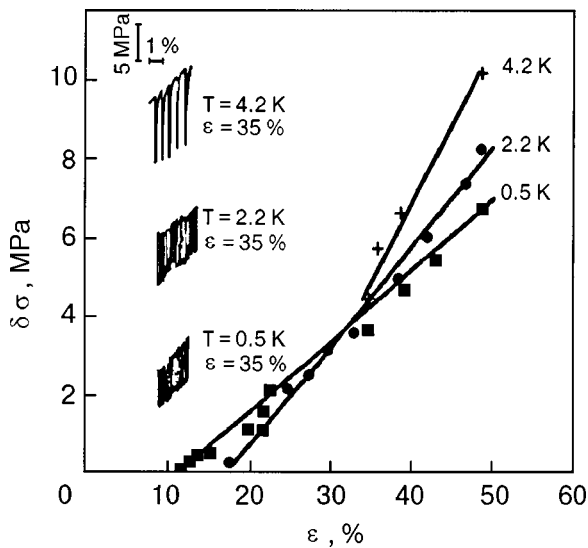
FIG. 11. Dependence of the amplitude $\delta\sigma$ of the jumps on the degree of strain ε at various temperatures in samples of the alloy Al–3.8 at.% Li in the normal state (Ref. 20).

perature decreases there is a characteristic decrease in the rate of growth of the amplitude of the jumps with increasing strain, and therefore the maximum amplitudes (at equal strains) are observed at 4.2 K. The data in Fig. 11 were obtained for a sample strained in the N state. Figures 12 and 13 show the influence of the electronic state of the sample on the jumplike deformation. Upon the transition of the sample to the S state the LJD are absent or markedly diminished, especially at low strains. In the N state the jumps begin at lower degrees of strain ε than in the S state. Starting from a certain strain, the NS transition is not reflected in the character of the plastic flow, as is seen in Fig. 13, which shows the curves of the amplitudes $\delta\sigma(\varepsilon)$ of the jumps for samples in the S state. This is probably due to macroscopic heating of the sample, bringing its temperature above T_c, i.e., a sample strained at 0.5 and 0.9 K is heated to $T_c \approx 1.2$ K, i.e., by only a fraction of a degree. It is possible that this heating is due to the brief temperature spikes (accompanying the breakdown of the load), which in Al–Li at 7 K is 5–8 K (Ref. 21). The

results mentioned above pertain to pure metals and alloys with the fcc structure. In those materials the plastic deformation is controlled by the interaction of dislocations with local obstacles.

In bcc and hcp metals and alloys the low-temperature jumplike deformation has been much less studied, since in those materials deformation twinning often develops as the temperature is lowered, and this is reflected in specific jumps on the work-hardening curve. For studying the LJD in crystals in which the plastic deformation is governed by the motion of dislocations through Peierls barriers, specially oriented single crystals of tin and Sn–Cd alloys turn out to be extremely convenient objects, and they were investigated in detail in Ref. 22. Single crystals of Sn–Cd alloys with 0.01, 0.04, 0.21, and 0.53 at.% Cd were studied. These concentrations lie in the region of the solid solution. The dimensions of the strained part of the sample were $1.5 \times 4.5 \times 25$ mm. The orientation of the axis of tension corresponded to the $\langle 110 \rangle$ direction, which was favorable for slip in the system $(100)\langle 010 \rangle$. It is important that for this orientation the plasticity is preserved as the temperature is lowered, and in this way the bcc-crystal analog, chosen from the standpoint of the deformation mechanism, differs from bcc metals and alloys, which, as a rule, become brittle at low temperatures. Highly pure samples of β-tin (99.9995% Sn) maintain a smooth plastic flow all the way down to 0.5 K (Fig. 14). Doping of the tin with cadmium increases the flow stress and the yield stress markedly, and, in addition, below 4.2 K it gives rise to jumplike deformation. The influence of the concentration on the LJD is manifested most clearly at the lowest temperature of the experiment, 0.5 K (Fig. 14). The lower the temperature and the higher the impurity concentration in the alloy, the lower the degree of strain at which the first jumps appear. The frequency of the jumps in the alloy Sn–0.01 at.% Cd increases with the strain, so that the segments of smooth flow become progressively shorter, especially below 1 K. For alloys with a large concentration of Cd (0.04 and 0.21 at.%), in the N state below 1 K the LJD begins directly at the yield stress and immediately takes on a sawtooth character. As the temperature is lowered, the LJD in the alloys develops to a higher degree.
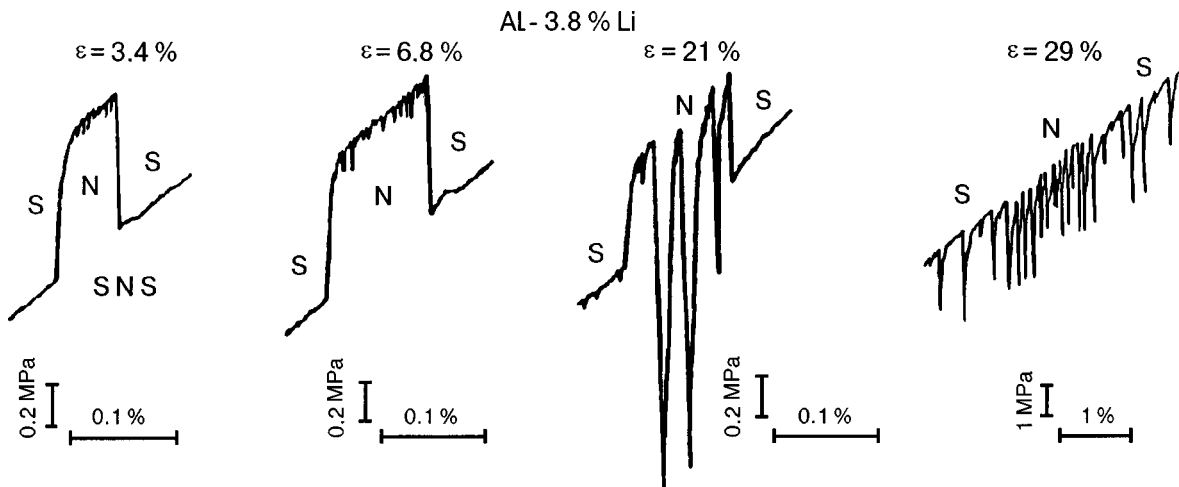

FIG. 12. Portions of the tension curves $\sigma(\varepsilon)$ illustrating the effect of the NS transition on the jumplike deformation of polycrystalline Al–3.8 at.% Li at different degrees of strain; $\dot{\varepsilon} = 1.1 \times 10^{-4}$ s^{-1}, $T = 0.5$ K (Ref. 20).
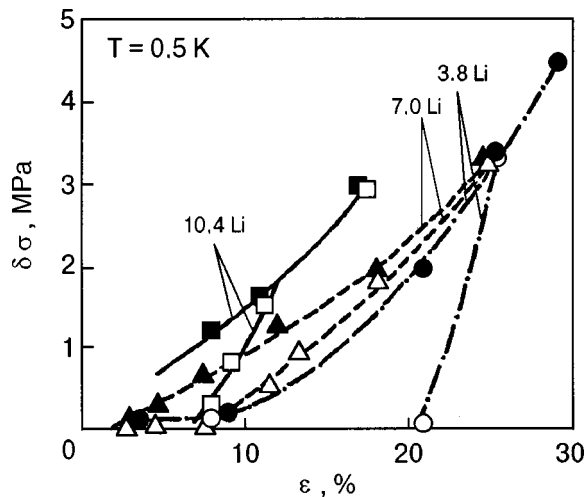
FIG. 13. Dependence of the amplitude $\delta\sigma$ of the jumps on the strain ε in the N (filled symbols) and S (unfilled symbols) states in polycrystalline Al–Li alloys (Ref. 20).

FIG. 15. Tension curves for single crystals of the alloy Sn–0.21 at.% Cd at various temperatures in the normal state. The experiments at 4.2 and 2.9 K were done in gaseous He-3, and those at 1.4 and 0.5 K in liquid He-3. Individual parts of the curves are shown in enlarged scale (Ref. 22).

In the alloy Sn–0.01 at.% Cd the individual jumps in the stress appear already at $T = 3$ K, but only at a strain rate of $\dot{\varepsilon} = 6.6 \times 10^{-5}$ s^{-1}. At lower temperatures the value of the strain corresponding to the first jump decreases from 6–7% to 3–4%. The number of jumps on the work-hardening curve increases from 2–3 at $T = 3$ K to 10–15 at 0.5 K. For the alloy Sn–0.04 at.% Cd isolated jumps are observed already at
4.2 K after a plastic deformation of 1–2%. As the temperature is lowered the number of these jumps increases, and for $T < 0.8$ K they start from the yield point. The alloy Sn–0.21 at.% Cd behaves in a similar way, but the LJD in it arises near the yield point already at 1.4 K. The influence of temperature on the character of the LJD for this alloy is shown in Fig. 15. In the alloy Sn–0.21 at.% Cd, besides the regularities of the LJD common to all the alloys studied, there are two features not shared by the other alloys. First, at 0.5 K the frequency of the jumps decreases with increasing strain rather than increasing, as is usually the case, and segments of smooth flow appear. Second, besides the stress jumps with an amplitude of the order of 1–2 MPa, which are identified as macroscopic, there are jumps with an amplitude an order
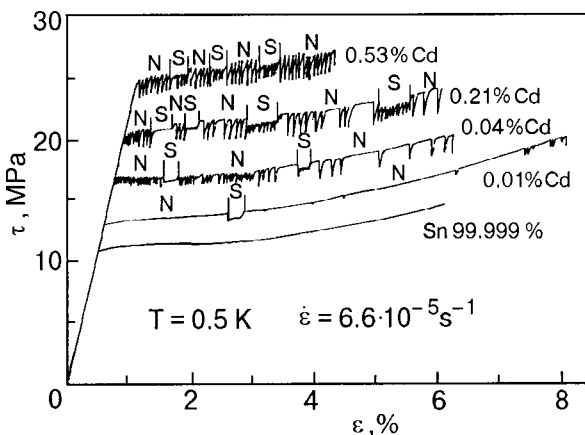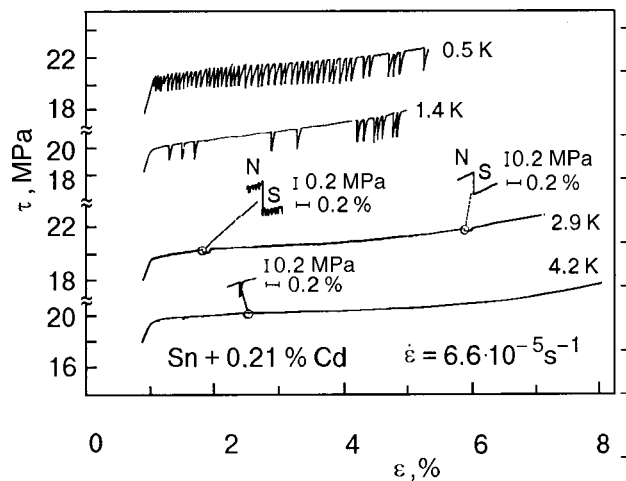

FIG. 14. Tension curves for single crystals of pure tin and alloys of tin with cadmium. During the straining the electronic state of the samples was changed many times; $\dot{\varepsilon} = 6.6 \times 10^{-4}$ s^{-1}, $T = 0.5$ K (Ref. 22).

of magnitude smaller (0.1 MPa) at 2.9 and 0.5 K. This microscopic jumplike deformation will be discussed separately in Sec. 4. The transition of the samples of the Sn–Cd alloys from the normal to the superconducting state under conditions of the LJD leads to substantial changes in the character of the deformation (Fig. 14 and 15). This influence is substantially correlated with the effect of such factors as the degree of strain, the impurity concentration, and the temperature. For the developed LJD, starting from the yield point (0.5 K), e.g., in the alloy Sn–0.53 at.% Cd the saw-tooth character of the deformation is preserved at the NS transition, but the amplitude of the jumps decreases considerably (see Fig. 14).

The most complex and multifaceted influence of the NS transition on the character of the LJD is realized in alloys with an intermediate cadmium concentration. From the curves for the alloy Sn–0.21 at.% Cd in Figs. 14 and 15, we can discern the following experimental regularities:

a) Near the yield point the LJD of the sample in the normal state goes over to a smooth flow upon transition to the superconducting state.

b) As the strain is increased, jumps appear in the S state also, but with a lower amplitude.

c) For the alloys with 0.04 and 0.21 at.% Cd the frequency of the jumps decreases with increasing strain in the N state, and extended segments of smooth flow appear; at the superconducting transition the character of the jumplike deformation changes substantially.

In the alloy with 0.04 at.% Cd the jumps practically vanish in the S state, and in the alloy with 0.21 at.% Cd their amplitude decreases substantially. Since these regularities were observed under conditions of multiple changes of the state of the sample, one wonders to what extent the LJD is influenced by the conditions of such an experiment. We therefore did experiments in which each of two samples was strained at 0.5 K in one of the states (Fig. 16). It is seen that all of the regularities listed above are preserved.
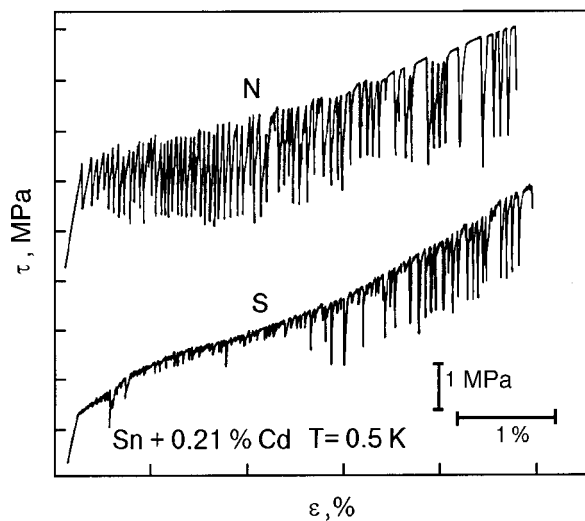
FIG. 16. Tension curves for samples of the alloy Sn–0.21 at.% Cd at 0.5 K in the N and S states (Ref. 22).

3.3. Composite superconductor

The effect of the superconducting transition on the jumplike deformation has also been noted in the tensile straining of multifiber copper–niobium composites obtained *in situ*.[23] The objects of study were Cu–40 wt.% Nb composites with a macrostructure in the form of a copper slab armored by strips of niobium several millimeters long and with transverse dimensions of 30×3 μm. The second critical field of this composite was ~ 9 kOe (0.9 T). Accordingly, in the process of straining at a rate of 1.3×10^{-5} s^{-1} the superconductivity was destroyed at a field of 1.2 T. At 4.2 K the work-hardening curve exhibits jumplike deformation at the stage where the deformation of the niobium begins. This deformation in annealed samples turned out to be sensitive to the electronic state of the sample (Fig. 17). Whereas in the S state the individual jumps alternate with extended segments of stable deformation, in the N state they follow continuously one after the other. Evidently this result can be attributed to the influence of the NS transition on the LJD of niobium.
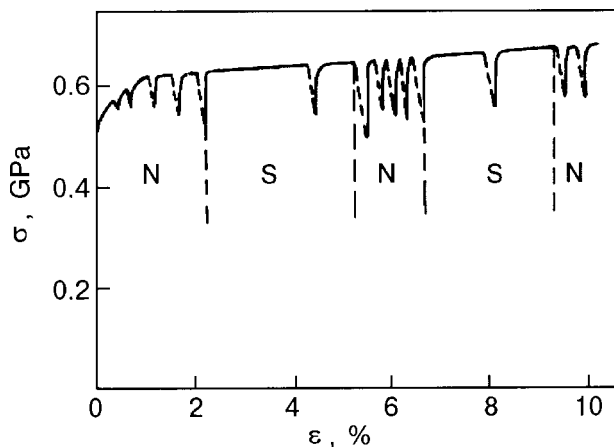

FIG. 17. Tension curve of a multifiber superconducting composite Cu–40 wt.% Nb obtained *in situ*. The electronic state of the sample was changed in the course of the straining; $\dot{\varepsilon} = 1.3 \times 10^{-5}$ s^{-1}, $T = 4.2$ K (Ref. 23).
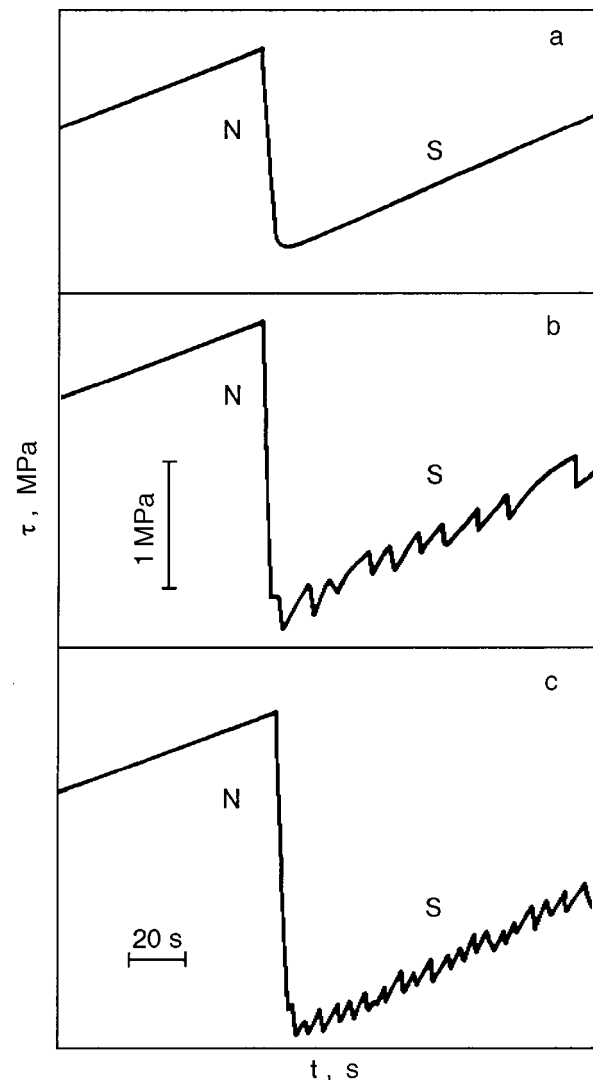
FIG. 18. Appearance of microscopic jumplike deformation τ in single-crystal lead in the superconducting state at $T = 4.2$ K, $\tau = 12.7$ MPa (a); $T = 2.6$ K, $\tau = 14.3$ MPa (b); $T = 1.9$ K, $\tau = 15.2$ MPa (c). The indicated stresses refer to the N state immediately prior to the superconducting transition (Ref. 24).

4. MICROSCOPIC JUMPLIKE DEFORMATION

Before generalizing the results presented, we must consider one more phenomenon occurring at low temperatures. Besides the low-temperature jumplike deformation on the macroscopic scale (the amplitude of which can reach tens of percent of the level of the flow stress), which has been the subject of numerous studies and the foregoing analysis, some experiments have detected a jumplike deformation of substantially smaller scale (of the order of 0.01% of the level of the flow stress). The first mention of microscopic jumps is found in Ref. 13. A microscopic jumplike deformation was observed in the compression of single-crystal and polycrystalline samples of Pb and Pb–In alloys at a temperature below 3–3.5 K. The detected jumps in the load appeared after a preliminary loading by several percent, their depth increasing with the strain. Upon the destruction of superconductivity the jumps vanished, and the strain curve became smooth. The microscopic-scale jumplike deformation was observed most clearly in the straining of pure lead (Fig. 18). The relative jump $\delta\sigma/\sigma$ was several hundredths of a percent. On

doping of the lead with indium, $\delta\sigma$ decreased, and at an In concentration above 5 at.% the jumplike deformation was practically absent. The depth of the jumps and their frequency depend on temperature in a complicated way, having a maximum at $T \approx 2.5$ K.

The regularities mentioned above differ substantially from those which obtain on the macroscopic scale. We recall that the macroscopic jumps become stronger as the temperature is lowered, at least to 0.5 K, while the microscopic jumps have a nonmonotonic temperature dependence, which in lead starts at ~ 3 K and goes to zero at ~ 1 K. The macroscopic jumplike deformation is enhanced as the concentration of the dopant increases, while the microscopic version becomes weaker, and in Pb–In it vanishes at 5 at.% In. This result was confirmed in Refs. 17 and 24 for single-crystal and polycrystalline lead. In Ref. 17, thanks to the possibility of expanding the temperature interval to 0.4 K, the jumps on both the macro- and microscopic scales were able to be observed. In a finding of fundamental importance, the influence of the superconducting transition on the jumplike deformations on the two scales was different: the superconducting transition led to weakening (or vanishing) of the macroscopic jumplike deformation, while the microscopic jumplike deformation appeared only in the S state.

All of these properties of the microscopic LJD suggest that this is a different type of jump which is governed by a different mechanism. Theoretical estimates and the analysis presented in Ref. 24 as to whether the criteria are met for one or another mechanism permit the conclusion that the microscopic jumps are a manifestation of inertial effects. Thus the microscopic jumplike deformation must be treated as a special phenomenon that does not have relevance to the regularities described in the previous Section. In a study of the jumplike deformation in the alloys Sn–Cd, in addition to the macroscopic jumps described above, some microscopic breakdown of the load were also detected. They we observed only in the alloy 0.21 at.% Cd at temperatures of 0.5 and 2.9 K; the amplitude of the microjumps is practically independent of the strain and temperature. Studies of the microscopic LJD in the alloy Sn–0.21 at.% Cd showed that at 2.9 K it is practically insensitive to the NS transition. At 0.5 K such measurements in pure form are difficult to make on account of the developed macroscopic LJD. The only thing that has been established is that microjumps are present at low strains in the S state and are absent in the N state at large strains (see Fig. 15).

5. HYPOTHESES AS TO THE EFFECT OF THE SUPERCONDUCTING TRANSITION ON THE JUMPLIKE DEFORMATION

In the first experimental study,[4] in which the LJD was investigated in niobium single crystals in the normal and superconducting states, the differences were linked with the value of the overheating of the sample during the straining. Taking into account the changes in the thermophysical characteristics at the NS transition, the authors observed that at 2.17 K the overheating in the N state, ΔT_0^N, is higher than the overheating in the S state, ΔT_0^N, whereas at 4.2 K it was the other way around, $\Delta T_0^N \le \Delta T_0^S$, which agreed qualitatively with the experimental findings. It followed, however,

that the character of the influence of the superconducting transition on the jumplike deformation is specific to each particular case (material, temperature, thermophysical characteristics) and there cannot be any general regularities.

In a theoretical paper[25] a criterion of instability of the thermally activated plastic deformation and thermal conductivity was obtained with allowance for the geometry of the sample and the heat exchange with the coolant. Analysis showed that steady-state uniform straining can occur only at stresses below a certain critical stress τ_c, which has the form

$$\tau_c = \frac{\lambda k T_0^2}{\dot{\varepsilon} w l^2} h, \tag{1}$$

where λ is the thermal conductivity of the sample, k is Boltzmann's constant, T_0 is the temperature of the coolant, $\dot{\varepsilon}$ is the rate of plastic deformation, $w(\tau)$ is the activation energy of the process, l is the dimension of the sample (the radius in the case of a cylinder, or the thickness in the case of a slab), and h is a parameter governing the heat exchange with the surrounding medium.

The expression for τ_c given above corresponds to the start of the jumplike deformation (the first jump). The mechanism responsible for the reproducibility of the jumps along the strain curve must include the dependence of W on the degree of strain (stress). Therefore, the development of avalanches and the calculation of the size of the stress jump are more complicated problems which were not considered in Ref. 25, where the possible changes in the instability at the superconducting transition were indicated on the basis of an analysis of Eq. (1). At the NS transition the thermal conductivity λ and the factor $\dot{\varepsilon}_0$ change sharply on account of the change in the electron drag coefficient for dislocations, B_e, since $\dot{\varepsilon}_0 \sim 1/B_e$, and $B_e^N > B_e^S$ always. In most cases $\lambda_S < \lambda_N$ (although there are a few alloys in which $\lambda_S > \lambda_N$; see Ref. 26). If these relationships are used in expression (1), it turns out that, as a rule, $\tau_c^S < \tau_c^N$, i.e., upon the transition to the superconducting state the jumplike deformation of the sample should start at lower stresses than in the normal state. However, later experiments (see Sec. 3) showed that this is not what happens. The macroscopic jumplike deformation in the superconducting state becomes weaker or vanishes entirely. At large strains in high-strength materials the LJD is insensitive to the superconducting transition; this is apparently because of the small heating and not a consequence of the physics of the phenomenon.

The disagreement between the theory based on low-temperature instability of the deformation and the experimental data stimulated the practically simultaneous publication in 1986 of several theoretical papers[23,27,28] devoted to investigation of the influence of the superconducting transition on the jumplike deformation. Essentially those papers advanced the same hypothesis: along with the the thermophysical characteristics, the characteristics of the plasticity, in particular, the temperature dependences of the yield strength and flow stress, can change at the superconducting transition. Qualitative arguments are presented in Ref. 23. If the thermally activated plastic deformation is described by the Arrhenius law,

$$\dot\varepsilon = \dot\varepsilon_0 \exp\left[-\frac{\Delta H(\sigma^*)}{kT}\right], \qquad (2)$$

where $\dot\varepsilon$ is the rate of plastic deformation, $\dot\varepsilon_0$ is the pre-exponential factor, σ^* is the effective stress, and T is the temperature, at a constant effective voltage the temperature sensitivity of the rate of plastic deformation can be written in general as

$$\frac{\partial \ln \dot\varepsilon}{\partial T} = \frac{\partial \ln \dot\varepsilon}{\partial T} + \frac{\Delta H}{kT^2}. \qquad (3)$$

In the normal state $\dot\varepsilon_0$ is practically independent of temperature and, consequently, $\partial\ln\dot\varepsilon/\partial T \approx \Delta H/(kT^2)$. Regardless of what process is limiting the rate of heat removal and of whether or not the localization of the slip is taken into account, the criterion for the onset of jumplike deformation due to thermomechanical instability will have the form

$$A(\Delta H/kT^2) > 1. \qquad (4)$$

The positive factor A contains the flow stress, strain rate, and the geometric and thermophysical parameters of the sample, which control the rate of heat removal. The presence of the factor $\Delta H/kT^2$ in criterion (4) is due to the influence of temperature on the rate of plastic deformation. In the superconducting state the temperature dependence of $\dot\varepsilon$ cannot be neglected, since $\dot\varepsilon_0 \sim 1/B$ (Ref. 29; B is the dynamic drag constant for dislocations, including the electronic component), i.e., the first term in expression (3) can be greater in absolute value than the second term. In that case the criterion of instability in the superconducting state must be written in the more general form

$$A\frac{\partial \ln \dot\varepsilon}{\partial T} = A\left(\frac{\partial \ln \dot\varepsilon_0}{\partial T} + \frac{\Delta H}{kT^2}\right) > 1. \qquad (5)$$

In the superconducting state the large negative term $\partial\ln\dot\varepsilon_0/\partial T$ cannot be neglected, and therefore the quantity in brackets in (5) decreases considerably or even becomes negative, and then the criterion of thermomechanical instability is not fulfilled. Thus in the superconducting state it is in principle possible to have a situation in which the LJD will vanish. Since specific estimates for the particular experimental conditions and materials were not made in Ref. 23, the situation under real conditions remained unclear.

A detailed investigation with an attempt at a quantitative analysis was given in Ref. 27. The initial formulation of the problem was the same as in Ref. 23, but it included a calculation of the stress for the onset of instability, τ_c. The temperature dependences of τ_c^N and τ_c^S were constructed for crystals that are fairly pure (Fig. 19). The relations between the physical parameters λ_S and λ_N and the parameters characterizing the interaction of dislocations with barriers, E_0 and $E_0^* \approx 5(b^3 GT_c)^{1/2} \lesssim 1$ eV (b is the Burgers vector, G is the shear modulus, and T_c is the superconducting transition temperature), determine whether there are two, one, or no crossing points of the curves τ_c^N and τ_c^S for $T < T_c$. For example, for lead and aluminum the characteristic interaction energy of dislocations with barriers has values $E_0 \ll 1$ eV, and $\lambda_S < \lambda_N$. Therefore, the situation shown for τ_c^S by curve 4 in Fig. 19 should be realized. This means that there exist temperatures (near T_c and T_b, $(T_c - T_b)T_c^{-1} < 0.4$) at which
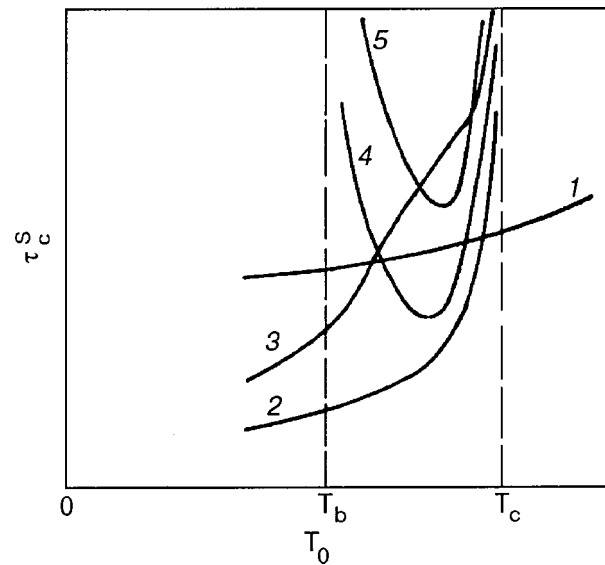

FIG. 19. Critical stress τ_c for the onset of unstable plastic flow for crystals in the normal τ_c^N (1) and superconducting τ_c^S (2–5) states as a function of the temperature T_0 of the medium: $\lambda_S < \lambda_N$, $\varepsilon_0 > \varepsilon_0^*$ (2); $\lambda_S > \lambda_N$, $\varepsilon_0 > \varepsilon_0^*$ (3); $\lambda_S < \lambda_N$, $\varepsilon \leqslant \varepsilon_0^*$ (4); $\lambda_S \leqslant \lambda_N$, $\varepsilon_0 < \varepsilon_0^*$ or $\lambda_S \leqslant \lambda_N$, $\varepsilon_0 > \varepsilon_0^*$ (5) (Ref. 27).

$\tau_c^S > \tau_c^N$, and an intermediate temperature interval in which $\tau_c^S < \tau_c^N$. Thus, as the temperature is lowered, one should observe different influences of the NS transition on the jumplike deformation. In the case of less pure crystals, if $\lambda_S > \lambda_N$, which apparently does not correspond to situation encountered in reality, one has $\tau_c^S > \tau_c^N$ always. Still less pure crystals (dilute alloys) and alloys were not considered.

A theoretical study of the influence of the superconducting transition on the LJD from a quantitative standpoint can be found in Refs. 28 and 29. In Ref. 28 the influence of the superconducting transition on the stability of plastic deformation at low temperatures was analyzed in a model based on thermal instability. There it was conjectured for the first time that the temperature dependence of the flow stress can change in the S state, in addition to the changes in the thermophysical characteristics of the material. A previously obtained criterion for the onset of thermal instability of the plastic deformation was used to derive general relations giving the temperature–rate region in which such instability is realized in the N and S states. The relations obtained were used to construct the existence regions in various states of some particular metals—aluminum, niobium, and lead. The region of instability of the deformation of Al is shown in Fig. 20. It follows from this figure that in the S state at a given temperature the LJD is is manifested over a narrower rate interval, and for rates in the interval $5 \times 10^{-4} - 10^{-6}$ s^{-1} the jumplike deformation should not depend on the electronic state of the sample. In niobium the existence region of the LJD in the N state lies inside its existence region in the S state. This means that in terms of the temperature and strain rate the LJD is more developed in the S state. There exists a range of temperatures (<0.9 K) and strain rates ($5 \times 10^{-4} - 10^{-5}$ s^{-1}) in which the LJD does not depend on the state.

Thus, if it is assumed that all the important changes at the superconducting transition are due to the specific heat of the strained sample, the influence of the NS transition can
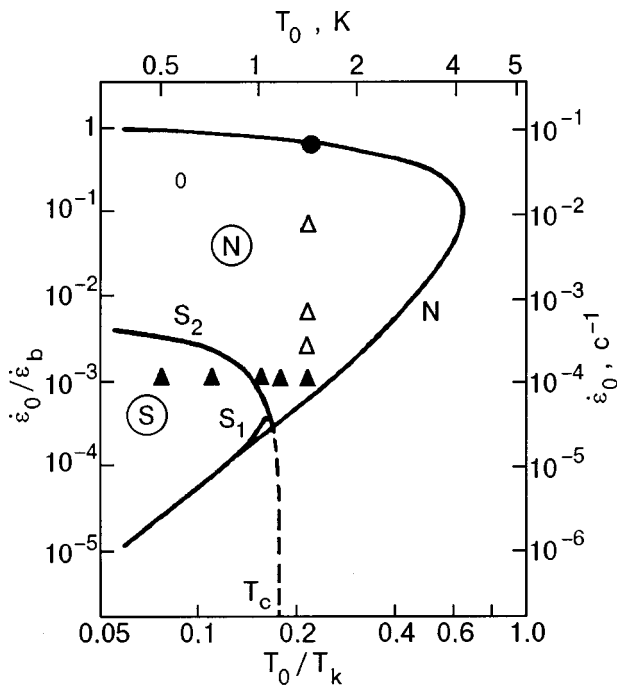
FIG. 20. Calculated temperature–rate existence regions of the jumplike deformation of Al in the N and S states;[28] ▲,△,○—experimental points; $\dot{\varepsilon}_b = 0.1\ s^{-1}$, $T_k = 6.6\ K$ (Ref. 28).

FIG. 21. Temperature dependence of the flow stress for a thermally activated character of the plastic deformation in the normal (1) and superconducting states ($2,3$) of a sample. Curve 2 was constructed on the basis of a calculation of Δ_{SN} according to the fluctuational theory; curve 3 was calculated according to the inertial theory (Ref. 30).

vary greatly, and there might be no sensitivity to the *NS* transition. Later, in Ref. 30, quantitative calculations were done in which the possible change in the sign of $\partial\tau/\partial T$ near the temperature of the superconducting transition was taken into account. The initial assumptions were as follows: in both the normal and superconducting states throughout the entire temperature interval the plastic deformation is of a thermally activated character, with $\partial\tau/\partial T < 0$; starting at T_c, the sign of $\partial\tau/\partial T$ changes because of the decrease in the flow stress at the superconducting transition due to the decrease of the electron drag on the dislocations.[1,2] Quantitative estimates of the value of $\Delta\tau_{NS}$ have been made on the basis of the fluctuational[29] and inertial[31] theories. These were used in Ref. 30 in a determination of the temperature dependence of the flow stress in the S state (see Fig. 21). It is seen that in the case of the fluctuational mechanism the value of $\partial\tau^*/\partial T$ decreases below T_c, but the sign does not change. In the framework of the inertial mechanism there is a segment near T_c with $\partial\tau^*/\partial T > 0$. The functions $\tau(T)$ obtained in Ref. 30 can then be used to obtain the temperature boundaries of the region of thermal instability of the deformation. In the framework of the fluctuation mechanism it is found that the *SN* transition has practically no effect on the thermal instability, whereas in the inertial model there is a temperature interval $(0.54T_c < T < T_c)$ in which the deformation in the S state, unlike the case of the normal state, is stable. This is a consequence of the existence of a positive value of $\partial\tau/\partial T$ at $T < T_c$. From the behavior of the boundary temperatures T_N and T_S as functions of the coolant temperature for this case one can determine the interval of strain rates $\dot{\varepsilon}_N$ and $\dot{\varepsilon}_S$ in which the deformation will be unstable in the N and S states, i.e., one can construct the existence regions illustrated in Fig. 22, which pertain to the situation when $T_c = 0.5T_k$ is lower than the maximum temperature T_{0k}
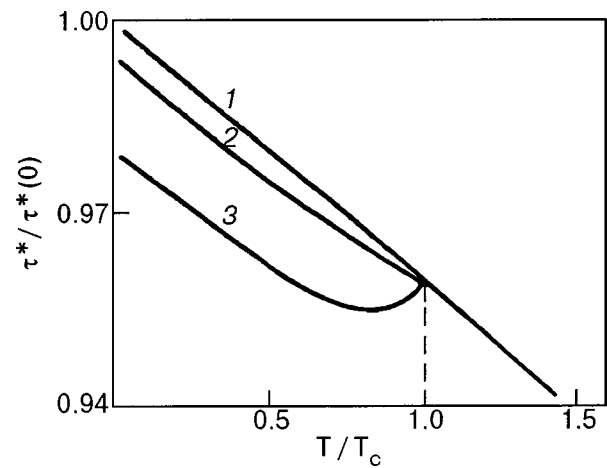
$=0.64T_k$ above which the deformation in the normal state remains stable for any strain rates and temperatures $(T_k = c_K/\gamma_e$, where γ_e is the electronic heat capacity and $c_k \sim \tau S_T/K\chi)$, where K is the stiffness of the machine, χ is the coefficient of work hardening, and $S_T = -(\partial\tau^*/\partial T)_{\dot{\varepsilon}}$. Such a situation is characteristic for superconductors with low T_c and also for high-strength materials with high T_c (e.g., Nb). For metals with high T_c but low strength (e.g., Pb) it can turn out that $T_k < T_c$. In that case a calculation shows that, regardless of the theoretical mechanism of the effect $(\Delta\tau_{NS})$, the region of thermomechanical instability in the N state lies inside the corresponding region for the S state, i.e., the *NS* transition will give rise to the appearance of jumps. Thus the existing theoretical calculations in the model of thermomechanical instability admit both situations in which
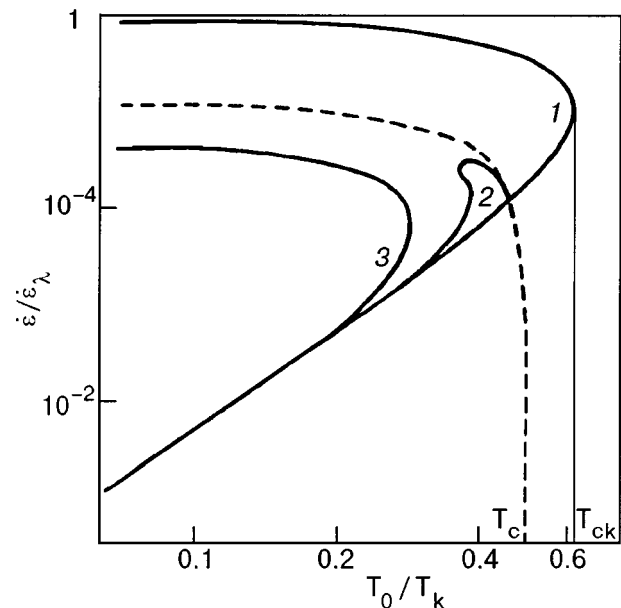

FIG. 22. Calculated temperature–rate regions for the onset of thermal instability of the deformation in the N (1) and S ($2,3$) states of a crystal. The dashed curve denotes the boundary of the existence region of the S state (Ref. 30).

the *NS* transition leads to an enhanced jumplike deformation and situations where the effect vanishes. Under certain conditions the LJD should be insensitive to the superconducting transition.

The dislocation hypothesis exists in the form of general plausibility arguments stated in a discussion of the first studies.[33] This hypothesis is based on an analysis of a situation that can lead to avalanche multiplication or to the motion of dislocations at low temperatures. The hypothesis was put forth in Ref. 10 and was investigated in detail in the framework of a theory of stage III of the work-hardening curve. The analysis treats the case of a crystal containing an appreciable number of dislocations which is plastically deformed through cross slip, which is most effective in fcc and hcp crystals. The process of cross slip of an isolated dislocation is preceded by the drawing of a split dislocation into a line. However, the experimentally measured values of the flow stress τ are insufficient for the drawing of a split dislocation unless it is assumed that the given dislocation is found in a planar pileup of n dislocations. Then the stress acting on the head dislocation is equal to $n\tau$. On the other hand, the force per unit length of dislocation needed for drawing a dislocation into a line is equal to $(bG\sqrt{2}/8\pi)-\gamma$ (b is the Burgers vector, G is the shear modulus, and γ is the energy of a stacking fault). The cross slip begins when $n\tau$ reaches values $(\sqrt{2}G/4\pi)-(\gamma/b)$. Using published data on γ, G, b, and τ_{III} (as τ), we obtain a value $n \sim 25$ for copper, lead, and aluminum. This means that a stress of the order of $G/10-G/20$ will arise at the head of the pileup, values close to the yield strength under shear. Thus at low temperatures an additional mechanism of plastic deformation arises, which consists in the breaking away of dislocation pileups from barriers, whereupon avalanchelike motion and multiplication of dislocations occur, which are reflected in the form of a jump in stress on the work-hardening curve.

6. DISCUSSION

The experimental study of the low-temperature macroscopic jumplike deformation in the normal and superconducting states and at *NS* and *SN* transitions has shown that, as a rule, the macroscopic LJD is less developed or absent altogether in the superconducting state. This sort of effect of the transition to the superconducting state can be regarded as typical. From this standpoint there is a discrepancy between the experimental data and the conclusions of the theory of thermomechanical instability in its present form, since that theory implies that the influence of the superconducting transition can vary, depending on the experimental conditions (the substance, temperature, strain rate).

Let us try to understand the reason for the disagreements between the experimental and theoretical results. Let us begin by noting that all of the theories of thermomechanical instability rest on the underlying assumption that the thermally activated character of the plastic deformation is preserved at low temperatures. However, special investigations done on a series of metals and alloys, including some that exhibit the macroscopic LJD, have shown that the process of thermally activated plasticity ceases to be effective. Let us illustrate this assertion with the results of a study of Al–Li alloys with concentrations of 1, 2, and 3 wt.% Li (3.8, 7.0,
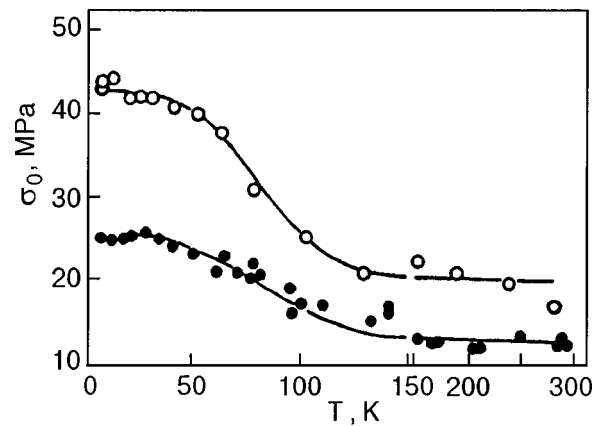

FIG. 23. Temperature dependence of the yield stress for polycrystalline samples of Al–Li alloys with 3.8 (●) and 7 (○) at.% Li; $\dot{\varepsilon}=0.1\times10^{-4}\,\mathrm{s}^{-1}$ (Ref. 32).

and 10.4 at.% Li, respectively). The yield stress σ_0 of these alloys as a function of T is presented in Fig. 23. It is important that in the temperature interval 170–40 K one observes a strong dependence $\sigma_0(T)$, characteristic for thermally activated plasticity, while in the interval 4.2–40 K the value of σ_0 varies weakly with temperature. Analysis[20,32] has shown that this behavior of σ_0 and the temperature dependence of the rate sensitivity $\Delta\sigma$ differ substantially from those for the case of thermally activated processes. It has been shown[34–36] that this is due to the influence of thermoinertial effects on the motion of dislocations at low temperatures. This finding has been confirmed by detailed studies done on alloys of lead with the tin, antimony,[37] and bismuth[41] without reference to the jumplike deformation. Moreover, in the region of anomalous temperature dependence (Fig. 24) the yield stress decreases as the temperature is lowered. Special experiments done at 0.5 K and their analysis from the standpoint of the existing theories have shown[35–37] that a quantum–inertial mechanism of dislocation motion is realized below 15 K, the basic elementary plasticity event of which is the quantum surmounting of an individual impurity atom by a dislocation
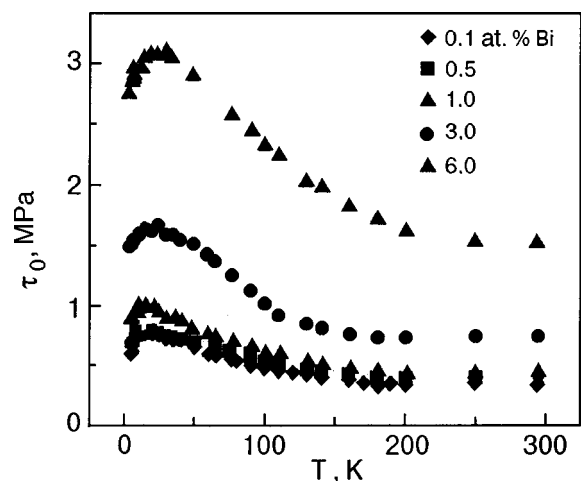

FIG. 24. Temperature dependence of the critical shear stress τ_0 for Pb–Bi single crystals of different Bi content in the temperature interval 295–0.5 K. The axis of tension is close to [110]; $\dot{\varepsilon}=1.1\times10^{-4}\,\mathrm{s}^{-1}$ (Ref. 41).

TABLE II. Characteristic temperatures of the anomaly of the yield stress and for the start of the jumplike deformation of some materials.

Material	T_c, K	T_i, K [Ref.]	T_{cr}, K [Ref.]
Al–3.8 at. % Li polycrystal	~1.2	34 [38]	10–4.2 [20]
Al–3.7 at. % Li polycrystal	-"-	39 [38]	10–4.2 [20]
Al–10.4 at. % Li polycrystal	-"-	50 [20]	10–4.2 [20]
Al–0.62 at. % Mg single crystal	-"-	21 [38]	6–8 [40]
Al–1.5 at. % Mg single crystal	-"-	27 [38]	6–8 [40]
Al–1.85 at. % Mg single crystal	-"-	28 [38]	6–8 [40]
Al–3.8 at. % Mg single crystal	-"-	31 [38]	6–8 [40]
Sn–0.01 at. % Cd single crystal	~3.72	1.5 [22]	3 [22]
Sn–0.04 at. % Cd single crystal	-"-	1.5 [22]	4.2 [22]
Sn–0.21 at. % Cd single crystal	-"-	1.0 [22]	4.2 [22]
Pb–99.9995 % single crystal	~7.2	no anomaly present [51]	2.4 polycrystal 99.9995 % [39]
Pb–1 at. % In single crystal	-"-	12 [51]	1.6 (0.85 at. % In) polycrystal [39]
Pb–10 at. % In single crystal	-"-	4.0 [51]	2.1 (13 at. % In) polycrystal [39]

Notes: T_i is the temperature of the start of the anomaly.

with a subsequent multiple depinning (unzipping) of the dislocation owing to the inertial effect.

Thus the underlying assumption of all the theories of thermomechanical instability, viz., that the plastic deformation is a thermally activated process all the way down to 0.5 K, is doubtful. There are also insufficient grounds to assume that the processes governing the macroscopic characteristics of the plastic deformation and the macroscopic jumplike deformation are identical. To convince ourselves that this is the case, let us compare the temperatures at which the anomalies of $\sigma_0(T)$ or $\tau_0(T)$ are observed with the temperature of the onset of the jumplike deformation. These last values are determined very roughly. The data are presented in Table II. In some cases (aluminum alloys) the temperatures T_i at which the anomaly of the yield stress begins is substantially higher than the temperatures T_c at which the jumplike deformation begins, while in other cases (alloys of tin with cadmium) the opposite is true: the jumplike deformation begins at higher temperatures than the anomaly of the yield stress. In other words, the appearance of a jumplike deformation cannot be correlated in temperature with the low-temperature anomaly of the plasticity. In the theories of thermomechanical instability which have been modified in respect to the influence of the superconducting transition on the jumplike deformation it is also assumed that the temperature dependence of the yield stress (flow stress) changes sign
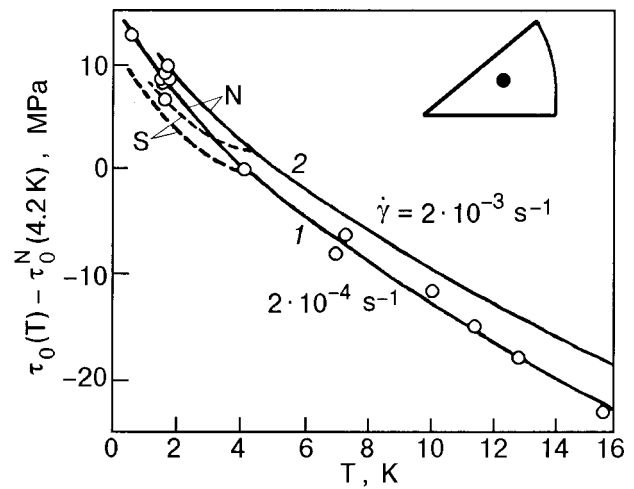

FIG. 25. Temperature dependence of the critical shear stress τ_0 for tantalum single crystals in the normal (solid curves) and superconducting (dashed curves) states; $\dot{\varepsilon} = 2\times10^{-3}$ s^{-1} (curve *1*), $\dot{\varepsilon} = 1.1\times10^{-4}$ s^{-1} (curve *2*) (Ref. 42).

at the superconducting transition, and that this is responsible for the vanishing or weakening of the macroscopic LJD. Numerous and varied experiments have been done to study the influence of the superconducting transition on the yield stress and the flow stress, including experiments to assess the temperature dependences in the normal and superconducting states. Analysis of the available data shows that the character of the temperature dependence of the yield stress τ_0 in the superconducting state is related to that observed in the normal state, and if $\tau_0(T)$ in the N state has an anomalous character, then it is determined by the position of T_c relative to the anomaly. If the temperature dependence of τ_0 down to the lowest temperatures of measurement corresponds to thermally activated processes and is characterized by a monotonic increase of τ_0 with decreasing temperature, then in the S state the derivative $d\tau/dT$ will decrease slightly near T_c, and as the temperature is decreased further it becomes close to the value of $d\tau/dT$ in the N state. This case has been observed in experiments with tantalum[42] (Fig. 25) and with the alloys Al–1.85 at.% Mg[43] and Sn–Cd.[44] In the presence of an anomalous temperature dependence of the yield stress (the critical shear stress for single crystals) the character of the change in $\tau_0(T)$ with temperature at the superconducting transition can vary. If the anomaly of $\tau_0(T)$ consists in a weakening of the temperature dependence of τ_0 in comparison with the thermally activated curve or in athermicity of τ_0, then in the superconducting state the sign of $d\tau_0/dT$ can change. This case is shown in Fig. 26 for single crystals of Al–0.3 at.% Mg.[25] If the anomaly of $\tau_0(T)$ consists in the fact that the sign of $d\tau/dT$ changes in the N state, i.e., the yield stress decreases with decreasing temperature, then the sign of $d\tau_0/dT$ does not change upon transition to the superconducting state, except in the region around T_c. A typical example is shown in Fig. 27 for single crystals of lead alloys.[37] Thus it seems unlikely that the vanishing of the macroscopic LJD is caused by a change in the character of $\tau_0(T)$.

Summing up the available data, one can conclude that the presence of anomalous temperature dependence in $\tau_0(T)$
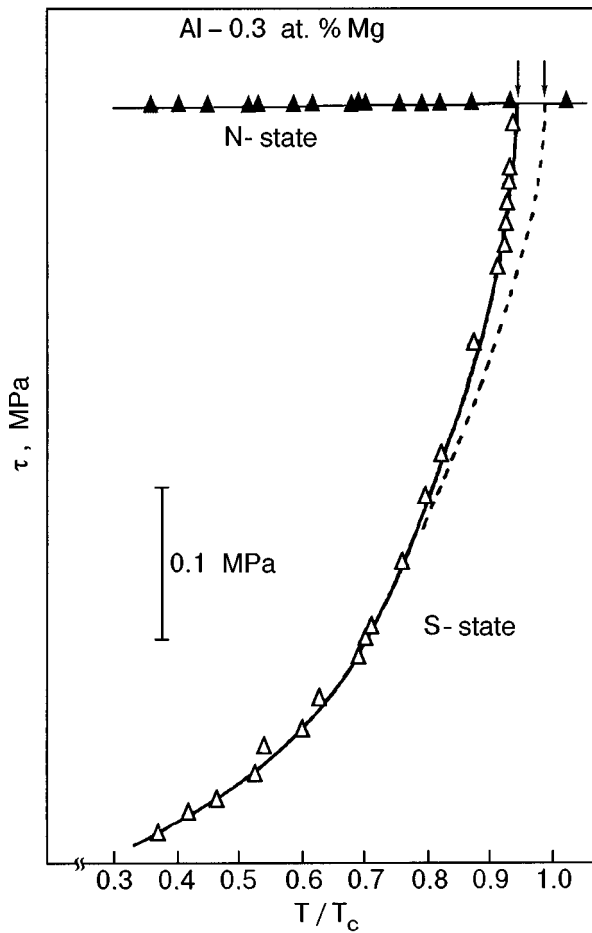
FIG. 26. Yield stresses τ_{0N} and τ_{0S} for single crystals of the alloy Al–0.3 at.% Mg strained by tension at a rate of $\dot{\varepsilon} = 6.9 \times 10^{-5}\ \mathrm{s}^{-1}$, as functions of temperature. The arrows indicate the critical temperature T_c determined from measurement of the specific heat and extrapolation of $\Delta\tau_{SN}$ to zero (Ref. 45).

FIG. 27. Temperature dependence of the critical shear stress τ_0 for single crystals of the alloys Pb–Sn (a) and Pb–Sb (b) in the normal (N) and superconducting (S) states. The dashed curves show the dependence that would obtain for a thermally activated character of the processes (Ref. 37).

is in no way related to the superconducting transition, although the transition can affect it somewhat. The superconducting transition can affect $\tau_0(T)$ in a variety of ways, and in individual cases can lead to a change in the sign of $d\tau_0/dT$. In the framework of the thermomechanical instability theories this means that only in the case of a change in sign of $\tau_0(T)$ will the superconducting transition affect the LJD, and this has not been established experimentally. However, the observed regularities in the influence of the superconducting transition on the macroscopic LJD and also the temperature dependences of the yield stress and its change at the superconducting transition do not confirm the hypothesis of thermomechanical instability.

The alternative hypothesis for the jumplike deformation, which attributes the appearance of jumps to the breakaway of dislocation pileups, unfortunately still remains hypothetical, without any theoretical calculations to back it up. Therefore, the comparison of the experimental results with the dynamic dislocation hypothesis can only be done on a qualitative level. Using the current ideas about the motion of dislocations in the normal and superconducting states,[1,2] one can explain the influence of the superconducting transition on the LJD as follows. In the superconducting state, as compared to the normal state, because of the undamped nature of their motion the dislocations will overcome a number of obstacles
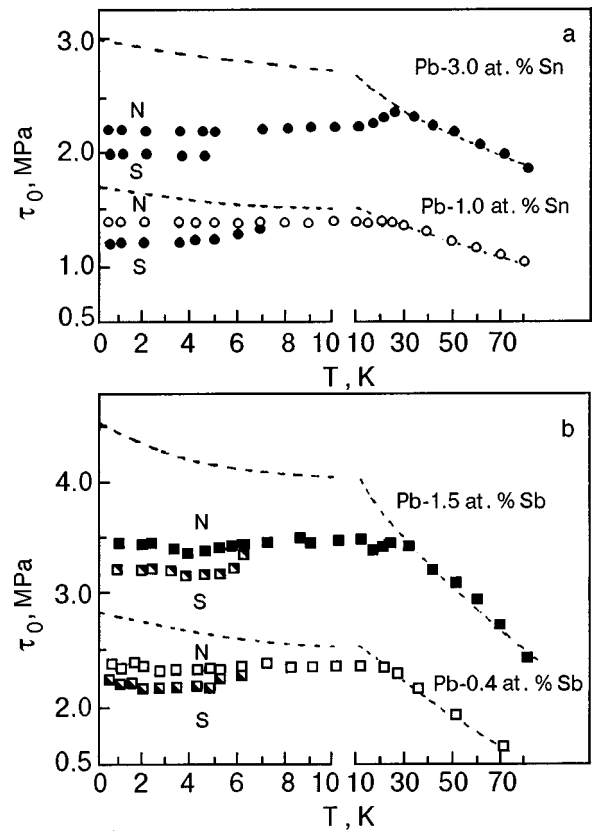
on account of inertial effects. Therefore, in the S state the jumps will begin later and their amplitude will be lower at the same strain. This process can occur for any character of $\tau_0(T)$, both in the form of individual jumps and in the form of a saw-tooth curve. For the process of jumplike deformation in the framework of this hypothesis it is not necessary that τ decrease as the temperature is lowered. There is convincing experimental evidence in favor of the dynamic hypothesis. The best evidence comes from experiments on the observation of electrical effects in the low-temperature deformation. These electrical effects are a consequence of the interaction of dislocations and conduction electrons and arise on account of the carrying of electrons by rapidly moving dislocations. This effect was predicted theoretically in Ref. 46 and observed experimentally in Ref. 47. Then, by a technique developed in Ref. 47, a study of the low-temperature jumplike deformation of 99.999% pure Al single crystals was carried out under conditions of compression.[48] At the time of the jumps in the load, pulsed electrical signals of various amplitudes, shapes, and durations appeared on the faces of the strained samples. Depending on their duration, the pulses can be divided into two groups: $t = 1 - 10\ \mathrm{ms}$ (millisecond pulses), and $t = 2 - 5\ \mu\mathrm{s}$ (microsecond pulses); see Fig. 28.

To establish the nature of the observed electrical effects some tests were done and some estimates made. They showed that the main role in the formation of the millisecond pulses is played by the thermopower arising at the contact of the wire leads with the sample owing to thermal processes in
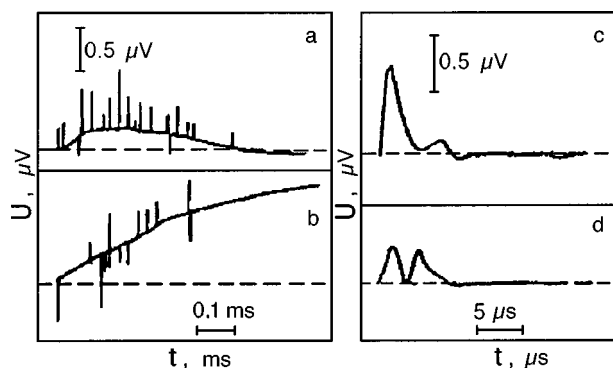
FIG. 28. Brief (microsecond) electrical pulses recorded against the background of the millisecond pulses at the times of deep jumps in the load (a,b), and individual microsecond pulses observed at small load jumps $\delta\varepsilon$ $\sim 10^{-5} – 10^{-4}$ (c,d) (Ref. 48).

the deformation. The microsecond pulses, unlike the millisecond, did not depend on the material of the wire leads or their geometric arrangement. When the temperature of the surface of the sample changed at the time of the jumps in the load, no sign of any brief temperature increases in the microsecond range were observed in any of the tests. From these observations it was concluded that the microsecond pulses may be due to the carrying of electrons along with the motion of dislocation pileups, and the duration of these pulses indicates that their motion is of a dynamic nature ($\sim 10^5$ cm/s). As to the millisecond pulses, an important role in their formation is played by deformation processes giving rise to a temperature field, i.e., apparently, by processes of thermomechanical instability. This interpretation of the millisecond pulses is supported by high-precision measurements made on niobium single crystals.[50] A very important clue for understanding the mechanisms of the LJD is the experimental fact that the jump begins with the microsecond pulses, i.e., usually the microsecond pulses are observed before the millisecond pulses; this suggests that rapidly moving pileups initiate the thermally stimulated formation of dislocation avalanches as the jump develops further. This temporal sequence of pulses is direct experimental evidence that the dynamic dislocation pileups are the initiator (in the terminology used in Ref. 48, the ''trigger'') of a situation that creates conditions for the onset of thermally stimulated dislocation avalanches. Using the results on the detection of electrical pulses, the authors of Ref. 48 estimated the contribution of the dynamic dislocation pileups to the total increment of deformation at the jumps in the load. Comparing these data with the total amplitude of the series of pulses corresponding to a single jump, we find for the large load jumps that they comprise 1–20 % of $\Delta\varepsilon$. Since the sensitivity of the detector did not permit the observation of small pileups, this estimate is a lower bound. Thus the studies of the kinetics of the jumps have made it possible to determine the sequence of events. A jump in the load begins with the fast motion of dislocation pileups, which lead to heating of slip bands and give rise to an ensuing thermomechanical instability. Therefore, the theory of jumplike deformation must include both purely dynamic effects and the effects of thermomechanical instability, the combination of which can apparently account for the regularities observed in the influence of the supercon-

ducting transition on the jumplike deformation.

In a recent paper[52] a highly sensitive quartz transducer placed near the sample was used to record the kinetics of a single load jump in nickel, copper, and construction materials. It was shown that the load jump is a two-stage process: the first stage ($\Delta\sigma_I$) lasts for microseconds and is followed by a slower, millisecond fall in the load ($\Delta\sigma_{II}$). In the first stage the load varies linearly with time, indicating a quasiviscous, dynamic character of the deformation. In the second stage, σ has a nonlinear time dependence, which is characteristic for a thermally activated process. This finding agrees with the results of the other papers mentioned above.

7. CONCLUSIONS

1. The transition to the superconducting state leads to a substantial weakening of the macroscopic jumplike deformation or to its complete vanishing.

2. The vanishing of the influence of the *NS* transition on the macroscopic LJD at large strains in high-strength aluminum alloys is most likely due to a small (from 0.5 to 1.2 K) heating of the sample and a transition to the normal state.

3. The observed regularities in the influence of the *NS* transition on the macroscopic LJD are in disagreement with the hypothesis of thermomechanical instability.

4. The available high-precision measurements of the kinetics of the jumps confirm that the initial breakdown of the load at a jump first arises as a consequence of purely dynamic motion of dislocations, and only after that do the complex thermomechanical processes occur. This picture of the kinetics of development of a jump is also supported by the influence of the superconducting transition on the low-temperature jumplike deformation.

[*]E-mail: pustovalov@ilt.kharkov.ua

[1] V. I. Startsev, V. Ya. Il'ichev, and V. V. Pustovalov, *Plasticity and Strength of Metals and Alloys at Low Temperatures* [in Russian], Metallurgizdat, Moscow (1975).
[2] V. I. Startsev, in *Dislocation in Solids*, Vol. 6, edited by F. R. N. Nabarro, North Holland, Amsterdam (1983), p. 145.
[3] L. S. Basinski, Proc. R. Soc. London, Ser. A **240**, 229 (1957).
[4] L. P. Kubin and B. Jouffrey, Philos. Mag. **24**, 437 (1971).
[5] E. Kuramoto, S. Takeuchi, and T. Suzuki, J. Phys. Soc. Jpn. **34**, 1217 (1973).
[6] G. A. Malygin, Phys. Status Solidi B **61**, K45 (1974).
[7] B. V. Petukov and Yu. Z. Estrin, Fiz. Tverd. Tela (Leningrad) **17**, 2041 (1975) [Sov. Phys. Solid State **17**, 1333 (1975)].
[8] I. S. Zhitomirskiĭ, I. N. Nechiporenko, Fiz. Nizk. Temp. **4**, 1053 (1978) [Sov. J. Low Temp. Phys. **17**, 499 (1978)].
[9] Yu. Z. Estrin and L. P. Kubin, Scr. Metall. **14**, 1359 (1980).
[10] A. Seger, in *Dislocations and Mechanical Properties of Crystals*, edited by J. C. Fisher, W. G. Johnston, R. Thomson, and T. Vreeland [Wiley, New York (1957); Izd. Inostr. Lit., Moscow (1960)].
[11] I. N. Kuz'menko, T. A. Parkhomenko, and V. V. Pustovalov, Fiz. Nizk.

Temp. **4**, 1340 (1978) [Sov. J. Low Temp. Phys. **4**, 632 (1978)].

[12] V. V. Pustovalov, V. S. Fomenko, and Yu. I. Gofman, Preprint FTINT AN USSR [in Russian], 6 October 1972, Kharkov (1973).

[13] V. S. Bobrov and I. V. Videnskiĭ, *Materials of the XX All-Union Conference on Low-Temperature Physics* [in Russian], Chernogolovka (1979), Part 3, pp. 79–81.

[14] I. N. Kuz'menko, V. V. Pustovalov, and S. É. Shumilin, Preprint FTINT AN USSR [in Russian], 58–86, Kharkov (1986).

[15] I. N. Kuz'menko and V. V. Pustovalov, Fiz. Nizk. Temp. **5**, 1433 (1979) [Sov. J. Low Temp. Phys. **5**, 676 (1979)].

[16] I. N. Kuz'menko, Candidate's Dissertation [in Russian], FTINT AN USSR, Kharkov (1983).

[17] I. N. Kuz'menko and V. V. Pustovalov, Dokl. AN USSR **282**, 599 (1985) [Sov. Phys. Dokl. **30**, 424 (1985)].

[18] I. N. Kuz'menko, S. V. Lubenets, V. V. Pustovalov, and L. S. Fomenko, Fiz. Nizk. Temp. **9**, 865 (1983) [Sov. J. Low Temp. Phys. **9**, 450 (1983)].

[19] V. V. Pustovalov and S. É. Shumilin, Fiz. Met. Metalloved. **62**, 171 (1986).

[20] N. V. Isaev, V. V. Pustovalov, V. S. Fomenko, and S. É. Shumilin, Fiz. Nizk. Temp. **20**, 832 (1994) [Low Temp. Phys. **20**, 653 (1994)].

[21] S. Saji, K. Yamamura, N. Furushiro, and S. Hori, J. Jpn. Inst. Light Metals **38**, 792 (1988).

[22] G. I. Kirichenko, V. D. Natsik, V. V. Pustovalov, V. P. Soldatov, and S. É. Shumilin, Fiz. Nizk. Temp. **23**, 1010 (1997) [Low Temp. Phys. **23**, 758 (1997)].

[23] V. I. Dotsenko, I. F. Kislyak, V. T. Petrenko, V. I. Startsev, and V. I. Tikhonovskiĭ, Fiz. Nizk. Temp. **12**, 741 (1986) [Sov. J. Low Temp. Phys. **12**, 420 (1986)].

[24] E. Y. Gutmanas and Y. Estrin, Phys. Status Solidi A **92**, 137 (1985).

[25] B. V. Petukov and Yu. Z. Éstrin, Fiz. Tverd. Tela (Leningrad) **17**, 2041 (1975) [Sov. Phys. Solid State **17**, 1333 (1975)].

[26] V. Bukkel', *Superconductivity* [in Russian], Mir, Moscow (1975).

[27] I. N. Nechiporenko, Fiz. Nizk. Temp. **12**, 75 (1986) [Sov. J. Low Temp. Phys. **12**, 43 (1986)].

[28] G. A. Malygin, Fiz. Nizk. Temp. **12**, 849 (1986) [Sov. J. Low Temp. Phys. **12**, 481 (1986)].

[29] V. D. Natsik, Zh. Éksp. Teor. Fiz. **61**, 2540 (1971) [Sov. Phys. JETP **34**, 1359 (1972)].

[30] G. A. Malygin, Fiz. Tverd. Tela (St. Petersburg) **40**, 1778 (1998) [Phys. Solid State **40**, 1611 (1998)].

[31] A. V. Granato, Phys. Rev. B **4**, 2196 (1971).

[32] V. S. Fomenko, N. V. Isaev, and V. V. Pustovalov, Fiz. Nizk. Temp. **19**, 429 (1993) [Low Temp. Phys. **19**, 301 (1993)].

[33] T. H. Blewitt, R. R. Coltman, and J. K. Redman, in *Conference on Defects in Crystalline Solids*, Physical Society, London (1955) [Russian translation in *Dislocations and the Mechanical Properties of Crystals*, Izd.-vo Inostr. Lit., Moscow (1960)].

[34] V. I. Dotsenko, A. I. Landau and V. V. Pustovalov, *Current Topics in the Low-Temperature Plasticity of Materials* [in Russian], Naukova Dumka, Kiev (1987).

[35] Th. Wille, W. Gieske, and Ch. Schwink, Acta Metall. **35**, 2679 (1987).

[36] I. A. Shepel', L. N. Zagoruĭko, V. D. Natsik, V. V. Pustovalov, and V. P. Soldatov, Fiz. Nizk. Temp. **17**, 390 (1991) [Sov. J. Low Temp. Phys. **17**, 202 (1991)].

[37] N. V. Isaev, V. D. Natsik, V. V. Pustovalov, I. A. Shepel', and S. É. Shumilin, Fiz. Nizk. Temp. **18**, 911 (1992) [Sov. J. Low Temp. Phys. **18**, 641 (1992)].

[38] N. V. Isaev, V. D. Natsik, and V. S. Fomenko, Fiz. Nizk. Temp. Phys. **25**, 987 (1999) [Low Temp. Phys. **25**, 740 (1999)].

[39] V. V. Pustovalov and V. S. Fomenko, Preprint FTINT AN USSR [in Russian], 9–78, Kharkov (1978).

[40] V. P. Podkuĭko, Fiz. Met. Metalloved. **40**, 1273 (1975).

[41] N. V. Isaev, V. D. Natsik, V. V. Pustovalov, V. S. Fomenko, and S. É. Shumilin, Fiz. Nizk. Temp. **24**, 786 (1998) [Low Temp. Phys. **24**, 593 (1998)].

[42] S. Takeuchi, K. Maeda, and T. Suzuki, Phys. Status Solidi A **43**, 289 (1977).

[43] S. É. Shumilin, Candidate's Dissertation [in Russian], FTINT AN USSR, Kharkov (1987).

[44] V. D. Natsik, G. I. Kirichenko, V. V. Pustovalov, and V. P. Soldatov, S. É. Shumilin, Fiz. Nizk. Temp. **22**, 965 (1996) [Low Temp. Phys. **22**, 740 (1996)].

[45] F. Iida, T. Suzuki, E. Kuramoto, and S. Takeuchi, Acta Metall. **27**, 637 (1979).

[46] V. Ya. Kravchenko, Fiz. Tverd. Tela (Leningrad) **9**, 1050 (1967) [Sov. Phys. Solid State **9**, 883 (1967)].

[47] V. S. Bobrov and M. A. Lebedkin, JETP Lett. **38**, 400 (1983).

[48] V. S. Bobrov and M. A. Lebedkin, Fiz. Tverd. Tela (Leningrad) **31**, 120 (1989) [Sov. Phys. Solid State **31**, 982 (1989)].

[49] V. S. Bobrov and M. A. Lebedkin, Fiz. Tverd. Tela (St. Petersburg) **35**, 1881 (1993) [Phys. Solid State **35**, 943 (1993)].

[50] A. M. Dolgin and V. Z. Bengus, Fiz. Nizk. Temp. **16**, 254 (1990) [Sov. J. Low Temp. Phys. **16**, 141 (1990)].

[51] T. A. Parkhomenko and V. S. Fomenko, Metallofizika (Kiev) **2**, 106 (1980).

[52] B. Obst and A. Nyilas, Adv. Cryog. Eng. **44**, 331 (1998).

Translated by Steve Torstveit

QUANTUM LIQUIDS AND QUANTUM CRYSTALS

Saturation effect in the problem of microwave energy absorption by two-dimensional electrons on a helium film

V. B. Shikin*

Institute of Solid State Physics, Russian Academy of Sciences, 142432 Chernogolovka, Moscow District, Russia

The details of the absorption of an rf electromagnetic field by two-dimensional (2D) electrons on a thin film of helium in relation to the confining electric field are discussed. The connection between this problem and the problem of saturation in a 2D electron system is noted. A special study is made for the case of cylindrical geometry, which corresponds qualitatively to the conditions of the experiment of B. Lehndorff and K. Dransfeld, J. Phys. (Paris) **50**, 2579 (1989). It is shown that the data obtained on the field dependence of the absorption of rf field energy by 2D electrons contains information about the supersaturated electronic states in the cell. © *2000 American Institute of Physics.* [S1063-777X(00)00206-1]

In Ref. 1 the absorption of rf energy by two-dimensional (2D) electrons was investigated by placing a charged 2D system in the central part of a cylindrically symmetric resonant cavity (where there is an antinode of the fundamental mode of the electric field of the cavity). It was noted by the authors of that interesting paper[1] that the introduction of 2D electrons sharply alters the characteristics of the cavity. In particular, its fundamental frequency decreases from 12 to 9 GHz, and the level of absorption P increases (in comparison with the value in the empty cell). In addition, a special study was made of the dependence of the absorption P on the potential difference V between the walls of the cavity and the central electrode (this potential difference is what confines the electrons to the surface of the helium). That study was motivated by the desire to fix the location of the free 2D electrons in one-electron ''sockets.'' The presence of a pronounced spike on the $P(V)$ curve (Fig. 2 of Ref. 1) confirms that this is a reasonable interpretation of the data of Ref. 1. Nevertheless, some accompanying details not mentioned in Ref. 1 indicate the possibility of an alternative scenario leading to the observed behavior of $P(V)$. The most significant of these is the finite (different from the vacuum) absorption in the activity for $V \rightarrow 0$. The existing ideas about the behavior of 2D electrons over helium would require that in such a situation the electron density in the active zone of the cavity go to zero, and that would mean small (comparable to the vacuum) absorption. In actuality the absorption P in a potential difference approaching zero is only a few percent less than the maximum value. This paradox deserves at least a qualitative explanation.

In this paper we discuss the popular procedure (which was used in Ref. 1) in which the free surface of helium is charged to saturation by electrons (the concept of saturation will be defined below). It is important to take the details of this procedure into account in order to understand the behav-

ior of $P(V)$. In particular, it becomes possible to resolve the aforementioned paradox.

1. Let us turn to the seemingly technical problem of introducing electrons into a resonant cavity and determining the density of the 2D electron system in the active zone lying closely along the axis of a cylindrical cavity. This procedure was carried out in Ref. 1 from an external source, by the standard procedure in which a helium film covering a conducting substrate (doped silicon) lying along the axis of the cavity is charged to saturation with electrons in the presence of a fixed potential difference between the substrate and walls of the cavity. Under such conditions one can obtain a simple estimate of the density n_s of 2D electrons in the cell, and for this reason it is extremely popular to study the properties of 2D electron systems above helium specifically in a state of saturation. Nevertheless, important details of the saturated state are in need of refinements that have not yet been explicitly elaborated. The essential features of these refinements will first be set forth for the particular case of a planar 2D electron system, and then we will address the specifics of the case of cylindrical geometry, which is qualitatively closer to the experiments of Ref. 1.

The conventional way of preparing a 2D electron system on a liquid helium surface presupposes the use of a flat capacitor, with a charged liquid interface between the plates (see, e.g., Ref. 2). The potential difference V on the capacitor plates produces electric fields E_+ and E_- above and below this interface):

$$E_+ = -\frac{4\pi e n_s d + V}{d+h}, \quad E_- = \frac{4\pi e n_s h - V}{d+h}, \tag{1}$$

which confine the 2D electron system with a finite density n_s near the vapor–liquid interface. Here d is the thickness of the helium film, h is the vacuum gap between the helium and the upper electrode, and $2W$ is the dimension of the capacitor in the horizontal directions.
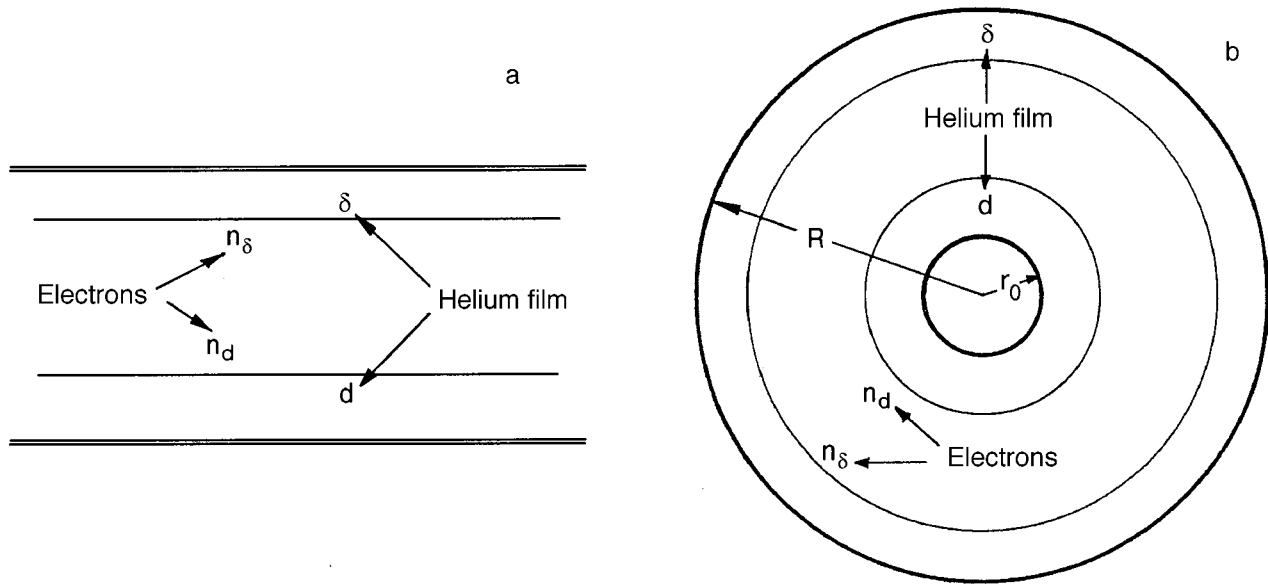
FIG. 1. Diagram of the arrangement of 2D electron layers above planar helium films in the two-component approximation (a) and for a cylindrical version of the cell (b).

Under the conditions $E_+ = 0$, or

$$V_s = -4\pi e n_s^* d, \tag{2}$$

the excess electrons with $n_s > n_2^*$ will no longer be confined by the external field on the liquid substrate and will "escape" into the volume of the gaseous phase of helium. Therefore, under condition (2) one speaks of a state of saturation in the 2D electron system, and the density n_s^* is assumed to be the maximum for the given V.

The ease with which can determine the density n_s^* using formula (2) is a great practical convenience in studies with 2D electrons. However, for formulas (1) and (2) to hold requires that the electrons have free access to the upper plate of the capacitor. In reality, however, in working with superfluid helium all the interior parts of the cell, including the upper capacitor plate, are covered by a thin film of helium (with a thickness of the order of the natural value $\delta \sim 10^{-6}$ cm). Under these conditions the overall picture of the filling of the vacuum gap above the helium with electrons changes, for during the charging process electrons settle not only on the lower film d to a density n_d but also on the upper film δ to a density n_δ,

$$n_d + n_\delta = n_s. \tag{3}$$

The state with two 2D electron layers is called supersaturated below. The state of supersaturation is illustrated schematically in Fig. 1a. For its description in the electrostatic approximation it is necessary [long with the set of conditions leading to formulas (1)] that the electric field between the two 2D electron layers vanish. Then

$$4\pi e n_d = \frac{4\pi e n_s \delta - V}{d + \delta}, \quad n_\delta = n_s - n_d. \tag{4}$$

It is easy to see that in the two-layer model a finite electron density above the helium is possible in the absence of a nonzero potential difference, for even at $V = 0$ one has

$$4\pi e n_d^0 = \frac{4\pi e n_s \delta}{d + \delta}, \quad 4\pi e n_\delta^0 = \frac{4\pi e n_s d}{d + \delta}. \tag{5}$$

Here the electrons are confined in local states on the upper and lower helium films by the internal Coulomb fields. The total number of electrons N_0 is limited only by the stability of the charged helium surface.

Of course, having specified a certain number N_0 one can choose the corresponding critical value V_s (2) for which, in the electrostatic approximation, all of the electrons will be found on the film d, i.e., $n_d = n_s = N_0 / \pi R^2$. However, the converse assertion, that for a fixed V the maximum value of n_s^* corresponds to the value (2) is incorrect. An example of their disagreement is contained in formulas (5); having $V = 0$, we nevertheless find that $n_d^0 \neq 0$.

Thus the existence region of 2D equilibrium electron states over helium is wider in the problem with films δ and d. Their existence becomes possible also under conditions of supersaturation,

$$0 \leq V \leq V_s, \tag{6}$$

and the state of saturation (2) can be interpreted as being one of the supersaturated states.

2. Now let the system of control electrodes be cylindrically symmetric (Fig. 1b). This type of cell is closer to the experimental situation of Ref. 1, although it is not 100% similar (the central electrode in Ref. 1 has the form of a plane of dimensions $w \ll R$, where R is the radius of the cavity). The corresponding densities, n_d in the central part of the system (Fig. 1b) and n_δ at the walls of the cavity, are determined from the expressions

$$2\pi[(r_0 + d_*)n_d + (R - \delta)n_\delta] = N, \tag{7}$$

$$4\pi e n_d = \frac{2eN - (R - \delta)V/\delta}{r_0 + d_* + (R - \delta)d/\delta}. \tag{7a}$$

Here N is the total electron density per unit length of the cylinder, and d_* is the effective distance between the helium

and the conducting silicon, consisting of the thickness d of the helium film and the thickness d_t of the dielectric interlayer (Khostopan or Teflon of the order of 10 μm thick).

The minimum electron density n_d^0 in the supersaturation regime at $V=0$ can be written

$$2\pi n_d^0 = \frac{N}{r_0 + d_* + (R-\delta)d/\delta}. \tag{8}$$

The maximum density in the saturation regime is, of course,

$$2\pi n_d^{\max} = \frac{N}{r_0 + d_*}. \tag{8a}$$

Finally, in the cylindrical version of the problem there also exists a regime in which the self-field of the electrons at the axis of the cylinder is less than the confining potential. But this limiting case does not have direct relevance to the data of Ref. 1, which are directly adjacent to the zero-V limit in the electron distribution inside the cavity.

It is also pertinent to note that in the case of different metals on the walls of the cavity (normal metal) and along its axis (doped silicon) it is quite likely that the contact potential difference ψ will play a role in the formation of the supersaturated states. In the absence of ψ, supersaturation can occur for arbitrary N in the region of small V. If $\psi \neq 0$, however, then for saturation to occur (only in that regime does the absorption grow with increasing V) it is necessary to have a finite N:

$$N \geqslant \frac{(r_0 + d_*)\psi}{2e d_*}. \tag{9}$$

3. Returning to Ref. 1 and taking into account what we have said above, we can conjecture that the measurements there were done under conditions of supersaturation of the cavity with electrons, when not only were the n_d states on the axis of the cavity filled but also the n_δ states on its walls, which were coated with a thin film of helium. Then, under the condition $V=0$ an appreciable fraction of the total electron charge introduced into the cell is retained at the silicon substrate [as follows, in particular, from formula (8)]. Then, as V increases, the charges begin to be redistributed between the fractions n_d and n_δ in favor of the first of these. This process is in general nonlinear in V due to the influence of the electron pressure on the helium film thickness d in the active zone.

Thus the discussion of the problem of the filling of fractions n_d and n_δ by the electrons provides the prerequisites for a correct understanding of the function $P(V)$. The fact that this absorption is finite for $V \to 0$ is a consequence of the fact that $n_d(V \to 0)$ is finite. As to the details of the absorption in the region $V \neq 0$, this problem must be solved using additional information about the structure of $P(V)$, e.g., in the Drude approximation.

By definition, the absorption $P(E_\perp)$ in the Drude approximation is

$$P = \mathrm{Re}(jE_\parallel) = n_d e^2 m^{-1} E_\parallel^2 \frac{\tau}{1 + \omega^2 \tau^2}. \tag{10}$$

Here n_d is taken from Eq. (7a), τ is the characteristic momentum relaxation time, and ω is the frequency of the rf excitation.

For τ we use the well-known expression[2]

$$\tau = 8\alpha\hbar / F^2,$$

$$F = F_e + F_d = eE_\perp + e^2/(4d^2), \quad E_\perp = 4\pi e n_d. \tag{11}$$

A helium film is typically of the order of 3×10^{-6} cm thick. Adopting this thickness and supposing that the Teflon substrate has a high dielectric constant, we find that the electrical part F_e of the force F is comparable to the dielectric part F_d at $n_d \sim 10^{10}$ cm^{-2}. Another geometric estimate concerns the thickness of the Teflon interlayer, $d_t \approx 6$ μm [this thickness appears in the definition of the quantity d_* appearing in (7) and (8)].

The typical value of τ in (10) for $d \sim 3 \times 10^{-6}$ cm does not exceed 10^{-11} s, i.e., for $\omega \sim 10^9$ s^{-1} we have $\omega\tau \ll 1$. One can determine R without difficulty ($R=1$ cm). As to r_0, here the estimates are extremely sketchy: 0.1 cm$< r_0 < 0.5$ cm, since the axial electrode (conducting silicon) is actually in the form of a plate of width 1 cm and thickness 0.1 cm.

As we are interested mainly in the behavior of the absorption in the neighborhood of small V, we write expressions (10) and (11) with allowance for the condition $\omega\tau \ll 1$ in dimensionless form:

$$\frac{P(V)}{P(0)} = \frac{n_d(V)\tau(V)}{n_d(0)\tau(0)} \equiv (1 + v_N)\left[\frac{n^* + 1}{n^*(1 + v_N) + 1}\right]^2,$$

$$v_N = V/V_N. \tag{12}$$

$$V_N^{-1} = R/(2\delta|e|N), \quad n^* = 16\pi d^2 n_d(0).$$

The relative absorption (12) has a maximum as a function of v_N at the point $v_N^{\max}$:

$$v_N^{\max} = \frac{1}{n_*} - 1. \tag{13}$$

It is clear that such a maximum exists if $n_* < 1$. In the opposite limiting case, $n_* > 1$, the absorption $P(V)/P(0)$ from (12) decreases monotonically, since the field dependence of the relaxation time is dominant.

Thus the finite value of the absorption of an rf electric field by a 2D electron system in a cavity at zero confining field and its growth with increasing V, which follow from the data of Ref. 1, provide a stimulus for introducing and discussing the properties of the supersaturated state of 2D electrons in closed cells (i.e., cells containing a closed system of electrodes for confining electrons on the surface of superfluid helium).

The case in Ref. 1 is not the only example. Supersaturated states should be invoked to explain the nonmonotonic field dependence of the capacitance of a capacitor containing 2D electrons (see, e.g., Ref. 3). Their presence influences the structure of the relaxation time in experiments such as those in Refs. 4–7, etc. Generally speaking, when the image forces (which we have neglected) are taken into account, a two-layer electron structure is the rule rather than the exception for electrons above superfluid helium in closed cells. In view of this circumstance one can consider the results set forth above as quite general, having a significance extending beyond the interpretation of the data of Ref. 1.

[*]E-mail: shikin@issp.ac.ru

[1] B. Lehndorff and K. Dransfeld, J. Phys. (France) **50**, 2579 (1989).

[2] V. B. Shikin and Yu. P. Monarkha, *Two-Dimensional Charged Systems in Helium* [in Russian], Nauka, Moscow (1989).

[3] D. Lambert and P. Richards, Phys. Rev. B **23**, 3282 (1981).

[4] Y. Iye, K. Kono, K. Kajita, and W. Sasaki, J. Low Temp. Phys. **34**, 539 (1979).

[5] Y. Iye, K. Kono, K. Kajita, and W. Sasaki, J. Low Temp. Phys. **38**, 293 (1980).

[6] K. Kono, K. Kajita, K. Kobayashi, and W. Sasaki, Surf. Sci. **113**, 438 (1982).

[7] E. Andrei, S. Yegel, and L. Menna, Phys. Rev. Lett. **67**, 3704 (1991).

[8] L. Menna, S. Yucel, and E. Andrei, Phys. Rev. Lett. **70**, 2154 (1993).

Translated by Steve Torstveit

Nuclear spin−spin relaxation in ³He−⁴He two-phase solid solutions at ultralow temperatures

N. P. Mikhin,[a] A. V. Polev, E. Ya. Rudavskii, Ye. V. Syrnikov, and V. A. Shvarts

B. Verkin Institute for Low Temperature Physics and Engineering, National Academy of Sciences of Ukraine, pr. Lenina 47, 61164 Kharkov, Ukraine
(Submitted January 14, 2000)

The spin−spin relaxation time in a ³He−⁴He solid solution is measured before and after phase separation in the temperature range 1−250 mK. The spin echo technique is used, which permits separating the contributions of the two separated phases to the magnetic relaxation. It is found that in the concentrated phase the spin−spin relaxation time is practically independent of temperature above 50 mK and is described by the same exchange mechanisms as in pure ³He. In the dilute phase the relaxation time is inversely proportional to the concentration and agrees with the corresponding values for homogeneous solutions. The dominant contribution to the spin−spin relaxation process is from ³He−⁴He tunneling exchange. At the lowest temperatures the spin echo exhibits anomalous behavior, which may be a manifestation of quasi-one-dimensional diffusion. © *2000 American Institute of Physics.* [S1063-777X(00)00306-6]

1. INTRODUCTION

The quantum nature of helium crystals is clearly manifested in the magnetic properties of solid ³He and of ³He−⁴He solutions. The large zero-point vibrations of the ³He atoms lead to a strong exchange interaction and make for an appreciable tunneling probability for the atoms. These processes play the dominant role in the nuclear magnetic relaxation in quantum crystals. Detailed studies[1–5] of this topic in ³He have shown that the spin−lattice relaxation time T_1 and the spin−spin relaxation time T_2 at low temperatures have a broad exchange plateau region where T_1 and T_2 do not depend on temperature.

The exchange mechanism of nuclear magnetic relaxation has also been observed in experiments on ³He−⁴He solid solutions[6–11] in the single-phase region at different concentrations and molar volumes in both the bcc and hcp phases. Here, as was shown in Ref. 8 on the basis of the Torrey theory,[12] in addition to the tunneling exchange of neighboring ³He−³He atoms in the solutions there is also appreciable mutual exchange ³He−⁴He. The effect depends on the concentration and molar volume of the solution.

At ultralow temperatures ³He−⁴He solid solutions can be used to realize another interesting quantum system—a two-phase crystal, which is formed as a result of phase separation and consists of a concentrated and a dilute phase. In particular, in weak solutions of ³He in ⁴He at high pressures, small inclusions of the concentrated bcc phase form, distributed in the crystalline matrix of the dilute hcp phase. As the temperature is lowered, the concentration of ³He in the inclusions approaches unity, and the matrix becomes practically pure ⁴He.

Research on the magnetic relaxation processes in two-phase systems of this kind was begun only recently[13–16] and has been devoted mainly to the spin–lattice relaxation. Experiments[13] have shown that in the concentrated phase of the separated solution the region of the exchange plateau for

the relaxation time T_1, unlike the case in bulk ³He, is observed throughout the entire existence region of this phase and extends all the way to millikelvin temperatures. In the dilute phase the time T_1 increases as the temperature is lowered, reflecting its concentration dependence, and the value of T_1 is practically equal to the corresponding values for single-phase (unseparated) solutions of the same concentration in the region of the exchange plateau.

In the present study we investigate the spin−spin relaxation in ³He−⁴He solid solutions over a wide range of temperatures both in the single-phase region (before separation) and in the coexistence region of the concentrated and dilute phases. The main focus of our attention is to compare the data obtained with the theoretical and experimental results for pure ³He and for single-phase solutions of the corresponding concentrations.

2. EXPERIMENTAL PROCEDURE

In the experiment we used the cell described previously,[17] which was cooled by a nuclear demagnetization refrigerator. Cylindrical samples of ³He−⁴He solid solutions 4 mm in diameter and 20 mm long were grown from an initial gaseous mixture containing 3.18% ³He by the method of capillary blocking. After annealing for a few days near the melting temperature, the molar volume of the samples was 20.3 ± 0.05 cm³/mole. Cooling of the samples was done in steps of 10 mK with a subsequent temperature stabilization. Measurements were made in the temperature interval 1−250 mK. The temperature of the sample was determined by a ³He crystallization thermometer placed on the same massive silver cold stage as the sample cell.

For the NMR measurements we used a pulsed spectrometer working at a frequency of 250 kHz. The relative non-uniformity of the magnetic field in the volume of the sample was $\approx 10^{-4}$. The measurements of the spin−spin relaxation time T_2 were made mainly by the spin echo method with a

$90° - \tau - 180°$ pulse sequence. The amplitude h of the echo for each value of the time interval τ was determined as the average of ten measurements with a time interval Δt between measurements. The damping of h in the general case is described by the expression

$$h(2\tau) = h_0 \exp\left(-\frac{2\tau}{T_2} - \frac{2}{3}\gamma^2 G^2 \tau^3 D\right), \qquad (1)$$

where the first term in the exponent describes the spin–spin relaxation, and the second term the diffusion damping; h_0 is the maximum value of the echo amplitude, G is the magnetic field gradient, and γ is the gyromagnetic ratio. An estimate shows that for $D \sim 10^{-6}$ cm^2/s and $G \sim 10^{-2}$ G/cm the influence of the second term in (1) becomes noticeable only for $\tau > 10$ s. Therefore, in the experiment we usually used values of τ no greater than 0.5 s. The echo signal was recorded by a Tektronix digital storage oscilloscope. The error in the values of T_2 obtained by a computer processing of the primary experimental data $h(2\tau)$ by the least-squares method using formula (1), was 10% or better and was mainly due to radio noise.

At high temperatures (usually above the phase separation temperature T_{ps}) the spin–spin relaxation times in the homogeneous (unseparated) initial solution T_2^0 were determined from the free induction decay (FID) after the application of a 90° pulse. The FID was also recorded by the Tektronix digital oscilloscope and was subjected to a computer processing based on the assumption that the instantaneous value of the FID amplitude $U(t)$ is described by an exponential function:

$$U(t) = U_0 \exp\left(-\frac{t}{T_2^*}\right), \qquad (2)$$

where U_0 is the maximum value of the FID amplitude and T_2^* is the observed damping time of the FID. The time T_2^* is related to the true spin–spin relaxation time T_2^0 by the relation

$$(T_2^*)^{-1} = (T_2^0)^{-1} + \gamma G d, \qquad (3)$$

where d is the characteristic dimension of the sample in the direction of the magnetic field gradient G. Estimates show that under the given experimental conditions the broadening of the resonance line due to the magnetic field gradient was negligibly small, $\gamma G d \approx 60$ Hz $\ll 1/T_2^0$, and within the accuracy of the measurements the observed damping time T_2^* of the FID can be assumed close to the true spin–spin relaxation time T_2^0.

It is for precisely this reason that it has turned out to be different to measure T_2^0 by the spin echo method at high temperatures. If the second term in the exponent in (1) is negligible, then, since $U_0 \gg h_0$ (Ref. 18), the functions (1) and (2) are nearly the same, and the echo signal therefore is nearly impossible to distinguish against the background of the FID.

We note that the FID method is inapplicable for measuring T_2 in the the melted solid solution in cases where the concentrated bcc phase is characterized by large values of T_2 (120–200 ms), since in that case the damping time of the
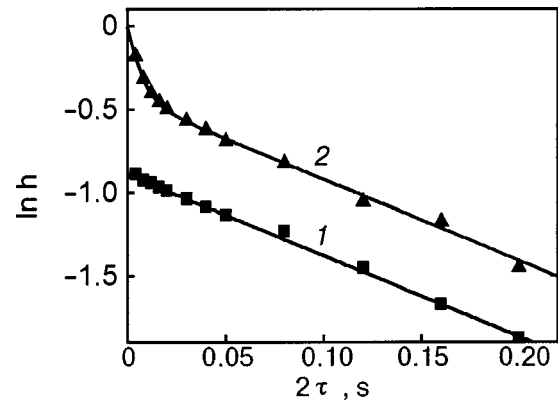

FIG. 1. Damping of the echo signal in a two-phase crystal at a temperature of 192 mK for different waiting times Δt, s: 0.3 (*1*) and 100 (*2*). The solid curves are the results of data processing according to formula (4) with the parameters $A = 0.25$, $T_2^c = 205$ ms, and $T_2^d = 6.5$ ms (see text).

FID observed in this phase $[T_2^* \approx 16 \text{ ms} \sim 1/(60 \text{ Hz})]$ is determined mainly by the magnetic field gradient in in accordance with formula (3).

3. TEMPERATURE DEPENDENCE OF THE SPIN–SPIN RELAXATION TIME

In the two-phase structure of ^{3}He–^{4}He solid solutions each of the phases—the concentrated and the dilute—are characterized by their own values of the spin–spin and spin–lattice relaxation times and have their own contributions to the amplitude of the echo signal:

$$h \approx h_0 \left\{ A \left[1 - \exp\left(-\frac{\Delta t}{T_1^c}\right)\right] \exp\left(-\frac{2\tau}{T_2^c}\right) + (1-A) \right.$$
$$\left. \times \left[1 - \exp\left(-\frac{\Delta t}{T_1^d}\right)\right] \exp\left(-\frac{2\tau}{T_2^d}\right) \right\}. \qquad (4)$$

Here the first term describes the contribution of the concentrated phase, with spin–lattice T_1^c and spin–spin T_2^c relaxation times; the second term is the contribution of the dilute phase, with times T_1^d and T_2^d, respectively; $A < 1$ is the relative fraction of the ^{3}He contained in the concentrated phase, and Δt is the waiting time between pulse trains.

It follows from formula (4) that the large difference in the spin–lattice relaxation times for the two daughter phases of the separated sample[13] enables one to separate the contribution of the concentrated phase to the amplitude of the echo signal. At short waiting times for the recovery of the magnetization, $\Delta t \sim T_1^c \ll T_1^d$, the contribution of the dilute phase is negligible, proportional to the unrecovered magnetization and the small ^{3}He content in this phase, i.e., the second term in (4) can be neglected in this case. If Δt is chosen much larger than T_1^d, then in the two daughter phases the complete recovery of the equilibrium magnetization will occur, and the dependence of the amplitude of the echo on τ can be used to separate the contributions of the two phases, which are characterized by different spin–spin relaxation times.

Figure 1 shows typical results of measurements of T_2 in a two-phase sample for short (curve *1*) and long (curve *2*) waiting times Δt. The solid curves in Fig. 1 are the result of a processing of the experimental data according to formula
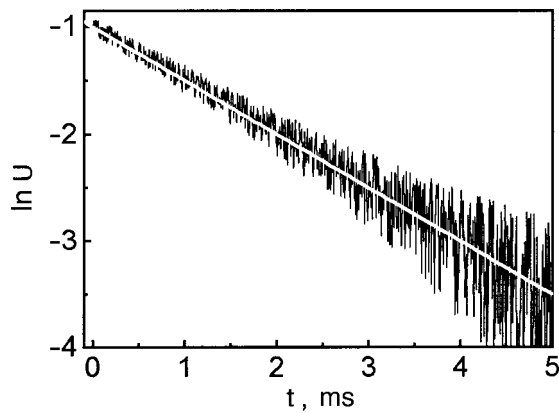
FIG. 2. The damping of the free induction signal (FID) after the application of a 90° pulse in the initial homogeneous sample at 220 mK. The straight line is the result of data processing by the least-squares method according to formula (2).

(4) by the least-squares method with the adjustable parameters A, T_2^c, and T_2^d. Here the cofactors containing the spin–lattice relaxation times T_1^c and T_1^d are constants. For short Δt one observes a single exponent, corresponding to the contribution of the concentrated phase, and at long Δt there are two exponents, reflecting the contributions of the two phases.

It should be noted that as the temperature is lowered, the ^{3}He content in the dilute phase falls off, in accordance with the phase diagram, and therefore the relative contribution to the NMR signal from this phase decreases, and below ~ 180 mK it becomes comparable to the noise level of the amplifier circuit of the spectrometer. For this reason the time T_2^d was measured only in the temperature interval 180–200 mK.

In the high-temperature region, as we have said, the spin–spin relaxation time was determined from the damping of the FIS. Figure 2 shows the form of the FID obtained after the application of a 90° pulse in a homogeneous initial sample at $T = 220$ mK. We can see that the damping of the amplitude of the FID is well described by an exponential function all the way down to the noise level. The straight line in Fig. 2—which is the result of a processing of the FID by the least-squares method according to formula (2)— corresponds to a value $T_2^0 = 2.1$ ms.

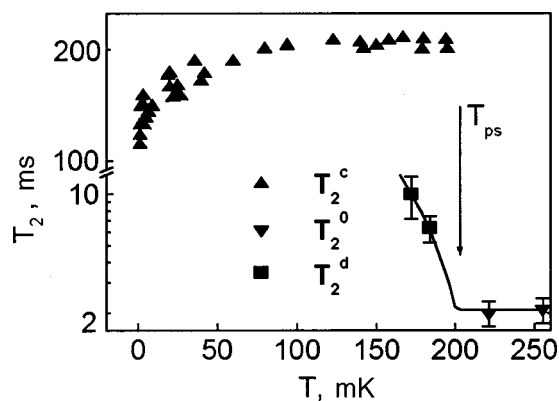Figure 3 shows the values of T_2 thus obtained over the

FIG. 3. Temperature dependence of the spin–spin relaxation time in the solution before and after phase separation. The arrow indicates the phase transition temperature.

whole range of temperatures investigated. In the initial hcp solution the spin–spin relaxation time T_2^0 is independent of temperature and agrees well with the results obtained previously[6–9,11] for homogeneous ^{3}He–^{4}He solid solutions in the region of the exchange plateau with allowance for the concentration and molar volume of the solution.

Below the separation temperature, after the formation of a two-phase crystal, two spin–spin relaxation times were observed–one short and one long. Using the technique described above to separate the contributions of the two phases to the amplitude of the echo signal, it was found that the long relaxation times T_2^c correspond to the concentrated phase and the short times T_2^d to the dilute phase.

3.1. Concentrated phase

Since according to the phase diagram, the concentrated phase of the separated ^{3}He–^{4}He solution at ultralow temperatures corresponds in concentration to practically pure ^{3}He, it is natural to compare the data obtained on T_2^c with the corresponding results for bulk solid ^{3}He. As we see in Fig. 3, the value of T_2^c is practically independent of temperature in the range 50–200 mK and equals 0.21 ± 0.02 s. The temperature independence of T_2^c suggests that the mechanism of the spin–spin relaxation is governed, as in pure ^{3}He, by exchange processes involving the tunneling motion of atoms.

For the region of the exchange plateau the time T_2 in solid ^{3}He is expressed as follows:[1]

$$(T_2^c)^{-1} = \frac{2}{3}\left(\frac{\pi}{2}\right)^{1/2}\frac{M_2}{\omega_E}\left(\frac{3}{2} + \frac{3}{2}e^{-\omega_0^2/2\omega_E^2} + e^{-2\omega_0^2/\omega_E^2}\right), \quad (5)$$

where ω_0 is the Larmor frequency, ω_E is the frequency of the tunneling exchange of neighboring atoms, M_2 is the Van Vleck second magnetic moment, which can be calculated for a bcc crystal with molar volume V from the relation[1]

$$M_2 = 22.8 \cdot 10^{10}/V^2. \quad (6)$$

The analysis in Ref. 1 showed that the best agreement with experiment for bcc ^{3}He is observed if the correlation function describing the pair interaction between nuclear spins is approximated by a Lorenzian. In that case the tunneling exchange frequency ω_E for neighboring atoms is related to the exchange integral J_{33} as

$$\omega_E = 3.36 J_{33}. \quad (7)$$

Previously this was used to obtain a good description of the experimental data for homogeneous solid ^{3}He (see, e.g., Ref. 1).

Under the given experimental conditions, when the Larmor frequency is much less than the tunneling exchange frequency ($\omega_0/\omega_E \ll 1$), formula (5) simplifies substantially, and with allowance for (6) and (7) it becomes

$$(T_2^c)^{-1} = \frac{10}{3}\left(\frac{\pi}{2}\right)^{1/2}\frac{M_2}{\omega_E}. \quad (8)$$

If the value of J_{33} typical for bulk solid ^{3}He and the corresponding molar volume are used in calculating ω_E, Eqs. (6)–(8) yield a value $T_2^c = 0.20 \pm 0.05$ s, which is in good agreement with experiment. We note that the use of the
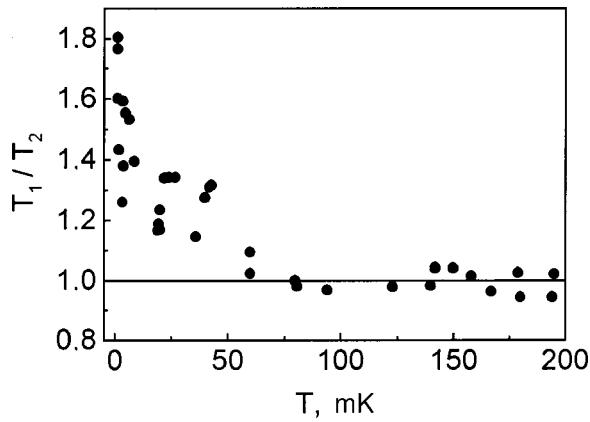
FIG. 4. Temperature dependence of the ratio of the spin–lattice and spin–spin relaxation times in the concentrated phase of the separated solution.
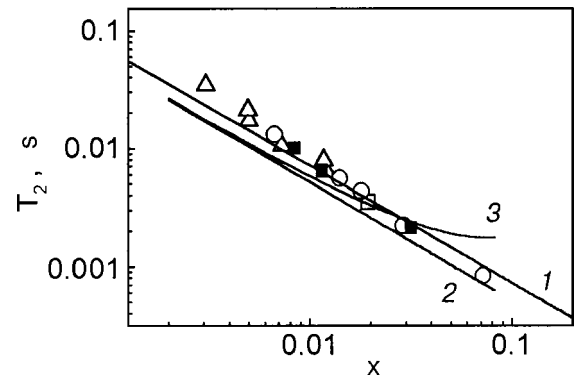

FIG. 5. Concentration dependence of the spin–spin relaxation time in the dilute hcp phase. The experimental data for the homogeneous crystal are denoted by $\square$ (Ref. 8) and $\bigcirc$ (Ref. 11); for the dilute phase of the separated solution by $\triangle$ (Ref. 16) and $\blacksquare$ (present study); line *1* is an approximation of the experimental data by formula (9); line *2* is the result of a calculation in the Torrey theory according to formula (11); line *3* is the result of a calculation according to formulas (12)–(16).

Gaussian approximation, in which case $\omega_E = 4.76 J_{33}$ (Ref. 1), gives $T_2^c = 0.28 \pm 0.05$ s. This does not agree as well with the measured values of T_2^c.

The good agreement of the experimental data on T_2^c for the concentrated phase with the calculation according to Eqs. (6)–(8) means that the spin–spin relaxation in this phase is governed mainly by the ^{3}He–^{3}He tunneling exchange, which is described by the exchange integral J_{33}. However, the concentrated phase contains an appreciable ^{4}He impurity (up to $\sim 3\%$ near the separation temperature), and therefore the data permit one to estimate the contribution of the ^{4}He–^{3}He exchange to the spin–spin relaxation and the corresponding value of the exchange integral J_{43}. If one considers a superposition of the exchange processes ^{3}He–^{3}He and ^{4}He–^{3}He with appropriate weight factors proportional to the concentration, then according to estimates the value of J_{43} cannot differ from J_{33} by more than a factor of 2–3. This means that the estimate of J_{43} in Ref. 1 is apparently somewhat too high.

It is seen from Fig. 3 that below ~ 50 mK the time T_2^c decreases smoothly to values of 0.12 s at the lowest temperatures. This behavior is more clearly seen from the temperature dependence of the ratio T_1^c/T_2^c, which is given in Fig. 4. Here the measurements of the two relaxation times were made in the same experiment. Analysis of expression (5) for T_2^c and the corresponding formula for T_1^c obtained by the same approach in Ref. 13 shows that at the resonance frequency used in the experiment the ratio T_1^c/T_2^c is close to unity. The experimental results in Fig. 4 agree with the prediction of the theory only in the region 50–200 mK, while at lower temperatures the ratio T_1^c/T_2^c increases monotonically on account of a decrease in T_2^c.

The decrease of the spin–spin relaxation time in a system is usually attributed to a weakening of the intensity of the motion of the nuclear spins,[18] i.e., of the value of the spin diffusion. The main mechanism for spin–spin relaxation is due to the interaction between nuclear spins, which is described in terms of local magnetic fields produced by the neighboring nuclear spins at lattice sites. Rapid relative motion of the spins leads to strong fluctuations of the local magnetic fields, and then only the averaged value of the local field, which is much less than the instantaneous value, is important. Thus an increase (decrease) of the diffusion coefficient usually leads to an increase (decrease) of the time T_2.

In the present study, along with measurements of the magnetic relaxation time we made some crude measurements of the spin diffusion coefficient D_s in the concentrated phase. The experiments showed that in the existence region of this phase, all the way down to 1.5 mK, the value of D_s is practically constant and equal to $(7 \pm 2) \times 10^{-8}$ cm^2/s, which is close to the value of the spin diffusion coefficient for bulk ^{3}He of the same density. Therefore the low-temperature decrease of T_2^c can scarcely be attributed to diffusion processes.

Thus, taken together, our experimental data on the times T_1^c and T_2^c and the diffusion coefficient D_s in the concentrated phase of a separated solution of ^{3}He in ^{4}He indicate that above ~ 50 mK the properties of the disperse concentrated phase are close to those of bulk ^{3}He. The reason for the elongation of the exchange plateau of T_1^c into the region of ultralow temperatures and the decrease of T_2^c for $T < 50$ mK remain unclear.

3.2. Dilute phase

The increase in the spin–spin relaxation time in the dilute phase, T_2^d, with decreasing temperature (see Fig. 3) is a reflection of the fact that the concentration of the dilute phase decreases as the temperature is lowered in accordance with the separation phase diagram. Therefore, a clearer and more physical view can be obtained from the concentration dependence of T_2^d, which is shown in Fig. 5, which summarizes the experimental data of different authors for weak solutions of ^{3}He in ^{4}He. Shown are the results of measurements of T_2 both in the homogeneous hcp solution in the region of the tunneling plateau and in the dilute hcp phase of the separated (two-phase) solution. Since in the present study measurements were made along the line of phase separation, the concentration of the dilute phase was determined from the phase diagram of Ref. 19. Out of all the available experimental data on the time T_2 in the hcp phase of the solution ^{3}He–^{4}He, Fig. 5 shows the results which pertain to a molar volume close to that used in the present study, and also for Larmor frequencies ω_0 much less than the energy frequency $\omega_E \sim 10^8$ rad/s. As we see in Fig. 5, the experimental data of the present study are in good agreement with the results of

Ref. 16 for the dilute phase in the two-phase crystal and with Refs. 6 and 8 for single-phase solutions of the corresponding concentrations. This shows that the spin–spin relaxation processes in separated and homogeneous solutions of the same concentration have the same character. A similar conclusion was reached previously in an analysis of the spin–lattice relaxation in separated phases of ^{3}He–^{4}He solid solutions.[13] We note that the experimental data presented in Fig. 5 can be approximated by the relation

$$T_2^d = \alpha/x, \tag{9}$$

where x is the concentration of the solution, and $\alpha = 7.5 \times 10^{-5}$ s. The results of such an approximation are shown by the line *1* in Fig. 5.

The results on the concentration dependence of the time T_2 can be compared to different model descriptions of the spin–spin relaxation in ^{3}He–^{4}He solid solutions. In a calculation of the magnetic relaxation in Ref. 6 only the tunneling exchange ^{3}He–^{3}He was taken into account, i.e., it was assumed that formula (5), which was obtained for ^{3}He, is valid for the solutions, and the specifics of the solutions were taken into account under the assumption that $M_2(x) = x M_2(1)$ and $\omega_E(x) = x^{1/2}\omega_E(1)$. In this approach the concentration dependence of T_2 was predicted to have the form $T_2^{-1} \sim x^{1/2}$, which does not agree with the experimental data. The numerical values of T_2 calculated in such a model are almost two orders of magnitude higher than the measured values.

The calculations of Greenberg *et al.*,[11] based on the Torrey model,[12] have proven more adequate. In those calculations it was assumed that a substantial role in the solutions should be played by the tunneling exchange ^{3}He–^{4}He, with the characteristic time

$$\tau_{34} = (z J_{34})^{-1}, \tag{10}$$

where J_{34} is the corresponding exchange frequency, and z is the number of nearest neighbors. In this approach the spin–spin relaxation time, according to Ref. 11, is written in the form

$$T_2^{-1} = 0.92 x M_2 \tau_{34}. \tag{11}$$

The value of τ_{34} was determined in Ref. 11 as a molar-volume-dependent adjustable parameter of the theory of Ref. 12. If the values of this parameter for the conditions of the present experiment are used, a calculation of T_2^d according to formula (11) gives the values shown by line *2* in Fig. 5, which are quite close to the experimental data.

Another approach to the calculation of T_2 in ^{3}He–^{4}He solutions was developed in Ref. 8, where both types of tunneling exchange, ^{3}He–^{3}He and ^{3}He–^{4}He, were taken into account. In that case

$$T_2^{-1} = \frac{3}{2}J(0) + \frac{5}{2}J(\omega) + J(2\omega), \tag{12}$$

where the spectral density function $J(\omega)$ is expressed in terms of the corresponding functions for the two types of exchange,

$$J(\omega) = c J(\omega)|_{3-4} + (1-c)J(\omega)|_{3-3}, \tag{13}$$

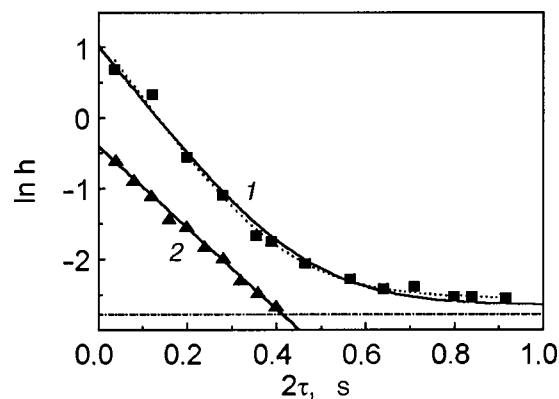and the weight factor c depends strongly on the concentration of the solution,

FIG. 6. Damping of the echo signal at ultralow temperatures T, mK: 5 (*1*), 20 (*2*). The waiting time was several minutes. The dot-and-dash line is the boundary of linearity of the amplifier circuit of the NMR spectrometer; the dotted line is an approximation according to formula (4); the solid line is a calculation according to formula (17).

$$c = (1-x)^{12}. \tag{14}$$

According to Ref. 8, the functions $J(\omega)|_{3-3}$ and $J(\omega)|_{3-4}$ have the form

$$J(\omega)|_{3-3} = 0.96 \frac{x^{1/2}M_2(1)}{\omega_E(1)}$$

$$\times \exp\left\{ -\frac{1.6\omega^2[x^{1/2}\omega_E(1)]^{-2}}{\omega[x^{1/2}\omega_E(1)]^{-1} + 1.0} \right\}, \tag{15}$$

$$J(\omega)|_{3-4} = x M_2(1)\tau_{34}G\left(\frac{\omega\tau_{34}}{2}\right). \tag{16}$$

Here the correlation time describing the tunneling exchange ^{3}He–^{4}He depends on the concentration as $\tau_{34} \sim x^{-1/3}$, and the function $G(\omega_0\tau_{34}/2)$ was calculated in Ref. 12.

The results of a calculation of T_2^d with both types of tunneling exchange taken into account, according to formulas (12)–(16), are shown in by line *3* in Fig. 5. We note that for weak solutions the approaches to the calculation of T_2 in Refs. 11, 12, and 8 are practically the same. This means that at low ^{3}He concentrations (less than 1%) in the solid solution the main tunneling process is the ^{3}He–^{4}He exchange, and the ^{3}He–^{3}He exchange can be neglected. The latter begins to play an appreciable role only at higher concentrations.

4. ANOMALOUS DAMPING OF THE SPIN ECHO AT ULTRALOW TEMPERATURES

The primary experimental data obtained at the lowest temperatures require a separate analysis. Here the behavior of the amplitude h as a function of twice the interval τ between 90° and 180° rf probe pulses differs substantially from the typical dependence shown in Fig. 1. It was found that below ~ 10 mK the $h(2\tau)$ plot, after a rapid exponential damping of the echo with a characteristic time T_2^c, one observes a much slower damping of the signal amplitude at $2\tau > 0.3$ s (curve *1* in Fig. 6). For comparison, curve *2* in Fig. 6 shows the corresponding plot of $\ln h(2\tau)$ at $T = 20$ mK, where this anomaly is not observed.

The cause of the anomaly cannot be attributed to nonlinearity of the amplifier circuit of the NMR spectrometer at low signal levels, since, as can be seen from Fig. 6, the data

at 20 mK contain echo signals of smaller amplitude than at 5 mK, but no appreciable deviations from a single exponential can be observed. A special check showed that the dynamic characteristics of the amplifier circuit of the spectrometer remained linear at signal levels above the dot-and-dash line in Fig. 6.

Analysis of curve *1* in Fig. 6 shows that it can be approximated by two different dependences: either a superposition of two exponential functions or the sum of one exponential function and a nonexponential function.

In the first case the presence of two exponentials would mean that at very low temperatures there are contributions to the damping of the echo signal from two phases: the concentrated phase with spin–spin relaxation time T_2^c, and some new phase with a very large characteristic relaxation time T_2^x. The result of such an approximation, obtained with the use of formula (4) with two adjustable parameters A and T_2^x, is shown by the dotted curve in Fig. 6. Here the value of the relaxation time T_2^x turns out to be so large (~ 20 s) that it can be characteristic of only an extremely weak solution ($x \ll 10^{-5}$). The sensitivity of the NMR spectrometer used does not permit the observation of a signal from such a small number of ^{3}He nuclei, and this hypothesis seems unrealistic.

A more plausible approach is to assume the presence of exponential damping with a time constant T_2^c at short τ and a nonexponential damping of the spin echo at long τ, which corresponds to a diffusion process with a large diffusion coefficient D_x. An analogous situation was observed previously in an NMR study of ^{3}He in solid hydrogen,[20] and the diffusion process was linked to the quasi-one-dimensional diffusion of ^{3}He along dislocations of the matrix.

In this case, with allowance for the results of Ref. 21 and by analogy with Eq. (4), we can write the dependence of the echo signal amplitude on the time τ in the form

$$\frac{h}{h_0} = A \exp\left(-\frac{2\tau}{T_2^c}\right) + (1-A)\frac{\sqrt{\pi}}{2}$$

$$\times \left(\frac{2}{3}\gamma^2 G^2 \tau^3 D_x\right)^{-1/2} \varphi(\tau), \tag{17}$$

where

$$\varphi(\tau) = \mathrm{erf}\left(\frac{2}{3}\gamma^2 G^2 \tau^3 D_x\right)^{-1/2},$$

and

$$\mathrm{erf}(y) = \frac{2}{\sqrt{\pi}}\int_0^y e^{-t^2}\,dt$$

is the error function.

Formula (17) can satisfactorily describe the experimental data in Fig. 6 for the following values of the adjustable parameters: $D_x = 5\times10^{-5}$ cm^2/s, $A = 0.97$ (solid curve). We note that in Ref. 20 a value of the same order of magnitude was obtained for the quasi-one-dimensional diffusion coefficient. The small relative contribution of the ''X'' phase, $1 - A = 0.03$, to the amplitude of the echo according to (17) precludes its observation at higher temperatures, where the amplitude of the NMR signal falls off in accordance with the Curie law.

CONCLUSION

A study of the spin–spin relaxation processes in phase-separated ^{3}He–^{4}He solid solutions has shown that in the concentrated phase the relaxation time is possibly independent of temperature down to 50 mK and can be described by exchange processes involving the tunneling motion of the ^{3}He atoms. Here the numerical values of the time T_2 are in good agreement with the corresponding values for pure bulk ^{3}He.

In the dilute phase of the separated solution the spin–spin relaxation time can be described in the Torrey model with allowance for the ^{3}He–^{4}He tunneling exchange. Here the concentration dependence of T_2 has the form $1/x$, and the values obtained for T_2 agree with the data on the spin–spin relaxation times for homogeneous ^{3}He–^{4}He solutions of the corresponding concentration.

The reason for the smooth decrease in the time T_2 in the concentrated phase below ~ 50 mK remains unclear. As to the anomalous behavior of the damping of the spin echo at temperatures below ~ 10 mK, it may be a manifestation of a quasi-one-dimensional diffusion process.

The authors thank V. N. Grigor'ev for a helpful discussion of the results.

a)E-mail: mikhin@ilt.kharkov.ua

[1] R. A. Guyer, R. C. Richardson, and L. I. Zane, Rev. Mod. Phys. **43**, 532 (1971).
[2] H. A. Reich and W. N. Yu, Phys. Rev. **129**, 630 (1963).
[3] R. C. Richardson, A. Landersman, E. R. Hunt, and H. Meyer, Phys. Rev. **146**, 244 (1966).
[4] M. Bernier, J. Low Temp. Phys. **56**, 205 (1984).
[5] R. L. Garwin and A. Landersman, Phys. Rev. **133**, A1503 (1964).
[6] D. S. Miyoshi, R. M. Gotts, A. S. Greenberg, and R. C. Richardson, Phys. Rev. A **2**, 870 (1970).
[7] M. G. Richards, J. Pope, P. S. Tofts, and J. H. Smith, J. Low Temp. Phys. **24**, 1 (1976).
[8] Y. Hirayoshi, T. Mizusaki, S. Maekawa, and A. Hirai, J. Low Temp. Phys. **30**, 137 (1978).
[9] A. R. Allen, M. G. Richards, and J. Shratter, J. Low Temp. Phys. **47**, 289 (1982).
[10] M. Bernier and G. Deville, J. Low Temp. Phys. **16**, 349 (1974).
[11] A. S. Greenberg, W. C. Thomlinson, and R. C. Richardson, J. Low Temp. Phys. **8**, 3 (1972).
[12] H. C. Torrey, Phys. Rev. **96**, 690 (1954); **92**, 962 (1953).
[13] N. P. Mikhin, A. V. Polev, E. Ya. Rudavskiĭ, and V. A. Shvarts, Fiz. Nizk. Temp. **23**, 607 (1997) [Low Temp. Phys. **23**, 455 (1997)].
[14] N. P. Mikhin, N. F. Omelaenko, A. V. Polev, E. Ya. Rudavskiĭ, and V. A. Shvarts, Fiz. Nizk. Temp. **24**, 1127 (1998) [Low Temp. Phys. **24**, 845 (1998)].
[15] S. C. J. Kingsley, I. Kosarev, L. Roobol, V. Maidanov, J. Saunders, and B. Cowan, J. Low Temp. Phys. **110**, 34 (1998).
[16] S. C. J. Kingsley, V. Maidanov, J. Saunders, and B. Cowan, J. Low Temp. Phys. **113**, 1017 (1998).
[17] A. A. Golub, V. A. Goncharov, V. R. Litvinov, V. A. Mikheev, E. Ya. Rudavskiĭ, Yu. A. Tokar', A. M. Usenko, and V. A. Shvarts, Fiz. Nizk. Temp. **21**, 974 (1995) [Low Temp. Phys. **21**, 751 (1995)].
[18] A. Abragam, *The Principles of Nuclear Magnetism*, Clarendon Press, Oxford (1961) [Izd. Inostr. Lit., Moscow (1963)].
[19] V. A. Shvarts, N. P. Mikhin, E. Ya. Rudavskiĭ, Yu. A. Tokar', A. M. Usenko, and V. A. Mikheev, Fiz. Nizk. Temp. **20**, 645 (1994) [Low Temp. Phys. **20**, 505 (1994)].
[20] V. A. Mikheev, V. A. Maĭdanov, and N. P. Mikhin, Fiz. Nizk. Temp. **7**, 670 (1981) [Sov. J. Low Temp. Phys. **7**, 330 (1981)].
[21] V. A. Mikheev and V. A. Slyusarev, Fiz. Nizk. Temp. **7**, 379 (1981) [Sov. J. Low Temp. Phys. **7**, 186 (1981)].

Translated by Steve Torstveit

Growth and dissolution of ³He liquid drops in a ⁴He crystalline matrix

A. N. Gan'shin, V. N. Grigor'ev, V. A. Maĭdanov, A. A. Penzev, É. Ya. Rudavskiĭ,* and A. S. Rybalko

B. Verkin Institute for Low Temperature Physics and Engineering, National Academy of Sciences of Ukraine, pr. Lenina 47, 61164 Kharkov, Ukraine
(Submitted January 17, 2000)
Fiz. Nizk. Temp. **26**, 550–556 (June 2000)

Pressure measurements are used to study the kinetics of phase separation of ³He–⁴He solid solutions under conditions such that after the transition a two-phase system is formed, consisting of liquid drops of the concentrated phase (nearly pure ³He) in a crystalline matrix of the dilute phase (nearly pure ⁴He). It is shown that under stepped cooling of the two-phase sample the growth of the liquid drops can be described by a superposition of two exponential functions representing processes with long and short time constants. This is due to the strong influence of the stresses arising in the crystal at the phase transition owing to the large difference in the molar volumes of the two phases and which probably cause plastic deformation of the matrix and the giving rise to nonequilibrium concentrations of ³He in it. The transport of ³He atoms occurs only in connection with stress relaxation. It is established that cyclic processes of growth and dissolution of the liquid drops strongly degrade the quality of the crystal and lead to an increase of the pressure. The possibility that a mixture of the liquid and crystal exists in the drops is also analyzed. © *2000 American Institute of Physics.* [S1063-777X(00)00406-0]

1. INTRODUCTION

The phase diagram of the system ³He–⁴He is in general extremely complex and admits various combinations of condensed phases found in equilibrium with one another. An important circumstance here is that phase diagram changes with pressure. Since the melting pressures of the pure isotopes ³He and ⁴He are very different, as can be seen from Fig. 1, one can use pressure as a parameter controlling the phase composition of the crystal in studies of ³He–⁴He solutions.

In this paper we continue the research begun earlier[1–4] on the kinetics of the processes occurring in a solid solution containing 2.05% ³He. The melting line of this solution practically coincides with the melting line of pure ⁴He on the scale in Fig. 1, and the line of phase separation is shown by the dot-and-dash line. Our previous experiments[1–4] on the kinetics were done at a pressure exceeding the melting pressure of pure ³He at $T=0$ (line *1*) and at a pressure exceeding the minimum on the melting curve of ³He, but below the melting pressure of ³He at $T=0$ (line *2*). In the second case the solid inclusions of ³He formed as a result of the phase separation are transformed into ³He liquid drops upon further cooling (after crossing the ³He melting curve). This system has also been studied in experiments at the University of Florida,[5–7] where incomplete melting of the ³He inclusions was detected.

In the present study we investigate the region of intermediate pressures—above the ⁴He melting line and below the minimum on the ³He melting curve (line *3* in Fig. 1). In this case, as a result of the phase separation a two-phase system arises which consists of liquid drops of the concentrated phase (close in concentration to pure ³He) in a crystalline matrix of the dilute phase (nearly pure ⁴He). Previous studies have investigated the specific heat[8,9] and magnetic relaxation processes[10,11] in such a system. However, there is practically no information about the kinetics of the growth and dissolution of liquid drops arising in the crystal. This is the subject of the present study.

2. EXPERIMENTAL PROCEDURE

The kinetic processes in ³He–⁴He two-phase solid solutions containing liquid drops were studied by means of precision measurements of the pressure of the crystal at constant volume. The measuring cell and procedures were described previously.[4] A solution with an initial concentration of 2.05% ³He was crystallized by the method of capillary blocking and then annealed for several days near the melting temperature. Then the homogeneous annealed crystal was cooled below the phase separation temperature, and a temperature cycling of the two-phase sample was carried out (as in Ref. 4). As was shown in Ref. 4, such a treatment usually improves the quality of the crystal and makes for better reproducibility of the results.

In the experiment we investigated the following kinetic processes:

— growth of liquid drops upon cooling of the two-phase system in small steps ($\approx 10\,\text{mK}$);

— dissolution of the drops during a stepped heating;

— growth and dissolution of the drops upon abrupt cooling and heating (large steps).

3. EFFECT OF TEMPERATURE CYCLING ON THE TWO-PHASE SAMPLES

Figure 2 shows the change in pressure in a two-phase crystal containing liquid drops during four cooling–heating
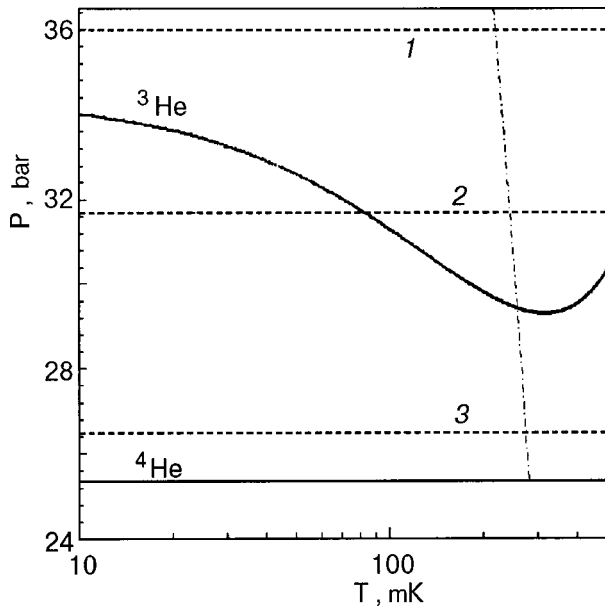
FIG. 1. Lines of melting of pure ^{4}He and ^{3}He and the lines of phase separation of a solid solution containing 2% ^{3}He (-··-). The dashed lines *1* and *2* correspond to the pressures at which the measurements were made in Refs. 1–4, and line *3* corresponds to the present measurements.

cycles and the corresponding thermogram $T(t)$. First of all it should be noted that the result of the temperature cycling in this case is markedly different from that of an analogous treatment at high pressure (≈ 36 bar), where the ^{3}He inclusions are solid.[4]

In the case of solid inclusions, after each cycle the pressure in the crystal became less than the initial pressure, apparently because of the elimination of defects and improvement of the quality of the crystal. The greatest decrease in the pressure was observed after the first cycle, and then the pressure rapidly went to saturation. In the case when liquid drops are formed, as we see in Fig. 2, the pressure after each cycle increases instead, and the rapid saturation does not occur. A clearer comparison of the behavior of these two-phase systems is presented in Fig. 3. Besides the difference in the dependence on the number of the cycle, one notices a difference in scales: whereas for the solid inclusions one is talking about values of the order of several millibars, in the case of the liquid drops the effect is an order of magnitude larger.

We note that an even more significant increase in pressure was observed during the melting and crystallization of originally solid inclusions (see Refs. 4 and 5). This circumstance is clearly correlated with the value of the stresses expected in these cases, which are primarily determined by the difference of the molar volumes of the initial and incipient phases. In the formation of liquid inclusions this difference is approximately 4 times as large as for solid inclusions (see below), and in the course of melting and crystallization of the inclusions the additional increase in stress may be due to the fact that the large change in the density is localized mainly just in the region of the inclusion. It can be stated unambiguously that the cyclic processes of growth and dissolution of the liquid drops as a result of the phase separation degrades the quality of the crystal appreciably.

One more difference in the behavior of the two-phase
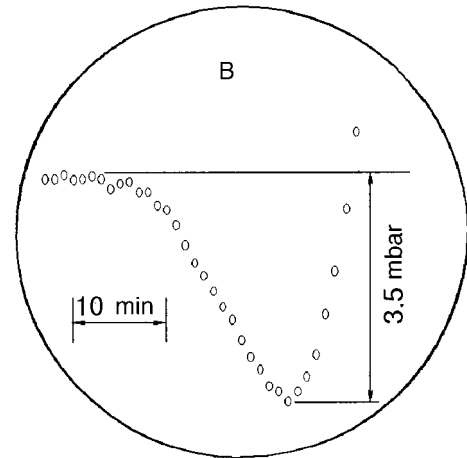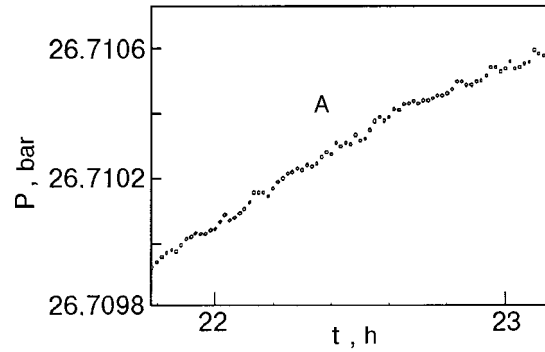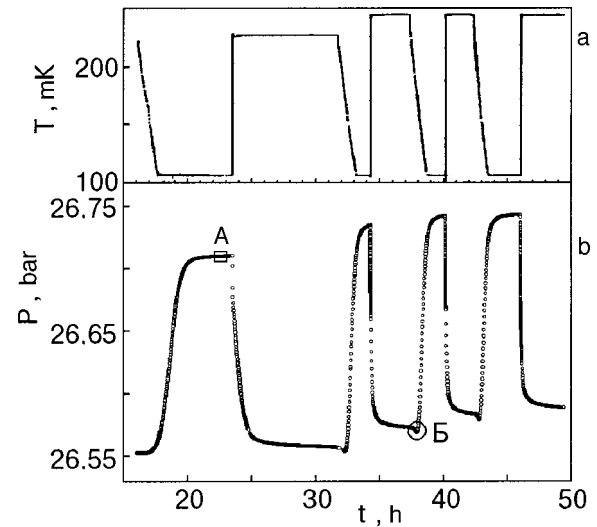
FIG. 2. Kinetics of the temperature cycling of the sample: the change in the temperature of the crystal in the course of four cooling–heating cycles (a) and the corresponding pressure change (b). Insets A and B show the irregularities in the last stage of the phase separation and the pressure anomaly before the start of the cycle, respectively.

crystal containing liquid drops of the concentrated phase in comparison with the two-phase crystal containing solid inclusions is the disagreement between the calculated value of the total pressure change ΔP at the phase transition. In the case of solid inclusions the value of ΔP observed in experiment was in satisfactory agreement with the calculated value of the pressure jump due to the phase separation at constant volume:

$$\Delta P = V^E / V \beta, \qquad (1)$$

FIG. 3. Pressure after a cooling–heating cycle versus the number of the cycle for two samples: solid inclusions (a) and liquid inclusions (b).

where V and β are the molar volume and compressibility of the crystal, and the excess molar volume, according to Ref. 12, is related to the concentration x of the solution as

$$V^E[\text{cm}^3/\text{mole}] = 0.4x(1-x). \qquad (2)$$

In the case of liquid drops the numerator of formula (1) should be replaced by the sum

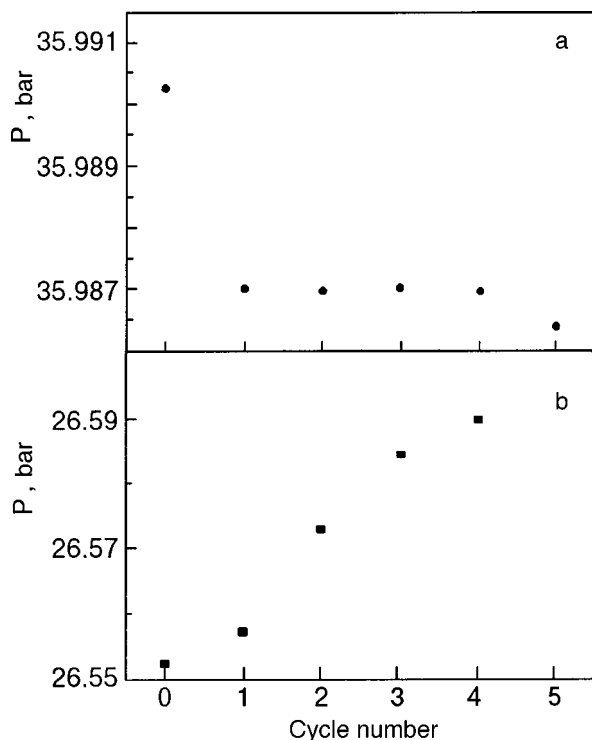$$V^E + x\Delta V, \qquad (3)$$

where ΔV is the difference of the molar volumes of the liquid and solid inclusions of the concentrated phase. Then an estimate of the size of the pressure jump due to the formation of the liquid drops, according to Eqs. (1)–(3), gives $\Delta P \approx 0.4$ bar, which is almost 3 times as large as that observed in experiment. We note the following circumstances that might lead to this disagreement.

1. The large change in volume upon the formation of the liquid phase can cause local stresses exceeding the yield stress and lead to plastic deformation of the layer surrounding a drop. This, on the one hand, can promote the formation of a quasi-equilibrium state, when the excess free energy in the matrix is counterbalanced by the increased pressure in the drop. Under such conditions the transport of ^{3}He into the drop can occur only in connection with stress relaxation. On the other hand, the presence of stresses leads to a slowing of the diffusion owing to the disruption of the energy levels of the ^{3}He impurities in the neighboring sites of the lattice and the direct influence of the elastic potential gradient on the diffusion flux, as was noted in Ref. 3. Confirmation of the reality of the influence of stress relaxation is provided by the presence of pronounced irregularities in the later stages of the phase separation (see inset A in Fig. 2). We note that the possibility of slowing of the phase transition under the influ-

ence of the stresses that arise was pointed out in Ref. 13. Unusual behavior of the pressure at the start of the second and subsequent cycles (inset B in Fig. 2) may also be interpreted as being a consequence of the partial stress relaxation on account of the increased mobility of the ^{3}He atoms upon the onset of large ∇x.

2. It could be that the crystals and liquid coexist in some inclusions. This would require that the pressure inside these inclusions be equal to the melting pressure P_m, which is around 29 bar, i.e., it would have to differ from the bulk value by approximately 3 bar. Such a pressure difference cannot arise in the later states of the phase separation process, since at such a ΔP it would not be possible to have equality of the chemical potentials. However, it could arise as a consequence of the specifics of nucleation in the given case. Because of the severalfold difference of the surface tension at the boundary of the solid separated phases[1] and the liquid and crystal, the critical radius of nucleation for liquid inclusions is larger than that for the solid inclusions by the same factor. Consequently, the formation of solid nuclei is more probable, and they will melt in the later stages. However, the melting involves a large increase in volume, which can lead to plastic deformation and hardening of a layer at the boundary of the nucleus. This, on the one hand, can tend to preserve the excess pressure, and, on the other, can hinder the influx of the ^{3}He atoms toward the nucleus. It is very difficult to estimate this effect; we note only that the possibility of coexistence of the liquid and crystal under nonequilibrium conditions was mentioned in Refs. 4 and 5.

4. GROWTH KINETICS OF THE LIQUID DROPS

The growth kinetics of liquid inclusions in a crystalline matrix was studied under stepped cooling of a two-phase crystal below the phase separation temperature. A thermogram of this cooling and the corresponding pressure change are shown in Fig. 4. As in the experiments with solid inclusions,[1,4] the temperature was changed in each cooling step by 10–15 mK, after which the a temperature stabilization was carried out. The state of the two-phase crystal was monitored from the change in pressure, and the establishment of equilibrium between the coexisting phases at each step corresponded to the condition that the pressure no longer changed with time (i.e., it reached a plateau).

Figure 5a shows in enlarged scale the typical pressure change over the course of a step, which reflects the growth kinetics of the liquid drops as the temperature is lowered. Previously[4] in the case of solid inclusions the analogous dependence was well described by an exponential law,

$$P = P_f - (P_f - P_i)\exp(-t/\tau), \qquad (4)$$

where P_i and P_f are the pressure in the crystal at the beginning and end of the step, respectively, and τ is a characteristic time that determines the rate of the process. The time dependence of $P(t)$ found in the present experiments cannot be satisfactorily described by relation (4). This is particularly evident in Fig. 5b, where the results are plotted on a logarithmic scale—one can see a clear deviation from linearity. An analytical description of the data obtained within the scatter of the experimental points turned out to be possible only by using a sum of two exponentials:
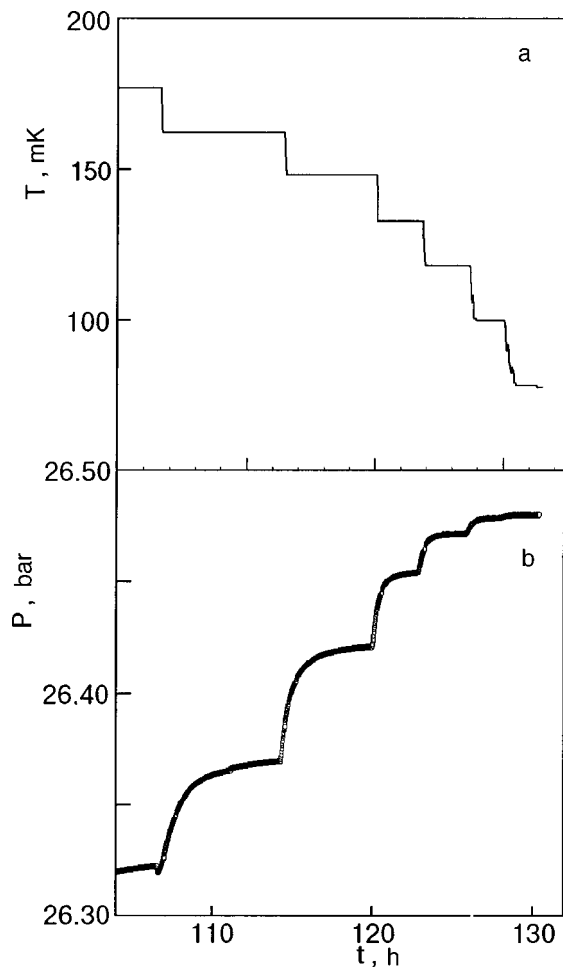
FIG. 4. Thermogram (a) and the kinetics of the pressure change (b) during the stepped cooling of a two-phase crystal containing liquid drops.

$$P = P_f + A \exp(-t/\tau_1) + B \exp(-t/\tau_2), \qquad (5)$$

which is natural to regard as evidence of a superposition of two processes. Figure 6a shows the temperature dependence of the time τ_1 characterizing the faster process, and $\tau(T)$ obtained in Ref. 1 for a sample with nearly the same molar volume, $V = 20.57 \, \mathrm{cm^3/mole}$. The good agreement of the results allows us to conclude that the faster process in our case is evidence of a diffusion mechanism of decay. The displacement of the minimum of the $\tau(T)$ curve to higher temperatures can be regarded as confirmation of the explanation of this minimum proposed in Ref. 3, where it was interpreted as being due to the fact that the diffusion processes are affected by the stresses arising in the decay. In our case these stresses are clearly greater and are therefore manifested at higher temperatures (concentrations). The shift of the minimum can turn out to be larger if the aforementioned departure from equilibrium of the concentrations is appreciable.

Figure 6b shows the temperature dependence of the longer time τ_2, which can be associated with the aforementioned relaxation of the local stress. If in accordance with the data of Ref. 4 we assume that the diffusion of atoms in the sample is promoted by stress relief, then the observed decrease in τ_2 as the temperature is lowered (to the temperature of the minimum on the $\tau(T)$ curve in Fig. 6a) can be explained by an increase in the mobility of the ^{3}He atoms.
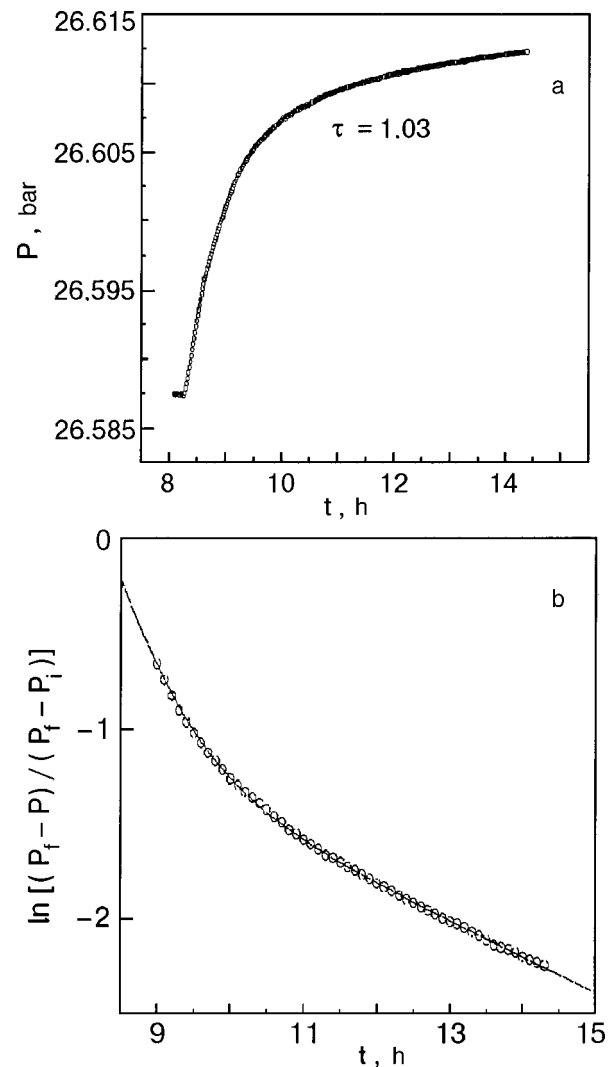
FIG. 5. a—Typical variation of the pressure in a two-phase crystal within a single temperature step ($T_i = 184 \, \mathrm{mK}$; $T_f = 173 \, \mathrm{mK}$); b—the same data plotted in the coordinates $\ln(P_f - P)/(P_f - P_i)(t)$. The curve corresponds to an approximation according to formula (5).

In the last stage of the decay processes, as in inset A of Fig. 2, a nonmonotonic dependence of $P(t)$ was observed, which is manifested especially clearly in the low-temperature region, when the concentration gradients are small from the very beginning. Figure 7 shows the data for the phase separation process at $T_f = 91 \, \mathrm{mK}$, and we see the instability of the pressure in the two-phase crystal.

5. KINETICS OF DISSOLUTION OF THE LIQUID DROPS

According to the state diagram, as the temperature of the two-phase crystal is increased the amount of the liquid or solid phase which is precipitated in the form of inclusions in the crystalline matrix should decrease. This corresponds to a process of ''dissolution'' of the drops, which leads to a decrease in the pressure of the system (see Fig. 8). Here analysis of the $P(t)$ curves obtained under the conditions of the present experiment showed that, as during the growth of the drops, these curves can be described by a superposition of two exponential functions [formula (5)] with time constants τ_1^* and τ_2^*, but in this case their values are poorly reproduc-

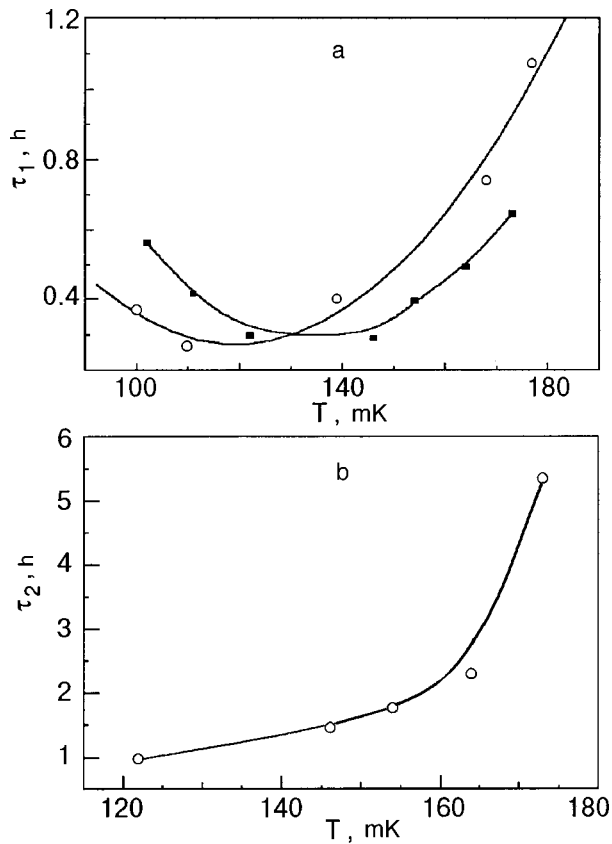FIG. 6. Temperature dependence of the characteristic time τ_1 ($\bigcirc$—V = 20.92 cm^3/mole); plotted for comparison are the values of $\tau(T)$ for solid inclusions ($\blacksquare$—V = 20.57 cm^3/mole; Ref. 1) (a) and τ_2 (b).

ible and a large scatter of the data is observed. Nevertheless, it can be noted that τ_1^* and τ_2^* depend weakly on the temperature (concentration).
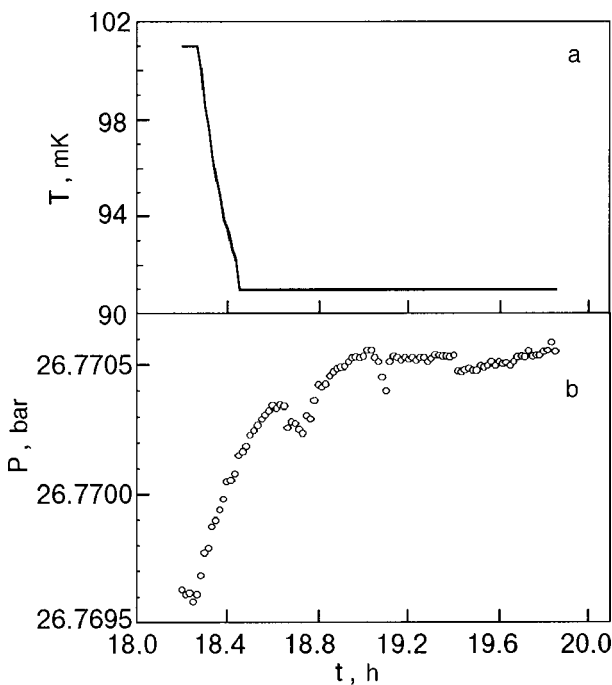

FIG. 7. Kinetics of the change in temperature (a) and pressure (b) during phase separation of a two-phase crystal containing liquid drops at low temperatures (T_i = 101 mK, T_f = 91 mK).
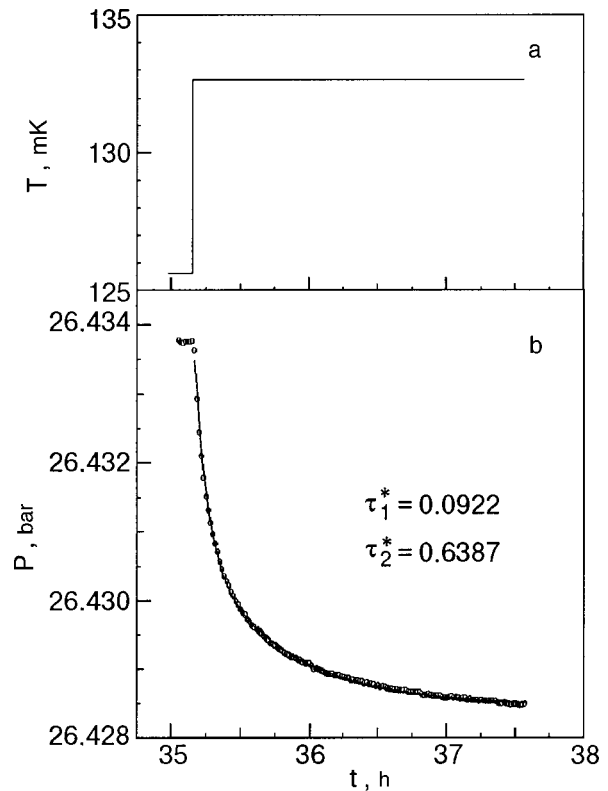
FIG. 8. Thermogram (a) and the kinetics of the pressure variation (b) during heating of a two-phase crystal (T_i = 125.6 mK, T_f = 132.7 mK).

Furthermore, whereas in the case of solid inclusions the time constants of the growth (τ) were always larger than the corresponding time constants for the dissolution (τ^*),[4] for inclusions in the form of liquid drops, τ_1 and τ_2 are approximately equal to τ_1^* and τ_2^*, respectively.

6. CONCLUSION

The present experiments have established that the kinetics of the liquid drops of the concentrated phase formed in a crystalline matrix of the dilute phase is substantially influenced by the large local stresses arising on account of the difference in the molar volumes of the phases. This leads to the situation that the diffusional transport of ^{3}He is greatly suppressed and occurs only in connection with the stress relaxation. For this reason the growth kinetics of the liquid drops can be described by a superposition of two exponential functions, corresponding to the presence of two processes—a diffusional decay with a short time constant, and stress relaxation with a long time constant.

We have shown that repeated cycles of growth and dissolution of the liquid drops lead to an increase in the pressure of the crystal (plastic deformation of the crystal occurs). Here the experimental value of the total pressure change due to the phase transition turns out to be almost a factor of three smaller than the calculated value of the pressure jump due to the phase separation at a constant volume.

These effects can be explained on the basis that the concentrated phase is a mixture of liquid and crystal, since in the initial stage of the transition the formation of solid nuclei is more probable. The subsequent melting of the new-phase inclusions enhances the stress in the crystal and can lead to

plastic deformation and the suppression of mass transport. This gives rise to a nonequilibrium concentration of ^{3}He in the matrix of solid ^{4}He. We have established that the dissolution of the liquid drops can also be described by a superposition of two processes, although, in view of the poor reproducibility of the results, it is difficult to analyze them as yet.

[*]E-mail: rudavskii@ilt.kharkov.ua

[1)]The surface tension at the phase boundary of the separated solid solutions was not measured, but one can assume that it is smaller than at the boundary of liquid solutions, where it has a value $\approx 2 \times 10^{-5}$ J/m^2 (see, e.g., Ref. 14) and becomes smaller as the pressure increases. The surface tension at the boundary of liquid and solid ^{3}He was measured in Ref. 15.

[1] A. N. Gan'shin, V. A. Maĭdanov, N. F. Omelaenko, A. A. Penzev, É. Ya. Rudavskiĭ, and A. S. Rybalko, Fiz. Nizk. Temp. **24**, 815 (1998) [Low Temp. Phys. **24**, 611 (1998)].

[2] A. N. Gan'shin, V. A. Maĭdanov, N. F. Omelaenko, A. A. Penzev, É. Ya. Rudavskiĭ, and A. S. Rybalko, Fiz. Nizk. Temp. **24**, 1117 (1998) [Low Temp. Phys. **24**, 840 (1998)].

[3] A. N. Gan'shin, V. N. Grigor'ev, V. A. Maĭdanov, N. F. Omelaenko, A. A. Penzev, É. Ya. Rudavskiĭ, and A. S. Rybalko, Fiz. Nizk. Temp. **25**, 356 (1999) [Low Temp. Phys. **25**, 259 (1999)].

[4] A. N. Gan'shin, V. N. Grigor'ev, V. A. Maĭdanov, N. F. Omelaenko, A. A. Penzev, É. Ya. Rudavskiĭ, A. S. Rybalko, and Yu. A. Tokar', Fiz. Nizk. Temp. **25**, 796 (1999) [Low Temp. Phys. **25**, 592 (1999); Erratum **25**, 928 (1999)].

[5] R. P. Haley, W. Ni, and E. D. Adams, Czech. J. Phys. **48**, Suppl. 1, 477 (1996).

[6] E. D. Adams, V. Shvarts, R. P. Haley, N. Matsunaga, and J. S. Xia, J. Low Temp. Phys. **113**, 375 (1998).

[7] R. P. Haley and E. D. Adams, J. Low Temp. Phys. **110**, 121 (1998).

[8] B. Herbal, A. S. Greenberg, M. T. Beal-Monod, M. Papoular, G. Frossati, H. Godfrin, and D. Thoulaze, Phys. Rev. Lett. **46**, 42 (1981).

[9] R. Schrenk, O. Friz, Y. Fujii, E. Syskakis, and F. Pobel, J. Low Temp. Phys. **84**, 133 (1991).

[10] A. S. Greenberg, W. C. Thomlinson, and R. C. Richardson, J. Low Temp. Phys. **8**, 3 (1972).

[11] S. C. J. Kingsley, I. Kosarev, L. Roobol, V. Maidanov, J. Saunders, and B. Cowan, J. Low Temp. Phys. **110**, 399 (1998).

[12] W. J. Mullin, Phys. Rev. Lett. **20**, 254 (1968).

[13] V. V. Slezov, Fiz. Tverd. Tela (Leningrad) **16**, 785 (1974) [Sov. Phys. Solid State **16**, 508 (1974)].

[14] K. Ohishi, H. Yamamoto, and M. Suzuki, J. Low Temp. Phys. **112**, 199 (1998).

[15] E. Rolley, S. Balibar, F. Gallet, F. Graner, and C. Guthann, Europhys. Lett. **8**, 523 (1989)

Translated by Steve Torstveit

SUPERCONDUCTIVITY, INCLUDING HIGH-TEMPERATURE SUPERCONDUCTIVITY

Superconducting transition temperature and isotope exponent in superconductors with low Fermi energies

M. E. Palistrant*

Institute of Applied Physics, ul. Akademicheskaya 5, 2028 Kishinev, Moldova

A study is made of superconductivity in systems with a variable density of charge carriers, strong electronic correlations (which influence the electron–phonon interaction), and low Fermi energies. This last circumstance leads to violation of the Migdal theorem and makes it necessary to take into account the vertex and crossed diagrams for the electron–phonon interaction (P_v, P_c). Two- and three-dimensional systems are considered. The values of P_v and P_c are found, and the equation for the momentum cutoff Q_c of the electron–phonon interaction is derived. The dependence of this quantity on the concentration of charge carriers is demonstrated. Expressions are obtained for the superconducting transition temperature T_c and the isotope exponent α, and their behavior as functions of the carrier concentration is analyzed. The values of the carrier densities for which superconductivity can occur in two- and three-dimensional systems are determined. © *2000 American Institute of Physics.* [S1063-777X(00)00506-5]

1. INTRODUCTION

A rich body of experimental and theoretical research material on oxide ceramics has been accumulated since the discovery of high-temperature superconductivity. However, the description of the physical properties of these materials remains one of the most difficult problems in low-temperature physics today. This is because of the complexity of the objects of study: they have a complex crystal structure, strong anisotropy, anomalies in the electronic energy spectrum, a variable concentration of charge carriers, strong electronic correlations, and so on. Models for the analysis of such systems apparently should be based on the Hubbard model, which takes into account the strong electronic correlations due to the Coulomb interaction of the electrons, and should take into account the strong electron–phonon interaction. A review of the different approaches to this problem and the approximations used in them is given in Ref. 1, for example.

A special diagrammatic technique that permits one to take into account the strong electronic correlations and strong electron–phonon interaction has been developed for such systems.[1–4] This theory contains dielectric and magnetic phase transitions and the possible onset of superconductivity. However, because of the great mathematical difficulties it is hard to obtain any meaningful physical results without making some substantial simplifications. Moreover, at a certain carrier density a metallic states arises in the system, in which the electronic states are modified but not destroyed by correlations. Consequently, there can be a transition to the superconducting state, with the formation of Cooper pairs (the BCS scenario) or local pairs (the Shafroth scenario). In this connection it is unquestionably of interest to apply Fermi-liquid concepts to the study of the superconducting properties of high-T_c superconductors (HTSCs) with allowance for their peculiar features, such as overlapping of the energy bands at the Fermi surface and the presence of various kinds of van Hove–Lifshitz singularities, strong anisotropy, variable carrier density (including small values) etc., when treating both phononic and nonphononic mechanisms of superconductivity.[5–15]

Another interesting question is the influence of nonadiabaticity effects on the superconducting transition temperature T_c, since in HTSC materials, as in fullerenes and organic superconductors, the Fermi energy E_F and Debye energy ω_0 are quantities of the same order. As a result, the Migdal theorem,[16] which is used in the BCS–Bogolyubov theory, is violated, and it becomes necessary to take into account vertex and ''crossed'' diagrams in the mass operators for the Green functions corresponding to additional many-particle effects. The matter of estimating the contribution of the vertex functions and their influence on T_c and the isotope exponent α has been the subject of a number of papers.[17–21] Besides the Migdal parameter $m = \omega_0 / E_F$, one introduces a momentum cutoff of the electron–phonon interaction, Q_c, the smallness of which is determined by the presence of strong electronic correlations in the system. Such an approach is based on the results of studies of the influence of strong electronic correlations on the electron–phonon interaction.[22,23]

A three-dimensional (3D) system with symmetric filling of the energy bands was considered in Refs. 18 and 19. Such a model can describe various nonadiabatic systems at fixed values of the parameters m and Q_c. The imaginary parts of the vertex functions were neglected as being small, since they are proportional to the parameter Q_c, which is assumed small. No attempt was made to obtain an equation for Q_c. Consequently, taking nonadiabaticity effects into account in

such systems in the region of small Q_c can lead to an appreciable increase in the superconducting transition temperature, and one can easily obtain values of T_c corresponding to HTSC materials even at intermediate values of the coupling parameter $\lambda \sim 0.5-1$.

In the case of adiabatic systems of Éliashberg equations it follows that such values of T_c can be attained at very large coupling constants $\lambda \approx 3$.[24]

It has been shown[25] that at very low carrier concentrations ($\omega_0 \gg E_F$) the Migdal theorem is valid, and, hence, the effects of nonadiabaticity are unimportant in that case.

In HTSCs the density of charge carriers is a variable quantity because of the introduction of oxygen or impurities. It therefore becomes necessary to construct a theory of superconductivity for nonadiabatic systems with an asymmetric (arbitrary) filling of the energy bands. Furthermore, the strong anisotropy of the system should be taken into account.

In this paper we investigate the dependence of the superconducting transition temperature T_c and the isotope exponent α on the density n of charge carriers for two-dimensional (quasi-two-dimensional) and three-dimensional systems. We do not neglect the imaginary parts of the vertex functions P_v and P_c (unlike Refs. 17–21), and we show that taking them into account will lead to a restriction on the values of the carrier density for which superconductivity can occur in the system. Here Q_c, the momentum cutoff of the electron–phonon interaction, is not a parameter of the theory but satisfies a certain equation and depends on n. The character of the dependence is dictated by the dimensionality of the system. In the case of symmetric filling of the energy band in the 3D case,[18,19] superconductivity can occur in the system only for $Q_c = 0$. Consequently, treating the value of Q_c as a parameter of the theory free to take on different values is unjustified in a system with symmetric filling of the energy band.

This paper is arranged as follows. In Sec. 2 we present expressions for the mass operators $M(\mathbf{p}, \Omega)$ and $\Sigma(\mathbf{p}, \Omega)$ and the vertex functions $P_v(\mathbf{pp}_1, \Omega\Omega_1)$, $P_c(\mathbf{pp}_1, \Omega\Omega_1)$. In Sec. 3 we calculate the vertex functions for a two-dimensional (2D) system. Section 4 is devoted to a determination of the superconducting transition temperature, an equation for Q_c, and the isotope exponent α in a 2D system. In Sec. 5 we consider the vertex functions and the equations for Q_c in a 3D system. In Sec. 6 we analyze the results and draw conclusions.

2. THE GREEN FUNCTIONS AND MASS OPERATORS

As in Refs. 18 and 19, we start with a Hamiltonian of the Frölich type, including an electron–phonon interaction with an interaction constant specified by the relation

$$g_{\mathbf{pp}'}^2 = g^2 \gamma \theta(q_c - |\mathbf{p} - \mathbf{p}'|). \tag{1}$$

The value of γ is found from the condition

$$\langle\langle g_{\mathbf{pp}'}^2 \rangle\rangle_{FS} = g^2, \tag{2}$$

where $\langle\langle ... \rangle\rangle_{FS}$ denotes averaging over the Fermi surface. In the 2D case $\gamma = \pi/Q_c$, and in the 3D case $\gamma = 1/Q_c^2$, $Q_c = q_c/2p_F$.

This model set of interaction constants is based on the results of Refs. 22 and 23, according to which the presence

of strong electronic correlations in the system introduces a structure to the electron–phonon interaction constant $g(q)$, with a momentum cutoff $q_c \ll 2p_F$.

On the basis of perturbation theory[26] for the mass operators, near the superconducting transition temperature (for $T \sim T_c$) we have

$$M(p) = \frac{1}{\beta V} \sum_{\mathbf{p}_1 \Omega_1} V_N(pp_1) G(\mathbf{p}_1 \Omega_1), \tag{3}$$

$$\Sigma(p) = -\frac{1}{\beta V} \sum_{\mathbf{p}_1 \Omega_1} V_S(pp_1) G(\mathbf{p}_1 \Omega_1) G(-\mathbf{p}_1 - \Omega_1), \tag{4}$$

where

$$V_N(pp_1) = -D(\mathbf{p} - \mathbf{p}_1, \Omega - \Omega_1)$$
$$\times \left[1 - \frac{1}{\beta V} \sum_{\mathbf{p}_2 Q_2} D(\mathbf{p} - \mathbf{p}_2, \Omega - \Omega_2) G(\mathbf{p}_1 + \mathbf{p}_2 \right.$$
$$\left. - p, \Omega_1 + \Omega_2 - \Omega) G(\mathbf{p}_2, \Omega_2) \right], \tag{5}$$

$$V_S(pp_1) = -D(\mathbf{p} - \mathbf{p}_1, \Omega - \Omega_1)$$
$$\times \left\{ 1 - \frac{1}{\beta V} \sum_{\mathbf{p}_2 \Omega_2} [D(\mathbf{p} - \mathbf{p}_2, \Omega - \Omega_2) G \right.$$
$$\times (\mathbf{p}_1 + \mathbf{p}_2 - \mathbf{p}, \Omega_1 + \Omega_2 - \Omega) G(\mathbf{p}_2, \Omega_2)$$
$$+ D(\mathbf{p} - \mathbf{p}_2, \Omega - \Omega_2) G(\mathbf{p} - \mathbf{p}_1 - \mathbf{p}_2, \Omega - \Omega_1$$
$$\left. - \Omega_2) G(-\mathbf{p}_2, -\Omega_2)] \right\} + \frac{1}{\beta V} \sum_{\mathbf{p}_2 \Omega_2} D$$
$$\times (\mathbf{p}_2 - \mathbf{p}_1, \Omega_2 - \Omega_1) D(\mathbf{p} - \mathbf{p}_2, \Omega - \Omega_2) G$$
$$\times (\mathbf{p}_2 - \mathbf{p} - \mathbf{p}_1, \Omega_2 - \Omega - \Omega) G(\mathbf{p}_2, \Omega_2). \tag{6}$$

The first term of the effective interactions (5) and (6) corresponds to the adiabatic contributions, while the remaining terms come from taking into account the diagrams with crossing lines of the electron–phonon interaction.

The expression for the Matsubara electron Green function has the form

$$G(p, \Omega) = \frac{1}{i\Omega - M(\mathbf{p}, \Omega) - \varepsilon_p}. \tag{7}$$

For the phonon Green function we choose an Einstein spectrum with frequency ω_0:

$$D(\mathbf{p} - \mathbf{p}_1, \Omega - \Omega_1) = -g_{\mathbf{pp}_1}^2 \frac{\omega_0^2}{(\Omega - \Omega_1)^2 + \omega_0^2}. \tag{8}$$

We introduce the notation

$$P_v(\mathbf{pp}_1, \Omega\Omega_1) = \frac{1}{\beta V} \frac{\gamma}{N_0} \sum_{\mathbf{p}_2 \Omega_2} \theta(q_c - |\mathbf{p} - \mathbf{p}_2|) \frac{\omega_0^2}{(\Omega - \Omega_2)^2}$$
$$+ \omega_0^2 G(\mathbf{p}_2, \Omega_2) G(\mathbf{p}_1 + \mathbf{p}_2 - \mathbf{p},$$
$$\Omega_1 + \Omega_2 - \Omega), \tag{9}$$

$$P_c(\mathbf{pp}_1,\Omega\Omega_1)=\frac{1}{\beta V}\frac{\gamma}{N_0}\sum_{\mathbf{p}_2\Omega_2}\theta(q_c-|\mathbf{p}-\mathbf{p}_2|)$$

$$\times\frac{\omega_0^2}{(\Omega-\Omega_2)^2}+\omega_0^2 G(\mathbf{p}_2-\mathbf{p}-\mathbf{p}_1,$$

$$\Omega_2-\Omega-\Omega_1)G(p_2,\Omega_2).$$

In this notation expressions (5) and (6) can be rewritten as

$$V_N(pp_1)=-D(\mathbf{p}-\mathbf{p}_1,\Omega-\Omega_1)[1+\lambda P_v(\mathbf{pp}_1,\Omega\Omega_1)], \tag{10}$$

$$V_S(pp_1)=-D(\mathbf{p}-\mathbf{p}_1,\Omega-\Omega_1)[1+\lambda P_v(\mathbf{pp}_1,\Omega\Omega_1)$$
$$+\lambda P_v(\mathbf{pp}_1,-\Omega-\Omega_1)+\lambda P_c(\mathbf{pp}_1,\Omega\Omega_1)]. \tag{11}$$

Let us consider a 2D system and introduce a quadratic dispersion relation for the electron:

$$\varepsilon_p=\frac{p_x^2+p_y^2}{2m}-\mu. \tag{12}$$

3. VERTEX FUNCTIONS

We substitute the zeroth approximation for the Green function (7) into expression (9) and change from summation over $\mathbf{p}_2,\Omega_2$ to integration. In the case of a 2D system this change is made according to the formula

$$\frac{1}{\beta V}\sum_{\mathbf{p}_2\Omega_2}F(\mathbf{p}_2,\Omega_2)=N_0\int_0^{2\pi}\frac{d\varphi}{2\pi}\int_{-\mu}^{W-\mu}d\varepsilon_{\mathbf{p}_2}\frac{1}{2\pi}$$

$$\times\int_{-\infty}^{\infty}d\Omega_2 F(\mathbf{p}_2,\Omega_2), \tag{13}$$

where $N_0=m/2\pi$ is the electronic density of states, W is the width of the energy band, and μ is the chemical potential. We assume that $T_c\ll\omega_0$, so that we can consider the limit $T_c\to 0$ and do the integration over the frequency Ω_2 in the usual way.

Now assuming that the momentum transfer is small, $q=|\mathbf{p}-\mathbf{p}_1|\ll 2p_F$, we do the integration over the energy $\varepsilon_{\mathbf{p}_2}$ and over the angular variable, using the computational method of Ref. 19 as applied to the 2D case. The expressions thus obtained for the functions $P_{v,c}(\mathbf{pp}_1,\Omega\Omega_1)$ are then substituted into (5) and (6) and the resulting expressions are averaged over the Fermi surface:

$$\langle V_N(pp_1)\rangle_{FS}=\frac{\omega_0^2}{(\Omega-\Omega_1)^2+\omega_0^2}g^2[1+\lambda P_v(Q_c,\Omega\Omega_1)], \tag{14}$$

$$\langle V_S(pp_1)\rangle_{FS}=\frac{\omega_0^2}{(\Omega-\Omega_1)^2+\omega_0^2}g^2[1+\lambda P_v(Q_c,\Omega\Omega_1)]$$
$$+\lambda P_c(Q_c,-\Omega-\Omega_1)$$
$$+[\lambda P_c(Q_c,\Omega\Omega_1)]. \tag{15}$$

Here

$$P_{v,c}(Q_c,\Omega\Omega_1)=\frac{\pi}{Q_c}\langle\langle\theta(q_c-|\mathbf{p}-\mathbf{p}_1|)$$
$$\times P_{v,c}(\mathbf{pp}_1,\Omega\Omega_1)\rangle\rangle_{FS}. \tag{16}$$

For $\Omega=0$, $\Omega_1=\omega_0$ and $2EQ_c^2<\mu<W/2$ the expressions for the functions $P_{v,c}(Q_c,\Omega\Omega_1)$ can be brought to the form

$$P_v(Q_c,0,\omega_0)=\omega_0 B(0,\omega_0)+\left[\frac{A(0,\omega_0)}{\omega_0}-\omega_0 B(0,\omega_0)\right]$$

$$\times\left[1-\frac{E^2}{\omega_0^2}\frac{4}{9}Q_c^4\right]+\frac{E}{\omega_0}C(0,\omega_0)\frac{Q_c^2}{2}$$

$$+i\left\{\omega_0 B_1(0,\omega_0)+\left[\frac{A_1(0,\omega_0)}{\omega_0}-\omega_0 B_1(0,\omega_0)\right]\right.$$

$$\left.\times\left[1-\frac{E^2}{\omega_0^2}\frac{4}{9}Q_c^4\right]+\frac{E}{\omega_0}C_1(0,Q_1)\frac{Q_c^2}{2}\right\}, \tag{17}$$

$$P_c(Q_c,0,\omega_0)=\omega_0 B(0,-\omega_0)+\left[\frac{A(0,-\omega_0)}{\omega_0}\right.$$

$$\left.-\omega_0 B(0,-\omega_0)\right]\left[1-\frac{E^2}{\omega_0^2}\frac{11}{45}Q_c^4\right]$$

$$+\frac{E}{\omega_0}C(0,-\omega_0)\frac{Q_c^2}{6}+i\left\{\omega_0 B_1(0,-\omega_0)\right.$$

$$+\left[\frac{A_1(0,-\omega_0)}{\omega_0}-\omega_0 B_1(0,-\omega_0)\right]$$

$$\left.\times\left[1-\frac{E^2}{\omega_0^2}\frac{11}{45}Q_c^4\right]+\frac{E}{\omega_0}C_1(0,-\Omega_1)\frac{Q_c^2}{6}\right\}, \tag{18}$$

where

$$E=4E_F,\quad E_F=\frac{p_F^2}{2m},\quad \frac{A(0,\omega_0)}{\omega_0}=\frac{\pi}{4}-\frac{1}{2}\arctan\frac{1}{1+\mu}$$

$$-\frac{1}{2}\arctan\frac{1}{\overline{W}-\overline{\mu}+1},$$

$$\omega_0 B(0,\omega_0)=-\frac{1}{2}\left\{\frac{(1+\overline{\mu})[(1+\overline{\mu})^2+2]}{[(1+\overline{\mu})^2+1]^2}\right.$$

$$\left.+\frac{(\overline{W}-\overline{\mu}+1)[(\overline{W}-\overline{\mu}+1)^2+2]}{[(\overline{W}-\overline{\mu}+1)^2+1]^2}\right\}, \tag{19}$$

$$\frac{E}{\omega_0}C(0,\omega_0)=\frac{1}{m}\left\{\ln\frac{\overline{W}-\overline{\mu}+1}{1+\overline{\mu}}-\frac{1}{2}\ln\frac{(\overline{W}-\overline{\mu}+1)^2+1}{(\overline{\mu}+1)^2+1}\right.$$

$$\left.-\frac{1}{(1+\overline{\mu})^2+1}+\frac{1}{(\overline{W}-\overline{\mu}+1)^2+1}\right\},$$

$$\frac{A_1(0,\omega_0)}{\omega_0}=-\frac{1}{4}\left\{\ln\frac{(\overline{W}-\overline{\mu}+1)^2+1}{(\overline{\mu}+1)^2+1}-2\ln\frac{\overline{W}-\overline{\mu}+1}{1+\overline{\mu}}\right\}.$$

$$\omega_0 B_1(0,\omega_0) = \frac{1}{2}\left[\frac{1}{(1+\bar\mu)^2+1}-\frac{1}{(\bar W-\bar\mu+1)^2+1}\right]$$

$$-\frac{1}{4}\left[\frac{(1+\bar\mu)^2-1}{[(1+\bar\mu)^2+1]^2}\right.$$

$$\left.-\frac{(\bar W-\bar\mu+1)^2-1}{[(\bar W-\bar\mu+1)^2+1]^2}\right], \qquad (20)$$

$$\frac{E}{\omega_0}C_1(0,\omega_0) = \frac{2}{m}\left\{\arctan\frac{1}{1+\bar\mu}-\frac{\pi}{2}+\arctan\frac{1}{\bar W-\bar\mu+1}\right.$$

$$\left.-\frac{1+\bar\mu}{(1+\bar\mu)^2+1}-\frac{\bar W-\bar\mu+1}{(\bar W+\bar\mu+1)^2+1}\right\}.$$

Here

$$\bar\mu=\frac{\mu}{\omega_0};\quad \bar W=\frac{W}{\omega_0};\quad m=\frac{2\omega_0}{E}.$$

4. CRITICAL TEMPERATURE AND EQUATION FOR Q_c

Substituting (14) and (15) for $\Omega=0$ and $\Omega_1=\omega_0$ into Eqs. (3) and (4) averaged over the Fermi surface, we obtain

$$M(\Omega) = \frac{g^2}{\beta V}\sum_{\mathbf{p}_1\Omega_1}\frac{\omega_0^2}{(\Omega-\Omega_1)^2+\omega_0^2}$$

$$\times[1+\lambda P_v(Q_c,0,\omega_0)]G(\mathbf{p}_1\Omega_1),$$

$$\Sigma(\Omega) = \frac{g^2}{\beta V}\sum_{\mathbf{p}_1\Omega_1}\frac{\omega_0^2}{(\Omega-\Omega_1)^2+\omega_0^2} \qquad (21)$$

$$[1+2\lambda P_v(Q_c,0,\omega_0)\lambda P_c(Q_c,0,\omega_0)]$$

$$\times G(p_1\Omega_1)\Sigma(\Omega_1)G(-p_1-\Omega_1). \qquad (22)$$

Substituting expression (7) into (21) and doing the integration over energy with allowance for the electron–hole asymmetry (13), we obtain

$$\operatorname{Im}M(\Omega) = -\lambda_z\frac{1}{\beta}\sum_{\Omega_1}\frac{\omega_0^2}{(\Omega-\Omega_1)^2+\omega_0^2}\frac{\tilde\Omega_1}{|\tilde\Omega_1|}$$

$$\times\left[\arctan\frac{W-\mu}{|\tilde\Omega_1|}+\arctan\frac{\mu}{|\tilde\Omega_1|}\right]$$

$$-\lambda^2 P_v(Q_c,0,\omega_0)\frac{1}{\beta}\sum_{\Omega_1}\frac{\omega_0^2}{(\Omega-\Omega_1)^2+\omega_0^2}$$

$$\times\frac{1}{2}\ln\frac{(W-\mu)^2+\tilde\Omega_1^2}{\mu^2+\tilde\Omega_1^2}, \qquad (23)$$

where

$$\lambda_z=\lambda[1+\lambda\operatorname{Re}P_v(Q_c,0,\omega_0)]. \qquad (24)$$

The expression for $\tilde\Omega$ reduces to the form

$$\tilde\Omega=\Omega-\operatorname{Im}M(\Omega)=\Omega Z+Z_1, \qquad (25)$$

where

$$Z=Z(0)=1+\lambda_z\frac{1}{2}\left[\frac{\bar W-\bar\mu}{\bar W-\bar\mu+1}+\frac{\bar\mu}{\bar\mu+1}\right],$$

$$Z_1=\lambda^2\operatorname{Im}P_v(Q_c,0,\omega_0)\frac{\omega_0}{4}\ln\frac{(\bar W-\bar\mu)^2+1}{\bar\mu^2+1}. \qquad (26)$$

As a result,

$$G(\mathbf{p}\Omega)=\frac{1}{i[\Omega Z+Z_1]-\varepsilon_{\mathbf{p}}}. \qquad (27)$$

Substituting (27) into (22) and doing the integration over energy, we obtain

$$\Sigma(\Omega) = \frac{1}{\beta}\sum_{\Omega_1}(\lambda_\Delta+i\lambda^2\delta)\Sigma(\Omega_1)\frac{1}{\Omega_1 Z}$$

$$\times[\Phi_1(\Omega_1)+i\Phi_2(\Omega_1)]\frac{\omega_0^2}{(\Omega-\Omega_1)^2+\omega_0^2}, \qquad (28)$$

where

$$\Phi_1(\Omega_1) = \frac{Z\Omega_1+Z_1}{|Z\Omega_1+Z_1|}\frac{1}{2}\left[\arctan\frac{W-\mu}{|Z\Omega_1+Z_1|}\right.$$

$$\left.+\arctan\frac{\mu}{|Z\Omega_1+Z_1|}\right]+\frac{ZQ_1-Z_1}{|Z\Omega_1-Z_1|}$$

$$\times\frac{1}{2}\left[\arctan\frac{W-\mu}{|Z\Omega_1-Z_1|}+\arctan\frac{\mu}{|Z\Omega_1-Z_1|}\right], \qquad (29)$$

$$\Phi_2(\Omega_1) = \frac{1}{2}\ln\frac{(W-\mu)^2+(Z\Omega_1-Z_1)^2}{\mu^2+(ZQ_1-Z_1)^2}$$

$$-\frac{1}{2}\ln\frac{(W-\mu)^2+(Z\Omega_1+Z_1)^2}{\mu^2+(Z\Omega_1+Z_1)^2}, \qquad (30)$$

$$\lambda_\Delta=\lambda(1+2\lambda\operatorname{Re}P_v(Q_c,0,\omega_0)+\lambda\operatorname{Re}P_c(Q_c,0,\omega_0)),$$

$$\delta=\operatorname{Im}[2P_v(Q_c,0,\omega_0)+P_c(Q_c,0,\omega_0)]. \qquad (31)$$

It follows from Eq. (28) that $\Sigma(\Omega)$ is a complex quantity. We make the substitution $\Sigma=\Sigma_1+i\Sigma_2$ in Eq. (28) and write a system of equations for the real and imaginary parts:

$$\Sigma_1(\Omega) = \frac{\omega_0^2}{\Omega^2+\omega^2}V_1A_1^0-\frac{\omega_0^2}{\Omega^2+\omega_0^2}V_2A_2^0;$$

$$\Sigma_2(\Omega) = \frac{\omega_0^2}{\Omega^2+\omega_0^2}V_2A_1^0+\frac{\omega_0^2}{\Omega^2+\omega_0^2}V_1A_2^0. \qquad (32)$$

Here

$$A_1^0=\frac{1}{\beta}\sum_{\Omega_1}\frac{\omega_0^2}{\Omega_1^2+\omega_0^2}\frac{\Phi_1(\Omega_1)}{\Omega_1 Z}\Sigma_1(\Omega_1);$$

$$A_2^0=\frac{1}{\beta}\sum_{\Omega_1}\frac{\omega_0^2}{\Omega_1^2+\omega_0^2}\frac{\Phi_1(\Omega_1)}{\Omega_1 Z}\Sigma_2(\Omega_1). \qquad (33)$$

Substituting (32) into (33), we obtain

$$A_1^0=A_1^0V_1\xi_c-A_2^0V_2\xi_c;\quad A_2^0=A_1^0V_2\xi_c+A_2^0V_1\xi_c, \qquad (34)$$

where

$$\xi_c = \frac{1}{\beta} \sum_{\Omega_1} \frac{\omega_0^4}{(\Omega_1^2 + \omega_0^2)^2} \frac{\Phi_1(\Omega_1)}{\Omega_1 Z}. \tag{35}$$

The superconducting transition temperature T_c is determined from the condition that the system of equations (34) be solvable, which gives

$$(V_1^2 + V_2^2)\xi_c^2 - 2V_1\xi_c + 1 = 0, \tag{36}$$

and, hence,

$$\xi_c = \frac{V_1 \pm \sqrt{-V_2^2}}{V_1^2 + V_2^2}. \tag{37}$$

The solution for ξ_c is real if $V_2 = 0$. This condition leads to the expression

$$\xi_c \simeq 1/V \approx 1/\lambda_\Delta \tag{38}$$

and to the additional equation

$$V_2 = \lambda_\Delta \frac{\Phi_2(\omega_0)}{\Phi_1(\omega_0)} + \lambda^2 \delta = 0. \tag{39}$$

Keeping only terms of order λ^2, we reduce this last equation to the form

$$\mathrm{Im}[2P_c(Q_c, \omega_0) + P_c(Q_c, \omega_0)] = 0. \tag{40}$$

This equation determines the cutoff parameter Q_c for the electron–phonon interaction for a given μ or n. On the basis of Eqs. (40), (17), and (18) we get

$$aQ_c^4 - bQ_c^2 - d = 0, \tag{41}$$

where

$$a = \frac{29}{45}\left(\frac{2}{m}\right)^2 \left[\frac{A_1(0,\omega_0)}{\omega_0} - \omega_0 B_1(0,\omega_0)\right];$$

$$b \approx \frac{5}{3m} C_1(0,\omega_0,\mu); d = \frac{A_1(0,\omega_0)}{\omega_0}. \tag{42}$$

From the definitions of the coefficients (42) it follows that $a \ll b$, and, since we are seeking a solution $Q_c^2 \ll 1$, this solution can be written in the form

$$Q_c^2 = -d/b. \tag{43}$$

Since $b < 0$, Q_c is real-valued for $d > 0$, which is equivalent to the condition $\mu < W/2$. Consequently, superconductivity can arise in the 2D system. Taking this lower limit on μ into account, we find that this theory can be used in the interval $2EQ_c^2 < \mu < W/2$. In this interval of carrier densities, superconductivity can exist in a quasi-2D system on the basis of the electron–phonon interaction in the presence of strong electronic correlations. For $\mu = W/2$ we have $d = 0$ and $b \neq 0$. Consequently, it follows from (43) that $Q_c = 0$. It can be shown that for $Q_c \neq 0$ and symmetric filling of the energy band, superconductivity is absent in the system, since condition (40) is not satisfied.

After doing the integration over Ω_1 in (35), we obtain an expression for the superconducting transition temperature T_c:

$$T_c = \frac{1.13\omega_0[(\bar{W} - \bar{\mu})\bar{\mu}]^{1/2}}{\sqrt{e}[\bar{W} - \bar{\mu} + 1)(\bar{\mu} + 1)]^{1/2}}$$

$$\times \exp\left\{-\frac{Z}{\lambda_\Delta} + \frac{1}{4}\left[\frac{1}{\bar{W} - \bar{\mu} + 1} + \frac{1}{\bar{\mu} + 1}\right]\right\}. \tag{44}$$

We supplement this expression with the equation for the chemical potential

$$n = \frac{2}{\beta V} \sum_{\mathbf{k}\Omega} G(\mathbf{k}\Omega) e^{i\Omega 0^+}, \tag{45}$$

where n is the density of charge carriers.

After substituting expression (27) into (45) and doing the integration over Ω in the limit $T_c/\omega_0 \ll 1$ and the integration over energy in the usual way, we obtain

$$\bar{\mu} = Z\bar{n}, \tag{46}$$

where $\bar{\mu} = \mu/\omega_0$, $\bar{n} = n/(2N_0\omega_0)$, and Z is determined from formula (26).

A joint analysis of (44) and (46) yields the dependence of T_c on the carrier concentration $\bar{n}$. As $\bar{n}$ increases, the value of T_c increases to a maximum value near the symmetric filling of the energy band, $\mu = W/2$. For $\mu > W/2$ one has $T_c = 0$, since the system of equations (34), which determines the value of T_c, is incompatible. It follows that superconductivity is possible in the interval $0 < \bar{\mu} < \bar{W}/2$ in 2D systems. Thanks to the inclusion of nonadiabaticity effects, high T_c's, corresponding to HTSCs, are attained at intermediate values of the coupling parameter $\lambda \sim 0.5 - 1$. In contrast, the values of the temperature T_c obtained on the basis of Eqs. (44) and (46) for adiabatic systems ($P_v = P_c = 0$) correspond to the case of ordinary superconductors and cannot reach high values at intermediate values of the coupling constant λ. In that case, high values of T_c are reached for $\lambda \approx 3$.

For the isotope exponent we obtain, on the basis of (44),

$$\alpha = -\frac{d\ln T_c}{d\ln M} = \frac{1}{2}\left[1 + \frac{d\ln(T_c/\omega_0)}{d\ln \omega_0}\right], \tag{47}$$

where

$$\frac{d\ln(T_c/\omega_0)}{d\ln \omega_0} = -\frac{1}{4}\left[\frac{\bar{W} - \bar{\mu} + 2}{(\bar{W} - \bar{\mu} + 1)^2} + \frac{\bar{\mu} + 2}{(\bar{\mu} + 1)^2}\right]$$

$$-\frac{1}{\lambda_\Delta}\frac{dZ}{d\ln \omega_0} + \frac{Z}{\lambda_\Delta^2}\frac{d\lambda_\Delta}{d\ln \omega_0}, \tag{48}$$

$$\frac{dZ}{d\ln \omega_0} = -\frac{1}{2}\left\{\frac{\lambda^2}{2}\left[\frac{\bar{\mu}}{(\bar{\mu} + 1)^2 + 1} + \frac{\bar{W} - \bar{\mu}}{(\bar{W} - \bar{\mu} + 1)^2 + 1}\right]\right.$$

$$\times \left[\frac{\bar{W} - \bar{\mu}}{\bar{W} - \bar{\mu} + 1} + \frac{\bar{\mu}}{\bar{\mu} + 1}\right]$$

$$\left. + \lambda_z\left[\frac{\bar{W} - \bar{\mu}}{(\bar{W} - \bar{\mu} + 1)^2} + \frac{\bar{\mu}}{(\bar{\mu} + 1)^2}\right]\right\},$$

$$\frac{d\lambda_\Delta}{d\ln\omega_0} = -\frac{3\lambda^2}{2}\left[\frac{\bar{\mu}}{(\bar{\mu}+1)^2+1} + \frac{\bar{W}-\bar{\mu}}{(\bar{W}-\bar{\mu}+1)^2+1}\right].$$

$$(49)$$

In obtaining these formulas we dropped terms containing a dependence on Q_c, since their contribution is negligible for $Q_c \ll 1$. Analysis of these formulas suggests that the value of the isotope exponent α depends substantially on the parameters λ and W. At small n the isotope exponent $\alpha \sim 0.2$–0.3 and increases with increasing n. For example, for $\lambda = 0.5$ and $\bar{W} = 6$, one obtains $\alpha \approx 0.4$ for values near $\mu = W/2$.

5. THE CASE OF A THREE-DIMENSIONAL SYSTEM

We now do the same calculation as in Ref. 19 but for a variable carrier density (electron–hole asymmetry) and without neglecting the imaginary part of the functions P_v and P_c. In this case we make the change from summation to integration in the vertex functions (9) according to the formula

$$\frac{1}{\beta V}\sum_{\mathbf{p}_2\Omega_2}F(\mathbf{p}_2,\Omega_2) = N_0\int_0^{2\pi}\frac{d\varphi}{2\pi}\int_0^\pi\frac{\sin\alpha}{2}d\alpha$$

$$\times\int_{-\mu}^{W-\mu}d\varepsilon_{\mathbf{p}_2}\frac{1}{2\pi}\int_{-\infty}^\infty d\Omega_2 F(\mathbf{p}_2,\Omega_2),$$

$$(50)$$

where $N_0 = mp_F/2\pi^2$.

Doing the calculation in a manner analogous to the 2D case with the use of (50), we obtain for the quantities averaged over the Fermi surface

$$P_{v,c}(Q_c,\Omega\Omega_1) = \frac{1}{Q_c^2}\langle\langle\theta(q_c - |\mathbf{p}$$

$$- \mathbf{p}_1|)P_{v,c}(\mathbf{p}\mathbf{p}_1,\Omega\Omega_1)\rangle\rangle_{FS},$$

$$(51)$$

$$P_v(Q_c,0,\omega_0) = \omega_0 B(0,\omega_0) + \left[\frac{A(0,\omega_0)}{\omega_0} - \omega_0 B(0,\omega_0)\right]$$

$$\times\left[1 - \frac{E^2}{\omega_0^2}\frac{1}{2}Q_c^4\right] + i\left[\omega_0 B_1(0,\omega_0)\right.$$

$$+ \left[\frac{A_1(0,\omega_0)}{\omega_0} - \omega_0 B_1(0,\omega_0)\right]$$

$$\times\left[1 - \frac{E^2}{\omega_0^2}\frac{1}{2}Q_c^4\right]\Bigg\},$$

$$(52)$$

$$P_c(Q_c,0,\omega_0) = \omega_0 B(0,-\omega_0)$$

$$+ \left[\frac{A(0,-\omega_0)}{\omega_0} - \omega_0 B(0,-\omega_0)\right]$$

$$\times\left[1 - \frac{E^2}{\omega_0^2}\frac{11}{6}Q_c^4\right] + \frac{E}{\omega_0}C(0,-\omega_c)Q_c^2$$

$$+ i\Bigg\{\omega_0 B_1(0,-\omega_0) + \left[\frac{A_1(0,-\omega_0)}{\omega_0}\right.$$

$$- \omega_0 B_1(0,-\omega_0)\right]\left[1 - \frac{E^2}{\omega_0^2}\frac{11}{6}Q_c^4\right]$$

$$+ \frac{E}{\omega_0}C_1(0,-\omega_c)Q_c^2\Bigg\}.$$

$$(53)$$

Expressions (52) and (53) differ from the corresponding expressions for the 2D case, (17) and (18), by the values of the numerical coefficients in the terms containing Q_c^2 and Q_c^4.

In a 3D system the quantities λ_Δ (31), λ_z (24), and Z are determined by the vertex functions (52) and (53).

On the basis of Eq. (40) and relations (52) and (53), we obtain an equation for determining the momentum cutoff Q_c of the electron–phonon interaction in a 3D system:

$$a_1 Q_c^4 - b_1 Q_c^2 + d_1 = 0,$$

$$(54)$$

where

$$a_1 = \frac{5}{6}\left(\frac{2}{m}\right)^2\left[\frac{A_1(0,\omega_0)}{\omega_0} - \omega_0 B_1(0,\omega_0)\right];$$

$$b_1 = \frac{2}{m}C_1(0,\omega_0); \quad d = \frac{A_1(0,\omega_0)}{\omega_0} = d,$$

$$(55)$$

or

$$Q_c^2 = d_1/b_1.$$

$$(56)$$

Since $b_1 < 0$, the values of Q_c are real if $d_1 < 0$. This condition corresponds to $\mu > W/2$. Consequently, at high carrier densities superconductivity can exist in a 3D nonadiabatic system with strong electronic correlations ($Q_c \ll 1$) on the basis of the electron–phonon interaction mechanism. The value of T_c is maximum for $\mu \approx W/2$ and falls off with increasing $n(\mu)$, and for $\mu = W$ we have $T_c = 0$ (Eq. (44)).

Let us now turn to the limit of symmetric filling of the energy band in a 3D system, in order to compare our results with Ref. 19. Making the substitution $W - \mu \to E/2$ and $\mu \to E/2$, we find that a number of the coefficients vanish: $C(0,\omega_0) = 0$, $A_1(0,\omega)/\omega_0 = 0$, $\omega_0 B_1(0,\omega_0) = 0$. The coefficients $A(0,\omega_0)/\omega_0/\omega_0$ and $\omega_0 B(0,\omega_0)$ go over to the corresponding expressions of Ref. 19 for $Q_c \ll 1$, but the quantity $b_1 = 2C_1(0,\omega_0)/m \neq 0$ is absent in Ref. 19. In our case Eq. (54) becomes

$$b_1 Q_c^2 = 0.$$

$$(57)$$

Since $b_1 \neq 0$, we must have $Q_c = 0$. On the other hand, if we set $b_1 = 0$, as was done in Ref. 19 as a result of neglecting the imaginary part of the vertex function P_c, then Eq. (57) is satisfied for any Q_c, and, consequently, in that case it can be treated as a parameter of the theory. Apparently, in the model considered in Ref. 19, after the calculations are done for $Q_c \ll 1$ one should let $Q_c \to 0$. For $Q_c \neq 0$ superconductivity is absent in such a system, since the quantity ξ_c (37), which determines the superconducting transition temperature, is a complex quantity.

6. CONCLUSION

We have proceeded from the assumption that the onset of superconductivity in the system is due to the electron–phonon interaction. The presence of strong electronic correlations, however, promotes the realization of small values of

the momentum transfer (small values of the momentum cut-off of the electron–photon interaction).[22,23] This theory is also applicable in the case of an arbitrary electron–boson interaction leading to superconductivity, provided the characteristic boson frequency $\omega_0 \sim E_F$ and $q_c \ll 2p_F$.

We have studied the influence of nonadiabaticity effects (the contribution of the vertex and crossed diagrams for the electron–phonon interaction in the mass operators) on the superconducting transition temperature T_c and the isotope exponent α in systems with a variable carrier density. We have considered quasi-2D and 3D systems without including fluctuations, which we have assumed to be small.

Main conclusions

1. A decisive role in determining whether or not superconductivity is possible at a given carrier density in HTSCs is played by the dimensionality of the system.

2. In a quasi-2D system superconductivity arises at low carrier concentrations, the value of T_c increases with increasing carrier concentration up to values $\mu \lesssim W/2$, after which further increase in μ leads to vanishing of the superconductivity.

3. In a 3D system superconductivity can arise for $\mu > W/2$, i.e., at high carrier concentrations; the value of T_c is maximum at $\mu = W/2$ and goes to zero at $\mu = W$.

4. It can be assumed that at low carrier concentrations the electronic system in the HTSC is quasi-2D (highly anisotropic), and with increasing carrier concentration due to the introduction of oxygen or an impurity, the distribution of electrons in space becomes more isotropic, and a transition from two-dimensionality to three-dimensionality occurs. Then superconductivity exists in the entire range of values $0 < \mu < W$, and the superconducting transition temperature will be given by formula (44) with all of the quantities appearing in it determined on the basis of a 2D system for $\mu < W/2$ and on the basis of a 3D system for $\mu > W/2$. Here the dependence of T_c on the carrier concentration will have a bell-shaped form. Owing to the nonadiabaticity effect, the maximum value of T_c will reach values typical of HTSCs at an intermediate value of the parameter λ.

5. The cutoff parameter of the electron–phonon interaction, Q_c, in the case of 2D and 3D systems obeys Eqs. (41) and (54), respectively, which derive from the condition (39) that ξ_c, which determines the superconducting transition temperature T_c, be real. At the point $\mu = W/2$ one has $Q_c = 0$. Accordingly, Q_c falls off with increasing μ for a 2D system and increases with μ for a 3D system, and thus it is a function of the carrier concentration.

6. The isotope exponent increases with increasing carrier concentration for a 2D system and decreases for a 3D system.

7. In the case of symmetric filling of the energy bands, $W - \mu \to E/2$ and $\mu \to E/2$ (Ref. 19), superconductivity does not arise in the system for $Q_c \neq 0$. It follows that the theory of Ref. 19 is applicable only in the limit $Q_c \to 0$, and in our opinion to treat Q_c as a parameter of the theory, free to take on different values, is unjustified.

*E-mail: statphys@asm.md

[1] V. A. Moskalenko, P. Entel, and D. F. Digor, Phys. Rev. **59**, 619 (1999).
[2] M. I. Vladimir and V. A. Moskalenko, Teor. Mat. Fiz. **82**, 3301 (1990).
[3] S. I. Vakaru, M. I. Vladimir, and V. A. Moskalenko, Teor. Mat. Fiz. **85**, 1185 (1990).
[4] V. A. Moskalenko, Teor. Mat. Fiz. **111**, 744 (1997).
[5] M. E. Palistrant and V. M. Vakalyuk, Sverkhprovodimost' (KIAE) **3**, 567 (1990) [Superconductivity **3**, 5215 (1990)].
[6] V. A. Moskalenko, M. E. Palistrant, and V. M. Vakalyuk, Usp. Fiz. Nauk **161**, 155 (1991) [Sov. Phys. Usp. **34**, 717 (1991)].
[7] M. E. Palistrant and F. G. Kochorbe, Physica C **194**, 351 (1992).
[8] M. G. Kalalb, F. G. Kochorbé, and M. E. Palistrant, Teor. Mat. Fiz. **91**, 483 (1992).
[9] F. G. Kochorbé and M. E. Palistrant, Zh. Éksp. Teor. Fiz. **104**, 3084 (1993) [JETP **77**, 422 (1993)]; Teor. Mat. Fiz. **96**, 459 (1993); Zh. Éksp. Teor. Fiz. **114**(3), 195 (1998) [JETP **87**, 570 (1998)].
[10] É. V. Gorbar, V. P. Gusynin, and V. M. Loktev, Sverkhprovodimost' (KIAE) **6**, 483 (1993); Fiz. Nizk. Temp. **19**, 1171 (1993) [Low Temp. Phys. **19**, 832 (1993)].
[11] N. Kristoffel, P. Konsin, and T. Ord, Nuovo Cimento **17**, 1 (1994).
[12] M. E. Palistrant, J. Supercond. **10**, 19 (1997); Teor. Mat. Fiz. **109**, 137 (1996); **111**, 289 (1997).
[13] V. Z. Kresin and S. A. Wolf, Physica C **169**, 476 (1990); **198**, 328 (1992).
[14] M. V. Loktev and V. M. Turkowski, Zh. Éksp. Teor. Fiz. **114**, 605 (1998) [JETP **87**, 329 (1998)]; Condens. Matter Phys. **1**, 113 (1998).
[15] M. V. Loktev, V. M. Turkowski, and S. G. Sharapov, Teor. Mat. Fiz. **115**, 419 (1998).
[16] A. B. Migdal, Zh. Éksp. Teor. Fiz. **34**, 1438 (1958) [Sov. Phys. JETP **7**, 996 (1958)].
[17] C. Grimaldi, L. Pietronero, and S. Strässler, Phys. Rev. Lett. **75**, 1158 (1995).
[18] L. Pietronero, S. Strässler, and C. Grimaldi, Phys. Rev. B **52**, 10516 (1995).
[19] C. Grimaldi, L. Pietronero, and S. Strässler, Phys. Rev. B **52**, 10530 (1995).
[20] E. Cappellati and L. Pietronero, Phys. Rev. B **53**, 932 (1996).
[21] A. Perali, C. Grimaldi, and L. Pietronero, Phys. Rev. B **58**, 5736 (1998).
[22] M. L. Kulic and R. Zeyher, Phys. Rev. B **49**, 4395 (1994).
[23] R. Zeyher and M. L. Kulic, Phys. Rev. B **53**, 2850 (1996).
[24] J. P. Garbotte, Rev. Mod. Phys. **62**, 1027 (1990).
[25] M. A. Ikeda, A. Ogasawara, and M. Sugihara, Phys. Lett. A **170**, 319 (1992).
[26] A. A. Abrikosov, L. D. Gor'kov, I. E. Dzyaloshinskiĭ, *Methods of Quantum Field Theory in Statistical Physics* [Prentice-Hall, Englewood Cliffs, NJ (1963); Fizmatgiz, Moscow (1962)].

Translated by Steve Torstveit

Phase fluctuations and pseudogap properties: influence of nonmagnetic impurities

V. M. Loktev* and S. G. Sharapov

Bogolyubov Institute for Theoretical Physics of National Academy of Sciences of Ukraine
14-b Metrologicheskaya St., Kiev 03143, Ukraine

R. M. Quick and S. G. Sharapov

Department of Physics, University of Pretoria, Pretoria 0002, South Africa
(Submitted January 11, 2000)
Fiz. Nizk. Temp. **26**, 567–573 (June 2000)

The presence of nonmagnetic impurities in a 2D ''bad'' metal depresses the superconducting Berezinskii–Kosterlitz–Thouless transition temperature while leaving the pairing energy scale unchanged. Thus the region of the pseudogap nonsuperconducting phase, in which the modulus of the order parameter is nonzero but its phase is random and which arises at the pairing temperature, is substantially bigger than for the clean system. This supports the premise that fluctuations in the phase of the order parameter can in principle describe the pseudogap phenomena in high-T_c materials over a rather wide range of temperatures and carrier densities. The temperature dependence of the bare superfluid density is also discussed. © *2000 American Institute of Physics.* [S1063-777X(00)00606-X]

1. INTRODUCTION

The differences between the BCS scenario of superconductivity and superconductivity in high-T_c materials are well accepted as experimental facts, although there is no theoretical consensus about their origin. One of the most convincing manifestations is the pseudogap, or a depletion of the single-particle spectral weight around the Fermi level (see, for example, Ref. 1). Another transparent manifestation is the temperature and carrier-density dependences of the superfluid density in high-T_c superconductors (HTSC),[2–4] which do not fit the canonical BCS behavior. In particular, the value of the zero-temperature superfluid density is substantially less than the total density of doped carriers.[5] Currently there are many possible explanations for the unusual properties of HTSC. One of these is based on the nearly antiferromagnetic Fermi liquid model.[6] Another explanation, proposed by Anderson, relies on the separation of spin and charge degrees of freedom. One more approach, which we will follow in this paper, relates the observed anomalies to precursor superconducting fluctuations. Some authors argue that alternative types of superconducting fluctuations are responsible for the pseudogap (e.g. Ref. 7), while Emergy and Kivelson[8] suggest a scenario based on fluctuations of the phase of the order parameter. The latter scenario we believe to be more relevant due to the low superfluid density and practically 2D character of the conductivity in HTSC mentioned above. A microscopic 2D model which elaborates the above-mentioned scenario[8] has been studied in Refs. 9 and 10. The results obtained show that the condensate phase fluctuations indeed lead to features which are experimentally observed in HTSC both in the normal and superconducting states.[1)] It is obvious, however, that the present treatment of the phase fluctuations is incomplete due to both the oversimplified character of the model and the absence of an explanation for the more recent advanced experiments[2–4] on the temperature and doping dependences of the superfluid density. It is well known, however, that the theoretical study of HTSC faces a lot of computational difficulties due to, for example, an unconventional order parameter symmetry, complex frequency–momentum dependence of the effective quasiparticle attraction general form of the quasiparticle dispersion relation, etc. Therefore, in order to obtain analytical results, we have to date only considered nonretarded s-wave pairing in the absence of impurities. (Attempts to consider retardation effects were made in Ref. 11).

Nevertheless, a discussion of the effect of impurities seems to be crucial for a realistic model of the HTSC. Indeed, it is known that the itinerant holes in HTSC are created by doping, which in turn introduces a considerable disorder into the system, for instance, from the random Coulomb fields of chaotically distributed charged impurities (doped ions).[12] Thus one of the purposes of the present paper is to study the model of Refs. 9 and 10 but in the presence of nonmagnetic impurities.

In the theory of ''common'' metals the Fermi energy ϵ_F and the mean transport quasiparticle time τ_{tr} are independent quantities which are always assumed to satisfy the criterion $\epsilon_F \tau_{tr} \gg 1$. In HTSC, which are ''bad'' metals,[8] both ϵ_F and τ_{tr} are dependent on the doping and the above-mentioned criterion may fail.[12] As an illustration, we refer to the remarkable linear dependence of the normal-state resistivity,[1] which implies that $\epsilon_F \tau_{tr}$ may indeed be ~ 1. It has been shown[12] for strongly disordered metallic systems that superconductivity

is absent if the scattering-to-pairing ratio exceeds a critical value and that superconductivity exists in a finite range of doping if this ratio is not exceeded. We shall not study this case but rather consider here the more usual (and in some sense simpler) situation originally studied in the papers of Anderson[13] and Abrikosov–Gor'kov (AG)[14] (see also Ref. 15), when the superconducting order is preexisting and the criterion $\epsilon_F \tau_{tr} \gg 1$ is satisfied.

The Anderson theorem[13] states that in 3D the BCS critical temperature is unchanged in the presence of nonmagnetic impurities. However, as discussed in,[9] the BCS critical temperature in 2D is the temperature T^* at which the pseudogap opens, while the superconducting transition temperature transition is the temperature T_{BKT} of the Berezinskii–Kosterlitz–Thouless (BKT) transition. In contrast to the former, the latter is defined by a bare superfluid density (given by the delocalized carriers) which is dependent on (see below) the concentration of impurities. Thus in the 2D case the superconducting transition temperature T_{BKT} decreases with increasing impurity concentration.

Thus in the model under consideration, the relative size of the pseudogap phase, $(T^* - T_{BKT})/T^*$, is larger in the presence of impurities than in the clean limit.[9] Therefore it can be observed over a wider range of densities. The second result obtained is that the value of the zero-temperature superfluid density is less than the total density of carriers (dopants), so that the presence of impurities may contribute to this diminishing and, in turn, explain the experimental results.[5] Finally, we attempt to interpret qualitatively the recent experiments on the temperature dependence of the superfluid density[2,3] within our scenario.

A brief overview of the paper follows: In Sec. 2 we present the model and derive the main equations. In Sec. 3 we compare the results obtained for the clean and dirty limits. In particular, we compare the values of T_{BKT}, the relative sizes of the pseudogap region, and the values of the bare superfluid density at $T=0$ and for T close to T_ρ. In Sec. 4 an attempt is made to give an explanation for the experimental results.[2,3]

2. MODEL AND MAIN EQUATIONS

Our starting point is a continuum version of the two-dimensional attractive Hubbard model defined by the Hamiltonian:[9,10]

$$H = \int d^2r \left[\psi_\sigma^+(x)\left(-\frac{\nabla^2}{2m} - \mu \right)\psi_\sigma(x) \right.$$
$$- V\psi_\uparrow^+(x)\psi_\downarrow^+(x)\psi_\downarrow(x)\psi_\uparrow(x)$$
$$\left. + U_{imp}(\mathbf{r})\psi_\sigma^+(x)\psi_\sigma(x) \right], \tag{1}$$

where $x=\mathbf{r}$; τ denotes the space and imaginary time variables; $\psi_\sigma(x)$ is a fermion field with spin $\sigma=\uparrow,\downarrow$; m is the effective fermion mass; μ is the chemical potential; V is an effective local attraction constant, and $U_{imp}(\mathbf{r})$ is the static potential of randomly distributed impurities; we take $\hbar=k_B=1$. The model with the Hamiltonian (1) is equivalent to a model with an auxiliary BCS-like pairing field which is given in terms of the Nambu variables as

$$H = \int d^2\tau \left\{ \Psi^+(x)\left[\tau_3\left(-\frac{\nabla^2}{2m} - \mu \right) - \tau_+ \Phi(x) \right.\right.$$
$$\left.\left. - \tau_- \Phi^*(x) + \tau_3 U_{imp}(\mathbf{r}) \right]\Psi(x) + \frac{|\Phi(x)|^2}{V} \right\}, \tag{2}$$

where $\tau_\pm=(\tau_1 \pm i\tau_2)/2$ and τ_3 are the Pauli matrices, and $\Phi(x)=V\Psi^+(x)\tau_-\Psi(x)=V\psi_\downarrow(x)\psi_\uparrow(x)$ is the complex ordering field. Then the partition function can be presented as a functional integral over Fermi fields (Nambu spinors) and the auxiliary fields Φ, Φ^*.

However, in contrast to the usual method, the modulus–phase parametrization $\Phi(x)=\rho(x)\exp[i\theta(x)]$ is necessary for the 2D model at finite temperatures (see Refs. 9, 10, 16 and references therein). To be consistent with this replacement one should also introduce the spin–charge variables for the Nambu spinors

$$\Psi(x) = \exp[i\tau_3\theta(x)/2]Y(x), \tag{3}$$

where $Y(x)$ is the field operator for neutral fermions.

From the Hamiltonian (1), following Ref. 9, one can derive an effective Hamiltonian which is the Hamiltonian of the classical XY model:

$$H_{XY} = \frac{1}{2}J(\mu,T,\rho)\int d^2r[\nabla\theta(x)]^2, \tag{4}$$

where

$$J(\mu,T,\rho) = \frac{T}{16m\pi^2}\sum_{n=-\infty}^{\infty}\int d^2k \; tr[\tau_3\langle\mathcal{G}(i\omega_n,\mathbf{k})\rangle]$$
$$+ \frac{T}{32m^2\pi^2}\sum_{n=-\infty}^{\infty}\int d^2k\mathbf{k}^2 \; tr[\langle\mathcal{G}(i\omega_n,\mathbf{k})\rangle$$
$$\times\langle\mathcal{G}(i\omega_n,\mathbf{k})\rangle] \tag{5}$$

is the bare (i.e., unrenormalized by the phase fluctuations, but including pair-breaking thermal fluctuations) superfluid stiffness. Here

$$\langle\mathcal{G}(i\omega_n,\mathbf{k})\rangle = -\frac{(i\omega_n\hat{I} - \tau_1\rho)\eta_n + \tau_3\xi(\mathbf{k})}{(\omega_n^2+\rho^2)\eta_n^2 + \xi^2(\mathbf{k})} \tag{6}$$

with

$$\eta_n = 1 + \frac{1}{2\tau_{tr}(\omega_n^2+\rho^2)^{1/2}},$$
$$\xi(\mathbf{k}) = \frac{\mathbf{k}^2}{2m} - \mu, \quad \omega_n = \pi(2n+1)T \tag{7}$$

is the AG[15] Green's function of neutral fermions averaged over a random distribution of impurities and written in the Nambu representation.[17,18] In writing (5) we assumed that $\langle\mathcal{G}(i\omega_n,\mathbf{k})\mathcal{G}(i\omega_n,\mathbf{k})\rangle \simeq \langle\mathcal{G}(i\omega_n,\mathbf{k})\rangle\langle\mathcal{G}(i\omega_n,\mathbf{k})\rangle$. This approximation, as was shown by AG,[15] does not change the final result for J. Note also that the Green's function (6) is valid only when $\epsilon_F\tau_{tr} \gg 1$, which demands the presence of a well-developed Fermi surface, which in turn implies that $\mu \simeq \epsilon_F$. Thus one cannot use expression (6) in the so called Bose limit with $\mu<0$.[9] On the other hand, a Fermi surface can be formed even in bad metals when the Ioffe–Regel–Mott criterion proves to be fulfilled.[12]

Substituting (6) into (5), and using the inequalities $\mu \gg T, \rho$ to extend the limits of integration to infinity, one arrives at

$$J = \frac{\mu}{4\pi} + \frac{T\mu}{4\pi} \sum_{n=-\infty}^{\infty} \int_{-\infty}^{\infty} dx \left(\frac{1}{x^2 + (\omega_n^2 + \rho^2)\eta_n^2} \right.$$
$$\left. - \frac{2\omega_n^2\eta_n^2}{[x^2 + (\omega_n^2 + \rho^2)\eta_n^2]^2} \right). \tag{8}$$

Equation (8) is formally divergent and demands special care due to the fact that one has to perform the integration over x before the summation.[15] Finally, one can formally cancel the divergence[15] to obtain

$$J = \frac{\mu\rho^2 T}{4} \sum_{n=-\infty}^{\infty} \frac{1}{(\omega_n^2 + \rho^2)(\sqrt{\omega_n^2 + \rho^2} + 1.2\tau_{tr})}. \tag{9}$$

The temperature of the BKT transition for the XY-model Hamiltonian (4) is determined by the equation

$$T_{BKT} = \frac{\pi}{2} J(\mu, T_{BKT}, \rho(\mu, T_{BKT})). \tag{10}$$

The self-consistent calculation of T_{BKT} as a function of the carrier density $n_f = m\epsilon_F/\pi$ requires additional equations for ρ and μ, which together with (10) form a complete set.[9]

When the modulus of the order parameter $\rho(x)$ is treated in the mean field approximation, the equation for ρ takes the form[9]

$$\frac{2\rho}{V} = \sum_{n=-\infty}^{\infty} \int \frac{d^2k}{(2\pi)^2} \text{tr}[\tau_1 \langle \mathcal{G}(i\omega_n, k) \rangle], \tag{11}$$

which formally coincides with the gap equation of the BCS theory. This coincidence allows one to use the Anderson theorem,[13] which states that the dependence of $\rho(T)$ is the same as that for the clean superconductor and is not affected by the presence of nonmagnetic impurities. It is important to recall that this theorem is, of course, valid only for *s*-wave pairing and low disorder.

There are, however, both physical and mathematical differences[9,10] between the gap in the BCS theory and ρ. In particular, the temperature T_ρ which is estimated from the condition $\rho = 0$ is not related to the temperature of the superconducting transition, but is interpreted as the pseudogap opening temperature T^* (see details in Ref. 9). The main point, which we would like only to stress here, is that by virtue of the Anderson theorem[13] the value of T_ρ does not depend on the presence of impurities, while the temperature T_{BKT}, as we will show, is lowered.

The chemical potential μ is defined by the number equation

$$\sum_{n=-\infty}^{\infty} \int \frac{d^2k}{(2\pi)^2} \text{tr}[\tau_3 \langle \mathcal{G}(i\omega_n, k) \rangle] = n_f. \tag{12}$$

Since we are interested in the high carrier density region, the solution of (12) is $\mu \simeq \epsilon_F$, so that in Eqs. (9)–(11) one can replace μ by ϵ_F.

Having the temperatures T_ρ and T_{BKT} as functions of carrier density, one can build the phase diagram of the model,[9] which consists of three regions. The first one is the

superconducting (here BKT) phase with $\rho \neq 0$ at $T < T_{BKT}$. In this region there is algebraic order, or a power-law decay of the $\langle \Phi^*\Phi \rangle$ correlations. The second region corresponds to the pseudogap phase ($T_{BKT} < T < T_\rho$). In this phase ρ is still nonzero but the correlations mentioned above decay exponentially. The third is the normal (Fermi-liquid) phase at $T > T_\rho$ where $\rho = 0$. Note that $\langle \Phi(x) \rangle = 0$ everywhere. While the given phase diagram was derived for the idealized 2D model, there are indications[19,20] that even for such complicated layered systems as HTSC the value of the critical temperature for them may be well estimated using T_{BKT}, even though the transition undoubtedly belongs to the 3D XY class. It was also pointed out in Ref. 19 that a nonzero gap in the one-particle excitation spectrum can persist even without long-range order.

3. COMPARISON OF THE CLEAN AND DIRTY LIMITS

3.1. Clean limit

The transport time τ_{tr} is infinite in the clean limit, so that

$$J(\epsilon_F, T, \rho(\epsilon_F, T)) = \frac{\epsilon_F \rho^2 T}{4} \sum_{n=-\infty}^{\infty} \frac{1}{(\omega_n^2 + \rho^2)^{3/2}}. \tag{13}$$

Near T_ρ one can obtain from (13)

$$J(\epsilon_F, T \to T_\rho^-, \rho \to 0) = \frac{7\zeta(3)}{16\pi^3} \frac{\rho^2}{T_\rho^2} \epsilon_F, \tag{14}$$

where $\zeta(x)$ is the zeta function. This expression must coincide with the result from Ref. 9, which was derived using the opposite order for the summation and integration. Inserting the well-known dependence of $\rho(T)$ (see, for example, Ref. 21)

$$\rho^2(T \to T_\rho^-) = \frac{8\pi^2}{7\zeta(3)} T_\rho^2 \left(1 - \frac{T}{T_\rho} \right) \tag{15}$$

and then substituting (14) into (10), one obtains the following asymptotic expression for the BKT temperature in the clean limit for high carrier densities:[9,22,23]

$$T_{BKT} = T_\rho \left(1 - \frac{4T_\rho}{\epsilon_F} \right), \quad T_{BKT} \lesssim T_\rho. \tag{16}$$

In the high-density limit one can also use the equation

$$T_\rho = \frac{\gamma}{\pi} \sqrt{2|\epsilon_b|\epsilon_F}, \tag{17}$$

where $\gamma = 1.781$ and ϵ_b is the energy of the two-particle bound state in vacuum, which is a more convenient parameter than the four-fermion constant V.[9,24]

It is obvious from (16) and (17) that the pseudogap region shrinks rapidly for high carrier densities,[2)] and one may ask (see, for example, Ref. 25) whether this scenario can explain the pseudogap anomalies which are observed over a wide range of temperatures and carrier densities, since in the clean limit the relative size of the pseudogap region ($T_\rho - T_{BKT})/T_\rho$ is, for instance, less than 1/2 when the dimensionless ratio $\epsilon_F/|\epsilon_b| \lesssim 128\gamma^2/\pi^2 \approx 41$. A crude estimate[26] for the dimensionless ratio for optimally doped cuprates gives $\epsilon_F/|\epsilon_b| \sim 3.10^2 - 10^3$, which indicates that in the clean superconductor the pseudogap region produced by the phase

fluctuations is too small. Of course, all these estimates are qualitative due to the simplicity of the model.

The value of the bare superfluid density $n_s(T)$ is straightforwardly expressed in terms of the bare phase stiffness, $n_s(T)=4mJ(T)$. In particular, it follows from (13) that $n_s(T=0)=n_f$. This is not surprising, since $n_s(T=0)$ must be equal to the total density n_f for any superfluid ground state in a translationally invariant system,[27] and the clean system is translationally invariant. We note, however, as stated above, that $n_s(T=0) \ll n_f$ in HTSC.[5] Substituting (15) into (13), one obtains, for T close to T_ρ, the bare superfluid density as $n_s(\tilde{T} \to T_\rho^-)=2n_f(1-T/T_\rho)$. This behavior of the bare superfluid density is formally the same as the behavior of the total superfluid density in the BCS theory. Nevertheless it is important to remember that the total superfluid density in the present model undergoes the Nelson–Kosterlitz jump at T_{BKT} and is zero for $T>T_{BKT}$. We note that one can probe experimentally both the bare superfluid density in high-frequency measurements[2] and the total superfluid density in low-frequency measurements.[3]

3.2. Dirty limit

In the dirty limit the quasiparticle transport time τ_{tr} is small ($\tau_{tr} \ll \rho^{-1}(T=0)$), so that one can neglect the radical inside the brackets in Eq. (9).[15] The remaining series is easily summed, and one obtains for the bare superfluid stiffness

$$J(\epsilon_F,T,\rho(\epsilon_F,T),\tau_{tr})=\frac{\epsilon_F \tau_{tr}\rho}{4}\tanh\frac{\rho}{2T}. \tag{18}$$

As explained above, by virtue of the Anderson theorem, the expressions (15) for ρ and (17) for T_ρ remain unchanged in the presence of impurities. Again substituting (15) into (18), one obtains

$$T_{BKT}=T_\rho\left(1-\frac{14\zeta(3)}{\pi^3}\frac{1}{\epsilon_F \tau_{tr}}\right), \quad T_{BKT}\lesssim T_\rho. \tag{19}$$

One can see that the size of the pseudogap region is now controlled by the new phenomenological parameter τ_{tr}, which is an unknown function of ϵ_F for HTSC. The experimental data[1] suggest that τ_{tr} is almost independent of the doping level in the under-doped region.

It is difficult to obtain more than a qualitative estimate using Eq. (19), since in its derivation we have assumed that $\epsilon_F \tau_{tr} \gg 1$. In HTSC however, as discussed above (see also Ref. 12), this assumption is not always justified. Bearing in mind that the dirty limit implies that the condition $\tau_{tr}^{-1} \gg \rho(T=0) \sim T_\rho$ is satisfied, one can easily see that the value of T_{BKT} for this case is less than that given by (16) for the clean superconductor. Since impurities are inevitably present in HTSC, phase fluctuations can in fact give rise to a pseudogap region that is of comparable size to that observed experimentally. We note that our arguments are in fact quite similar to that given in Ref. 22 as to the best conditions for observing BKT physics in superconducting films. However, in contrast to this paper, the gap opening below T_ρ is particularly emphasized here.

While Eq. (19) was derived under the assumption $T_{BKT} \lesssim T_\rho$, in the general case when T_{BKT} can be substantially less than T_ρ one must solve the self-consistent Equation (10)

with $J(\epsilon_F,T_{BKT},\rho(\epsilon_F,T_{BKT}))$ given by (18). Recall, however, that to make any quantitative estimates, the more realistic *d*-wave model has to be considered, and the inequality $\epsilon_F \tau_{tr} \gg 1$ should not be assumed.[12]

The value of the zero-temperature superfluid density is now given by $n_s(T=0)=\pi n_f \tau_{tr}\rho \ll n_f$, since $\tau_{tr}\rho \ll 1$. This does not contradict the results of Ref. 27 because the system is not translationally invariant in the presence of impurities.[28] Furthermore, as one can see, the low value of the superfluid density in HTSC[5] may be related to the impurities which are inevitably present in HTSC. Another factor that leads to lowering of the superfluid density is the presence of the lattice, which also destroys a continuous translational invariance. We note that, as was pointed out in Ref. 29, quantum fluctuations also lead to a decrease in the superfluid density.

4. THE TEMPERATURE DEPENDENCE OF THE BARE SUPERFLUID DENSITY

In this Section we try to correlate the temperature dependence of the observed in-plane resistivity $\rho_{ab}(T)$ with the recently measured temperature dependence of the bare superfluid density.[2]

For $T>T_{BKT}$ the expression for the bare superfluid density in the dirty limit (18) can be rewritten in terms of the in-plane conductivity, $\sigma=e^2 n_f \tau_{tr}/m$, where e is the charge of an electron:

$$J(\sigma(\epsilon_F,T),\rho(\epsilon_F,T))=\frac{\pi}{4}\frac{\sigma\rho}{e^2}\tanh\frac{\rho}{2T}. \tag{20}$$

The in-plane resistivity $\rho_{ab} \sim \sigma^{-1}$ in cuprates has been extensively studied,[1] and its temperature and concentration dependences must reflect the pseudogap properties observed in other experiments. One can say that $\rho_{ab}(T)$ is linear above $T^* \simeq T_\rho$ and roughly linear between T_{BKT} and T_ρ, but with a lower slope. Thus in the interval $T_{BKT}<T<T_\rho$ the resistivity can be approximately written as $\rho_{ab}(T)=aT+b$, where a and b are functions of ϵ_F but not of temperature.

Now, substituting $\sigma \sim \rho_{ab}^{-1}(T)$ into Eq. (20), one obtains

$$n_s(T) \sim \frac{\rho}{aT+b}\tanh\frac{\rho}{2T}. \tag{21}$$

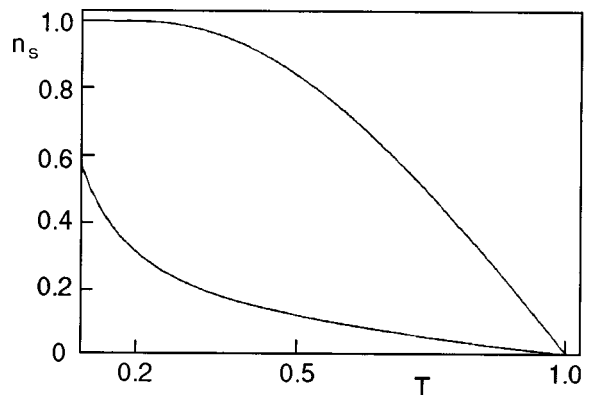Our estimates based on Eq. (21) are shown in Fig. 1. One can

FIG. 1. The behavior of $n_s(T)$ in the clean (upper curve) and dirty (lower curve) limits. The value of $n_s(T)$ is normalized to $n_s(T=0)$ for the clean system; T is given in units of T_ρ.

see that, in contrast to the almost linear BCS dependence of $n_s(T)$, we have convex behavior, and the superfluid density becomes zero at T_ρ. We stress that the curvature of $n_s(T)$ is the result of the temperature dependence of both $\rho(T)$ and $\sigma(T)$ for $T_{BKT} < T < T_\rho$. More importantly, the slope of the curve $n_s(T)$ at T_ρ for the dirty metal is substantially less than for the clean one. The experiment [2] shows the same curvature for $n_s(T)$ but indicates that the bare superfluid density disappears at a lower temperature, $T_s < T^*$. Since the slope $dn_s(T)/dT$ at T_ρ is very small, as is predicted by Eq. (21) and observed experimentally, the nonzero value of $n_s(T)$ between T_s and T_ρ may, however, simply be too small to be experimentally observed. A definitive answer to this question demands further experiments and theoretical studies. In particular, fluctuations of ρ should be taken into account. [9,10]

One can also comment on the experimentally observed change in the curvature of the total superfluid density, $N_s(T)$, with changing carrier density,[3] even though $N_s(T)$ cannot be directly related to the bare superfluid density $n_s(T)$ discussed here. Although the total superfluid density $n_s(T)$ disappears above T_{BKT}, the curvature present in the bare superfluid density $n_s(T)$ seems to be retained as a curvature in the total superfluid density, $N_s(T)$, below T_{BKT} (Refs. 2 and 3). For low carrier densities (the underdoped region) the pseudogap region, $T_{BKT} < T < T_\rho$, is larger, and therefore the curvature in $n_s(T)$ is more pronounced. This behavior seems to be reflected in the total superfluid density $N_s(T)$ below T_{BKT} (Ref. 3). It is important, however, to study experimentally and theoretically the concentration dependence of the bare superfluid density $n_s(T)$ in order to make a full comparison with the results of Ref. 3 for $N_s(T)$.

The experimental data of Ref. 3 also show that $N_s(T)$ does not display the Nelson–Kosterlitz jump. This is probably related to the influence of the interlayer coupling (see the references cited in Ref. 10).

5. CONCLUSION

Since in HTSC the pairing scale T^* is different from the superconducting transition temperature, the role of nonmagnetic impurities is not traditional, and they in fact govern the superconducting properties of a ''bad'' metal. In particular, the presence of nonmagnetic impurities strongly increases the size of the pseudogap phase originating from the fluctuations of the phase of the order parameter. In addition, the behavior of the superfluid density in the presence of impurities is closer to that experimentally observed.

Our results are only qualitative, since we have considered a model with nonretarded *s*-wave attraction and an isotropic fermion spectrum. However, it is likely that the properties obtained will persist for *d*-wave pairing. There is, of course, the problem of why strong disorder does not destroy the *d*-wave superconductivity, when nonmagnetic impurities are pair-breaking. As was suggested by Sadovskii,[30] even the *d*-wave pairing may persist if the coupling is strong enough. Further studies are necessary; for example, it is important to explain the concentration dependence of the superfluid slope, $dn_s(T)/dT$ at $T = 0$.[3,4] Our results also indicate that it would be interesting to study the BCS–Bose crossover problem in the presence of impurities, especially in the *d*-wave case.[30]

*E-mail: vloktev@bitp.kiev.ua
[1] Of course, the contribution from the phase fluctuations need not be the only or even the major contribution.
[2] In 2D for *s*-wave pairing the high-density limit is in fact equivalent to the weak-coupling BCS limit.

[1] T. Timusk and B. Statt, Rep. Prog. Phys. **62**, 61 (1999).
[2] J. Corson, R. Mallozi, J. Orenstein, J. N. Eckstein, and I. Bozovic, Nature (London) **398**, 221 (1999).
[3] C. Panagopoulos, B. D. Rainford, J. R. Cooper, W. Lo, J. L. Tallon, J. W. Loram, J. Betouras, Y. S. Wang, and C. W. Chu, *Preprint cond-mat/9903117*, submitted to Phys. Rev. Lett.
[4] J. Mesot, M. R. Norman, H. Ding, M. Randeria, J. C. Campuzano, A. Paramekanti, H. M. Fretwell, A. Kaminski, T. Takeuchi, T. Yokoya, T. Sato, T. Takahashi, T. Mochiku, and K. Kadowaki, Phys. Rev. Lett. **83**, 840 (1999).
[5] V. Emery and S. A. Kivelson, *Preprint cond-mat/9809083*, to be published in the proceedings of ''Stripes 98.''
[6] J. Schmalian, D. Pines, and B. Stojkovic, Phys. Rev. B **60**, 667 (1999).
[7] B. Janko, J. Maly, and K. Levin, Phys. Rev. B **56**, R11407 (1997); Physica C **321**, 113 (1999); I. Kosztin, Q. Chen, B. Janko, and K. Levin, Phys. Rev. B **58**, R5936 (1998); Phys. Rev. Lett. **81**, 4708 (1998).
[8] V. Emery and S. A. Kivelson, Nature (London) **374**, 434 (1995); Phys. Rev. Lett. **74**, 3253 (1995).
[9] V. P. Gusynin, V. M. Loktev, and S. G. Sharapov, JETP Lett. **65**, 182 (1997); Low Temp. Phys. **23**, 612 (1997); *ibid.* **23**, 936 (1997); JETP **88**, 685 (1999).
[10] V. P. Gusynin, V. M. Loktev, and S. G. Sharapov, JETP Lett. **69**, 141 (1999); *Preprint cond-mat/9811207*, to appear in JETP **90**, No. 7 (2000).
[11] V. M. Loktev, S. G. Sharapov, and V. M. Turkowski, Physica C **296**, 84 (1998); V. M. Loktev and V. M. Turkowski, JETP **87**, 329 (1998).
[12] V. M. Loktev and Yu. G. Pogorelov, Physica C **272**, 151 (1996).
[13] P. W. Anderson, J. Phys. Chem. Solids **11**, 26 (1959).
[14] A. A. Abrikosov and L. P. Gor'kov, Sov. Phys. JETP **8**, 1090 (1959); *ibid.* **9**, 220 (1959).
[15] A. A. Abrikosov, L. P. Gorkov, and I. E. Dzyaloshinski, *Methods of Quantum Field Theory in Statistical Physics*, Dover, New York (1975).
[16] B. K. Chakraverty and T. V. Ramakrishnan, Physica C **282**, 290 (1997).
[17] W. A. B. Evans and G. Rickayzen, Ann. Phys. (N.Y.) **33**, 275 (1965).
[18] G. Rickayzen, *Green's Functions and Condensed Matter*, Academic Press, London (1980).
[19] A. A. Abrikosov, Phys. Rev. B **55**, R6149 (1997).
[20] R. M. Quick and S. G. Sharapov, Physica C **301**, 262 (1998); V. M. Loktev, R. M. Quick, and S. G. Sharapov, Low Temp. Phys. **25**, 381 (1999) [Fiz. Nizk. Temp. **25** 515 (1999)]; Physica C **314**, 233 (1999).
[21] R. Schrieffer, *Theory of Superconductivity*, Benjamin, New York (1964).
[22] B. I. Halperin and D. R. Nelson, J. Low Temp. Phys. **36**, 599 (1979).
[23] E. Babaev and H. Kleinert, Phys. Rev. B **59**, 12083 (1999); *Preprint cond-mat/9804206*.
[24] K. Miyake, Prog. Theor. Phys. **69**, 1794 (1983).
[25] M. Randeria, *Proceedings of the International School of Physics*, ''Enrico Fermi,'' Varenna, 1997 (IOS Press, Amsterdam, 1998); *Preprint cond-mat/9710223*.
[26] M. Casas, J. M. Getino, M. de Llano, A. Puente, R. M. Quick, H. Rubio, and D. M. van der Walt, Phys. Rev. B **50**, 15945 (1994).
[27] A. J. Leggett, Physica Fennica **8**, 125 (1973).
[28] A. Paramekanti, N. Trivedi, and M. Randeria, Phys. Rev. B **57**, 11639 (1998).
[29] B. K. Chakraverty, *Preprint cond-mat/9907035*, submitted to Phys. Rev. Lett.
[30] M. V. Sadovskii and A. I. Posazhennikova, JETP Lett. **65**, 270 (1997).

LOW TEMPERATURE MAGNETISM

On the magnetoelectric effect in LiNiPO$_4$

I. E. Chupis*

*B. Verkin Institute for Low Temperature Physics and Engineering,
National Academy of Sciences of Ukraine, pr. Lenina 47, 61164 Kharkov, Ukraine*
(Submitted November 18, 1999)
Fiz. Nizk. Temp. **26**, 574–578 (June 2000)

It is shown that the ''butterfly'' magnetoelectric hysteresis loop usually associated with the presence of a spontaneous magnetic moment in a crystal can also be observed in the case of an ''angled cross'' type of antiferromagnetic ordering of the spins. The magnetoelectric hysteresis observed in LiNiPO$_4$ is explained by the cross-shaped antiferromagnetic ordering of the spins in this compound. It is assumed that the jump in the electric polarization near the Néel temperature in a high magnetic field is the result of a first-order phase transition from the antiferromagnetic cross-shaped to a weak ferromagnetic state. © *2000 American Institute of Physics.* [S1063-777X(00)00706-4]

The compound LiNiPO$_4$ belongs to a family of antiferromagnetic olivines with the general formula LiMPO$_4$ (M=Fe^{2+}, Mn^{2+}, Co^{2+}, Ni^{2+}) which are magnetoelectrics,[1] i.e., they exhibit the linear magnetoelectric effect. Recent measurements of the magnetoelectric (ME) effect in LiCoPO$_4$ and LiNiPO$_4$ have revealed the presence of hysteresis of the induced electric polarization in a magnetic field.[2] The existence of ME hysteresis, which is typical of weak ferromagnets, was unexpected for the olivines, whose neutron diffraction patterns attest, with a high probability, to their antiferromagnetic structure.[3] It is known, however, that the linear ME effect, which depends substantially on the equilibrium spin configurations, can yield more accurate information about this matter.

To explain the magnetic hysteresis of the electric polarization in LiCoPO$_4$ and LiNiPO$_4$, it was hypothesized in Ref. 4 that there is a spin structure modulated along the Z axis, with small nonzero values of the spontaneous magnetization (m_z for LiNiPO$_4$ and m_y for LiCoPO$_4$) and polarization p_x.

In this paper we offer an explanation for the ME hysteresis loop in LiNiPO$_4$ in the framework of homogeneous magnetic configurations, without the hypothesis of spatial modulation of the spin structure or the presence of spontaneous magnetization. It is shown that in LiNiPO$_4$ there is an allowed antiferromagnetic configuration of the ''angled cross'' type (Fig. 1). This is consistent with the neutron diffraction data,[3] which do not confirm the presence of collinear antiferromagnetism in LiNiPO$_4$ but only indicate that the magnetic moments are possibly collinear with the $c(Z)$ axis in LiNiPO$_4$, where the magnetic intensities are very weak. When a magnetic field of the order of one tesla is applied along the X axis, the cross-shaped antiferromagnetic structure becomes unstable, and a ME hysteresis loop appears. An explanation is also proposed for the jump observed in the electric polarization near the Néel temperature in sufficiently high magnetic fields.[2] It is conjectured that this jump is the result of a first-order magnetic phase transition from the cross-shaped (Fig. 1) to a weak ferromagnetic state (Fig. 2).

LiNiPO$_4$ has the orthorhombic symmetry D_{2h} and a Néel temperature $T_N \approx 20.5$ K. Four crystallographically equivalent magnetic ions are located at the positions 1(0.28,0.25,0.98), 2(0.22,0.75,0.48), 3(0.72,0.75,0.02), and 4(0.78,0.25,0.52). The ion pairs (1,2) and (3,4) lie in neighboring planes perpendicular to the $a(X)$ axis. The exchange interaction of the ions between planes is indirect and substantially weaker than the antiferromagnetic interaction of the ions within the planes.

The free energy density of the crystal is written in the form
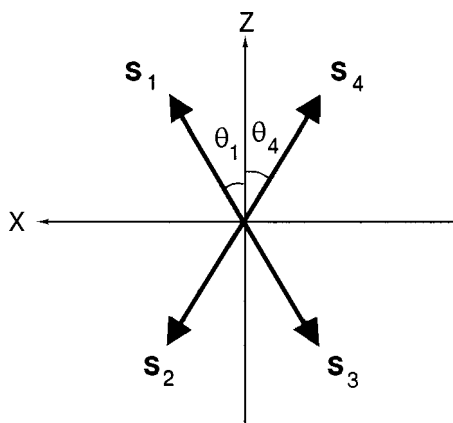
FIG. 1. Equilibrium antiferromagnetic configuration of spins of the ''angled cross'' (C) type, with the arrangement of spins in the XZ plane in a field $H_x \lesssim H_n$.

$$W = \sum_{j=1}^{3} \left(\frac{1}{2} a_j l_j^2 - \frac{1}{2} a_{jx} l_{jx}^2 + \frac{1}{2} a_{jz} l_{jz}^2 + \frac{1}{4} B_j l_j^4 + \frac{1}{2} D_j m^2 l_j^2 \right)$$

$$+ \frac{b}{2} m^2 - \mathbf{mH} + d_1 m_x l_{1z} + d_2 m_z l_{1x}$$

$$+ \xi_1 l_{2x} l_{3z} + \xi_2 l_{3x} l_{2z} + \frac{1}{2\chi^e} P_z^2 + W_{ME},$$

$$W_{ME} = P_z m_x (\gamma_1 l_{2z} + \gamma_2 l_{3x}) + P_z l_{1z} (\Gamma_1 l_{2z} + \Gamma_2 l_{3x}) + \dots \tag{1}$$

Here we have introduced the antiferromagnetism vectors l_j, which are related to the spins S_i of the ions as follows:

$$l_1 = S_1 - S_2 + S_3 - S_4, \quad l_2 = S_1 - S_2 - S_3 + S_4,$$

$$l_3 = S_1 + S_2 - S_3 - S_4, \quad m = S_1 + S_2 + S_3 + S_4, \tag{2}$$

where m is the magnetization, P is the electric polarization, and χ^e is the static dielectric susceptibility. In the ME part of the free energy, W_{ME}, with constants γ_1, γ_2, Γ_1, and Γ_2, we have written out only those terms which are necessary for analysis of the results of Ref. 2. In that paper the electric polarization induced along the Z axis by a magnetic field H_x of up to 20 T was measured over the temperature interval 4.2–25 K. Below T_N in a field of the order of 1 T the function $P_z(H)$ exhibited a hysteresis loop which vanished below a temperature of 8 K. A detailed study of the ME effect near T_N showed that at a considerably higher magnetic field, of the order of 10 T, the electric polarization undergoes a jump essentially to zero.

To explain the aforementioned effects requires analysis of the equilibrium spin configurations in LiNiPO$_4$. Here it is sufficient to proceed from a free energy of the form (1), assuming a uniform distribution of spins and (unlike Ref. 4) not including invariants containing spatial derivatives.

Another difference is that expression (1) contains terms with the coefficients d_1 and d_2, which were not taken into account in Ref. 4. It should be noted that, despite a different system of numbering for the magnetic ions in the present paper and in Ref. 4, the notation for the antiferromagnetism vectors (2) are the same in both papers. Expression (1) for the free energy is general for the whole family of olivines.

The equilibrium spin configurations are found by minimizing the free energy (1). It is easy to see that collinear antiferromagnetism is possible only along the Y axis (the case of LiCoPO$_4$). Collinear antiferromagnetism along the Z axis (the state when $S_1 = -S_2 = S_4 = -S_3$, i.e., $l_1 = l_3 = 0$, $l_2 \neq 0$) cannot exist because of the presence in (1) of the anisotropy energy with the coefficient ξ_2. We shall henceforth assume that the anisotropy energy with coefficients d_i, ξ_i is much larger than the exchange.

The minimum of the energy (1) for a predominant direction of the antiferromagnetism vector along the Z axis for $H=0$ corresponds to two states:

1. Antiferromagnetic states of the "angled cross" (C) type (Fig. 1, magnetic symmetry $mm'm$). The spins lie in the XZ plane near the Z axis, $S_3 = -S_1$, $S_4 = -S_2$, $l_1 = m = 0$. The order parameter is $l_{2z} = 2(S_{1z} - S_{2z})$,

$$l_{2z}^2 \approx -\frac{\tilde{a}_2}{B_2}, \quad l_{3x} = \frac{\xi_2}{a_3 + a_{3x}} l_{2z}, \quad B_2 \geqslant 0,$$

$$\theta_4 = \theta_1 = \theta_0 \approx \frac{\xi_2}{\tilde{a}_2 - a_3}, \quad \tilde{a}_2 = a_2 + a_{2z} \leqslant 0. \tag{3}$$

2. Weak ferromagnetic state (WF) (Fig. 2, symmetry $mm'm'$). The spins lie in the XZ plane,

$$S_3 = S_1, \quad S_4 = S_2, \quad l_2 = l_3 = 0, \quad m_x \neq 0.$$

The order parameter is l_{1z},

$$l_{1z}^2 \approx -\frac{\tilde{a}_1}{B_1}, \quad m_x = -\frac{d_1}{b + D_1 l_{1z}^2} l_{1z}, \quad \tilde{a}_1 = a_1 + a_{1z} \leqslant 0. \tag{4}$$

If the interplane and intrasublattice exchange interactions are neglected, the constants obey $a_2 = a_1 = -b = -a_3 = -8J \leqslant 0$, where J is the exchange integral in the interaction energy $J(S_1 \cdot S_2 + S_3 \cdot S_4)$.

It follows from Eq. (1) that the equilibrium electric polarization P_z is given by

$$P_z = -\chi^e [m_x(\gamma_1 l_{2z} + \gamma_2 l_{3x}) + l_{1z}(\Gamma_1 l_{2z} + \Gamma_2 l_{3x})]. \tag{5}$$

We see from (5) that spontaneous polarization is absent in the C and WF states.

The linear ME effect, with a ME component of the susceptibility $\alpha_{zx} = \partial P_z / \partial H_x$, which was observed in Ref. 2 for $T \leqslant T_N$, can exist only in the C state. Consequently, below the Néel temperature in weak magnetic fields an antiferromagnetic cross-shaped spin configuration C is realized in LiNiPO$_4$.

The behavior of this antiferromagnetic structure in a magnetic field directed along the X axis is similar to the behavior of a weak ferromagnet containing domains with opposite directions of the weak ferromagnetic moment.

For analysis of the behavior of the spin configuration C in a magnetic field, we set $S_i^2 = S_0^2$ and we treat the polar angles θ_i and azimuthal angle φ_i of the spins as the variables in the energy (1). In the absence of magnetic field one has $\theta_4 = \theta_1 = \theta_0$, $\theta_2 = \theta_3 = \pi - \theta_0$. In the presence of a magnetic field $H_x \geqslant 0$ the angles θ_1 and θ_2 increase, while θ_4 and θ_3 decrease. In weak magnetic fields we obtain from Eq. (1) the following equilibrium values of the angles:

$$\theta_1 = \theta_0 - \frac{H_x}{4S_0(b - \tilde{a}_2)}, \quad \theta_4 = \theta_0 - \frac{H}{4S_0(b - \tilde{a}_2)},$$

$$\theta_2 = \pi - \theta_1, \quad \theta = \pi - \theta_4. \tag{6}$$

We shall assume that $\theta_0 \geqslant 0$, i.e., $\xi_2 \leqslant 0$, although the sign of ξ_2 is not of fundamental importance. For the magnetization and the ME susceptibility of the linear ME effect we obtain from (5) and (6) the expressions
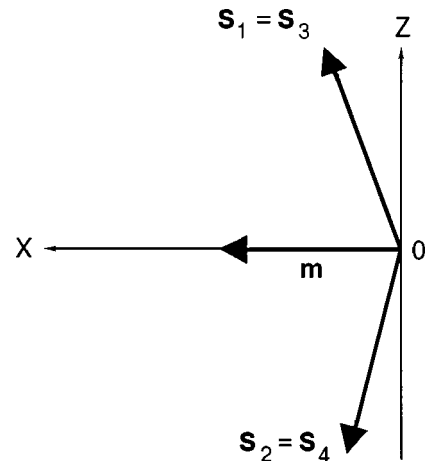

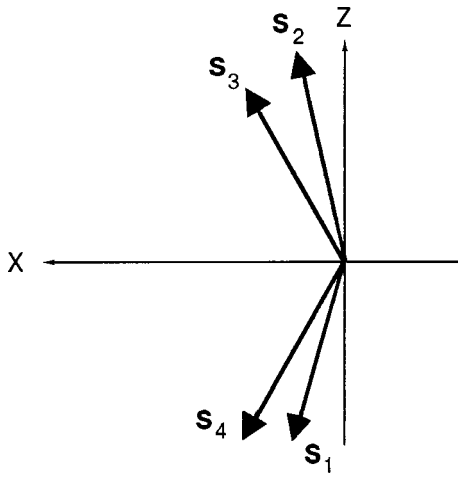
FIG. 2. Weak ferromagnetic state WF.

FIG. 3. Spin configuration C in a field $H_x \gg H_n$.

$$m_x = \chi_\perp^m H_x, \quad \chi_\perp^m = \frac{1}{b - \tilde{a}_2},$$

$$\alpha_{zx} = -\chi^e \chi_\perp^m l_{z0} \left[\gamma_1 + \frac{\gamma_2 \xi_2}{a_3 + a_{3x}} \right], \quad l_{z0} = l_{2x}(H=0). \quad (7)$$

We see from formulas (6) that the angles θ_4 and θ_3 decrease with increasing field strength, and at $H_x = H_0 = 4S_0(b - \tilde{a}_2)\theta_0 = 4S_0|\xi_2|$ they are equal to zero. In a field $H_n \leqslant H_0$ the azimuthal angle of the spins S_3 and S_4 change abruptly from π to 0, the spins turn over into the half plane with $\varphi = 0$ (Fig. 3). The situation is analogous to that observed during the magnetization reversal of a weak ferromagnet, except in the cross-shaped antiferromagnetic configuration the instability arises in planes in which the direction of the magnetic moment antiparallel to the field direction corresponds to a canting of the spins. In the case we are considering here, this is the plane in which the spins S_3 and S_4 are located. In a field H_n the spins are reoriented, and a first-order phase transition occurs in the system, as a result of which the system passes into the stable state illustrated in Fig. 3, where

$$\theta_3 = \theta_0 + \frac{H_x}{4S_0(b - \tilde{a}_2)}, \quad \theta_2 = \frac{H_x}{4S_0(b - \tilde{a}_2)} - \theta_0,$$

$$H_x \gg H_n. \quad (8)$$

In a field $H_x = H_n$ the energies of states (6) and (8) are equal. States (6) and (8) differ in the signs of l_{2z} and l_{3x}, and therefore α_{zx} (i.e., P_z) changes sign (segment 2 in Fig. 4). If now the field is decreased and reversed in sign, the instability will arise for spins S_1 and S_2, located in the other atomic
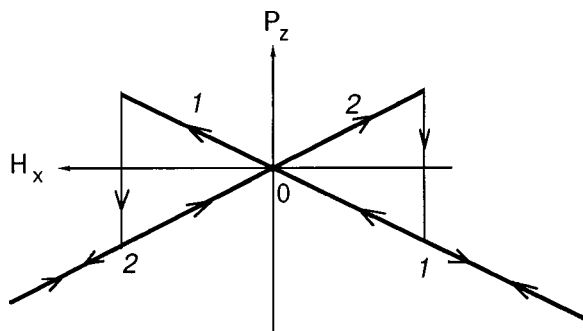
plane. The electric polarization in Fig. 4 jumps from segment 2 to segment 1, and the sign of the ME effect again changes to the opposite. Thus a ME hysteresis loop of the ''butterfly'' type, which is observed in weak ferromagnets, also exists in an antiferromagnet with a cross-shaped spin configuration. The value of the reorientation field $H_n \approx 4S_0|\xi_2|$ is of the order of the anisotropy field, a finding is consistent with the experimentally measured[2] values of the order of 1 T. The vanishing of the hysteresis loop below 8 K may be a consequence of a decrease in ξ_2 with decreasing temperature and a transition of the spins to a collinear antiferromagnetic orientation.

Besides the ME loop considered here, at temperatures close to the Néel temperature and in considerably higher fields, of the order of 10 T, LiNiPO$_4$ also exhibits a jump in the polarization P_z to a value close to zero; this jump is accompanied by ME hysteresis, i.e., there is a second-order phase transition to a state in which the linear ME effect is absent. This state is the weak ferromagnetic state WF. In fact, it is easy to obtain an expression for the free energies of the the C and WF states near T_N for the case of weak magnetic fields:

$$W_C = -\frac{\tilde{a}_2^2}{4B_2} - \frac{H^2}{2(b + D_2 l_{2z}^2)},$$

$$W_{WF} = -\frac{\tilde{a}_1^2}{4B_1} - \frac{H^2}{2(b + D_1 l_{1z}^2)} + \frac{d_1}{(b + D_1 l_{1z}^2)}$$

$$\times \left(-\frac{\tilde{a}_1}{B_1} \right)^{1/2} H - \frac{d_1^2}{4(b + D_1 l_{1z}^2)^2 |\tilde{a}_1|} H^2. \quad (9)$$

The presence in the energy W_{WF} of a term linear in H and a term quadratic in H with a coefficient inversely proportional to $|\tilde{a}_1|$, i.e., to the square of the order parameter l_{1z}^2, is characteristic of a weak ferromagnet.

In weak magnetic fields the C state, i.e., $|\tilde{a}_1| \leqslant |\tilde{a}_2|$, is realized in LiNiPO$_4$. We note that since $a_2 = a_1$, near T_N, at small values of $|\tilde{a}_2|$, the value of $|\tilde{a}_1|$ is also small. With increasing magnetic field at temperatures near T_N, the last term in W_{WF}, which lowers the energy, becomes larger, so that the WF state can become more favorable. In other words, a weak ferromagnetic state WF can be realized near T_N in sufficiently high magnetic fields; this is apparently what is observed in the experiments.

[1] M. Mercier, J. Gareyt, and E. F. Bertaut, C. R. Acad. Sci. Ser. B **264**, 979 (1967).
[2] I. Kornev, J.-P. Rivera, S. Gentil, A. G. M. Jansen, M. Bichurin, H. Schmid, and P. Wyder, Phys. Rev. B (manuscript No. BX6643), to be published.
[3] R. P. Santoro, D. J. Segal, and R. E. Newman, J. Phys. Chem. Solids **27**, 1192 (1966).
[4] I. Kornev, J.-P. Rivera, S. Gentil, A. G. M. Jansen, M. Bichurin, H. Schmid, and P. Wyder, Phys. Rev. B (manuscript No. BX6645), to be published.

FIG. 4. Magnetoelectric hysteresis loop of the ''butterfly'' type.

Translated by Steve Torstveit

Backward electromagnetic waves in a magnetically disordered dielectric

E. A. Ivanchenko*

*National Science Center ''Kharkov Institute of Physics and Technology,'' Institute for Theoretical Physics
1 Akademicheskaya St., 61108 Kharkov, Ukraine*
(Submitted November 30, 1999)

A nonlinear-evolution set of equations of the hydrodynamic type describing a magnet with a noncollinear arrangement of spins is investigated. An explicit expression invariant to right and left spin rotations is used for the energy density. The model under consideration can be interpreted as a continuum limit of a system of distributed symmetric tops. In the three-dimensional case exact solutions for the spin density are obtained in the form of helical waves for the quadratic–biquadratic energy density (in terms of Cartan's invariant functions). Solutions are also obtained for the magnon fields inducing these waves. The existence of backward helical waves is predicted. Energy transport may occur at an angle greater than $\pi/2$ relative to the direction of the helical waves. The analytical dependences of the wave vector and of the frequency on the helical wave amplitude, magnetic susceptibility, rigidity, and other constants of the model are found. The predicted property would allow for the construction of backward wave generators based on the use of disordered magnetic materials. The backward electromagnetic waves in a layered disordered magnetodielectric are considered. The relationship between the parameters of electromagnetic waves of the (e) layer and of the (i) layer is obtained. © *2000 American Institute of Physics.* [S1063-777X(00)00806-9]

INTRODUCTION

The spin excitations in magnetic media with a noncollinear arrangement of spins are investigated using the hypothesis of spontaneous symmetry breaking of the statistical equilibrium state.[1,2] Using this hypothesis, Halperin and Hohenberg[3] proposed a hydrodynamic approach which was used to derive dynamic equations for magnetic media with a spontaneously broken symmetry with respect to spin rotations. Linear dynamical equations were obtained by Halperin and Saslov,[4,5] while nonlinear dynamics was considered in the Lagrangian approach by Volkov and Zheltukhin[6] and by Andreev and Marchenko.[7] Dzyaloshinskii and Volovik used the Hamiltonian formalism for this purpose.[8] Peletminskii and co-workers developed this formalism for different magnetic structures.[9,10]

The dynamical variables describing the nonequilibrium state of magnetic media with a spontaneously broken symmetry include the spin density $s_\alpha(\mathbf{x},t)$ ($\alpha = x, y, z$) and the order parameter, i.e., the orthogonal rotation matrix $a_{\alpha\beta}(\mathbf{x},t)$. In the long-wavelength limit, where spatial non-uniformities of the dynamical variables are small, we investigate the dynamics and take into consideration the possible nonlinear interactions of spin waves, using the concept of spontaneous breaking of the $SO(3)$ symmetry of spin rotations that leave the exchange interactions invariant. We shall assume that the energy density is a function of s, a, and ∇a or, what is the same, of the variables $\underline{s}_\alpha \equiv a_{\alpha\beta} s_\beta$ and $\underline{\omega}_{\alpha k} \equiv 1/2 e_{\alpha\beta\gamma} a_{\beta\gamma} \nabla_k a_{\gamma\lambda}$, which is Cartan's right form. The evolution equations in terms of $\underline{s}_\alpha$ and $\underline{\omega}_{\alpha k}$ assume the form of equations with constraints:[10,11]

$$\partial_t \underline{s}_\alpha = -\nabla_k \partial_{\underline{\omega}_{\alpha k}} \varepsilon + e_{\alpha\beta\gamma}(\underline{s}_\beta \partial_{\underline{s}_\gamma} \varepsilon + \underline{\omega}_{\beta k} \partial_{\underline{\omega}_{\gamma k}} \varepsilon),$$

$$\partial_t \underline{\omega}_{\alpha k} = -\nabla_k \partial_{\underline{s}_\alpha} \varepsilon + e_{\alpha\beta\gamma} \underline{\omega}_{\beta k} \partial_{\underline{s}_\gamma} \varepsilon,$$

$$\nabla_k \underline{\omega}_{\alpha i} - \nabla_i \underline{\omega}_{\alpha k} = e_{\alpha\beta\gamma} \underline{\omega}_{\beta k} \underline{\omega}_{\gamma i}, \tag{1}$$

$$s_\alpha = a_{\beta\alpha} \underline{s}_\beta.$$

In these equations $\partial_{\underline{s}_\alpha} \varepsilon = -\underline{\omega}_\alpha$, where $\underline{\omega}_\alpha = 1/2 e_{\alpha\beta\gamma} \times (\partial_t a a^T)_{\gamma\beta}$ is the right form associated with the time derivative. The set (1) determines the dynamical properties of the system without taking dissipation into account and describes the low frequency dynamics with an exchange interaction, when, for long enough times, rigid spin complexes are formed because of the strong exchange. These complexes remain practically undeformed, and their orientation is determined by the orthogonal rotation matrix $a_{\alpha\beta}(\mathbf{x},t)$. It follows from the set of Equations (1) that the energy density ε and the momentum components $\pi_i = \underline{s}_\alpha \underline{\omega}_{\alpha i}$ are conserved locally:

$$\partial_t \varepsilon = -\nabla_k \partial_{\underline{s}_\alpha} \varepsilon \partial_{\underline{\omega}_{\alpha k}} \varepsilon, \quad \partial_t \pi_\alpha = -\nabla_k t_{ik},$$

$$t_{ik} = -\delta_{ik}(\varepsilon - \underline{s}_\alpha \partial_{\underline{s}_\alpha} \varepsilon) + \underline{\omega}_{\alpha i} \partial_{\underline{\omega}_{\alpha k}} \varepsilon, \tag{2}$$

where t_{ik} is the momentum flux density tensor. In practice we used the following expression for the energy density:

$$\varepsilon = \varepsilon_i + \varepsilon_a,$$

where

$$\varepsilon_i = \frac{1}{2\chi} \underline{s}_\alpha^2 + \frac{\rho}{2} \underline{\omega}_{\alpha k}^2 + \frac{1}{4\chi_1} \underline{s}_\alpha^4 + \frac{\rho_1}{4} \underline{\omega}_{\alpha k}^4 + \frac{q}{2} \pi_i^2 \tag{3}$$

is the isotropic component and

$$\varepsilon_a = \frac{\rho_2}{4}(\underline{\omega}_{\alpha x}^2 \underline{\omega}_{\alpha y}^2 + \underline{\omega}_{\alpha x}^2 \underline{\omega}_{\alpha z}^2 + \underline{\omega}_{\alpha y}^2 \underline{\omega}_{\alpha z}^2) \tag{4}$$

is the ''anisotropic'' component (without taking into account the differential equations of coupling between $\underline{\omega}_{\alpha x}$, $\underline{\omega}_{\alpha y}$, $\underline{\omega}_{\alpha z}$) of the energy; χ is the magnetic susceptibility; ρ is the ''stiffness'' constant, and χ_1, ρ_1, ρ_2, and q are phenomenological coupling constants. This energy density is invariant to left and right spin rotations. The general set of Equations (1) has been studied by us previously (see Ref. 11). Ivanov[12] used the Lagrangian approach for a quadratic dependence of the energy density (amorphous magnet) to obtain topological solitons in spin glasses.

BACKWARD SPIN DENSITY WAVES

Let us determine the exact nonlinear solutions of stationary profile of the system (1). These solutions are helical waves with helical vector $\mathbf{k}$ and frequency ω (Ref. 13):

$$s_x = c_3 \sin \varphi_0 \sin \theta + c_1 \cos \varphi_0,$$
$$s_y = -c_3 \cos \varphi_0 \sin \theta + c_1 \sin \varphi_0, \tag{5}$$
$$s_z = c_3 \cos \theta$$

where

$$\mathbf{k} = \frac{c_1}{\rho}\left[\frac{|C_3|}{2c_3} \pm \left(\frac{C_3^2}{4c_3^2} + \frac{q^2\rho}{\chi}\right)^{1/2}\right]\mathbf{q},$$

$$\omega = \frac{c_1}{\chi}, \quad \theta(\mathbf{x},t) = \omega t - \mathbf{k}\mathbf{x} + \theta_0, \tag{6}$$

$$\mathbf{s}^2 = c_1^2 + c_3^2,$$

and c_1, c_3, C_3, θ_0, $\mathbf{q}$ are constants.

We have used the parametrization of the orthogonal rotation matrix $a_{\alpha\beta}(\mathbf{x},t)$ with Eulerian angles φ, θ, ψ.[13,14] For the sake of simplicity we have not written out the contribution of the biquadratic terms (see Ref. 13). The self-consistent magnetic field $\mathbf{h}$ forming a helical spin density wave $s(\mathbf{x},t)$ is given by the relation $h_\alpha \equiv \partial_{s_\alpha}\varepsilon$ and is defined as

$$\mathbf{h} = \frac{1}{\chi}\mathbf{s}. \tag{7}$$

It follows from formulas (5) and (7) that the self-consistent static magnetic field has the form $\mathbf{h}_0 = (c_1/\chi \cos \varphi_0, c_1/\chi \sin \varphi_0, 0)$ and determines the eigenfrequency of the magnetic moments. Obviously, the magnitude of this frequency equals $|c_1|/\chi$, $\chi > 0$.

According to Eqs. (2), the energy flux density is defined as

$$j_k = \partial_{\underline{s}_\alpha}\varepsilon \partial_{\underline{\omega}_{\alpha k}}\varepsilon. \tag{8}$$

Let us now determine the cosine of the angle w between the direction of wave propagation $\mathbf{k}$ and the direction of the energy flux density $\mathbf{j}$:

$$\cos w = \frac{\mathbf{k}\cdot\mathbf{j}}{|\mathbf{k}||\mathbf{j}|}. \tag{9}$$

Formula (9) assumes a simple form for all positive phenomenological coupling constants:

$$\cos w = \frac{|q_x|}{(q_x^2 + q_y^2 + q_z^2)^{1/2}}\,\mathrm{sgn}\,c_1. \tag{10}$$

Since the constant c_1 can be positive or negative in the model under consideration, we arrive at the conclusion that helical waves in a disordered magnet can propagate in the direction opposite (at an angle greater than $\pi/2$) to the energy transport direction.

ELECTROMAGNETIC WAVES IN A LAYERED MAGNETICALLY DISORDERED DIELECTRIC

In a dielectric medium without free charges and currents, the electromagnetic vectors $\mathbf{e}$, $\mathbf{h}$ obey the Maxwell equations

$$\mathrm{curl}\,\mathbf{e} = -\frac{1}{c}\partial_t \mathbf{b}, \quad \mathrm{div}\,\mathbf{b} = 0,$$

$$\mathrm{curl}\,\mathbf{h} = \frac{1}{c}\partial_t \mathbf{d}, \quad \mathrm{div}\,\mathbf{d} = 0, \tag{11}$$

where c is the speed of light; $\mathbf{b} = \mu\mathbf{h}$ is the magnetic induction, μ is the magnetic permeability; $\mathbf{d} = \varepsilon\mathbf{e}$ is the electric displacement, and ε is the dielectric permittivity.

Since $\omega^2 = (c^2/\varepsilon\mu)\mathbf{k}^2$, as follows from Eqs. (11), taking into account formula (6), we find

$$\frac{|C_3|}{c_3} = \pm\left(1 - \frac{\varepsilon\mu\rho}{c^2\chi}\right)\left(\frac{\varepsilon\mu\rho}{c^2\chi}\right)^{-1/2}. \tag{12}$$

It is evident that this ratio tends to zero if $\varepsilon \to 1$, $\mu \to 1$, and $\rho/\chi \to c^2$. From the equation div $\mathbf{b} = 0$, we obtain two conditions:

$$k_x \sin \varphi_0 = k_y \cos \varphi_0, \quad k_z = 0, \quad |\mathbf{k}| = \sqrt{k_x^2 + k_y^2}. \tag{13}$$

The fact that the solution is independent of the space variable z in the three-dimensional space indicates that the waves are ''cylindrical.'' According to Eqs. (5), (7), and (11), the self-consistent electric field in the magnetodielectric has the form

$$e_x = -\frac{cc_3 k_y}{\omega\chi\varepsilon}\cos\theta + e_{0x},$$

$$e_y = \frac{cc_3 k_x}{\omega\chi\varepsilon}\cos\theta + e_{0y}, \tag{14}$$

$$e_z = \frac{cc_3|\mathbf{k}|}{\omega\chi\varepsilon}\sin\theta + e_{0z},$$

where $\mathbf{e}_0 = (e_{0x}, e_{0y}, e_{0z})$ is a self-consistent static electric field in the dielectric.

In this phenomenological approach, we cannot determine the parameters c_1, $\mathbf{q}$, $\mathbf{e}_0$, but the boundary conditions

$$\mathbf{n}\times(\mathbf{h}^e - \mathbf{h}^i) = 0, \quad \mathbf{n}(\varepsilon^e\mathbf{e}^e - \varepsilon^i\mathbf{e}^i) = 0,$$

$$\mathbf{n}\times(\mathbf{e}^e - \mathbf{e}^i) = 0, \quad \mathbf{n}(\mu^e\mathbf{h}^e - \mu^i\mathbf{h}^i) = 0 \tag{15}$$

define the relationship between the parameters of the dielectric medium (i) and the medium (e). Here $\mathbf{n}$ is the unit vector normal to the boundary surface of the medium (i) and medium (e).

From relations (15) for the boundary surface $z = 0$, $\mathbf{n} = (0,0,1)$ we obtain, after eliminating the coordinates of the boundary surface, the following:

$$c|\mathbf{k}^e|\left(\frac{\omega^i}{\omega^e}-\cos(\varphi_0^i-\varphi_0^e)\right)+c|\mathbf{k}^i|\left(\frac{\omega^e}{\omega^i}-\cos(\varphi_0^i-\varphi_0^e)\right)$$

$$+(\varepsilon^i e_{0z}^i-\varepsilon^e e_{0z}^e)\sin(\varphi_0^i-\varphi_0^e)=0,$$

$$\sin(\varphi_0^i-\varphi_0^e)\neq 0. \tag{16}$$

$$\left(\frac{1}{\mu^i\varepsilon^i}\frac{\mathbf{k}^i}{\omega^i}-\frac{1}{\mu^e\varepsilon^e}\frac{\mathbf{k}^e}{\omega^e}\right)(\mathbf{e}_0^i-\mathbf{e}_0^e)=0,\quad k_x^e k_y^i-k_y^e k_x^i\neq 0. \tag{17}$$

Now we consider the case when the static electric field in the dielectric medium is $\mathbf{e}_0=(0,0,e_{0z})$. Since the energy flux density in the dielectric is $\mathbf{j}=(c/4\pi)\mathbf{e}\times\mathbf{h}$, as follows from Eqs. (11), we find

$$\cos w^i=\frac{\mathbf{k}^i\cdot\mathbf{j}^i}{|\mathbf{k}^i||\mathbf{j}^i|}=\frac{\sqrt{\mu^i/\varepsilon^i}(c_3^{i^2}/\chi^{i^2})\operatorname{sgn}\omega^i+e_{0z}^i(c_3^i/\chi^i)\sin\theta^i}{\left[\left(\frac{\mu^i}{\varepsilon^i}\frac{c_3^{i^2}}{\chi^{i^2}}+2e_{0z}^i\sqrt{\mu^i/\varepsilon^i}\frac{c_3^i}{\chi^i}\operatorname{sgn}\omega^i\sin\theta^i\right)\frac{(c_1^{i^2}+c_3^{i^2})}{\chi^{i^2}}+e_{0z}^{i^2}\frac{c_1^{i^2}}{\chi^{i^2}}+e_{0z}^{i^2}\frac{c_3^{i^2}}{\chi^{i^2}}\sin^2\theta^i\right]^{1/2}}, \tag{18}$$

where $\theta^i\equiv\omega^i t-\mathbf{k}^i\mathbf{x}+\theta_0^i$, and $\mathbf{x}$ belongs to the medium (i).

Equation (16), when Eq. (13) is taken into account, has the real solution

$$\frac{\omega^i}{\omega^e}=\frac{-b\pm\sqrt{b^2-4|\mathbf{k}^i||\mathbf{k}^e|}}{2|\mathbf{k}^e|},$$

$$b\equiv(\varepsilon^i e_{0z}^i-\varepsilon^e e_{0z}^e)\frac{k_y^i k_x^e-k_x^i k_y^e}{|\mathbf{k}^i||\mathbf{k}^e|}$$

$$-(|\mathbf{k}|^i+|\mathbf{k}^e|)\frac{k_x^i k_x^e+k_y^i k_y^e}{|\mathbf{k}^i||\mathbf{k}^e|}\gtreqless\pm 2\sqrt{|\mathbf{k}^i||\mathbf{k}^e|}. \tag{19}$$

Solution (19) points to the existence of the backward electromagnetic waves according to (18), provided that, for example,

$$\sqrt{\mu^i/\varepsilon^i}c_3^i\operatorname{sgn}\omega^i+e_{0z}^i\sin\theta^i<0,\quad c_3^i>0.$$

If we choose the boundary surface $y=0$, $n=(0,1,0)$, then we obtain the following conditions of coupling between the parameters in the model under consideration:

$$\frac{c}{\varepsilon^e}|\mathbf{k}^e|\left(\mu^i\frac{\omega^i}{\omega^e}-\mu^i\cos\varphi_0^i\cos\varphi_0^e-\mu^e\sin\varphi_0^i\sin\varphi_0^e\right)$$

$$+\frac{c}{\varepsilon^i}|\mathbf{k}^i|\left(\mu^e\frac{\omega^e}{\omega^i}-\mu^e\cos\varphi_0^i\cos\varphi_0^e\right.$$

$$\left.-\mu^i\sin\varphi_0^i\sin\varphi_0^e\right)+(e_{0z}^i-e_{0z}^e)$$

$$\times(\mu^e\sin\varphi_0^i\cos\varphi_0^e-\mu^i\cos\varphi_0^i\sin\varphi_0^e)=0. \tag{20}$$

$$\mu^e\sin\varphi_0^i\cos\varphi_0^e-\mu^i\cos\varphi_0^i\sin\varphi_0^e\neq 0.$$

$$\left(\frac{k_x^i}{\omega^i}-\frac{k_x^e}{\omega^e}\right)(e_{0x}^i-e_{0x}^e)+\left(\frac{k_y^i}{\omega^i}-\frac{\varepsilon^i}{\varepsilon^e}\frac{k_y^e}{\omega^e}\right)e_{0y}^i$$

$$-\left(\frac{\varepsilon^e}{\varepsilon^i}\frac{k_y^i}{\omega^i}-\frac{k_y^e}{\omega^e}\right)e_{0y}^e=0,\quad \varepsilon^e k_x^e k_y^i-\varepsilon^i k_x^i k_y^e\neq 0. \tag{21}$$

Formulas (7), (14), (16), and (17) can be applied to a layered magnetically disordered dielectric medium.

CONCLUSION

According to Eq. (5), the exact nonlinear solutions presented here are helical waves. The contribution of biquadratic terms to the energy density (3), (4) increases with the spin density in the system.[13] Energy transport can occur at an angle greater than $\pi/2$ with respect to the direction of propagation of the helical spin wave. Formulas (7) and (14), together with the boundary conditions (15), can be verified in an experiment. The relation between the parameters of the electromagnetic waves and the properties of the layer (e) and the layer (i) for a flat boundary (formulas (16), (17)) is established.

The author is obliged to Prof. S. V. Peletminskii for discussions.

*E-mail: yevgeny@kipt.kharkov.ua

[1] N. N. Bogolubov, Physica (Amsterdam) **26**, 1 (1960).
[2] J. J. Goldstone, Nuovo Cimento **19**, 154 (1961).
[3] B. I. Halperin and P. C. Hohenberg, Phys. Rev. **188**, 898 (1969).
[4] B. I. Halperin and W. M. Saslov, Phys. Rev. B **16**, 2154 (1977).
[5] W. M. Saslov, Phys. Rev. B **22**, 1174 (1980).
[6] D. V. Volkov and A. A. Zheltukhin, Solid State Commun. **36**, 733 (1980).
[7] A. F. Andreev and V. I. Marchenko, Usp. Fiz Nauk **130**, 39 (1980) [Sov. Phys. Usp. **130**, 39 (1980)].
[8] I. E. Dzyaloshinskii and G. E. Volovik, Ann. Phys. **125**, 67 (1980).
[9] M. Yu. Kovalevskii, S. V. Peletminskii, and A. L. Shishkin, Ukr. Fiz. Zh. (Russ. Ed.) **36**, 245 (1991).
[10] A. A. Isayev, M. Yu. Kovalevskii, and S. V. Peletminskii, Fiz. Met. Metalloved. **77**, 4, 20 (1994).
[11] E. A. Ivanchenko, Fiz. Nizk. Temp. **20**, 150 (1994) [Low Temp. Phys. **20**, 121 (1994)].
[12] B. A. Ivanov, Solid State Commun. **34**, 437 (1980).
[13] E. A. Ivanchenko, Fiz. Nizk. Temp. **24** 468 (1998) [Low Temp. Phys. **24**, 354 (1998)].
[14] H. Goldstein, *Classical Mechanics*, Addison-Wesley, Reading, Mass. (1980).

ELECTRONIC PROPERTIES OF METALS AND ALLOYS

Compensation effects in the interaction of the electron and ion subsystems of a metal

L. T. Tsymbal,* A. N. Cherkasov, and O. F. Panchenko

*A. A. Galkin Donetsk Physicotechnical Institute, National Academy of Sciences of Ukraine,
ul. R. Lyuksemburg 72, 83114 Donetsk, Ukraine*

A detailed theoretical analysis is made of the interaction of the electron and ion subsystems in normal metals. Simple, but realistic models of the Fermi surface and deformation-potential tensor are used which permit numerical solution of the dispersion relation. To elucidate the consequences of the partial or total mutual compensation of the electron and hole concentrations, both the external parameters (sound frequency, magnetic field) and the model parameters for the metal (the constant of the deformation-potential tensor, the ratio of electron and hole concentrations, the free carrier relaxation rate) are varied. It is shown that in compensated metals the compensation effects lead to strong suppression of the interaction of the lattice with one of the groups of free carriers. The theoretical results are in qualitative agreement with the experimental data obtained in cadmium and tungsten. A quantitative comparison of the theory with experiment is carried out which, in particular, yields an estimate for the values of the constants of the deformation potential in cadmium. © *2000 American Institute of Physics.* [S1063-777X(00)00906-3]

INTRODUCTION

The interaction of the different subsystems in condensed matter (metals, in particular) and of the collective excitations of these subsystems is one of the fundamental problems of solid state physics. We have previously[1] done a detailed analysis of the coupling of helicons and dopplerons – weakly damped electromagnetic modes that are excitations of the same subsystem of a metal. In a subsequently paper[2] we investigated in detail the interaction of electrons with the lattice and of ultrasonic waves with weakly damped electromagnetic modes, and we analyzed a simple but realistic model of an uncompensated metal having one group of carriers. It was found that, independently of the type of coupled mode, there exist some general regularities that characterize the problem of coupling on the whole. The present paper, which concludes this cycle of studies, is a logical continuation of Ref. 2 and is devoted to a detailed examination of the interaction of electrons with the lattice in compensated metals, i.e., in metals having at least two groups of carriers—electrons and holes. We believe this to be a topical problem in view of some seemingly illogical and contradictory experimental results that have been obtained. It turns out that the presence of another group of carriers in a metal can (and does) lead to dramatic consequences which are manifested in a fundamental change in the character of the interaction of the lattice with one of the groups of carriers (it turns out to be of fundamental importance that the metal is compensated, i.e., having equal electron and hole concentrations). This group, which we shall call the majority carriers, is the group having the maximum pitch u_{max} of the helical trajectory in a magnetic field **H**: $u = |2\pi v_H / \omega_c|$ (v_H is the average drift velocity of the carriers along **H**, and $\omega_c = eH/mc$ is the cy-

clotron frequency; here and below we assume that the orbits of all the carriers are closed). Accordingly, the dopplerons due to the Doppler-shifted cyclotron resonance (DSCR) of the carriers of this group will be called long-wavelength dopplerons[3] (with increasing field the doppleron wavelength $\lambda_D \to u_{max}$).

The most unexpected experimental results have been obtained in cadmium. It was in this compensated metal that the doppleron–phonon resonance (DPR) was first observed.[4] Cadmium has two groups of carriers with practically equal concentrations—majority carriers of the electron type (the ''lens''), and minority carriers of the hole type (the ''monster'').[5] Accordingly, in radio spectroscopic studies one observes oscillations of the surface resistance, which are the result of the excitation of the long-wavelength electron[6,7] and short-wavelength hole[7] dopplerons. The hole doppleron is manifested much more weakly, primarily because of collisionless resonance absorption of the doppleron wave by electrons of the ''lens.'' At first glance the data from magnetoacoustic studies appear to be in complete contradiction with these results. Figure 1 shows examples of the experimental dependence of the damping coefficient of transverse ultrasound $\Gamma \equiv \operatorname{Im} k$ in cadmium (see also Refs. 8 and 9). Here **k** is the wave vector of the linearly polarized transverse sound wave. The field H_L corresponds to the edge of the single-particle collisionless absorption of sound by electrons of the ''lens'' as a consequence of the DSCR (magnetoacoustic resonance), and H_M is the edge of the absorption of sound by holes of the ''monster.'' We see that at low frequencies in fields $H_M < H < H_L$ the magnetoacoustic resonance hardly shows up at all. The anomaly D_L, which is observed in fields $H > H_L$ and is a result of the interaction of
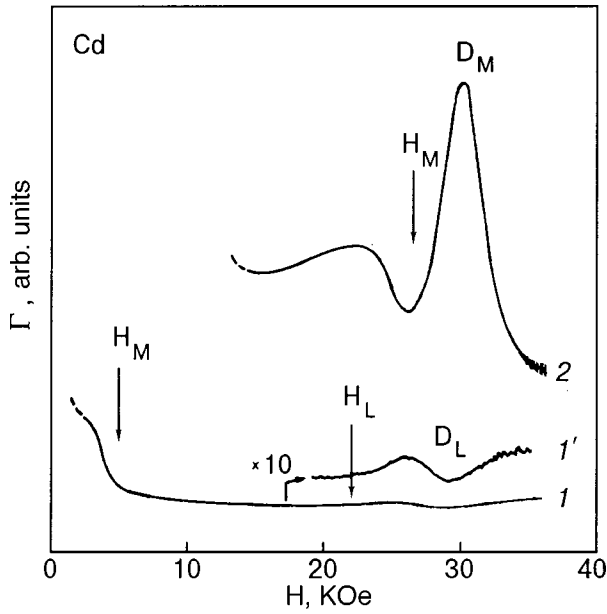
FIG. 1. Damping of linearly polarized transverse sound ($\Gamma \equiv \mathrm{Im}\, k$) in cadmium as a function of the magnetic field for different frequencies $\omega/2\pi$, MHz: 60 (*1,1'*), 300 (*2*); $\mathbf{k}\|\mathbf{H}\|[0001]$, $T=4.2$ K. The fields H_L and H_M correspond to the edge of the collisionless absorption of sound by electrons of the "lens" and holes of the "monster," respectively. The features D_L and D_M are due to the doppleron–phonon resonance (DPR).

sound with an electron doppleron,[4] has a very small amplitude. It should also be noted that this anomaly does not have the shape of an absorption peak but more closely resembles the anomalies of the dispersion of the sound velocity, which would be expected to appear in the vicinity of the DPR.[2] These anomalies have been observed experimentally in Ref. 10, for example. A much stronger role in the absorption of sound in cadmium is played by the holes, which are the minority carriers. It is seen from curve *1* in Fig. 1 that as H decreases, in fields $H < H_M$, the damping of sound increases sharply as a result of the "turning on" of the collisionless absorption of sound by holes of the "monster." With increasing frequency this feature in the absorption, which has the form of a "Kjeldaas edge,"[11] is transformed into an asymmetric peak in fields less than H_M. In fields $H > H_M$ a strong absorption peak D_M appears, which has the "classical" shape of an absorption curve and is due to the interaction of sound with the hole doppleron.[8]

An attempted theoretical analysis of the DPR in cadmium was reported in Ref. 12. However, the authors used a very simplified model of the metal and restricted the analysis of the interaction to the limit of strong coupling of the dopplerons with the sound. As a result, the calculated magnetic field dependence of the damping coefficient of sound did not agree even qualitatively with the experimental dependence.

The immediate goal of the present study is to carry out a theoretical analysis of the damping of transverse sound in compensated metals due to the interaction of the electrons with the lattice in the presence of an external magnetic field. A reasonable realistic model of the metal is used. The dispersion relation was solved numerically by Muller's method (generalized method of secants) with deflation.[13] For specificity some of the nonvariable parameters of the model (the

density of the metal, the sound velocity, etc.) were taken equal to the corresponding parameters in cadmium. This does not limit the generality of the analysis, however. On the contrary, the dispersion obtained in this study makes it possible to extend the scope of the analysis substantially. In particular, we have examined the consequences of a gradual decompensation of the concentrations of electrons and holes.

DISPERSION RELATION AND THE MODEL OF THE METAL

1. The elastic and electromagnetic oscillation in metals are described by the equations of the theory of elasticity and Maxwell's equations, supplemented by the constitutive relations (see, e.g., the papers[14,15] and the reviews[16,17]). We restrict the discussion to an analysis of the interaction of monochromatic plane waves ($\mathbf{u}, \mathbf{E} \propto \exp(i\mathbf{k}\cdot\mathbf{r} - i\omega t)$, where $\mathbf{u}$ is the lattice displacement vector and $\mathbf{E}$ is the electric field) in the geometry $\mathbf{k}\|\mathbf{H}\|\hat{z}$ in a metal for which all parts of the Fermi surface are symmetric with respect to the $\hat{z}$ axis. Then for the circularly polarized transverse components of the oscillations, $\psi_\pm = \psi_x \pm i\psi_y$ ($\pm$ indicates the polarization, and $\psi = u, E$) the dispersion relation of coupled electromagnetic and acoustical modes can be written in the form[2,18]

$$(k^2 c^2 - 4\pi i\omega\sigma_\pm(k^2 v_s^2 - \omega^2 - L_\pm/\rho)$$

$$= (4\pi i\omega/\rho)g_\pm G_\pm, \qquad (1)$$

where ω and $\mathbf{k}$ are the frequency and wave vector, ρ is the density of the metal, $v_s = (\lambda_{xzzx}/\rho)^{1/2}$ is the velocity of a transverse sound wave, which is determined by the elastic-constant tensor $\hat{\lambda}$, and $\hat{G}$, $\hat{L}$, $\hat{\sigma}$, and $\hat{g}$ are the material tensors ($\varphi_\pm = \varphi_{xx} \pm i\varphi_{yx}$ for $\varphi = \sigma, L, g, G$). It should be noted that Eq. (1) takes into account not only the coupling of the acoustical modes with the collective electromagnetic modes but also the single-particle interaction of electrons with the lattice (magnetoacoustic resonance).

The material tensors $\hat{g}$, $\hat{G}$, and $\hat{L}$ are linear combinations of electroacoutic coefficients for which exact expressions have been obtained by Kontorovich.[17] If we neglect the Stewart–Tolman effect, as we may do in sufficiently strong magnetic fields, we have

$$\sigma_\pm = e^2 \langle v_\pm v_\pm^* \rangle, \qquad (2)$$

$$g_\pm = \mp \frac{\omega e^2 H}{c} \left\langle v_\pm^* \left(v_\pm \pm \frac{ck}{eH}\Lambda_\pm \right) \right\rangle, \qquad (3)$$

$$G_\pm = \mp i \frac{e^2 H}{c} \left\langle \left(v_\pm \pm \frac{ck}{eH}\Lambda_\pm \right)^* v_\pm \right\rangle, \qquad (4)$$

$$L_\pm = i\omega \left[\frac{eH}{c} \right]^2 \left\langle \left| v_\pm \pm \frac{ck}{eH}\Lambda_\pm \right|^2 \right\rangle. \qquad (5)$$

Here $\mathbf{v}$ is the electron velocity ($v_\pm = v_x \pm iv_y$), $\hat{\Lambda}$ is the deformation-potential tensor ($\Lambda_\pm = \Lambda_{xz} \pm i\Lambda_{yz}$), the asterisk $*$ denotes the complex conjugate, and the angle brackets denote integration over the Fermi surface (FS) in momentum ($\mathbf{p}$) space:

$$\langle \varphi_\pm \rangle = i \frac{2\pi}{(2\pi\hbar)^3} \int_{FS} \frac{\varphi_\pm |m| dp_z}{\omega + i\nu \pm \omega_c - kv_z}. \qquad (6)$$

Here ν is the electron relaxation rate. Since we are interested in the region of relatively low frequencies and high fields, restricted by the inequality $\omega < \nu \ll |\omega_c|$, we shall henceforth set $\omega = 0$ in Eq. (6).

2. For metals with anisotropic Fermi surfaces the form of the tensor $\hat{\Lambda}$ is unknown. However, for a qualitative analysis one can assume that it corresponds to the deformation-potential tensor in the case of an isotropic electron dispersion relation:

$$\Lambda_{\alpha\beta} = \lambda_0 m\left(\frac{1}{3}v^2 \delta_{\alpha\beta} - v_\alpha v_\beta\right), \tag{7}$$

where λ_0 is a constant which is equal to unity for free electrons.

We consider a model metal having two groups of carriers: electrons and holes, with concentrations N_e and N_h (here and below the indices e and h are used to indicate the electron and hole parameters). In spite of the two-band nature of the spectrum and, hence, the corresponding symmetry considerations and the requirement of electrical neutrality ($\langle \Lambda_{\alpha\beta}\rangle = 0$), to avoid complicating the analysis we shall assume that the tensor $\Lambda_{\alpha\beta}$ is given by expression (7) for both holes and electrons, but with different constants λ_0. We shall assume that the cyclotron masses m_e and m_h and the quantities λ_{0e} and λ_{0h} are constants for each group of carriers, and that $\nu = \text{const}$ for all of the carriers. Then, after evaluating the coefficients (3)–(5) and transforming Eq. (1), we rewrite the dispersion relation in the form

$$q^2 - q_s^2 = \frac{\alpha_1(q)}{\Omega^2 q^2/q_s^2 \pm F_\pm(q)} - \alpha_2(q), \tag{8}$$

where

$$\alpha_1(q) = \alpha_0 q_s\{(1-\lambda_e)\Omega^2 q^2/q_s^3 \mp \lambda_e F_\pm(0)$$
$$\mp \Delta\lambda(N_h/N_e)[F_\pm^h(q) - F_\pm^h(0)]\}^2, \tag{9}$$

$$\alpha_2(q) = \alpha_0 q_s\{(1-\lambda_e)^2\Omega^2 q^2/q_s^3 \pm \lambda_e^2 F_\pm(0)$$
$$\pm (\Delta\lambda)^2(N_h/N_e)[F_\pm^h(q) - F_\pm^h(0)]\}. \tag{10}$$

Here for convenience of analysis we have introduced the dimensionless parameters

$$q = kv_e/\omega_{ce}; \quad q_s = q|_{k=k_s}; \Omega = \omega/\omega_0. \tag{11}$$

In Eqs. (8)–(11) the function $F_\pm(q)$ is a nonlocal factor in the conductivity ($\sigma_\pm = \pm i(N_e ec/H)F_\pm$; $F_\pm = F_\pm^e + (N_h/N_e)F_\pm^h$); $\alpha_0 = (N_e m_e/\rho)(v_e/v_s)$; $\Delta\lambda = \lambda_e - \lambda_h$; $\lambda_{e,h} = \lambda_{0e,h}(1\pm i\gamma_{e,h})$; $\gamma_{e,h} = \nu/\omega_{ce,h}$; v_e is a characteristic electron velocity, which in this paper is taken equal to the velocity of the electrons for which u is maximum; $k_s = \omega/v_s$; $\omega_0 = (\omega_{pe}^2 v_s^3/c^2 v_e)^{1/2}$; $\omega_{pe}^2 = 4\pi N_e e^2/m_e$. It should be noted that Eq. (8) with coefficients (9) and (10) is invariant with respect to interchange of the indices e and h.

3. The electron and hole Fermi surfaces are approximated by axially symmetric (with respect to the $\hat{z}$ axis) surfaces of the "corrugated cylinder" type:[2,19]

$$S(p_z) = S_0 + S_1 \cos(\pi p_z/P_0), |p_z| \leq p_0, \tag{12}$$

where $S(p_z)$ is the area of the cross section of the Fermi surface on a plane $p_z = \text{const}$; S_0, $S_1 \leq S_0$, and $p_0 > 0$ are parameters of the model. Taking into account that $v_\pm v_\pm^* = S(p_z)/\pi m^2$ and $v_z = -(\partial S/\partial p_z)/2\pi m$, we obtain from (6)

$$F_\pm(q) = F_\pm^e(q) + (N_h/N_e)F_\pm^h(q) = [(1\pm i\gamma_e)^2 - q^2]^{-1/2}$$
$$- (N_h/N_e)[(1\pm i\gamma_h)^2 - \beta^2 q^2]^{-1/2}. \tag{13}$$

Here $\beta = |\partial S_h/\partial p_z|_m/|\partial S_e/\partial p_z|_m$, where $|\partial S_{e,h}/\partial p_z|_m$ are the maximum values of the derivatives $\partial S_{e,h}/\partial p_z$. For the model of the Fermi surface that we have adopted, v_e is given by the relation $v_e = |\partial S_e/\partial p_z|_m/2\pi m_e$.

The scope of our analysis is not limited to the experimental results of magnetoacoustic studies of the absorption of sound in cadmium. Nevertheless, as we have said, for specificity we have taken some of the parameters of our model metal equal to those for cadmium. The relative position of the singularities in the conductivity (13) ($F_0 \to \infty$ for $q^2 \to 1$ and $q^2 \to \beta^{-2}$; $F_0 = F_\pm|_{\gamma_{e,h}=0}$) is determined by the differential characteristics of the Fermi surface, more precisely, by the values of $R_m = |\partial S/\partial p_z|_m/2\pi\hbar$. For cadmium $R_m^e = 1.43$ Å^{-1} ("lens") and $R_m^h = 0.342$ Å^{-1} ("monster").[20] In accordance with these and the other known data, we shall assume the following values in (8) and (13):

$$\rho = 8.65 \text{ g/cm}^3, \quad v_s = 1.57\cdot 10^5 \text{ cm/s},$$
$$m_e = 3|m_h| = 0.9\cdot 10^{-27} \text{ g},$$
$$N_e = N_h = 0.5\cdot 10^{22} \text{ cm}^{-3}, \quad \beta = 0.24. \tag{14}$$

Of course, in approximating the cadmium hole "monster," which has a 3-fold axis of rotational symmetry [0001], by an axially symmetric surface, we are excluding from consideration the multiple resonances observed in the experiment of Ref. 8. The singularity in the conductivity due to the DSCR of the electrons of the "lens" is apparently also weaker [logarithmic[21] rather than square-root, as in Eq. (13)]. However, this simplification of the model Fermi surface in our treatment is not of a fundamental nature, particularly since we have already made some serious assumptions in the choice of the model deformation potential. The function $F_0(q)$ in (13) for a metal with the parameters (14) is shown in Fig. 2.

DAMPING OF SOUND

A numerical solution of the dispersion relation (8) will be used to determine how the damping coefficients $k_\pm''$ ($k_\pm = k_\pm' + ik_\pm''$) for the acoustical modes depend on the external parameters and the parameters of the model for the metal. The external parameters are the frequency, i.e., the value of Ω (for the parameters given in (14) one has $\omega_0/2\pi \cong 102$ MHz) and the dimensionless magnetic field $h \equiv q_s^{-1}$. We see in Fig. 2 that for $q^2 > 1$ the function F_0 is complex. This is indicative of collisionless damping of the electromagnetic and sound waves due to the DSCR. In the interval $\beta \leq h \leq 1$ the condition of DSCR ($kv_z/\omega_c = 1$) is satisfied for the electrons, and for $h \leq \beta$ it is satisfied for both the electrons and holes. Collisions lead to a smearing of the absorption edge, as a result of which the collective modes will be damped for $h > 1$ as well. For our model of the Fermi surface the values $h = 1$ and $h = \beta$ correspond to the fields H_L and H_M in Fig. 1.
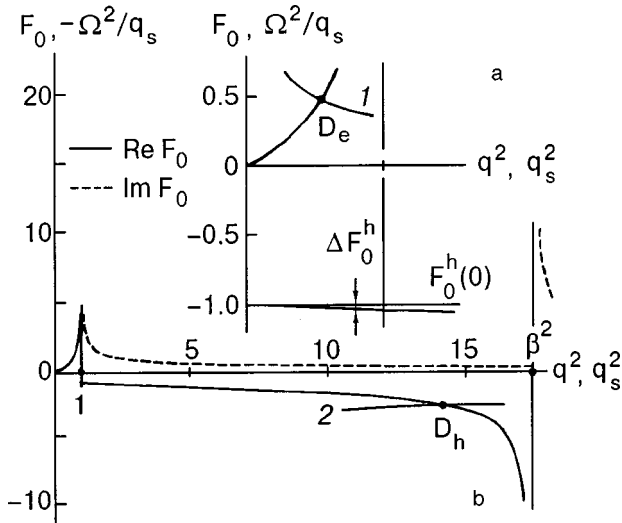
FIG. 2. The function F_0 of Eq. (13) ($F_0 = F_{\pm}|_{\gamma_{e,h}=0}$) and a graphical solution of Eq. (15). Curve *1* is the left-hand side of (15) in the "−" polarization at a frequency $\Omega = 0.59$ (for the parameters given in (14) this frequency corresponds to a value $\omega/2\pi = 60$ MHz) (a); curve *2* is the left-hand side of (15) in the "+" polarization at a frequency $\Omega = 2.95$ ($\omega/2\pi = 300$ MHz) (b). At the points D_e and D_h the acoustical modes interact resonantly with the electron and hole dopplerons, respectively.

The zeros of the denominator in the first term on the right-hand side of (8) are the roots of the dispersion relation for electromagnetic modes in the absence of their interaction with sound. Setting $q = q_s$ and $F_{\pm} = F_0$ in this denominator, we obtain the equation

$$\mp \Omega^2/q_s = F_0(q_s), \qquad (15)$$

which enables us to find the fields near which the acoustical modes are resonantly coupled with the weakly damped electromagnetic modes. In compensated metals these are dopplerons. In Fig. 2 we show as an example the graphical solution of Eq. (15) for two values of Ω. We see that at the point D_e the sound component in the "−" polarization is coupled with the electron doppleron, while at the point D_h the component in the "+" polarization is coupled with the hole doppleron. Consequently, the corresponding resonance features in the absorption of sound should be observed in fields $h > 1$ and $h > \beta$. It is important to note that $\mathrm{Re}\, F_0 \gg \mathrm{Im}\, F_0$ at the point D_h. At lower velocities this condition no longer holds, the electromagnetic mode is not weakly damped, and Eq. (15) can no longer be used.

Qualitative analysis

The interaction of electrons with the lattice is described by the dispersion relation (8). The character of this interaction and the sound absorption due to it are completely determined by the form of the coefficients α_1 and α_2. Let us start with a comparative analysis of the absorption of sound in uncompensated ($N_h = 0$) and compensated ($N_e = N_h$) metals. We make the simplification of setting $q = q_s$ ($\Omega^2 q^2/q_s^3 \rightarrow \Omega^2 h$) and $\gamma_{e,h} = 0$ in Eqs. (9) and (10). We shall also assume that in the general case $\lambda_{0e} \neq 1$ and $\Delta\lambda \neq 0$.

Uncompensated metal. In the curly brackets on the right-hand sides of Eqs. (9) and (10) there are three terms in each of these equations that can be paired with a similar counterpart in the other. In the case of an uncompensated metal

($N_h \rightarrow 0$) the third terms vanish, and in the second terms $\lambda_e F_{\pm}(0) \rightarrow \lambda_{0e}$. It is these terms that govern the character of the interaction of electrons with the lattice at low frequencies, when the first terms are relatively small. This is particularly true for the free-electron model ($\lambda_{0e} = 1$).[11] It was shown previously that at low frequencies a substantial role in the interaction is played by eddy currents.[22,23] As a result, in fields $h < 1$ the absorption of sound will exhibit a feature having the form of a "Kjeldaas edge."[11,16] As the frequency increases, the first terms grow in size. A purely deformational absorption of sound begins to play a role,[22,23] and the feature of the "Kjeldaas edge" type is transformed into an asymmetric peak in fields less than the resonance field $h = 1$.[23] Of course, the indicated features of the coefficients α_1 and α_2 in the uncompensated metal also determine the character of the coupling of the acoustical modes with helicons and dopplerons. This question is discussed in detail in our previous paper.[2]

Compensated metal. In going to the case of a compensated metal ($N_h \rightarrow N_e$) the form of the coefficients α_1 and α_2 changes substantially. As a result of compensation effects in the conductivity the second terms in the curly brackets on the right-hand sides of Eqs. (9) and (10) go to zero (see Eq. (13) and Fig. 2). However, now the third terms are nonzero; their value is determined by the difference $\Delta\lambda$ and the purely nonlocal contribution from the holes to the conductivity of the metal: $\Delta F_0^h = F_0^h(q_s) - F_0^h(0)$. Let us first consider the interaction of free carriers with the lattice in the field region $h \sim 1$ ($q_s \sim 1$). Since $\beta^2 \ll 1$, in this field region $\Delta F_0^h \approx \beta^2 q_s^2/2 \ll 1$ (see Fig. 2), and for reasonable values of $\Delta\lambda$ the third terms will also be relatively small. At low frequencies the first terms are also small. As a result, unlike the case for an uncompensated metal, the magnetoacoustic and doppleron–phonon resonances due to the interaction of the lattice with electrons (in this case majority carriers) will be weakly manifested in experiment. For $\lambda_{0e} \sim 1$ this interaction will be weak even at rather high frequencies.

The smallness of the third terms in (9) and (10) in the field region under discussion is to a certain degree due to the relatively weak deformational interaction of the lattice with holes. This is easily shown by considering, e.g., the structure of the expressions for the coefficients $g_{\pm}$ and $G_{\pm}$. For the deformation potential (7)

$$g_{\pm}^{e,h}, G_{\pm}^{e,h} \propto \{F_{\pm}^{e,h}(q) - \lambda_{e,h}[F_{\pm}^{e,h}(q) - F_{\pm}^{e,h}(0)]\}. \qquad (16)$$

The first terms on the right-hand side of Eq. (16) arise as a result of the induction interaction of free carriers with the lattice and are determined by the induction currents and forces acting on the lattice. The second terms are the result of the deformation interaction. For a compensated metal we have $g_{\pm} = g_{\pm}^e + g_{\pm}^h$, $G_{\pm} = G_{\pm}^e + G_{\pm}^h$ in (1). We see from (9) that the third term in the curly brackets consists of two terms, one of which, $\lambda_h \Delta F_0^h$, is directly related to the deformation terms in $g_{\pm}^h$ and $G_{\pm}^h$. The second term, $\lambda_e \Delta F_0^h$, arises in the summation of the total contribution of the electrons and the induction contribution of the holes. Consequently, we can conclude that the weakness of the interaction of the electron and ion subsystems of a compensated metal at low frequencies in fields with values in the vicinity of $h \sim 1$ is due, first, to compensation of the "electron" contribution to the inter-

action of the subsystems of the metal by the induction contribution of the holes, and, second, to the weakness of the deformation interaction of the lattice with minority carriers, in this case holes.

Let us now consider the field region $h \sim \beta$ and below. As we see from Eq. (13) and Fig. 2, as the field is decreased the purely nonlocal contribution of the holes to the conductivity increases ($\Delta F_0^h \to -\infty$). Accordingly, α_1 and α_2 increase in modulus. However, the competition of the terms singular at $h \sim \beta$ in the expressions for α_1 and α_2 and in the denominator of the first term on the right-hand side of Eq. (8) complicates the qualitative analysis. To clarify this, let us eliminate this competition by interchanging the indices e and h in Eqs. (8)–(10). As a result, the coefficients α_1 and α_2 will no longer be singular, since after interchanging the indices a factor $\Delta F_0^e = F_0^e(q) - F_0^e(0) \approx -1 \mp ih$ appears in the third terms in the curly brackets on the right-hand sides of (9) and (10). Now at small β one has $|\Delta F_0^e| \sim 1$ in fields $h \lesssim \beta$, and, depending on the value of $\Delta\lambda$ these terms can turn out to be relatively large. As a result, a situation arises which is analogous to that considered above in the uncompensated metal. At low frequencies the magnetoacoustic resonance due to the holes will be manifested in the absorption of sound in the form of a feature of the ''Kjeldaas edge'' type. Now, however, the character of the interaction of the free carriers with the lattice is determined mainly by the third terms rather than the second terms in (9) and (10). With increasing frequency this feature will be transformed into an asymmetric peak in fields below the resonance field $h = \beta$.

Illustrative quantitative analysis

Let us turn to an examination of the numerical results of equation (8) with the conductivity (13). The solutions will be obtained for a model metal with the parameters in (14), only now we can no longer neglect collisions. We shall show below that collisions can have a substantial influence on the shape of the manifestation of the DPR in fields $h > 1$. For the values of the rates ν we take the corresponding typical values for the mean free path of resonant electrons along **H**, $l_e = v_e/\nu$, equal to 0.2, 0.5 and 1.0 mm. There remain two unknown parameters—the constants of the deformation potential. We base our choice of values of λ_{0e} and λ_{0h} on the following considerations. In Eq. (7) m is the cyclotron mass. For a spherical Fermi surface of free electrons it is equal to the free electron mass m_0, and $\lambda_0 = 1$. It is known[24] that cadmium is among the metals for which the free-electron model gives a very realistic first approximation for the actual band structure and Fermi surface. In this approximation the Fermi surface is made up of portions of the free-electron spheres. We assume that on each of the portions, as in the case of a spherical Fermi surface, the relation $\lambda_0|m| \sim m_0$ holds. The electron ''lens'' in cadmium consists of two spherical segments. In the geometry of interest to us here, $\mathbf{k} \| \mathbf{H} \| [0001]$ the electron orbits are the circular orbits of free electrons. Therefore, there are grounds for assuming that for the electron Fermi surface $m_e \sim m_0$ and $\lambda_{0e} \sim 1$. The value of λ_{0e} will be varied in a certain interval including the ''special'' point $\lambda_{0e} = 1$. A qualitative analysis of the shape of the hole ''monster'' in cadmium and also the known data indicate that the averaged cyclotron mass of the holes is approxi-
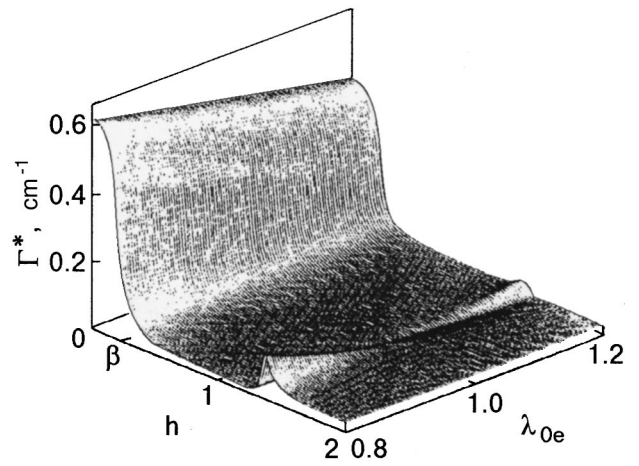

FIG. 3. $\Gamma^* = (k''_+ + k''_-)/2$ as a function of the dimensionless magnetic field h and the constant λ_{0e} (numerical solutions of (8) and (13), obtained for the parameters in (14) and $\lambda_{0h} = 3$, $\Omega = 0.59$ ($\omega/2\pi = 60$ MHz), and $\nu = 1.66 \times 10^9$ s^{-1} ($l_e = 0.2$ mm)).

mately one-third the value of m_0 in modulus. Consequently, $\lambda_{0h} \sim 3$ in the framework of our assumptions, and we have set $\lambda_{0h} = 3$ in the calculations.

The solutions of the dispersion relation are presented in the form of plots of $\Gamma^* = (k''_+ + k''_-)/2$ as a function of two variables: the dimensionless magnetic field h and a different one of the other variables each time. If the inequality $k''_\pm d \ll 1$ and $|\Delta k'_\pm d| \ll 1$, then the coefficient Γ^* is practically equal to the damping coefficient Γ of linearly polarized transverse sound. Here d is the thickness of the sample, and $\Delta k'_\pm = k'_\pm - k_s$.

Figure 3 shows the dependence of Γ^* on h and λ_{0e}. The most characteristic feature of this plot is the weak expression of the interaction of the lattice with the electrons. In particular, this is true for the interaction of electrons with sound due to the magnetoacoustic resonance in fields $h < 1$ [see also Fig. 6(a), in which the field value H_e corresponds to $h = 1$). Also of small amplitude is the anomaly observed in fields $h \sim 1.35$, which is due to the interaction of sound with the long-wavelength electron doppleron. It position corresponds to the position of the point D_e in Fig. 2 ($h = q_s^{-1}$). When λ_{0e} deviates from the critical value $\lambda_{0e} = 1$ the anomaly takes the form of an absorption peak, with an amplitude that increases as the deviation increases. This is due to the growth in modulus of the first term in the curly brackets on the right-hand side of (9). The second characteristic feature of the plot in Fig. 3 is the pronounced anomaly in the sound damping observed in fields $h \lesssim \beta$. This anomaly, which has the form of a ''Kjeldaas edge,''[11] is obviously due to the ''turning on'' of the collisionless resonance absorption of sound by holes.

Figure 4 shows the dependence of Γ^* on h and Ω (the range of variable of Ω corresponds to a frequency interval $\omega/2\pi \cong 50-200$ MHz). As in Fig. 3, in fields $h > 1$ one observes a feature due to the interaction of the sound with the electron doppleron. As the frequency increases, in agreement with the graphical solution of Eq. (15), the feature shifts in field toward the asymptotic value $h = 1$. Indeed, it is seen in Fig. 2 that as Ω increases, the point D_e shifts upward along the F_0 curve, approaching the asymptote $q_s^2 = 1$. At high frequencies the feature takes on the form of an absorption peak,
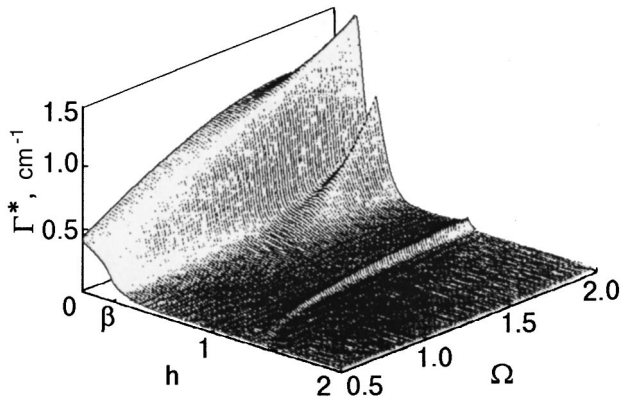
FIG. 4. $\Gamma^* = (k''_+ + k''_-)/2$ as a function of the dimensionless magnetic field h and the frequency Ω (numerical solutions of (8) and (13), obtained for the parameters in (14) and $\lambda_{0e} = 1.1$, $\lambda_{0h} = 3$, and $\nu = 1.66 \times 10^9$ s^{-1} ($l_e = 0.2$ mm)).

which is due to the growth of the first term in curly brackets on the right-hand side of (9). The anomaly observed in Fig. 4 at fields $h \lesssim \beta$, as in Fig. 3, is due to collisionless resonance absorption of sound by holes. As the frequency increases, this anomaly, which has the form of a ''Kjeldaas edge,'' [11] is transformed into an asymmetric peak in the field region below the resonance field $h = \beta$. In fields $h > \beta$ a strong absorption peak appears, which is the result of the interaction of sound with the short-wavelength hole doppleron. At a frequency $\Omega = 2.95$ its position corresponds to the position of the point D_h in Fig. 2 ($h = q_s^{-1}$).

We see that the given quantitative results are in good agreement in their most important details with the results of our qualitative analysis of the interaction of free carriers with the lattice. We should, however, make special mention of one of the most important results of this analysis, which we can confirm by a numerical calculation. As we have shown, the main reason for the weakness of the interaction of electrons (majority carriers) with the lattice at low frequencies is due to compensation effects, which are most clearly manifested in the smallness of the modulus of the second terms in curly brackets on the right-hand sides of (9) and (10). This compensation is maximum precisely in compensated metals, in which $N_h = N_e$. Figure 5 shows the numerical solutions of
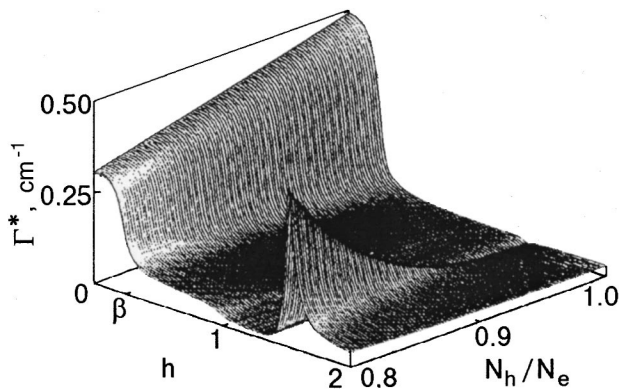

FIG. 5. $\Gamma^* = (k''_+ + k''_-)/2$ as a function of the dimensionless magnetic field h and the ratio N_h/N_e (numerical solutions of (8) and (13), obtained for the parameters in (14) and $\lambda_{0e} = 1.1$, $\lambda_{0h} = 3$, and $\nu = 1.66 \times 10^9$ s^{-1} ($l_e = 0.2$ mm)).
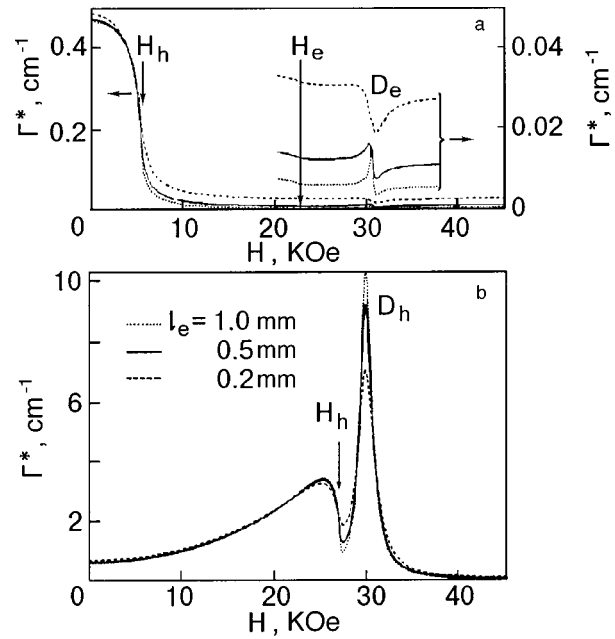

FIG. 6. $\Gamma^* = (k''_+ + k''_-)/2$ as a function of the magnetic field H (numerical solutions of (8) and (13), obtained for the parameters in (14) and $\lambda_{0e} = 1.1$, $\lambda_{0h} = 3$; a—$\Omega = 0.59$ ($\omega/2\pi = 60$ MHz); b—$\Omega = 2.95$ ($\omega/2\pi = 300$ MHz) and various values of the mean free path l_e.

equation (8) for different values of N_h/N_e. It is clearly seen that a quite small deviation of N_h/N_e from unity is sufficient to transform the anomaly D_e observed in fields $h > 1$ from a weak minimum (antiresonance) of the sound absorption to a pronounced absorption peak. This is clearly due to the growth in modulus of the second term in curly brackets on the right-hand side of (9) (in strong fields $F_{\pm} \approx 1 - N_h/N_e$), while the modulus of the third term, on the contrary, decreases.

Cadmium

Let us now turn to a quantitative analysis of the experimental results obtained in cadmium (Fig. 1). For this we choose values of λ_{0e} such that the experimental and calculated functions $\Gamma^*(h)$ are similar, particularly at 60 MHz (at 300 MHz we are interested in the field region $h \lesssim \beta$, since fields $h \sim 1$ were inaccessible in the experiment). A variation of λ_{0e} in a certain interval around the value $\lambda_{0e} = 1$ has a weak effect on the shape of $\Gamma^*(h)$ curve in this field region at high frequencies. This is clearly seen from (9) and (10) if in those expressions the indices e and h are interchanged.

Figure 6 shows the calculated dependence of Γ^* on the external magnetic field H, obtained at frequencies of 60 and 300 MHz for $\lambda_{0e} = 1.1$ and three values of l_e. The corresponding experimental curves are presented in Fig. 1. The field H_e (the ''Kjeldaas edge'' for electrons) corresponds to the field H_L in Fig. 1 and to $h = 1$ in Figs. 3 and 4, and the field H_h (the ''Kjeldaas edge'' for holes) corresponds to the field H_M in Fig. 1 and to $h = \beta$ in Figs. 3 and 4. The features D_e and D_h (D_L and D_M in Fig. 1) are due to the interaction of sound with the electron and hole dopplerons, respectively. We see that the curves $\Gamma^*(H)$ obtained for $l_e = 0.5$ mm are qualitatively similar to the experimental curves (quantitative measurements were not made in the experiment). However,

if an assessment can be based simply on a comparison of the ratios of the amplitudes of the features due to the magnetoacoustic resonance and the DPR at each of the frequencies, then the quantitative agreement of the calculation with experiment can be judged quite good as well. Of course, the choice of λ_{0e} is rather arbitrary. For example, we see that on the curve obtained for $l_e = 0.5$ mm the distance between the maximum and minimum of Γ^* in the neighborhood of the resonance D_e is approximately half that on the experimental curve. Better agreement is achieved for $l_e = 0.2$ mm and $\lambda_{0e} = 1.14$. For us, however, this is not of fundamental importance. Here we wanted to show, besides the overall qualitative agreement of the experimental result with the calculation, that there is one more interesting feature on the $\Gamma^*(H)$ curves that can appear in experiment.

Let us examine this feature. We see in Fig. 6(a) that collisions lead, first, to a ''smearing'' of the ''Kjeldaas edge'' for electrons. In Fig. 6(a) this is manifested as very weak kinks on the $\Gamma^*(H)$ curves at $H = H_e$. Second, they lead to a background damping of sound which at high fields $H > H_e$ is constant and proportional to the value of the relaxation rate ν. Against the background of this damping the shape of the resonance feature can be transformed as ν is increased. In Fig. 6(a) we see that for $l_e = 1$ mm this feature has the form of a peak or maximum, whereas for $l_e = 0.2$ mm it has taken on the form of a peak with a negative amplitude relative to the background, i.e., a minimum or antiresonance. The collective interaction of the free carriers with the lattice and, hence, the DPR are described by the first term on the right-hand side of (8). Restricting discussion to the relevant regime of weak coupling of the dopplerons with sound, we set $q = q_s$ on the right-hand side of (8). Then the denominator in this term can be rewritten in the form $[\Omega^2 h - F'_-(h)] - iF''_-(h)$, where $F''_-(h) > 0$ ($F'_- + iF''_- = F_-$). In fields $h > 1$ the function F''_- is proportional to ν. The question of the form of the functions $F'_\pm$ and $F''_\pm$ and of the correctness of the use of the weak coupling approximation have been discussed in detail in our previous paper.[25] Assuming that the inequality $q'' \ll q'$ holds ($q = q' + iq''$), the left-hand side of (8) can be written in the form $(q'^2 - q_s^2) + 2iq'q''$. The condition of DPR is that the difference $\Omega^2 h - F'_-$ go to zero. When collisions are taken into account, the expression in curly brackets on the right-hand side of (9) is complex-valued. We write it in the form $a + ib$. Then $\alpha_1 \propto (a^2 - b^2) + 2iab$. In typical cases $a^2 \gg b^2$, and the DPR will be manifested as a maximum of the sound absorption. However, as was shown above, in compensated metals the value of $|\alpha_1|$ can be very small. Then a situation arises in which, despite the smallness of the parameters γ_e and $|\gamma_h|$, the values of a^2 and b^2 are of the same order. Since $b \propto \nu$ in fields $h > 1$, at large values of ν the quantity $a^2 - b^2$ will change sign if the inequality $a^2 \gg b^2$ holds; then a minimum or antiresonance will be observed in the sound damping. An intermediate case arises for $a^2 \approx b^2$. It is this case that is realized in cadmium. In conclusion we note that the same situation can also arise in an uncompensated metal ($N_h = 0$) as the result of a competition between the first and second terms in curly brackets on the right-hand side of (9) (see Fig. 8 of Ref. 2).

CONCLUSION

In this paper we have analyzed the damping of transverse ultrasonic waves in normal and compensated metals due to both single-particle (magnetoacoustic resonance) and collective (doppleron–phonon resonance) interactions of free carriers with the lattice. The dispersion relation describing the interaction of the ion and electron subsystems of the metal has been obtained in a form (8) which is compact, transparent, and convenient for analysis. Equation (8) was obtained for a specific model of the deformation potential (7), but the shape of the Fermi surface was not specified. As a result, this equation can be used for any metal model with two groups of free carriers, holes are electrons, in any combination (ee, eh, he, hh). Here the ratio N_1/N_2 (where 1 and 2 stand for e or h) can be arbitrary. The main results of this study can be summarized as follows.

1. We have shown that in compensated metals a certain ''discrimination'' arises in respect to the majority carriers, particularly at low sound frequencies. Here it is not at all important whether those majority carriers are electrons or holes. This ''discrimination'' is manifested in a relatively weak interaction of the carriers of this group with the lattice at low frequencies as compared with the interaction of the lattice with the carriers of the other, minority group. This is due primarily to compensation effects, which are reflected in the smallness of the second and third terms in the curly brackets on the right-hand sides of (9) and (10). The compensation effects are most clearly manifested specifically in compensated metals. This is clearly seen in Fig. 5, which shows the results of a numerical solution of Eq. (8) for different values of N_h/N_e.

In strong fields the second terms in the curly brackets on the right-hand sides of (9) and (10) are always small in compensated metals on account of compensation effects. The smallness of the third terms in fields $h \sim 1$, as, for example, in the case of cadmium considered here, is due to the smallness of the purely nonlocal contribution to the conductivity from holes and, hence, to the smallness of the deformational interaction of the lattice with holes. It is clear that the quantity $|F^h_\pm(q) - F^h_\pm(0)|$ in fields $h \sim 1$ is determined by the value of β, which is small in cadmium (in cadmium $|\Delta F^h_\pm| \approx \beta^2/2$). In other compensated metals, however, it may not be so small. For example, in tungsten and molybdenum, in which one can also distinguish two groups of carriers[3,25–27] (the electrons of the ''jack,'' which comprise the majority group, and the holes of the ''octahedron''), the value of β is approximately twice as large as in cadmium ($\beta \sim 1/2$). As a result, the DPR, due to the interaction of sound with the electron doppleron, is manifested in experiment (unlike the case of cadmium) as a pronounced peak of the sound absorption, although the magnetoacoustic resonance, as the ''weaker'' resonance in this case, is, as before, hardly visible.

It should be noted that the relative weakness of the interaction of the majority carriers with the lattice is an inherent property of compensated metals regardless of the number of resonant groups of carriers. This is easily shown. Suppose a metal contains several groups of carriers. We number these groups and the corresponding parameters by the index i, setting $i = 1$ for the majority group. Transforming Eq. (1), we

obtain a version of Eq. (8) in which the first two terms in curly brackets on the right-hand sides of (9) and (10) remain as before (with the index e replaced by 1), while the third terms of the respective equations are replaced by the following sums:

$$\mp \sum_{i>1} (N_i/N_1)(\lambda_i - \lambda_1)[F_{\pm}^{(i)}(q) - F_{\pm}^{(i)}(0)] \tag{17}$$

and

$$\pm \sum_{i>1} (N_i/N_1)(\lambda_i - \lambda_1)^2[F_{\pm}^{(i)}(q) - F_{\pm}^{(i)}(0)]. \tag{18}$$

In (17) and (18) the summation is over all the minority groups of carriers. We see that increasing the number of groups leads only to an increase in the number of terms in (17) and (18), these terms being of the same type and proportional to the purely nonlocal contributions to the conductivity from the carriers of these groups. Consequently, all of the conclusions reached in our qualitative analysis of the interaction of the electron and ion subsystems in a compensated metal with two groups of carriers will remain valid.

2. Under conditions that can arise in compensated metals in a particular experiment, the value of $|\alpha_1|$ in (9) may turn out to be very small. In that case, depending on the values of ν and the other parameters, the shape with which the DPR, which is due to the interaction of sound with the majority carriers, is manifested in the absorption can be extremely unusual. This is clearly seen in the case of cadmium, for example. Interestingly, from the standpoint of the understanding we have gained, it is surprising that this was the metal in which the DPR due to the interaction of sound with the long-wavelength doppleron was first detected.[4] The compensation effects in the interaction of the ion and electron subsystems of a metal are very pronounced in cadmium, since the constant of the deformation potential $\lambda_{0e} \sim 1$ and the parameter β is relatively small. However, these effects are also manifested clearly in other compensated metals. In particular, we have previously[28] investigated the damping of sound in tungsten as a function of the magnetic field H and the angle θ between the direction of **H** and the [001] axis. This experiment revealed a large number of resonance features. As the angle θ was varied, some of them were transformed from a feature having the form of a maximum of the sound damping into a step and then into an antiresonance. It is perfectly clear that this transformation can be interpreted as being a result of the compensation effects indicated above. Like the transformation of the shape of the sound absorption curves observed in Fig. 6(a), this transformation can be explained by a change in the sign of the difference $a^2 - b^2$. Now, however, this sign change is due not to a change in ν but to a change in the Landau magnetic damping. This damping is manifested in the appearance of dissipative terms, approximately proportional to $\sin^2 \theta$, in the conductivity.[29]

*E-mail: tsymbal@host.dipt.donetsk.ua

[1] L. T. Tsymbal, A. N. Cherkasov, and O. F. Panchenko, Fiz. Nizk. Temp. **24**, 1157 (1998) [Low Temp. Phys. **24**, 868 (1998)].

[2] L. T. Tsymbal, A. N. Cherkasov, and O. F. Panchenko, Fiz. Nizk. Temp. **25**, 876 (1999) [Low Temp. Phys. **25**, 656 (1999)].

[3] T. F. Butenko, V. T. Vitchinkin, A. A. Galkin, A. M. Grishin, V. A. Mishin, L. T. Tsymbal, and A. N. Cherkasov, Zh. Éksp. Teor. Fiz. **78**, 1811 (1980) [Sov. Phys. JETP **51**, 909 (1980)].

[4] L. T. Tsymbal and T. F. Butenko, Solid State Commun. **13**, 633 (1973).

[5] R. C. Jones, R. G. Goodrich, and L. M. Falicov, Phys. Rev. **174**, 672 (1968).

[6] L. M. Fisher, V. V. Lavrova, V. A. Yudin, O. V. Konstantinov, and V. G. Skobov, Zh. Éksp. Teor. Fiz. **60**, 759 (1971) [Sov. Phys. JETP **33**, 410 (1971)].

[7] V. P. Naberezhnikh, D. E. Zherebchevskii, L. T. Tsymbal, and T. M. Yeryomenko, Solid State Commun. **11**, 1529 (1972).

[8] L. P. Volkova, L. T. Tsymbal, A. N. Cherkasov, Fiz. Nizk. Temp. **9**, 1262 (1983) [Sov. J. Low Temp. Phys. **9**, 649 (1983)].

[9] L. P. Volkova, Candidate's Dissertation [in Russian], Donetsk (1984).

[10] N. G. Burma, T. F. Butenko, A. M. Grishin, and L. T. Tsymbal, Fiz. Nizk. Temp. **7**, 1070 (1981) [Sov. J. Low Temp. Phys. **7**, 521 (1981)].

[11] T. Kjeldaas, Phys. Rev. **113**, 1473 (1959).

[12] S. V. Medvedev, V. G. Skobov, L. M. Fisher, and V. A. Yudin, Zh. Éksp. Teor. Fiz. **69**, 2267 (1975) [Sov. Phys. JETP **42**, 1152 (1975)].

[13] D. E. Muller, Math. Tables and Other Aids to Comput. **10**, 208 (1956).

[14] V. G. Skobov and É. A. Kaner, Zh. Éksp. Teor. Fiz. **46**, 273 (1964) [Sov. Phys. JETP **19**, 189 (1964)].

[15] V. M. Kontorovich, Zh. Éksp. Teor. Fiz. **45**, 1638 (1963) [Sov. Phys. JETP **18**, 1125 (1964)]; **59**, 2116 (1970) [**32**, 1146 (1971)]; **61**, 1181 (1971) [**34**, 630 (1972)].

[16] J. Mertsching, Phys. Status Solidi B **14**, 3 (1966); **37**, 465 (1970).

[17] V. M. Kontorovich, Usp. Fiz. Nauk **142**, 265 (1984) [Sov. Phys. Usp. **27**, 134 (1984)].

[18] A. M. Grishin, Doctoral Dissertation [in Russian], Donetsk (1983).

[19] D. S. Falk, B. Gerson, and J. F. Carolan, Phys. Rev. B **1**, 406 (1970).

[20] P. D. Hambourger and J. A. Marcus, Phys. Rev. B **8**, 5567 (1973).

[21] O. V. Konstantinov, V. G. Skobov, V. V. Lavrova, and L. M. Fisher, Zh. Éksp. Teor. Fiz. **63**, 224 (1972) [Sov. Phys. JETP **36**, 118 (1973)].

[22] V. L. Gurevich, I. G. Lang, and S. T. Pavlov, Zh. Éksp. Teor. Fiz. **59**, 1679 (1970) [Sov. Phys. JETP **32**, 914 (1971)].

[23] A. M. Grishin, V. G. Skobov, L. M. Fisher, and A. S. Chernov, JETP Lett. **35**, 455 (1982).

[24] A. P. Cracknell and K. C. Wong, *The Fermi Surface*, [Clarendon Press, Oxford (1973); Atomizdat, Moscow (1978)].

[25] L. T. Tsymbal and A. N. Cherkasov, Fiz. Nizk. Temp. **24**, 250 (1998) [Low Temp. Phys. **24**, 189 (1998)].

[26] A. A. Galkin, L. T. Tsymbal, and A. N. Cherkasov, JETP Lett. **33**, 1 (1981).

[27] A. N. Cherkasov, Candidate's Dissertation [in Russian], Donetsk (1983).

[28] L. P. Volkova, L. T. Tsymbal, and A. N. Cherkasov, Fiz. Nizk. Temp. **9**, 1262 (1983) [Sov. J. Low Temp. Phys. **9**, 649 (1983)].

[29] É. A. Kaner, V. G. Skobov, Zh. Éksp. Teor. Fiz. **46**, 1106 (1964) [Sov. Phys. JETP **19**, 749 (1964)]

Translated by Steve Torstveit

LOW DIMENSIONAL AND DISORDERED SYSTEMS

Magnetomechanics of mesoscopic wires

S. Blom*

*Department of Applied Physics, Chalmers University of Technology and Göteborg University,
SE-412 96 Göteborg, Sweden*

We have studied the force in mesoscopic wires in the presence of an external magnetic field along the wire, using a free electron model. We show that the applied magnetic field can be used to affect the force in the wire. The magnetic field breaks the degeneracy of the eigenenergies of the conduction modes, resulting in more structure in the force as a function of wire length. The use of an external magnetic field is an equilibrium method of controlling the number of transporting channels. Under the least favorable circumstances (on the middle of a low conduction step) one needs about 1.3 T to see an abrupt change in the force at fixed wire length for a mesoscopic bismuth wire. © *2000 American Institute of Physics.* [S1063-777X(00)01006-9]

1. INTRODUCTION

The electrical conductance in a ballistic wire with dimensions comparable to the Fermi wave-length increases in steps of $G_0 = 2e^2/h$ as the cross section increases. This conductance quantization is observable at room temperature in metallic nanowires formed by pressing two pieces of metal together into a metallic contact. When the two pieces are separated, the contact is stretched into a nanowire, a wire of nanometer dimensions. Several experiments varying this principle have been performed, e.g., using scanning tunneling microscopy,[1] mechanically controlled break junctions,[2] or just plain macroscopic wires.[3] Although most nanowire experiments have been performed on metals, conductance quantization has been seen in bismuth at 4 K.[4] Since bismuth has a Fermi wavelength $\lambda_F = 26$ nm,[4] these semimetal ''nanowires'' are larger than the metallic nanowires.

The stepwise variation of the conductance in such a mesoscopic wire is accompanied by an abrupt change of the force in the wire.[5] Using a free-electron model, neglecting all atomic structure of the wire, it has been shown[6–9] that the size of the electronic contribution to the force fluctuations is comparable to the values found experimentally and that the qualitative behavior, i.e., the abrupt change that accompanies the conductance steps, is the same.

In the wire the transverse motion of the electrons gives rise to quantized modes α of energy E_α. In the simplest version of the Landauer formalism, a mode is considered fully transmitting (open) if $E_F > E_\alpha$ and closed otherwise.[10] Each open mode contributes an amount e^2/h to the conductance, if modes with different spin are considered separately. As the wire is elongated and the cross section decreases, more and more modes are pushed above the Fermi level and closed, thus decreasing the conductance stepwise. This has been shown in two dimensions[11] and in three dimensions.[12]

It has been suggested[13] that the conductance and the mechanical force in a nanowire can be controlled by an applied driving voltage. This effect originates from the injection of additional electrons with voltage-dependent energy, because of the different chemical potentials of the two reservoirs. Since a relatively large applied voltage is needed, one will have to worry about heating in this case.

The eigenenergies of the transverse motion can be affected by an external magnetic field B perpendicular to the cross section of the wire. This will show up in the conductance and in the force as a function of B. The effect of magnetic field on the conductance was considered in Ref. 14. To use an external magnetic field is an equilibrium method of controlling the number of transporting channels, without significant risk of relaxation.

Because of band bending, due to the small size of the wire, the eigenenergies will have to be corrected. This can, however, be taken care of by introducing an effective Fermi energy $\tilde{E}_F$ in the wire. Assuming that the number of electrons (per unit volume) is constant, $\tilde{E}_F$ can be determined self-consistently and will vary with wire length and magnetic field.

In this paper we present force calculations for different applied magnetic fields and wire lengths, using a free-electron model. We take into account the effect of band bending, adjusting the Fermi energy in the wire. In order to resolve any effect for moderate magnetic fields, a low cyclotron effective mass (which enters in the cyclotron frequency) is needed, which can be found in semimetals. Metals are less favorable since, because of a larger cyclotron effective mass (larger Fermi energy), we would need a larger magnetic field in order to resolve any effect. For numerical estimates we have used values for bismuth, a typical semimetal. For bismuth the spin splitting is also important, since bismuth has a large spectroscopic spin splitting factor g.

2. MODEL

We consider a cylindrical ballistic wire of length L with circular cross section and a parabolic confining potential

$$\omega(r) = \frac{\omega_0^2 m^* r^2}{2} \equiv E_F \frac{r^2}{R^2}, \tag{1}$$

using cylindrical coordinates (r, φ, z); here m^* is the effective electron mass. The wire is along the z direction. The last equality in Eq. (1) defines ω_0. In this equation E_F is the zero-B-field bulk value, yielding a magnetic-field-independent confining potential. We assume that the volume $V = \pi R^2 L$ of the wire is kept constant during elongation, which makes R and L mutually dependent.

With the above confining potential and an applied magnetic field along the wire, the Schrödinger equation was solved in Ref. 15. If also spin is included, the eigenenergies are

$$E_\alpha = \hbar \left(\frac{\omega_c^2}{4} + \omega_0^2 \right)^{1/2} n + \frac{1}{2} l \hbar \omega_c + s g \mu_B B, \tag{2}$$

$$n = 2m + |l| + 1, \quad m = 0, 1, 2, ...,$$

$$l = 0, \pm 1, \pm 2, ..., \quad s = \pm 1/2, \quad \alpha = \{m, l, s\},$$

where $\omega_c = eB/m^*$ is the cyclotron frequency; μ_B is the Bohr magneton: $sg\mu_B$ is the magnetic moment associated with the electron spin.

Since our system is open, the electronic contribution to the force in the wire is given by the derivative of the grand potential $\Omega = E - \mu N$ with respect to elongation. Here E is the total energy of the electrons in the wire, μ is the chemical potential, and N is the number of electrons in the wire. If the Fermi energy E_F is much higher than the thermal energy (as in metals or at low temperature), we have $\mu \approx E_F$. The grand potential is then[9]

$$\Omega(E_F) = -\sum_\alpha \frac{4}{3} L \left(\frac{2m^*}{\pi^2 \hbar^2} \right)^{1/2} (E_F - E_\alpha)^{3/2}, \tag{3}$$

where the sum is over all open modes. The force in the wire is given by

$$F = -\frac{\delta \Omega}{\delta L}, \tag{4}$$

which in general has to be calculated numerically.

The magnetic field affects the system primarily by splitting the otherwise degenerate eigenenergies of the conduction modes [Eq. (2)]. Since then the conduction modes will open one-by-one, this will cause more structure in the force and conductance when displayed as functions of wire length. Subsequently, when applying an external magnetic field we will see the (clearest) effect when the highest open level or the lowest closed level goes through the Fermi level (whichever happens first). If one does not adjust the Fermi energy for band bending but uses the bulk Fermi energy for zero magnetic field, one can analytically calculate the B field needed when the wire is kept at a specified length. The least favorable situation would be on the middle of a conduction step.

3. RESULTS AND DISCUSSION

We have used numerical values for bismuth, a typical semimetal with $E_F = 25$ meV.[4] Bismuth has an anisotropic Fermi surface resulting in different effective masses in dif-
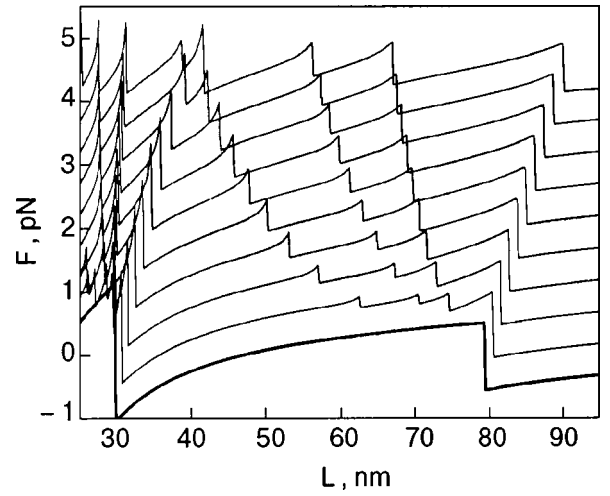

FIG. 1. The force in a mesoscopic wire as a function of wire length for different magnetic fields. The lowest, heavy, curve is for $B = 0$. The next curves, each displaced by 0.5 pN, are for $B = 0.5$; 1T etc., the uppermost curve being for $B = 4.5$ T. The splitting of the eigenenergies of the conduction modes is clearly visible: for larger B fields the curves have more structure, since now each mode closes one-by-one as the wire is elongated. We have used a spectroscopic splitting factor $g = 20$ and an effective Fermi energy $\tilde{E}_F$.

ferent directions, between $0.009 m_e - 1.8 m_e$ (Ref. 16). The cyclotron effective mass is in the range $0.009 m_e - 0.13 m_e$ (Ref. 16). For an isotropic Fermi surface and a quadratic dispersion relation, both effective masses are the same: $m^* = 0.07 m_e$ for $E_F = 25$ meV. The spectroscopic splitting factor g can be as high as 260 or an order of magnitude smaller, depending on the direction of the magnetic field.[17] For $g = 20$ the spin splitting is roughly of the same order as the Landau level distance, and becomes dominant for g as large as 200. We have used $g = 20$. The wire volume was kept constant at 30 000 nm[3] (Ref. 3).

To find the effective Fermi energy of the wire we have adjusted the value in order to keep the number of electrons constant, with a tolerance of $10^{-4}\%$.

Figure 1 shows the force in the wire as a function of wire length for different magnetic fields. For nonzero fields the force curves show more structure, since now the eigenenergies of the conduction channels are nondegenerate and close one-by-one, each time resulting in a sharp change of the force.

The force and conductance for two particular magnetic fields, $B = 0$ and 2.5 T, are shown in Fig. 2. Each step in the conductance is accompanied by an abrupt change in the force. We also show the corresponding picture for the simplest possible case[9] when we use the bulk value of the Fermi energy, E_F, in Fig. 3. In this case the force is one order of magnitude smaller than in the more realistic case with $\tilde{E}_F$. This is because the effective Fermi energy has to be larger then the bulk value in order to keep the number of electrons per unit volume in the wire constant in spite of the quantization of levels. Also, the conduction modes close much later in the $\tilde{E}_F$ case than in the simpler case when the wire is elongated. The reason for this is that the effective Fermi energy, as a function of wire length, follows each eigenenergy before intercepting it and closing the channel.

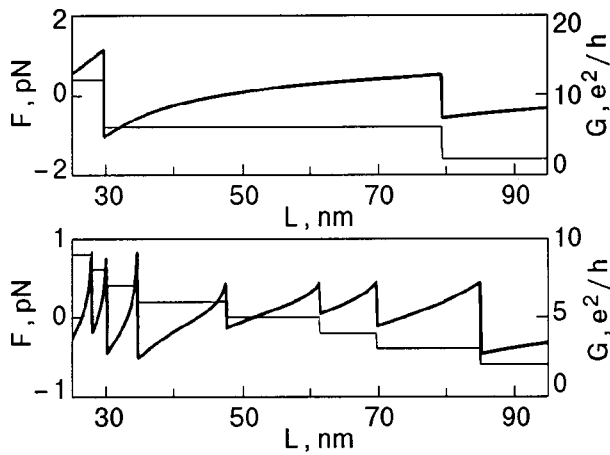On the middle of the second conduction step (G

FIG. 2. The force (heavy curve) and the conductance in a mesoscopic wire for two different magnetic fields: in the upper figure $B=0$, and in the lower figure $B=2.5$ T. We clearly see that the abrupt change in the force happens when a channel closes, i.e., when there is a step in the conductance. We have used an effective Fermi energy $\tilde{E}_F$.

FIG. 4. In the upper figure we show the force (heavy curve) and conductance for $L=54.6$ nm. This length corresponds to the middle of the second conduction step. In the lower figure we show the eigenenergies of the second conduction step and the effective Fermi energy of the wire (heavy curve). We see that when the highest level goes through the Fermi level (for approximately $B=1.3$ T) there is a step in the conductance and an abrupt change in the force.

$=3G_0$, $n=2$) the circumstances are least favorable to see the effect of the magnetic field. For the case with the zero-B-field bulk value of the Fermi energy ($L=19.8$ nm), we have analytically calculated that one needs $B=2.4$ T in order to see the highest open level go through the Fermi energy, thus giving a sharp change in the force as well as in the conductance. For higher conduction modes one will see the effect for smaller fields, since the splitting is proportional to l, whose absolute maximum is equal to n.

In Fig. 4 we see the force and the conductance as a function of magnetic field for a fixed wire length, $L=54.6$ nm. This is for the case with an effective wire Fermi energy and a length corresponding to the middle of the second conduction step ($G=3G_0$, $n=2$). We see that we need about 1.3 T before the highest open level goes through the Fermi surface, showing us the pronounced effect of the magnetic field. In the lower part of the same figure we also see the effective Fermi energy (thick line) and the eigenenergies of the second conduction steps. Notice how the Fermi level

increases with the eigenenergy before it intercepts. However, these variations are small compared to the overall magnitude of the Fermi energy.

So far we have used a spectroscopic splitting factor $g=20$. In Fig. 5 we show the force as a function of length for $B=1$ T for different g factors: $g=0$, 2, 20, and 200. For $g=0$ there is no spin splitting, but we still see more structure than for $B=0$ (cf. Fig. 1). This is due to the breaking of the degeneracy into the Landau levels. With increasing g factor the spin splitting becomes larger and larger; however, whatever the size of the spin splitting, more structure appears in the force with an applied magnetic field.

The Fermi energy of the bulk will also be affected by the magnetic field, due to the de Haas–van Alphen effect. In the
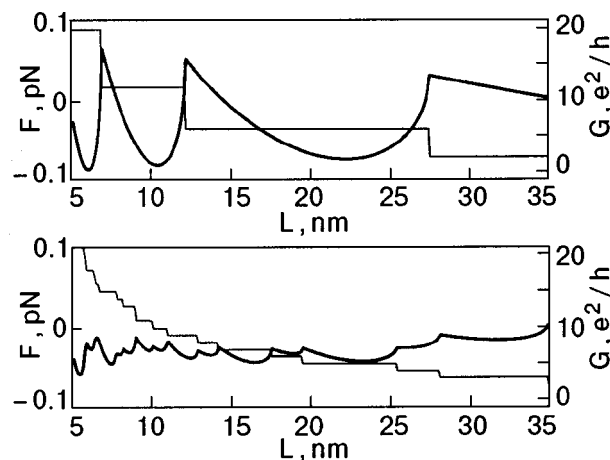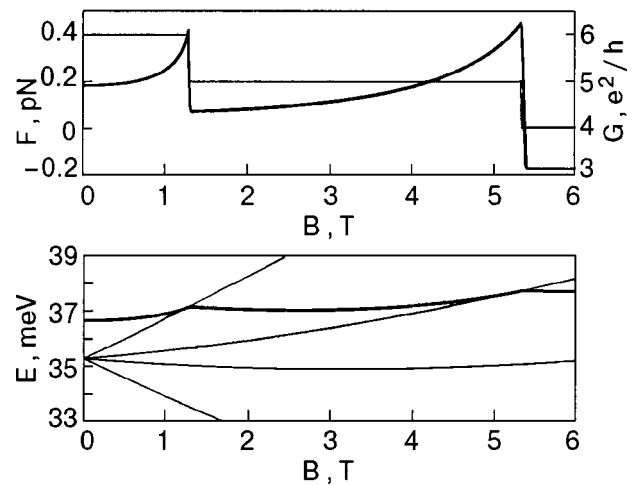

FIG. 3. The force (thick line) and the conductance in a mesoscopic wire for the less realistic case of a constant Fermi energy in the wire equal to the zero-B-field bulk value (25 meV). Results for two different magnetic fields are shown; in the upper figure $B=0$, and in the lower figure $B=2.5$ T.
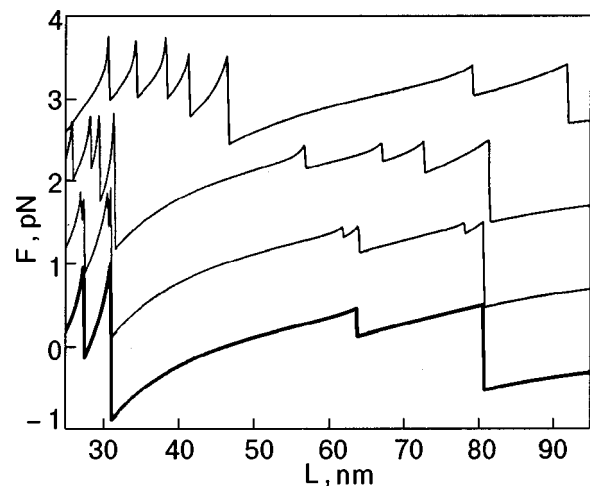

FIG. 5. Force as a function of length for $B=1$ T for different g factors. The lowest curve is for $g=0$, and the following curves, each displaced by 1 pN, are for $g=2$, 20, and 200, respectively. We see that no matter what the g factor is, an external magnetic field will give the force curves more structure than for $B=0$ (cf. Fig. 1).

case when an effective Fermi energy $\widetilde{E}_F$ is used, this does not affect the results, since the bulk Fermi energy does not enter into the calculations. When the bulk Fermi energy is adjusted for de Haas–van Alphen effect, in the simpler case shown in Fig. 3 there is no significant change of the force. We have also studied the influence of a moderate applied voltage (in the mV range) but have seen no significant effect.

For metals the Fermi energy is in the eV range, demanding much higher magnetic fields to resolve results similar to those for bismuth above. Since the size of the splitting is proportional to the number of open channels, having more channels will decrease the magnetic field needed. Therefore, if we design the circumstances to be more favorable, i.e., having more open channels and being close to a conduction step, a moderate magnetic field will be enough to make an eigenenergy go through the Fermi level, thus giving an effect in the force and in the conductance.

4. CONCLUSION

Using a free-electron model, we have shown that the force in a mesoscopic wire can be affected by an external magnetic field parallel to the wire. With a magnetic field present the degenerate eigenenergies of the conduction modes split and become conducting (open) at different elongations, resulting in more force fluctuations with increasing wire length. At fixed wire length we propose that applying an external magnetic field is an equilibrium method that can be used to affect the force as well as the conductance in mesoscopic wires. Since no atomic rearrangement is required (contrary to elongation experiments) in an experiment along these lines, it may give new insight into the nature of the intrinsic mechanical properties of these wires.

[*]E-mail: sara@fy.chalmers.se

[1] J. I. Pascual, J. Méndez, J. Gómez-Herrero, A. M. Baró, N. Garcia, and Vu Thien Binh, Phys. Rev. Lett. **71**, 1852 (1993).
[2] C. J. Muller, J. M. van Ruitenbeek, and L. J. de Jongh, Phys. Rev. Lett. **69**, 140 (1992).
[3] J. L. Costa-Krämer, N. Garcia, P. Garcia-Mochales, and P. A. Serena, Surf. Sci. **342**, L1144 (1995).
[4] J. L. Costa-Krämer, N. Garcia, and H. Olin, Phys. Rev. Lett. **78**, 4990 (1997).
[5] G. Rubio, N. Araït, and S. Viera, Phys. Rev. Lett. **76**, 2302 (1996).
[6] C. A. Stafford, D. Baeriswyl and J. Bürki, Phys. Rev. Lett. **79**, 2863 (1997).
[7] J. M. van Ruitenbeek, M. H. Devoret, D. Esteve, and C. Urbina, Phys. Rev. B **56**, 12567 (1997).
[8] Constantine Yannouleas and Uzi Landman, J. Phys. Chem. B **101**, 5780 (1997).
[9] S. Blom, H. Olin, J. L. Costa-Krämer, N. Garcia, M. Jonson, P. A. Serena, and R. Shekhter, Phys. Rev. B **57**, 8830 (1998).
[10] T. Dittrich, P. Hänggi, G.-L. Ingold, B. Kramer, G. Schön, and W. Zwerger, *Quantum Transport and Dissipation*, Wiley-VCH, Weinheim (1998).
[11] L. I. Glazman, G. B. Lesovik, D. E. Khmelnitskii, and R. I. Shekhter, JETP Lett. **48**, 239 (1988).
[12] E. N. Bogachek, A. N. Zagoskin, and I. O. Kulik, Sov. J. Low Temp. Phys. **16**, 796 (1990).
[13] Alexandre M. Zagoskin, Phys. Rev. B **58**, 15827 (1998).
[14] E. N. Bogachek, A. G. Scherbakov, and Uzi Landman, Phys. Rev. B **56**, 14917 (1997).
[15] C. T. Liu, K. Nakamura, D. C. Tsui, K. Ismail, D. A. Antoniadis, and Henry I. Smith, Appl. Phys. Lett. **55**, 168 (1989).
[16] J. K. Galt, W. A. Yager, F. R. Merritt, B. B. Cetlin, and A. D. Brailsford, Phys. Rev. **114**, 1396 (1959).
[17] M. H. Cohen and E. I. Blount, Philos. Mag. **5**, 115 (1960).

Hot electrons in nanocontacts

S. I. Kulinich, R. I. Shekhter, and I. V. Krive*

*Department of Applied Physics, Chalmers University of Technology and Göteborg University,
SE-412 96 Göteborg, Sweden*

S. I. Kulinich and I. V. Krive

*B. Verkin Institute for Low Temperature Physics and Engineering, National Academy of Sciences
of Ukraine, pr. Lenina 47, 61164 Kharkov, Ukraine*

A theoretical study is made of the temperature of the electron subsystem in a microcontact as a
function of the applied voltage. It is shown that in microcontacts whose characteristic
linear dimension is of the order of several lattice constants (nanocontacts) a breakdown of
thermodynamic equilibrium between the electrons and phonons occurs at high applied voltages.
Then the temperature of the electron subsystem is a linear function of the applied voltage,
and its absolute magnitude can reach values of the order of the Fermi energy. These results agree
with recent experimental data. © *2000 American Institute of Physics.* [S1063-777X(00)01106-3]

INTRODUCTION

In normal metals the electric current is transported by electrons whose energy relaxes mainly through electron–phonon collisions. This means that the electron and phonon subsystems in metals are found in conditions of thermodynamic equilibrium, and therefore, the electron temperature, even at high applied voltages, cannot appreciably (by an order of magnitude) exceed the Debye temperature without causing substantial structural changes.

In experiments[1,2] investigating the glow of metallic nanocontacts an unusual effect was observed: an anomalously strong overheating of the electron subsystem at high voltages (1.5–2 V) applied to a nanocontact. By analysis of the emission spectrum it was established that the electron temperature in the nanocontact had reached the Fermi energies (0.7–1 eV) and increased linearly with increasing voltage. In spite of the fact that the measured electron temperature significantly exceeded the melting temperature of the lattice, no significant structural changes in the sample were observed.

These experiments raise an important question: under what conditions will the phonons not affect the charge and heat transport in metallic microcontacts, and what parameters will control the electron temperature in that case?

The problem of creating a highly nonequilibrium state with respect to temperature between the electron and phonon subsystems in metals has been studied for quite some time.[3,4] Although a situation in which each of the subsystems is described by its own temperature can arise even in macroscopic samples, under ordinary conditions a strong departure from equilibrium cannot be achieved. The possibility of a strong heating of the electrons in thin metallic films and granules was discussed in Refs. 5 and 6, and the general conclusion was that the quantization of the electron energy levels effectively suppresses the electron–phonon interaction and can thus make it possible to destroy the thermodynamic equilibrium between the electrons and phonons.

Micro- and nanocontacts are considerably more attractive objects for implementing this possibility. As we know,[7] the mean free path of an electron in the case when the electron and phonon subsystems are in thermodynamic equilibrium is a sharp function of the the temperature, $l_{ep}(T) \sim T^{-3}$, at low temperatures $T \ll T_D = \hbar\omega_D$ ($\omega_D = s\pi/a$ is the Debye frequency, s is the speed of sound, and a is the lattice period), and for $T \gtrsim T_D$ it goes over to a smoother dependence $l_{ep}(T) \sim \hbar v_F/T$. For microcontacts the condition of thermodynamic equilibrium between the electrons and phonons is violated, and for estimating the minimum electron–phonon relaxation length $l_i^{(\text{ph})}$ the lattice can be considered cold. Simple estimates analogous to those made in Ref. 7 show that if the energy of the electrons in the contact exceeds the Debye energy (as in the experiments discussed here) and all of the phonon modes are involved in the energy relaxation of the electron, then the ''phononic'' mean free path of the electrons ceases to depend on energy and becomes equal to $l_i^{(\text{ph})} \sim a(v_F/s) \gg a$ (for an electron–phonon interaction constant $\gamma_{ep} \sim 1$). Thus for microcontacts with a length $d < l_i^{(\text{ph})}$ the electron–phonon interaction occurs far from the region of the microconstriction, in the peripheral region of the contact, where heating of the lattice occurs. Since the fraction of ''hot'' electrons in this region is relatively small, the establishment of thermodynamic equilibrium between the electrons and phonons in the peripheral regions does not lead to melting of the lattice.

Thus for metallic contacts of small dimensions (nanocontacts) the electron–phonon interaction cannot bring about relaxation of the electron energy within the contact region, and if it were not for electron–electron collisions, the charge transport in such a system would be phase-coherent. As we know, for $T \ll \varepsilon_F$ the probability of electron–electron collisions is strongly suppressed by the Pauli principle, and therefore for ''cold'' electrons (i.e., electrons with a temperature $T \ll T_D \sqrt{\varepsilon_F/T_D}$) and at low voltages $eU \ll T$ the ''electronic'' relaxation length $l_{ee}(T) \sim \varepsilon_F \hbar v_F/T^2$ turns out to be

larger than the analogous phononic length. In this case the transport of change and heat through the contact are described by the Landauer–Buttiker theory (see, e.g., Ref. 8), and the electron temperature is determined by the average temperature of the peripheral regions of the contact.

To explain the results of the experiments[1,2] we shall assume that both the momentum and energy relaxation of the electrons occurs within the microconstriction (thermal transport regime). This case is always realized at high temperatures $T \sim \varepsilon_F$ (plasma limit), when the electronic relaxation lengths become of the same order as the interatomic distance. For degenerate electron statistics, $T \ll \varepsilon_F$ (metallic limit) the electron collisions can also form a thermal transport regime if the voltage applied to the contact is sufficiently high, $eU \gg \sqrt{\hbar v_F \varepsilon_F / d} \gg T_D \sqrt{\varepsilon_F / T_D}$ (we note that in the experiments of Refs. 1 and 2 anomalous heating of the electrons was observed only at high applied voltages).

The thermal transport regime in microcontacts was first studied in Refs. 9 and 10, in which only the case of ''low'' temperatures, $T \ll \varepsilon_F$, was considered. Since the temperatures recorded in the experiments[1,2] were of the order of ε_F, it seems advisable to do additional studies of the plasma limit $T \gg \varepsilon_F$. That is our goal in the present paper. (The plasma limit for an electron–phonon mechanism of electron heating in a microcontact between semiconductors was also investigated in Ref. 11). We have shown that for $T \gg \varepsilon_F$ the problem also admits an analytical solution and we have found an explicit expression for the maximum temperature T_m of the contact as a function of the applied voltage. A comparison of the formulas obtained in the metallic and plasma limits, after extrapolation to the region $T \sim \varepsilon_F$, with the experimental data suggests that the anomalously strong overheating of the electron subsystem observed in Refs. 1 and 2 can be well explained by the existing theory of charge and heat transport through microcontacts.

THERMAL TRANSPORT REGIME FOR ELECTRONS IN MICROCONTACTS

In the thermal regime of charge transport through a microcontact[9,10] both the momentum and energy of the electrons relax within the region of the microconstriction. In this case the equations governing the thermal and electrical characteristics of the contact are the continuity equations expressing the conservation laws for the energy and number of particles:

$$\text{div}\,\mathbf{j} = 0; \quad \text{div}\,\mathbf{q} = 0, \tag{1}$$

where the electrical current density $\mathbf{j}$ and total energy flux density $\mathbf{q}$ have the form[12,13]

$$\mathbf{j} = \sigma(T)\left[-\nabla\varphi - \frac{T}{e}\nabla\frac{\mu}{T} + \lambda(T)\nabla T \right],$$

$$\mathbf{q} = -\kappa(T)\nabla T - [\varphi - \lambda(T)T]\mathbf{j}. \tag{2}$$

Here φ is the electrostatic potential, e is the electron charge, and μ is the chemical potential. The temperature dependence of the coefficients σ, κ, and λ is found from the solution of the kinetic equation and can be written as

$$\sigma(T) = -eI_1(T); \quad \lambda(T) = -\frac{1}{eT}\frac{I_2(T)}{I_1(T)},$$

$$\kappa(T) = -\frac{1}{eT}\left[I_3(T) - \frac{I_2^2(T)}{I_1(T)} \right], \tag{3}$$

where

$$I_n(T) = \frac{2e}{3m}\int \frac{d^3p}{(2\pi\hbar)^3}\,\varepsilon^n \tau_i(\varepsilon)\frac{\partial f_0}{\partial\varepsilon}. \tag{4}$$

Here $f_0(\varepsilon)$ is the equilibrium (Fermi) distribution function, and $\tau_i(\varepsilon)$ is the relaxation time. For contacts with lengths shorter than the electron–phonon mean free path, and $\tau_i(\varepsilon)$ is determined by electron–electron collision processes. In the voltage region of interest to us here, $eU \gg T_D\sqrt{\varepsilon_F/T_D}$ it is just these processes that promote the rapid relaxation of the electron energy and lead to anomalously strong heating of the electron subsystem.

The temperature dependence of the chemical potential $\mu(T)$ is determined from the condition of conservation of the total number of particles. For metals the condition of electrical neutrality guarantees that this relation will be satisfied in both the cases of weak ($T \ll \varepsilon_F$) and strong ($T \gg \varepsilon_F$) heating.

The system of equations (1)–(3) must be supplemented by boundary conditions. For a microcontact the natural boundary conditions are the absence of heat and charge transport through the boundary of the contact:

$$j_n(\mathbf{r}\in\Sigma) = q_n(\mathbf{r}\in\Sigma) = 0, \tag{5}$$

where $\mathbf{n}$ is the normal to the boundary Σ of the microcontact. Furthermore, for a symmetric contact we have

$$\varphi(z\to\pm\infty) = \frac{U}{2}\,\text{sgn}(z); \quad T(z\to\pm\infty) = T_0. \tag{6}$$

Here U is the potential difference applied to the contact, and T_0 is the temperature of the peripheral regions of the contact (the z axis is directed along the axis of the contact).

The system of equations (1)–(3) together with the boundary conditions (5) and (6) represent a closed system of equations for determining the coordinate dependence of the electrical potential $\varphi(\mathbf{r})$ and the temperature distribution $T(\mathbf{r})$ for any relationship between the Fermi energy $\mu(T=0)$ and the maximum temperature T_m in the microcontact. However, the problem has analytical solutions only in the limiting cases of weak heating $T_m \ll \varepsilon_F$ (the ''metallic'' limit) and strong heating $T_m \gg \varepsilon_F$ (the ''plasma'' limit). To explain the strong ($T_m \sim \varepsilon_F$) heating of the electrons that is observed in experiment we must solve the problem in the plasma limit. The case of weak heating ($T_m \ll \varepsilon_F$) was studied theoretically in Refs. 9 and 10, where a convenient method was proposed for solving Eqs. (1)–(3).

It is physically obvious that in the thermal transport regime the maximum temperature T_m of the electrons in a microcontact must be controlled by the voltage applied to the contact and should depend weakly on the geometry of the contact. In view of the azimuthal symmetry of a 3D metallic contact it is convenient mathematically to solve the stated problem in the geometry of an oblate ellipsoid of

revolution:[9,10] $0 \leqslant u \leqslant \theta$; $-\infty \leqslant v \leqslant \infty$; $0 < \phi < 2\pi$. The coordinate system $\{u, v, \phi\}$ is related to the Cartesian coordinate system $\{x, y, z\}$ by the expressions

$$x = d_0 \sin u \cosh v \cos \phi; \quad y = d_0 \sin u \cosh v \sin \phi;$$

$$z = d_0 \cos u \sinh v,$$

where $d_0 = d/2 \sin \theta$ is the effective length of the microcontact ($u = \theta = $ const at the boundary Σ of the microcontact).

It follows from the symmetry of the problem that the temperature T and electrical potential φ can only be functions zof the coordinate v and, hence, the system of equations (1)–(3) reduces to

$$\frac{\partial}{\partial v}\left\{\sigma(T)\cosh v\left[\frac{\partial \varphi}{\partial v} + \frac{T}{e}\frac{\partial}{\partial v}\frac{\mu}{T} - \lambda(T)\frac{\partial T}{\partial v}\right]\right\} = 0,$$

$$\frac{\partial}{\partial v}\left\{\kappa(T)\cosh v\frac{\partial T}{\partial v} + \sigma(T)\cosh v\right.$$

$$\times\left[\frac{\partial \varphi}{\partial c} + \frac{T}{e}\frac{\partial}{\partial v}\frac{\mu}{T} - \lambda(T)\frac{\partial T}{\partial v}\right]\frac{\partial}{\partial v}[\varphi - \lambda(T)T] = 0.$$

$$(7)$$

Let us first briefly consider the low-temperature case, following Refs. 9 and 10. In the metallic limit the temperature dependence of the chemical potential can be neglected: $\mu(T \ll \varepsilon_F) \simeq \varepsilon_F$. To determine the maximum electron heating temperature T_m in the microcontact we do not need to specify the temperature dependence of the kinetic coefficients appearing in Eq. (7). Actually, in this limit the thermopower $\alpha(T) \equiv \lambda(T) + \mu/eT$ is small by a factor T/ε_F, and in the leading approximation it can be set equal to zero. Then the system (7) takes the form

$$\frac{\partial}{\partial v}\left(\sigma(T)\cosh v\frac{\partial \varphi}{\partial v}\right) = 0,$$

$$\frac{\partial}{\partial v}\left(\kappa(T)\cosh v\frac{\partial T}{\partial v}\right) + \sigma(T)\cosh v\left(\frac{g!\varphi}{\partial v}\right)^2 = 0. \quad (8)$$

In these equations it is convenient to make the change of variable $\xi = \xi(v)$, $\xi_1 < \xi < \xi_2$, where

$$\xi(v) = \int_0^v \frac{dv}{\sigma(T)\cosh v}; \quad \xi_{1,2} = \xi(\mp\infty).$$

In terms of the variable ξ the system of equations (8) simplifies considerably:

$$\frac{\partial}{\partial \xi}\left(L(T)T\frac{\partial T}{\partial \xi}\right) + \left(\frac{\partial \varphi}{\partial \xi}\right)^2 = 0, \quad \frac{\partial^2 \varphi}{\partial \xi^2} = 0, \quad (9)$$

where

$$L(T) = \frac{\kappa(T)}{T\sigma(T)}.$$

Thus for integrating equations (9) we need to know only the ratio of the thermal and electrical conductivities. For elastic collisions the Wiedemann–Franz law holds (see, e.g., Ref. 12), and $L(T) = L_0$ ($L_0 = \pi^2/3e^2$ is the Lorentz number; here and below we set Boltzmann's constant $k_B = 1$). Although in the thermal transport regime considered here the relaxation of the electron energy occurs inside the microcon-

tact on account of inelastic electron–electron collisions, in dirty samples the main contribution to the thermal and electric resistance comes from elastic scattering on impurities, and in that case one can set $L(T) = L_0$ in Eqs. (9).

An elementary integration of Eq. (9) with the boundary conditions (5) and (6) (for simplicity we have set the temperature at the periphery of the contact $T_0 = 0$) leads to the following expression for the maximum temperature of the microcontact:[9,10]

$$T_M = \frac{U}{2\sqrt{L_0}}.$$

Using the theoretical value of the Lorentz number, we obtain from T_m the estimate $T_m \approx 0.27$ eV, which agrees in order of magnitude with the temperature dependence measured in Refs. 1 and 2. Nevertheless, it is clear that at such high temperatures the ''low-temperature'' ($T \ll \varepsilon_F$) approximation we have used is incorrect. Therefore, to explain the results of the experiments[1,2] we must also study the ''plasma'' limit ($T \gg \varepsilon_F$).

ELECTRON PLASMA IN METALLIC MICROCONTACTS

In the limiting case considered below, unlike the case treated above, while replacing the Fermi distribution by a Maxwellian distribution (''plasma'') we nevertheless assume that the condition of electronic neutrality (''metal'') holds. As a consequence,

$$\nabla\left(\frac{\mu}{T}\right) = -\frac{3}{2}\frac{\nabla T}{T}$$

and Eq. (7) becomes

$$\frac{\partial}{\partial v}\left[\sigma(T)\cosh v\frac{\partial}{\partial v}(\varphi - \tilde{\lambda}T)\right] = 0,$$

$$\frac{\partial}{\partial v}\left\{\sigma(T)\cosh v\left[\frac{\kappa(T)}{\sigma(T)}\frac{\partial T}{\partial v} + (\varphi - \lambda T)\frac{\partial}{\partial v}(\varphi - \tilde{\lambda}T)\right]\right\} = 0,$$

$$(10)$$

where $\tilde{\lambda} = \lambda + 3/2e$.

At high temperatures $T \gg \varepsilon_F$ the electronic relaxation length becomes of the same order as the interatomic distances and, consequently, inelastic electron–electron collisions can contribute to the thermal and electrical resistance an amount comparable to the contribution from scattering on impurities. Then, strictly speaking, the Wiedemann–Franz law ceases to be valid. However, since each electron–electron collision changes both the energy and momentum of the electron substantially, the relaxation time $\tau(\varepsilon)$ appearing in various kinetic coefficients turns out to be the same in order of magnitude. In other words, in the plasma limit, too, the ratio $L(T) = \kappa(T)/T\sigma(T)$ can be regarded as temperature independent, $L(T \gg \varepsilon_F) = L_p$. The numerical value of the constant L_p can be found from a comparison of the formulas with the experimental results.

Thus in terms of the variable ξ the equation for the temperature distribution $T(\xi)$ in the microcontact in the plasma limit as the form

$$L_p T\frac{\partial T}{\partial \xi} + C_1^2(\xi - \xi_0) + \frac{3C_1}{2e}T = 0, \quad (11)$$

and the distribution of the electric potential $\varphi(\xi)$ is given by the expression

$$\varphi(\xi) - \tilde{\lambda} T(\xi) = C_1 \xi + C_2,$$

where C_i and ξ_0 are constants of integration determined by the boundary conditions (5) and (6) (here the temperature T_0 at the periphery of the microcontact is assumed to be quite high—''plasma'').

After the substitution $T(\xi) = (\xi - \xi_0) t(\xi)$ equation (11) becomes

$$(\xi - \xi_0) t \frac{\partial T}{\partial \xi} + P(t) = 0,$$

where

$$P(t) = L_p t^2 + \frac{3C_1}{2e} t + C_1^2 \equiv L_p(t - t_1)(t - t_2),$$

which admits a solution in quadratures. Here the character of the solution depends on the ratio L_c/L_p, where $L_c = 9/16 e^2$. For the most plausible inequality $L_c/L_p < 1$ the zeros t_i of the polynomial $P(t)$ are complex conjugate pairs, and the solution $T(\xi)$ describing the temperature distribution in the microcontact can be written in the form

$$\left| \left[T(\xi) + \frac{C_1}{\sqrt{L_p}} e^{i\rho}(\xi - \xi_0) \right]^{\beta} \right|^2 = C_3, \qquad (12)$$

where

$$\beta = -\frac{1}{2} + \frac{i}{2} \cot \rho, \quad \rho = \arccos \sqrt{L_c/L_p},$$

and C_3 is a constant of integration. For uniqueness we choose the branch of the argument in expression (12) as

$$-\pi < \arg\left[T(\xi) + \frac{C_1}{\sqrt{L_p}} e^{i\rho}(\xi - \xi_0) \right] \leq \pi.$$

We investigate the extremum of expression (12) in the usual way. According to (11) and (12) we have

$$T_m = \frac{1}{C_3} \exp\left[(\pi - 2\rho) \cot \rho \right],$$

and, consequently, the problem of determining T_m reduces to one of finding the integration constant C_3. In the general case the equations for determining the integration constants C_i, ξ_0 are transcendental, but their evaluation is simplified considerably in the limiting case $T_0 \sqrt{L_p}/U \ll 1$, a restriction that we shall adopt, whereupon we obtain the following expression for T_m:

$$T_m = \frac{U}{2\sqrt{L_p}} \exp\left[\left(\frac{\pi}{2} - \rho \right) \cot \rho \right] \cosh^{-1}\left[\frac{\pi}{2} \cot \rho \right]. \qquad (13)$$

Thus in the plasma limit, too, the maximum temperature is a linear function of the applied voltage. To estimate the absolute value of T_m we use the value of L_p for a hydrogen plasma,[12] where $L_p \simeq 3/2e^2$. Then, as follows from (13), we obtain the relation $T_m \sim 0.37 e U$, which gives a better extrapolation of the experimental data obtained in Refs. 1 and 2 than does the ''low-temperature'' approximation.

CONCLUSION

The results of the experimental papers[1,2] show that nano-contact afford a unique possibility of ''separating'' the electron and phonon subsystems and, in principle, make it possible to study the electronic characteristics of a metal ''in pure form,'' i.e., without the influence of the electron–phonon interaction. Theoretical estimates permitting determination of the maximum temperature of a microcontact as a function of the applied voltage show that in both the metallic and plasma limits T_m is a linear function of U, but with a different slope in the two limiting cases. As a consequence, it can be stated that in the intermediate region $T \sim \varepsilon_F$ the function $T_m = T_m(U)$ has a more complicated analytical character, and this problem requires further analysis. The relatively small difference of the slopes indicates that both the metallic and plasma limits will admit satisfactory extrapolation to the transition region $T \sim \varepsilon_F$.

*E-mail: krive@ilt.kharkov.ua

[1] A. Downes and M. Welland, ''Measurement of high electron temperatures in atomic size metal contacts by photon emission,'' preprint, Cambridge (1998).

[2] A. Gil, M. Sharonov, N. Garcia, J. M. Calleja, and J. K. Sass, in *Proceedings of the NATO Advanced Research Workshop on Nanowires*, edited by P. A. Serena and N. Garcia, **327**, Miraflores de la Sierra, Madrid (1996).

[3] V. L. Ginzburg and V. P. Shabanskiĭ, Dokl. Akad. Nauk SSSR **100**, 445 (1955).

[4] M. I. Kaganov, I. M. Lifshits, and L. V. Tanatorov, Zh. Éksp. Teor. Fiz. **31**, 232 (1956) [Sov. Phys. JETP **4**, 173 (1957)].

[5] P. M. Tomchuk and Z. D. Fedorovich, Fiz. Tverd. Tela (Leningrad) **8**, 276 (1966) [Sov. Phys. Solid State **8**, 226 (1966)].

[6] E. D. Belotskii and P. M. Tomchuk, Surf. Sci. **239**, 143 (1990).

[7] A. A. Abrikosov, in *Solid State Physics*, Suppl. 12, Academic Press, New York (1972) [*Introduction to the Theory of Normal Metals*, Nauka, Moscow (1972)].

[8] R. Landauer, IBM J. Res. Dev. **1**, 233 (1957); Philos. Mag. **21**, 863 (1970).

[9] I. O. Kulik, Phys. Lett. A **106**, 187 (1984).

[10] I. F. Itskovich, M. V. Moskalets, R. I. Shekhter, and I. O. Kulik, Fiz. Nizk. Temp. **13**, 1034 (1987) [Sov. J. Low Temp. Phys. **13**, 588 (1987)].

[11] E. N. Bogachek, I. O. Kulik, and A. G. Shkorbatov, J. Phys.: Condens. Matter **3**, 8877 (1991).

[12] E. M. Lifshits and L. P. Pitaevskiĭ, *Physical Kinetics* [Pergamon Press, Oxford (1981); Nauka, Moscow (1979)].

[13] F. G. Bass and Yu. G. Gurevich, *Hot Electrons and Strong Electromagnetic Waves in Semiconductor and Gas-Discharge Plasmas* (Nauka, Moscow, 1975).

Translated by Steve Torstveit

PHYSICAL PROPERTIES OF CRYOCRYSTALS

Single-phonon damping of polaritons in cryocrystals of inert elements

N. A. Goncharuk and E. I. Tarasova*

*B. Verkin Institute for Low Temperature Physics and Engineering, National Academy of Sciences
of Ukraine, pr. Lenina 47, 61164 Kharkov, Ukraine*

The single-phonon damping of polaritons governs the most important characteristics of the
relaxation processes of excitations in the region of the resonance energy E_T. Here the single-
phonon damping of polaritons by acoustical phonons is calculated in the deformation-
potential approximation for the lowest excitons $\Gamma(3/2)$ in Ar, Kr, and Xe cryocrystals. The
results of a numerical calculation of the curves of the energy dependence of the damping $\Gamma(E,T
=\text{const})$ at several temperatures spanning the free exciton existence region for each crystal
are presented. Analytical expressions are obtained for $\Gamma(E,T)$ at $T=0$ and $T>2\hbar ks$.
A comparison with the data from the numerical calculation indicates that a linear temperature
dependence $\Gamma(E=\text{const},T)$ holds over a wide temperature range, except at very low
temperatures. It is shown that at temperatures above the critical point there exists a region of
energies in the neighborhood of E_T in which processes involving the absorption of
phonons are dominant and prevent the relaxation of the polaritons down the dispersion curve.
The width of this region is comparable to the maximum phonon energy and increases
with increasing temperature.   © *2000 American Institute of Physics.* [S1063-777X(00)01206-8]

INTRODUCTION

Cryocrystals of inert elements, owing to the high quantum yield, are attractive objects for converting the energy of high-frequency electronic excitations into VUV and visible radiation. The lowest excitonic states in cryocrystals of inert elements, being the last stage of relaxation of the intrinsic electronic excitations of the crystal, possess a combination of unique properties. The distribution of the emission intensities depends on the features of the exciton–phonon and exciton–photon interactions. The existence of wide bands (with a width $2B \lesssim 1$ eV) of collective states of excitons with weak single-phonon damping ensures a high mobility of the free excitons.[1–5] In crystals there occurs an efficient transfer of excitation to the surface and also to impurity centers, even at low impurity concentrations.[5–8] At the same time, the strong coupling of excitons with local deformations of the lattice leads to intense processes of self-trapping of excitations in cryocrystals of all inert elements.[1–3] In pure Ne, Ar, and Kr crystals the main part of the emission is the VUV emission of self-trapped excitons,[1–3] and it is only in Xe, according to the recent results for especially perfect crystals,[9] that the emission from free and self-trapped excitons is comparable in intensity. In the process of relaxation of the excitations within the limits of a wide band their distribution over these competing channels changes; it depends on the kinetic energy of the exciton (i.e., the positions of the quasiparticles on the dispersion curve). Relaxation of free excitons within a band is governed by the competition of three processes: single-phonon scattering (its probability is predominant and provides relaxation along the band), transitions to a self-trapped state, and transfer to impurities (defects). In the

neighborhood of the band bottom the processes of single-phonon relaxation slow down on account of the influence of energy and momentum conservation,[4] and the last two relaxation channels acquire more significance. Furthermore, in the immediate proximity of the resonance energy E_T of the excitons with transverse polarization the probability of radiative decay of the exciton increases sharply.

In cryocrystals of the inert elements Ar, Kr, and Xe the radiative decay of the excitons $\Gamma(3/2)$ is characterized by a comparatively large oscillator strength ($F \sim 0.1$), which makes for a rather strong exciton–phonon coupling. This leads to efficient exciton–photon mixing in the crossing region of the dispersion curves for light and excitons and to the formation of a polariton dispersion relation.[10,11] Polariton features are manifested in the energy region $|E-E_T| \lesssim \Delta_{LT}$ ($\Delta_{LT} \sim 0.1$ eV is the transverse–longitudinal splitting, which is proportional to F)[10,11] and has a substantial effect on processes of relaxation and transfer of excitation energy in the crystal.

The first studies of polariton effects (with allowance for spatial dispersion) in cryocrystals of inert elements were undertaken primarily in order to explain the anomalous width and shape of the reflection spectra in Ar and Kr crystals.[12] Then a systematic analysis of the influence of polariton effects on the transmission and reflection spectra in Xe was performed.[13,14] This analysis confirmed the importance of taking the light–exciton mixing into account in studying the optical characteristics. In those calculations a constant value of the exciton damping Γ_{ex} was used, which had the meaning of an average over a rather wide energy interval from E_T to $E \sim E_T + \Delta_{LT}$. This choice of Γ_{ex} was based on the results of

TABLE I. Polariton parameters for $\Gamma(3/2)$ experimental values of F, E_T, C, and Δ_{LT} were taken from Refs. 3 and 6.

Crystal	$\dfrac{m}{m_0}$	F	f	E_T	C	$A, 10^{-3}$	Δ_{LT}	λ	$2hk_{res}s$,	$Q, 10^{35}$
					eV				K	$ev^{-2} \cdot cm^{-2} \cdot s^{-1}$
Xe	2.0	0.166	2.0	8.36	1.97	5.62	0.11	0.021	7.4	5.55
Kr	2.7	0.158	2.2	10.17	2.11	5.38	0.13	0.056	9	8.07
Ar	3.6	0.065	1.54	12.06	2.02	4.0	0.06	0.18	10.2	7.6

a calculation of the single-phonon damping of ''pure'' excitons (without taking into account the mixing with photons),[4] since the dependence of $\Gamma(E,T)$ for the polaritons and their energy distribution function (PEDF) were not known.

In this paper we do a consistent calculation of the single-phonon damping of polaritons as a function of energy and temperature and show that the energy dependence of Γ in the neighborhood of E_T and below is shaped by the strong influence of polariton effects. The single-phonon damping governs the most important characteristics of the relaxation processes, both those occurring within a band (see above) and those involving radiative decay.

The characteristics of the luminescence band in the region of the exciton resonance of a crystal are directly related to the change in the exciton dispersion relations upon mixing with photons, and, in particular, to the possibility of polariton relaxation in the region of energies below E_T. This process is intimately intertwined (depending on the energy) with the aforementioned relaxation processes and reflects the behavior of the PEDF, which is determined by solving the kinetic equation with allowance for the phonon scattering Γ and the polariton lifetime, including all the decay channels of itinerant quasiparticles.[15] Knowledge of the PEDF is also necessary for finding the kinetic parameters of the energy transport processes as average values over the distribution— the velocity, various components of the lifetime, the mean free path of the polaritons, and their diffusion coefficient.

The most direct method of determining the lifetime of polaritons is to measure the damping time of the emission intensity following a pulsed excitation of excitons. In Ref. 16 an attempt was made to describe the ''decay curves'' in Xe with the aid of a computer simulation of the propagation of excitations in the lattice. An estimate was thus obtained for the contribution of the self-trapping process to the formation of the polariton lifetime. However the calculation contained the following inaccuracies. It ignored the spatial diffusion of the high-energy excitons during the time of relaxation over the entire exciton band. The group velocity of the polaritons was taken as the average thermal velocity of ''pure'' excitons (as we shall show, at a temperature of 4 K this is completely unjustified). Also, for the polariton damping Γ a value typical of thermalized excitons was used.

Knowledge of the energy and temperature dependences of the scattering probability of polaritons on phonons and the use of these energy and temperature dependences for calculating the PEDF and the correct averaging of the kinetic parameters will make it possible to analyze the aforementioned experimental data in an adequate way.

The first calculation of the single-phonon damping of

polaritons, including preliminary estimates for cryocrystals of inert elements, was done in Ref. 17 on the basis of the same expression of the damping Γ that is used in the present study (see Eq. (2) below). The authors of Ref. 17 performed an analysis in terms of the dependence of Γ on the polariton wave vector **k** and did not obtain data for $\Gamma(E)$, which makes it hard to compare with experiment and to find the PEDF.[15] The analytical dependence of Γ as a function of the quasimomentum and temperature for arbitrary temperatures was given in Ref. 15 in implicit form without any accompanying numerical calculations, and the explicit analytical dependence of $\Gamma(k,T)$ is given only for $T \rightarrow 0$, but the given expression does not have a limiting transition to Γ_{ex} as a function of energy for $E > E_T$ and can be used only in a narrow vicinity of the resonance energy and at very low temperatures.

In the present paper we calculate the single-phonon damping as a function of the energy of the quasiparticles and the temperature of the crystal for the lowest polariton states in Ar, Kr, and Xe cryocrystals. We use the known polariton dispersion relation obtained in the dipole approximation for the interaction of excitons with an electromagnetic field (linear in the exciton and photon operators). The interaction of polaritons with acoustical phonons is taken into account in an approximation linear in the phonon operators and in the model of an isotropic deformation potential. We present the results of a numerical calculation of the energy dependences of the damping for a wide set of values of the temperatures, and also analytical relations describing the polariton damping in the pertinent energy and temperature regions.

GENERAL CONSIDERATIONS

The width of the energy region in which the polariton effects are experimentally manifested is of the order of Δ_{LT} (see Table I). As we shall show below, for the excitonic states under consideration the inequality $\Delta_{LT} \gg \hbar\Gamma(E_T)$ holds, where $\Gamma(E_T)$ is the damping of polaritons on phonons in the resonance region. This fact lets one clearly single out the states of the lower branch of transverse polaritons as the final stage of the relaxation of the excitonic band states $\Gamma(3/2)$. It is these states that we shall consider below. The solution of the dispersion relation $\varepsilon(\omega,\mathbf{k})[\omega^2\varepsilon(\omega,\mathbf{k}) - k^2c^2]^2 = 0$ for the lower branch of transverse polaritons has the well-known form[1,2]

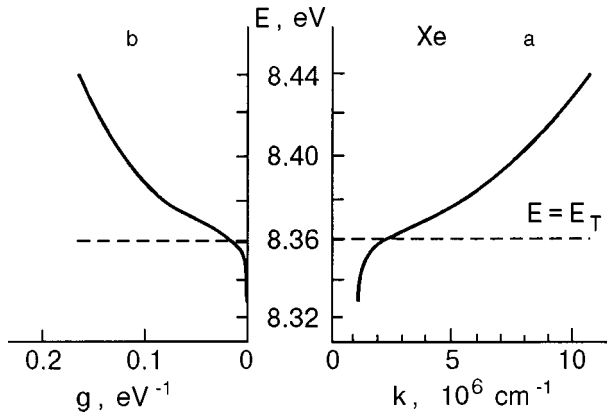FIG. 1. Dispersion curve $E(k)$ for Xe (a); energy dependence of the polariton density of (energy) states $g(E)$ (b).

$$\omega_\perp^-(k) = \left\{ \frac{1}{2} \left(\omega_k^2 + \frac{k^2 c^2 + f^2}{\varepsilon_\infty} - i\omega_k \gamma_k \right) \right.$$
$$- \left[\frac{1}{4} \left(\omega_k^2 + \frac{k^2 c^2 + f^2}{\varepsilon_\infty} - i\omega_k \gamma_k \right)^2 \right.$$
$$\left. \left. - \frac{k^2 c^2}{\varepsilon_\infty} (\omega_k^2 - i\omega_k \gamma_k) \right]^{1/2} \right\}^{1/2} . \tag{1}$$

Here $f = 4\pi e^2 F/(m_0 V_0)$ is the frequency, which characterizes the oscillator strength F, m_0 is the mass of the free electron, $V_0 = a^3/4$ is the volume of the unit cell for an fcc crystal, a is the lattice constant, ε_∞ is the dielectric constant at high frequencies ($\omega \gg \omega_T$); and $\omega_k = \omega_T + \hbar k^2/2m$ is the dispersion relation for excitons, m is the exciton mass, and $\hbar\omega_T = E_T$. The imaginary term $i\gamma_k \omega_k$ is introduced to take the damping into account: $\gamma_k \equiv 2\Gamma(E(k))$. As our results have shown, one can neglect the quantity γ_k in a calculation of the dispersion relation; this is later used in the derivation of analytical expressions for $\Gamma(E,T)$. The transverse–longitudinal splitting is expressed in terms of the parameters of the dispersion relation in the form $\Delta_{LT} = f^2\hbar^2/2\varepsilon_\infty E_T$. The dispersion curve (1) for polaritons in Xe is shown in Fig. 1a. For $\omega > \omega_T + \Delta_{LT}/\hbar$ the polaritons of the lower branch $\omega_\perp(k)$ are no different from the excitons that do not interact with the electromagnetic field. At frequencies $\omega < \omega_T - \Delta_{LT}/\hbar$ the dispersion relation (1) goes over to the linear dependence of low-frequency photons.

The interaction of polaritons with phonons is of the nature of multiple, successive inelastic scattering events, and this process causes the quasiparticles to move in energy along the dispersion curve. This scattering is determined by the probability of a transition from a state $\omega(\mathbf{k})$ to a state $\omega(\mathbf{k}')$. In Xe, Kr, and Ar the case of weak exciton–phonon interaction is realized,[3,4] and therefore the main role is played by single-phonon processes, which are the subject of this study. To a first approximation in perturbation theory in the exciton–phonon interaction the damping of a polariton with energy $\hbar\omega(\mathbf{k})$ at temperature T is written in the form[10,11]

$$\Gamma(\omega,T) = \frac{2\pi}{\hbar} \sum_{\mathbf{k}'} |G_{|\mathbf{k}-\mathbf{k}'|}|^2 P(\omega)P(\omega')$$
$$\times \{ (n_{\mathbf{k}-\mathbf{k}'}+1)\delta[\omega(\mathbf{k}') - s|\mathbf{k}-\mathbf{k}'|]$$
$$+ n_{|\mathbf{k}-\mathbf{k}'|}\delta[\omega(\mathbf{k}) - \omega(\mathbf{k}') + s|\mathbf{k}-\mathbf{k}'|] \}, \tag{2}$$

where $\mathbf{k} - \mathbf{k}' = \mathbf{q}$, $\mathbf{q}$ is the phonon wave vector, the δ function expresses energy conservation during scattering, the 1 in parentheses in front of the first δ function in formula (2) takes into account the contribution of spontaneous phonon emission processes to the scattering, $n_\mathbf{q} = [\exp(\hbar\omega_\mathbf{q}/T) - 1]^{-1}$ is the occupation number of phonons with wave vector $\mathbf{q}$ (which completely determines the temperature dependence of Γ), $\hbar\omega_\mathbf{q} = s|\mathbf{k}-\mathbf{k}'|$ is the phonon energy in the Debye model, s is the speed of sound, $P(E)$ and $P(E')$ are the strength functions of the polaritons, which describe the contribution of the exciton component to the polariton state (see p. 385 of Ref. 11):

$$P(E) = \frac{f^2 E^2}{\varepsilon_\infty (E_T^2 - E^2) + f^2 E_T^2} .$$

In a calculation of the probability of single-phonon scattering of polaritons in cryocrystals of inert elements, in view of the high symmetry of these crystals, we adopt a model of the deformation potential for the exciton–phonon interaction in the form $H_{int} = -C \operatorname{div} \mathbf{u}$, where C is the deformation potential of the exciton and $\mathbf{u}$ is the relative deformation. Since this interaction contains a contribution only from longitudinal acoustical phonons, in this paper we use for s the values of the longitudinal sound velocity s_l. In this model G_q is expressed in the form $|G_q| = C(\hbar\omega_q/2Ms^2)^{1/2}$, where M is the mass of an atom. The criterion of a low strength of the exciton–phonon scattering is that the nonadiabaticity parameter be small:[1–5]

$$\lambda = \frac{4m^2 C^2}{3\pi\rho s\hbar^3} \cdot \frac{\hbar\omega_D}{B} \ll 1. \tag{3}$$

Here $\rho = M/V_0$ is the density of the crystal, ω_D is the Debye frequency of the phonons, and B is the half width of the exciton band. Values of λ are given in Table I.

Since we are interested in the energy relaxation process, we change in (2) from a sum over wave vectors to integration over energy, and we represent the damping in the form

$$\Gamma(E,T) = \int_0^\infty dE W(E \to E', T) g(E'), \tag{4}$$

where $g(E)$ is the polariton density of (energy) states, and we have introduced the probability of transition of a polariton with energy E to a state with energy E':

$$W(E \to E', T)$$
$$= \frac{\pi C^2}{2\hbar^3 M s^4} \frac{(E-E')^2 P(E)P(E')}{k(E)k(E')|\exp[(E'-E)/T] - 1|}$$
$$\times \theta(|E-E'| - \hbar s|k-k'|) \theta[\hbar s(k+k')$$
$$- |E-E'|]. \tag{5}$$

The function $\theta(x) = 1$ if $x \geq 0$ and $\theta(x) = 0$ if $x < 0$; the θ function reflects the conservation of energy in the scattering. The last cofactor in (5) means that the energy imparted
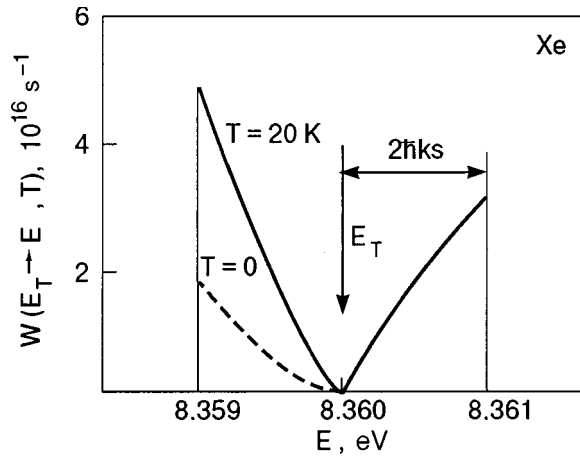
FIG. 2. Probability of single-phonon scattering $W(E_T \to E,T)$ for polaritons in Xe for $E_T = 8.36$ eV and $T = 20$ K.

to the phonon cannot exceed the value $\hbar s(k+k')$, where $k \equiv k(E)$ and $k' \equiv k(E')$ are the moduli of the polariton wave vectors before and after scattering. The divergence $W(E_T \to E', T = 20\,\text{K})$ for Xe is shown in Fig. 2. The higher wing of the function on the left as compared to the right is due to the contribution from spontaneous phonon emission, which governs the polariton damping at $T = 0$.

Taking into account the θ function in (5), we can write a general expression for the damping (4) in the form

$$\Gamma(E,T) = \frac{Q}{k(E)} \int_{E-2\hbar sk(E)}^{E+2\hbar sk(E)} \frac{(E-E')^2 g(E')dE'}{k(E')|\exp[(E'-E)/T]-1|}, \quad (6)$$

where we have introduced the notation $Q = \pi C^2/(2\hbar^3 M s^4)$. A calculation shows that the function $P(E)$ in the pertinent interval of energies below E_T decreases by only 2%, and we have therefore put $P(E) = 1$.

RESULTS OF A NUMERICAL CALCULATION OF THE FUNCTION $\Gamma(E, T = \text{const})$

The polariton kinetic parameters and the shape of the luminescence line are determined by the energy distribution function of the particles, $F(E)$. In turn, $F(E)$ is the result of a competition between polariton energy relaxation processes with the probability $W(E \to E', T)$ and polariton decay processes. The polariton lifetime τ (the radiative lifetime or the lifetime with respect to trapping by defects or impurities or to self-trapping) can vary in a crystal by orders of magnitude, e.g., due to changes in the thickness, defect density, or impurity concentration. It is therefore important to know the exact behavior of $\Gamma(E,T)$ in the low-energy part, on scales of the possible variation of the polariton loss probability τ^{-1}. Since integral (6) is nontrivial (the limits of integration contain the inverse dispersion curve $k(E)$), we shall give a complete set of results of a numerical calculation of the damping (6), where the functions $g(E)$ and $k(E)$ are found by numerical methods directly from Eq. (1). Figure 3 shows the set of functions $\Gamma(E, T = \text{const})$ in logarithmic scale for the entire temperature region in which free excitons exist in Xe, Kr, and Ar crystals. The exciton–phonon interaction increases in the sequence from heavy to light inert gases, corresponding to the growth of the nonadiabaticity parameter λ
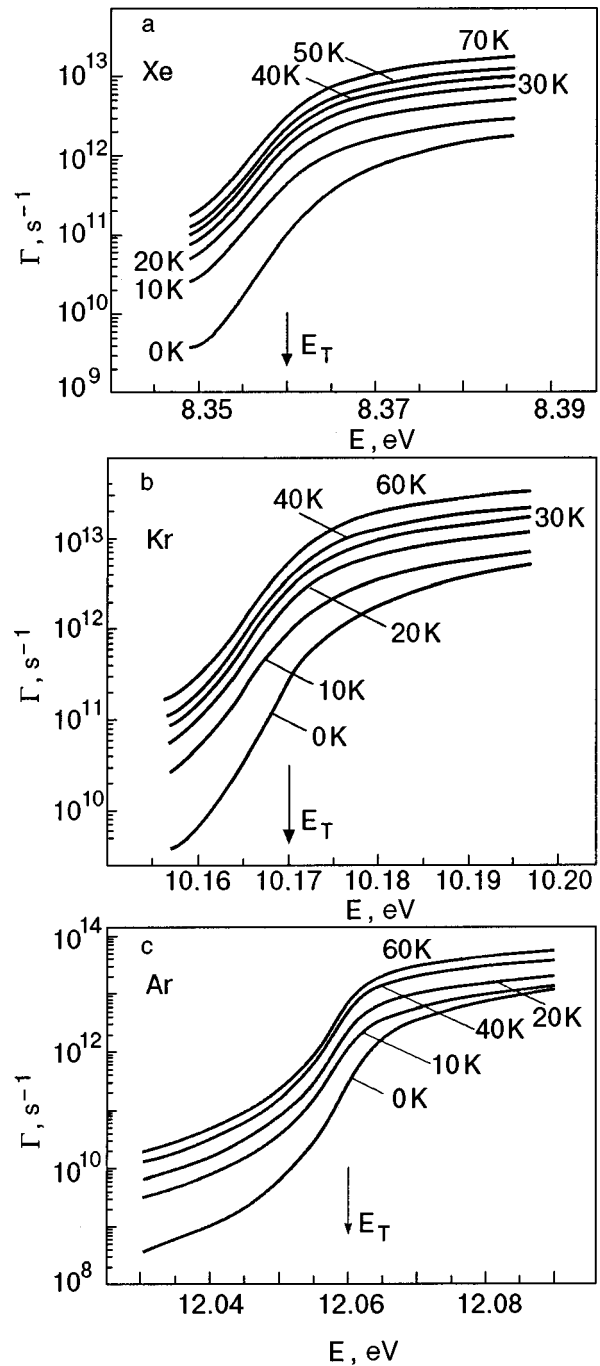
FIG. 3. Numerical calculation of the polariton damping $\Gamma(E, T = \text{const})$ according to formula (6) for $\Gamma(3/2)$ excitons in Xe (a), Kr (b), Ar (c) at various temperatures.

(see Table I). Accordingly, an increase in $\Gamma(E,T)$ is observed on going from Xe to Ar (at equal temperatures). This effect is analogous to that found earlier for the damping of excitons[4] and is explained by the weak variation of the exciton component of the polariton ($P(E) \sim 1$) in the energy region under study for the given cryocrystals.

ANALYTICAL DEPENDENCE OF $\Gamma(E, T)$

Here we investigate the function $\Gamma(E,T)$ analytically. First, to evaluate the integral (6) we must find analytical expressions for $k(E)$ and $g(E)$. As we see from Eq. (1), the function $\omega_\perp(\mathbf{k})$ has a complicated form, and therefore to
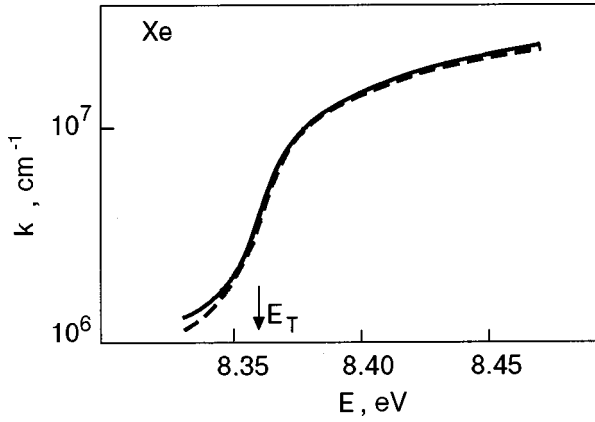
FIG. 4. Comparison of the $k(E)$ curves for Xe obtained from the exact formula (1) of the theory (solid curve) and from formula (8) (dashed curve).

obtain an exact inverse dispersion relation would be an awkward procedure. To simplify the calculations we use the following inequalities, which ordinarily hold for optically observable excitonic transitions:

$$\frac{E_T \varepsilon_\infty}{mc^2} \ll \frac{f^2}{\varepsilon_\infty E_T^2} \ll 1. \tag{7}$$

Making the corresponding approximations, we can reduce the dispersion relation to the form

$$k(E) = \left(\frac{m}{\hbar^2}\right)^{1/2} \{[(E-E_T)^2 + A^2]^{1/2} + (E-E_T)\}^{1/2}, \tag{8}$$

where $A^2 = E_T f^2/(mc^2)$ determines the energy interval near E_T in which the dispersion relation exhibits the characteristic polariton variation. At energies $E - E_T \gg A$ and in the limit $f \to 0$ $(A \to 0)$, expression (8) goes over to the usual square-root dependence typical of ''mechanical'' excitons (having a quadratic dispersion relation). Figure 4 shows a comparison of the $k(E)$ curves for Xe, one of which was obtained from formula (8) and the other by a numerical calculation using the exact formula (1). We see that the curves differ in the low-frequency region by $\sim 2-5\%$. This is explained by the absence of the dielectric constant in expression (8) after condition (7) was used. Nevertheless, in the region where polariton effects are actually manifested, near E_T, the agreement is good.

Let us now calculate the polariton density of states, taking into account the twofold degeneracy of the transverse states with respect to polarization and the spherical symmetry of the dispersion relation:

$$g(E) = \frac{V_0}{\pi^2} k(E)^2 \left|\frac{dk}{dE}\right|. \tag{9}$$

Using (8), we obtain the following expression:

$$g(E) = \frac{V_0}{2\pi^2} \left(\frac{m}{\hbar^2}\right)^{3/2} \frac{\{[(E-E_T)^2 + A^2]^{1/2} + (E-E_T)\}^{3/2}}{[(E-E_T)^2 + A^2]^{1/2}}. \tag{10}$$

Relation (10) is plotted (with a 90° rotation) in Fig. 1(b) for polaritons in Xe. In the limit $f \to 0$ we again have the square-root dependence for excitons.

Let us now turn directly to an analysis of $\Gamma(E,T)$ in the form (6).

We first consider the case when $T=0$ and the absolute value term containing the exponential function in the denominator of Eq. (6) is equal to unity. Furthermore, only processes involving the emission of phonons are realized, i.e., in the integral (6) only the half with the lower limit of integration remains. Introducing some notation, we let $2\hbar s k(E) = \delta$ (keeping in mind that $\delta \equiv \delta(E)$) and $g(E)/k(E) = f(E)$. Changing to the new variable of integration $x = E - E'$, we get

$$\Gamma(E,0) = \frac{Q}{k(E)} \int_0^\delta x^2 f(E-x) dx. \tag{11}$$

The interval of the characteristic variation of the functions $g(E)$ and $k(E)$ is the quantity $A \sim 5 \times 10^{-3}$ eV, and the range of integration is $\delta \leq 10 \, \text{K} \sim 5 \times 10^{-4}$ eV (see Table I). Since $\delta \ll A$, we can consider the function $f(E)$ in (11) to be slowly varying and expand it in a power series in the neighborhood of the point E:

$$f(E-x) = f(E) - \frac{df}{dE} x + \frac{d^2 f}{dE^2} x^2 + \ldots \tag{12}$$

Keeping the first two terms, we obtain

$$\Gamma(E,0) = \frac{Q}{k(E)} \frac{\delta^3(E)}{3} \left[f(E) - \frac{3}{4} \delta(E) \frac{df(E)}{dE} \right]. \tag{13}$$

Taking into account the form of the functions $k(E)$ and $g(E)$ in Eqs. (8) and (10), we arrive at the final expression

$$\Gamma(E,0) = \pm \frac{Q(2\hbar s)^3}{3} g(E) k(E)$$

$$\times \left\{ 1 - \frac{3}{2} \frac{ms}{\hbar} \frac{A^2}{k(E)[(E-E_T)^2 + A^2]} \right\}. \tag{14}$$

The function (14) in the limit $f \to 0$ goes over to the well-known linear energy dependence for excitons.[4,5] The numerically calculated damping curves at $T=0$ K (Fig. 4) for the crystals investigated here can be approximated by expression (14) to one-percent accuracy. The second term is an appreciable correction ($<10\%$) in a narrow energy region near the resonance.

Let us now consider the temperature dependence of the damping. Transforming Eq. (8) in analogy with the previous case, we obtain

$$\Gamma(E,T) = \frac{Q}{k(E)} \int_0^\delta \frac{x^2 e^{x/T} dx}{e^{x/T} - 1} [f(E-x) + f(E+x) e^{-x/T}]. \tag{15}$$

We expand the functions $f(E-x)$ and $F(E+x)$ as in (12). The first term of this expansion gives

$$\Gamma_0(E,T) = \frac{Qf(E)}{k(E)} \int_0^\delta \frac{\cosh(x/2T)}{\sinh(x/2T)} x^2 dx. \tag{16}$$

The integral in Eq. (16) can be done exactly and is expressed in the form of a series:

$$I = \int y^2 \coth y \, dy = \sum_{n=0}^\infty \frac{2^{2n} B_{2n} y^{2(n+1)}}{2(n+1)(2n)!}, \quad |y| < \pi. \tag{17}$$

where the B_{2n} are the Bernoulli numbers: $B_0 = 1$, $B_2 = 1/6$, $B_4 = -1/30,\ldots$. The first terms in (17) can be written as

$$I = \frac{y^2}{2} + \frac{y^4}{12} - \frac{y^6}{270} + \cdots .$$

It is clear that because of the rapid decrease in the coefficients the series converges very well under the simple condition $y < 1/2$. In our case $y = \delta/2T$. We consider the situation $T > \delta$, where we need to keep only the first two terms in (17) to achieve an accuracy of 4% or better. As a result, we get

$$\Gamma_0(E,T) = Q(2\hbar s)^2 Tg(E)\left[1 - \frac{[\hbar s k(E)]^2}{6T^2}\right]. \qquad (18)$$

Next, the linear term in the expansion of $f(E)$ in the form (12) gives a temperature-independent contribution:

$$\Gamma_1(E,T) = -\frac{Q}{k(E)}\frac{df}{dE}\int_0^\delta x^3 dx$$

$$= -\frac{B}{k(E)}\frac{df}{dE}\frac{[2\hbar s k(E)]^4}{4}. \qquad (19)$$

Evaluating the derivative of $f(E)$ and taking into account the relations for the functions $k(E)$ and $g(E)$ from (8) and (10), we bring Eq. (19) to the form

$$\Gamma_1(E,T) = -Q\frac{(2\hbar s)^4 \pi^2}{2V_0}g(E)\frac{A^2}{(E-E_T)^2+A^2}. \qquad (20)$$

We have done these calculations with allowance for the quadratic terms in the expansion of the function $f(E)$ in the form (12). Since the corrections for the cryocrystals under discussion were less than one percent, we will not write out the rather awkward expressions for them.

Summing the contributions (18) and (20) for the case $T > 2\hbar sk$, we obtain the final expression for the temperature dependence of the damping:

$$\Gamma(E,T) = Q(2\hbar s)^2 Tg(E)$$

$$\times\left\{1 - \frac{(2\hbar s)^2 \pi^2}{2V_0 T}\frac{A^2}{(E-E_T)^2+A^2}\right.$$

$$\left. + \frac{[\hbar s k(E)]^2}{6T^2}\right\}. \qquad (21)$$

Figure 5 shows the temperature dependence of the polariton damping $\Gamma(E,T)$ in Xe, Kr, and Ar for fixed values of the energy ($E = E_T$). We see that the function $\Gamma(T,E = \text{const})$ obtained numerically from the original formula (6) is linear over a wide temperature interval. This corresponds to the first two terms in expression (21). The deviation from the linear trend in the low-temperature region reflects a transition to the corresponding value of the constant contribution $\Gamma(E,0)$.

DISCUSSION OF THE RESULTS

The regularities found for the polariton damping have a certain analogy with previous calculations for the damping of ''pure'' excitons with a quadratic dispersion relation.[4] In both cases the damping depends on temperature through the occupation numbers $n_q(T)$ of phonon states. The minimum
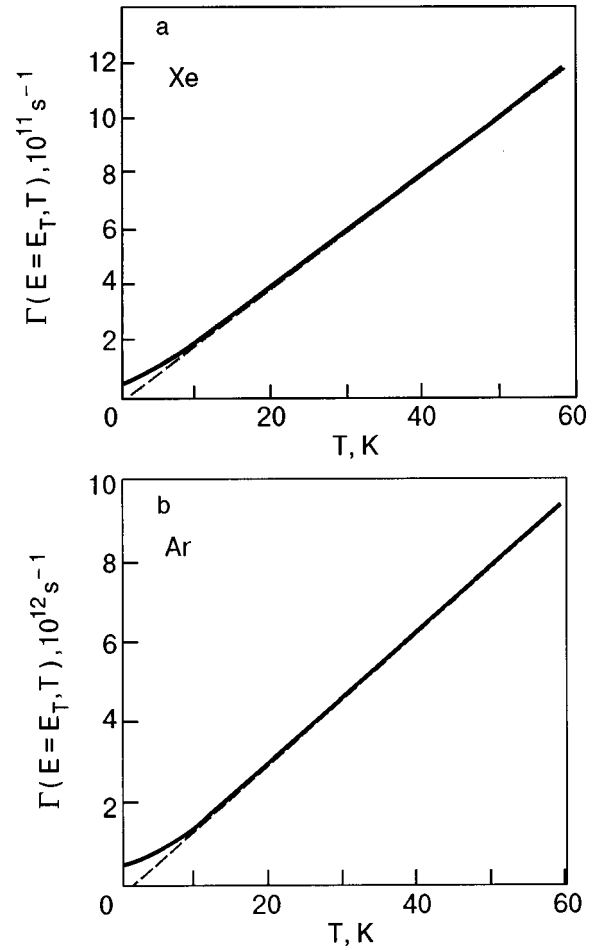

FIG. 5. Temperature dependence of the polariton damping $\Gamma(E_T,T)$ in Xe (a) and Ar (b).

values of the polariton group velocity v_g in cryocrystals of inert elements are rather large ($v_{min} \sim 10^6$ cm/s) and satisfy the criterion $v_g \gg s \sim 10^5$ cm/s. We therefore have a linear temperature dependence for polaritons, just as for excitons with high velocities (meeting the above criterion). The position of the minimum of v_g nearly coincides with E_T, and therefore, as we have said more than once, as the energy increases in the region above the resonance there is a smooth transition of all the polariton properties, including $\Gamma(E,T)$, to the exciton ones.

Substantial differences arise directly in the resonance region and below. Figure 6 shows a comparison of the energy dependence of the damping for excitons and polaritons in Xe at $T = 0$ (with a logarithmic scale along the ordinate). Then for excitons at $T = 0$ the dependence has the simple form of a linear function $\Gamma_{ex}(E,T=0) = \lambda(E - E_T)$ (Refs. 4 and 18) and practically vanishes at $E = E_T$. In perfect crystals of large size, Γ_{pol} decreases by an order of magnitude in an energy interval with a width equal to the luminescence bandwidth ΔE.[9]

The observed position of the maximum of the luminescence band at low temperatures is related to the total decay probability of the polaritons. At sufficiently low temperatures only processes involving the emission of phonons can occur. Thus the function Γ_{pol} shown in Fig. 6 describes the probability of transition of polaritons down the dispersion curve. The energy relaxation process can be stopped only by
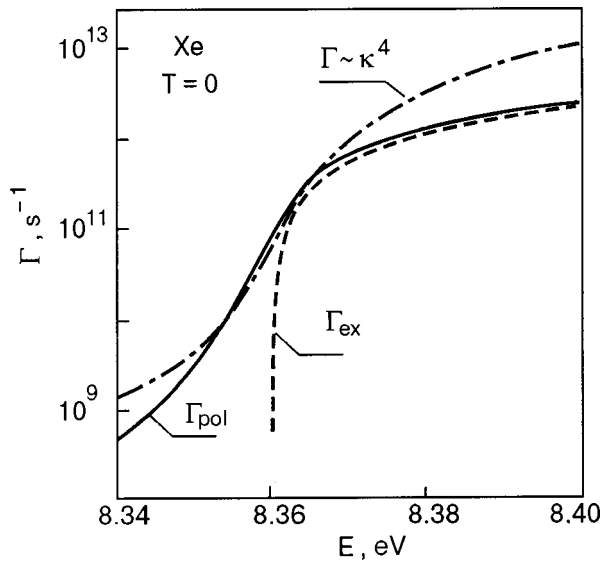
FIG. 6. Single-phonon damping of polaritons $\Gamma_{\text{pol}}(E)$ (solid curve) and excitons $\Gamma_{\text{ex}}(E)$ (dashed curve) for Xe at $T=0$. The dot-and-dash curve corresponds to the dependence $\Gamma \propto k^4$ from Ref. 17.
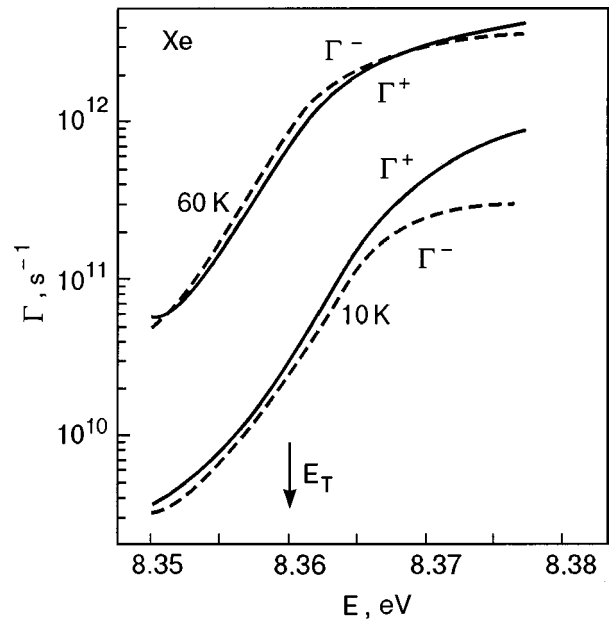

FIG. 7. Integral characteristics of polariton scattering in Xe with phonon emission (Γ^+, solid curves) and absorption (Γ^-, dashed curves) in single-phonon processes at $T=10$ and 60 K.

the loss of the polariton: either it reaches the surface of the crystal and is converted to radiation or it is trapped by an impurity (or defect center) or is self-trapped. The maximum of the polariton energy distribution function (near the maximum of the luminescence band) for low temperatures is approximately the same as the energy at which the inverse lifetime of the polariton (its total decay probability) is equal to the value of the single-phonon damping. The standard concept of ''thermal equilibrium with the lattice'' adopted for ordinary excitons is completely inapplicable for determining the kinetic parameters of polaritons at low temperatures. One must first solve the problem of the formation of the polariton energy distribution function with allowance for the energy and temperature dependence of the polariton lifetime, and then find the average velocity of the polaritons, their mean free path, diffusion coefficient, etc.

For comparison, Fig. 6 shows the damping curve corresponding to the dependence obtained in Ref. 17: $\Gamma(E,T=0) \propto k^4(E)$ (the dot-and-dash curve). These results are in fair agreement in a certain energy region $E<E_T$.

Let us now discuss the influence of temperature on the polariton energy relaxation process. The expression for the total damping (6) can be written in the form of a sum of two integrals (for $E'<E$ and for $E'>E$), i.e.,

$$\Gamma(E,T)=\Gamma^+(E,T)+\Gamma^-(E,T), \qquad (22)$$

where $\Gamma^+(E,T)$ corresponds to the contribution of phonon emission processes, and $\Gamma^-(E,T)$ corresponds to absorption processes. The lower the temperature, the greater the relative contribution to the damping $\Gamma^+(E,T)$ from spontaneous (temperature-independent) phonon emission processes, which are described by $\Gamma(E,0)$. Here the probability $W(E \to E',T)$ has a clearly dominant left wing (see Fig. 3). A feature of the polariton dispersion relation—the sharp change in the derivative (i.e., the quasiparticle group velocity) in the vicinity of E_T—leads to nontrivial temperature dependence of the ratio of Γ^+ and Γ^- in this energy region. Figure 7 shows the integral probabilities $\Gamma^{\mp}(E)$ corresponding to the

scattering of polaritons in Xe at $T=10$ and 60 K. The sharp increase in the density of states $g(E)$ in the resonance region compensates the asymmetry of the right and left wings of the function $W(E \to E',T)$ in the integral (6), which at temperatures above a certain critical temperature ($T_c \approx 35$ K in the case of Xe) leads to a dominance of phonon absorption processes. This is responsible for the so-called thermal-barrier effect for the relaxation of quasiparticles down the dispersion curve.[17,19] At high temperatures the region in which $\Gamma^- > \Gamma^+$ has a width $\sim 2\hbar\omega_D \gg \delta$. To overcome such a wide region in single-phonon scattering events with an inelasticity δ is improbable, and so the relaxation process slows down, and an excitonlike distribution function with a maximum above E_T is formed.

This study of single-phonon damping of polaritons has laid the groundwork for a detailed study of the polariton energy distribution function and the shape of the luminescence band and for determination of the kinetic parameters of polaritons in Xe, Kr, and Ar.

*E-mail: tarasova@ilt.kharkov.ua

[1] I. Ya. Fugol' and E. I. Tarasova, Fiz. Nizk. Temp. **3**, 366 (1977) [Sov. J. Low Temp. Phys. **3**, 176 (1977)].

[2] I. Ya. Fugol', Adv. Phys. **27**, 1 (1978).

[3] A. F. Prikhot'ko, V. G. Manzheliĭ, I. Ya. Fugol', Yu. B. Gaĭdideĭ, I. N. Krupskiĭ, V. M. Loktev, E. V. Savchenko, V. A. Slyusarev, M. A. Strzhemechnyĭ, Yu. A. Freĭman, and L. I. Shanskiĭ, *Cryocrystals* [in Russian], edited by B. I. Verkin and A. F. Prikhot'ko, Naukova Dumka, Kiev (1983), Part 4.

[4] I. Ya. Fugol' and E. I. Tarasova, Fiz. Nizk. Temp. **7**, 1325 (1981) [Sov. J. Low Temp. Phys. **7**, 644 (1981)].

[5] I. Ya. Fugol', Adv. Phys. **37**, 1 (1988).

[6] N. Schwentner, E. E. Koch, and J. Jortner, *Electronic Excitations in Condensed Rare Gases*, Springer Tracts in Modern Physics 107, Springer-Verlag, Berlin (1985).

[7] M. Runne and G. Zimmerer, Nucl. Instrum. Methods Phys. Res. B **101**, 156 (1995).

[8] A. G. Belov, I. Ya. Fugol', and E. M. Yurtaeva, Phys. Status Solidi B **175**, 123 (1993).

[9] D. Varding, J. Becker, L. Frankenstein, B. Peters, M. Runne, A. Schroder, and G. Zimmerer, Low Temp. Phys. **19**, 427 (1993).

[10] A. S. Davydov, *Solid State Theory* [in Russian], Nauka, Moscow (1976).

[11] V. M. Agranovich and V. L. Ginzburg, *Spatial Dispersion in Crystal Optics and The Theory of Excitons* [Springer-Verlag, Berlin (1984); Nauka, Moscow (1979)].

[12] W. Andreoni, M. DeCrescenzi, and E. Tosatti, Solid State Commun. **26**, 425 (1978).

[13] I. Ya. Fugol', O. N. Grigoraschenko, A. M. Ratner, and E. V. Savchenko, Solid State Commun. **38**, 1031 (1981).

[14] I. Ya. Fugol', O. N. Grigoraschenko, and E. V. Savchenko, Phys. Status Solidi B **111**, 397 (1981).

[15] H. Sumi, Solid State Commun. **17**, 701 (1975).

[16] D. Varding, I. Reimand, and G. Zimmerer, Phys. Status Solidi B **185**, 301 (1994).

[17] É. N. Myasnikov and G. V. Fomin, Fiz. Nizk. Temp. **7**, 1053 (1981) [Sov. J. Low Temp. Phys. **7**, 512 (1981)].

[18] É. I. Rashba, Izv. Akad. Nauk SSSR, Ser. Fiz. **40**, 1793 (1976).

[19] É. I. Adirovich, *Some Topics in the Theory of Crystal Luminescence* [in Russian], Gostekhteorizdat, Moscow (1956).

Translated by Steve Torstveit

LATTICE DYNAMICS

Waveguiding properties of two parallel defects under conditions of two-channel scattering

A. M. Kosevich*

B. Verkin Institute for Low Temperature Physics and Engineering, National Academy of Sciences of Ukraine, pr. Lenina 47, 61164 Kharkov, Ukraine

D. V. Matsokin

V. N. Karazin Kharkov National University, pl. Svobody 4, 61077 Kharkov, Ukraine

It is shown that a pair of parallel planar defects in a crystal can act as a waveguide for a quantum particle or wave having two branches of the dispersion relation. The energies (or frequencies) for which the excitations are localized between the defects and propagate freely along them are determined. In a two-dimensional system there exists a discrete set of energies at which two-dimensional excitations can be ''held in'' between two parallel linear defects. © *2000 American Institute of Physics.* [S1063-777X(00)01306-2]

There has been increasing interest of late in effects due to the the interaction of freely propagating states of a particle or wave and states of the same particle or wave localized at defects. The nature of these effects is intimately connected with the properties of quasilocal states of the continuum.[1] The simplest of the effects of interest arises in the study of the motion of a particle along a channel, which leads to size quantization of its transverse energy. The presence of a point defect in such a system will lead to an interaction of the states of the discrete and continuous spectra, and this gives rise to a number of resonance phenomena. The authors of Refs. 2 and 3 called attention to the resonance features in transmission factor for electrons through a two-dimensional (2D) channel containing an attractive impurity. Conductance resonances due to the interaction of particles corresponding to different branches of the spectrum at impurities were observed experimentally in Refs. 4 and 5. A detailed analysis of the interaction with local defects for waves having several branches of the dispersion relation was carried out in Refs. 6 and 7, and it was shown that for certain relations between the parameters of the system, both total reflection and total transmission of the wave through the defect are possible. In Ref. 7 it was pointed out that a wave in a 2D quantum channel can be blocked in by the two point defects at ''critical'' values of the energy of the wave and the distance between these impurities.

In this paper we discuss the waveguiding properties of two parallel planar defects in a crystal in respect to a wave having a dispersion relation with two branches.

We consider a system in which a quantum particle has a dispersion relation with two branches:

$$\varepsilon = \frac{1}{2m_1}(k_x^2 + k_y^2 + k_z^2), \tag{1}$$

$$\varepsilon = \varepsilon_0 + \frac{1}{2m_2}(k_y^2 + k_z^2) + \frac{1}{2m_3}(k_x - k_0)^2. \tag{2}$$

In the case of an electron, ε and m are its energy and effective mass, while for a phonon ε is the square of the frequency and $1/m$ is the square of the phase velocity (we have $\hbar = 1$). Figure 1 shows a sketch, in arbitrary scale, of the dispersion relation for $k_y = $ const and $k_z = $ const.

In an ideal system the wave functions ψ_1 and ψ_2 corresponding to these branches of the dispersion relation are independent states. In the presence of defects in the system the equation for the wave functions can be written in the form

$$\frac{1}{2m_1}\Delta\psi_1 + \varepsilon\psi_1 - U_1\{\psi_1, \psi_2\} = 0, \tag{3}$$

$$\frac{1}{2m_2}\left(\frac{\partial^2\psi_2}{\partial y^2} + \frac{\partial^2\psi_2}{\partial z^2}\right) + \frac{1}{2m_3}\left(\frac{\partial}{\partial x} - ik_0\right)^2\psi_2$$
$$+ (\varepsilon - \varepsilon_0)\psi_2 - U_2\{\psi_1, \psi_2\} = 0, \tag{4}$$

where U_1 and U_2 are terms describing the ''two-channel'' interaction of the waves with the defect, and the notation Δ is used for the Laplacian operator.

Suppose that a particle is propagating along two identical parallel planar defects lying parallel to the symmetry plane of the two dispersion relations (1), (2) and a distance h apart. Then, if we assume that the defects are of a local character, the interaction of two waves in the simplest case will be described as follows:[6]

$$U_1 = (\alpha_1\psi_1 + \beta\psi_2)\left[\delta\left(z - \frac{h}{2}\right) + \delta\left(z + \frac{h}{2}\right)\right],$$

$$U_2 = (\alpha_2\psi_2 + \beta\psi_1)\left[\delta\left(z - \frac{h}{2}\right) + \delta\left(z + \frac{h}{2}\right)\right], \tag{5}$$
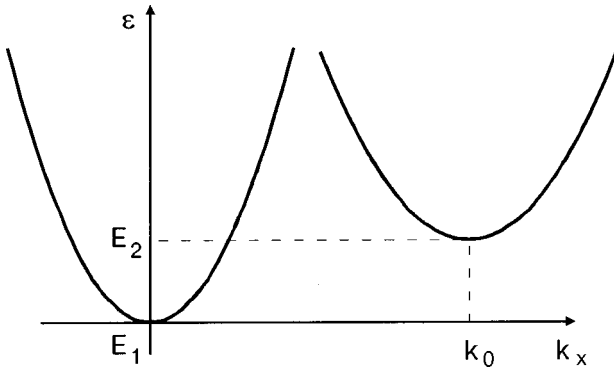
FIG. 1. Two branches of the dispersion relation for a particle with fixed k_y, k_z. $E_1 = (k_y^2 + k_z^2)/2m_1$, $E_2 = \varepsilon_0 + (k_y^2 + k_z^2)/2m_2$.

where α_1, α_2, and β are parameters that determine the character of the interaction of the given waves with an individual defect. Since the interaction Hamiltonian for this is usually (in the linear approximation) quadratic in ψ_1 and ψ_2, it follows from the Hermitianity of such a Hamiltonian that the number of independent factors in the the aforementioned quadratic form is three. Naturally, the values and signs of the parameters α_1, α_2, and β depend on the type of planar defect. In the case of electrons these defects could be intercalated planes of foreign atoms, and in the case of phonons they could be intercalated planes, thin twin interlayers, or the faces of a thick twin (in that case the difference between the elastic properties of the parent and twinned crystals is neglected).

All the lengths in the formulas will be measured in units of the thickness a_0 of the planar defect (which is of the order of an interatomic distance).

Equations (3) and (4) are solved jointly with the boundary conditions on the planes $z = \pm h/2$:

$$\begin{cases} \psi_s\left(x,y,\pm\dfrac{h}{2}+0\right) = \psi_s\left(x,y,\pm\dfrac{h}{2}-0\right), \quad s=1,2; \\[2mm] \dfrac{1}{2m_1}\left(\dfrac{\partial\psi_1(x,y,\pm h/2+0)}{\partial z} - \dfrac{\partial\psi_1(x,y,\pm h/2-0)}{\partial z}\right) = \alpha_1\psi_1(x,y,\pm h/2) + \beta\psi_2(x,y,\pm h/2); \\[2mm] \dfrac{1}{2m_2}\left(\dfrac{\partial\psi_2(x,y,\pm h/2+0)}{\partial z} - \dfrac{\partial\psi_2(x,y,\pm h/2-0)}{\partial z}\right) = \alpha_2\psi_2(x,y,\pm h/2) + \beta\psi_1(x,y,\pm h/2). \end{cases} \quad (6)$$

We will be interested in the energy region corresponding to the freely propagating waves of the first kind of particle and to localized states of the second kind of particle, i.e.,

$$\varepsilon_1 \equiv \frac{k_x^2 + k_y^2}{2m_1} < \varepsilon < \varepsilon_2 \equiv \varepsilon_0 + \frac{(k_x - k_0)^2}{2m_3} + \frac{k_y^2}{2m_2}. \quad (7)$$

1. We seek a wave propagating along the xy plane and having wave vector $\mathbf{k} = (k_x, k_y)$ ($k_x = k\cos\varphi$, $k_y = k\sin\varphi$) and localized near a pair of defects. We take the solution in the form of a symmetric function of z:

$$\psi_1 = \begin{cases} A\cos(k_z z)e^{i(k_x x + k_y y)} & |z| < h/2, \\ 0 & |z| > h/2; \end{cases}$$

$$\psi_2 = \begin{cases} D\cosh\kappa z\, e^{i(k_x x + k_y y)} & |z| < h/2, \\ Be^{-\kappa(|z|-h/2)}e^{i(k_x x + k_y y)} & |z| > h/2, \end{cases} \quad (8)$$

where

$$k_z^2 = 2m_1\varepsilon - k^2,$$

$$\kappa^2 = 2m_2(\varepsilon_0 - \varepsilon) + k^2\sin^2\varphi + \frac{m_2}{m_3}(k\cos\varphi - k_0)^2. \quad (9)$$

Solution (8) describes a wave propagating along parallel defects and "held in" between them, i.e., a pair of such defects acts like a planar waveguide.

Substituting (8) into the boundary conditions (6), we find the possible discrete values of k_z:

$$k_z = q(n) \equiv \frac{\pi}{h}(1 + 2n), \quad n = 0,1,2,... \quad (10)$$

and we obtain the equations

$$A\frac{(-1)^n\pi}{2m_1 h}(1 + 2n) = D\beta\cosh\left(\kappa\frac{h}{2}\right), \quad n = 0,1,2,... \quad (11)$$

$$1 + \tanh\left(\kappa\frac{h}{2}\right) = -\frac{2m_2\alpha_2}{\kappa}. \quad (12)$$

Equation (11) determines the coupling of the amplitudes A and D, and the solutions of the transcendental equation (12) can be used to find that value of the parameter κ for which the system under study has waveguiding properties. It is easily seen that a real solution of equation (12) is possible only for $\alpha_2 < 0$, in which case this solution exists for all values of positive m_2 and negative α_2. For $\kappa h \ll 1$ we obtain $\kappa \approx 2|\alpha_2|m_2$, which is possible if $|\alpha_2|m_2 h \ll 1$. If $\kappa h \gg 1$ then $\kappa \approx |\alpha_2|m_2$, which is possible if $|\alpha_2|m_2 h \gg 1$. Thus we always have $\kappa \sim |\alpha_2|m_2$.

The values found for κ and k_z determine, according to Eqs. (9), a discrete set ($n = 0,1,2,...$) of possible values of the energy ε at a fixed direction of the wave vector, i.e., at a fixed angle φ. Otherwise, if the energy ε is specified and the number n fixed, we will find the direction of the wave vector of those waves that can be confined between the two defects.
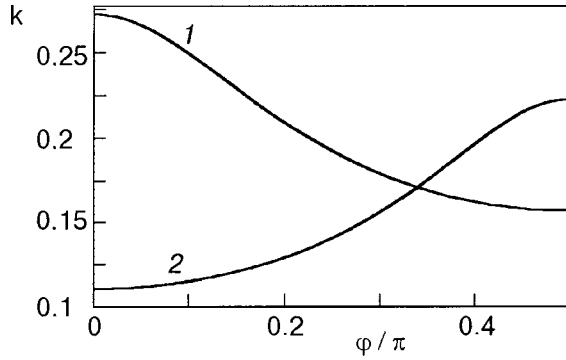
FIG. 2. Modulus of the wave vector k versus the angle φ for $h=20$, $\alpha_2 = -1$, $\varepsilon_0 = 0.5$, $m_2 = 1$, $n=0$: $m_1 = 2$, $m_3 = 1.5$ (*1*); $m_1 = 1.5$, $m_3 = 0.5$ (*2*).

It is more convenient, however, to use the relation between the wave vector k and the angle φ. The dependence of k on φ is given implicitly by the following algebraic equation:

$$k^2\left[1 - \frac{m_2}{m_1} + \cos^2\varphi\left(\frac{m_2}{m_3} - 1\right)\right] - 2\frac{m_2}{m_3}kk_0\cos\varphi$$

$$+ 2m_2\varepsilon_0 - \frac{m_2\pi^2}{m_1h^2}(1+2n)^2 + \frac{m_2}{m_3}k_0^2 - \kappa^2 = 0. \quad (13)$$

We recall that $k_z = q(n)$ is given by formula (10), while $\kappa(h)$ is found as a solution of equation (12). The resulting dependence is characterized by four parameters: k_0, $m_2\varepsilon_0$, m_2/m_1, and m_2/m_3, the values of which are essentially determined by the form of the function $k = k(\varphi)$.

In discussing the above relations let us refine the units of measurement of the dimensional physical quantities appearing in the formulas. As we have said, the lengths are measured in interatomic distances a_0. Consequently, the wave vectors are measured in units of $1/a_0$. The effective masses of the electron are naturally measured in units of the electron mass m_0. Then the energy ε and the parameters α and β are measured in units of $1/(m_0a_0^2)$, i.e., in atomic energy units (recall that $\hbar = 1$). When one is talking about phonons (acoustical waves), then $1/m$ is measured in units of the squared phase velocities of sound, s^2, and the square of the frequency ε is in units of $(s/a_0)^2$, i.e., in units of the square of the Debye frequency.

Let us analyze relation (13) in some limiting cases:

1. Let $k_0 = 0$, $m_2 \neq m_3$. Then

$$k^2 = \frac{\kappa^2 + (m_2/m_1)q^2(n) - 2m_2\varepsilon_0}{1 - m_2/m_1 - (1 - m_2/m_3)\cos^2\varphi}. \quad (14)$$

Here the following variables are possible:

a) For arbitrary φ the system will play the role of a planar waveguide for waves with wave vectors lying in a certain interval (Fig. 2). This can occur if the numerator in (14) is positive and either $m_3 < m_2 < m_1$ or $m_2 < m_3 < m_1$. If the numerator in (14) is negative, then the necessary condition is satisfied for $m_1 < m_2 < m_3$ or $m_1 < m_3 < m_2$.

b) For waves with arbitrary energies greater than a certain ε^*, there exists an angle φ such that waveguiding properties will arise (Fig. 3). This will be for $m_2 < m_1 < m_3$ and $m_3 < m_1 < m_2$. The function $\varepsilon(\varphi)$ can be ascending or descending, depending on the sign of the numerator in (14).
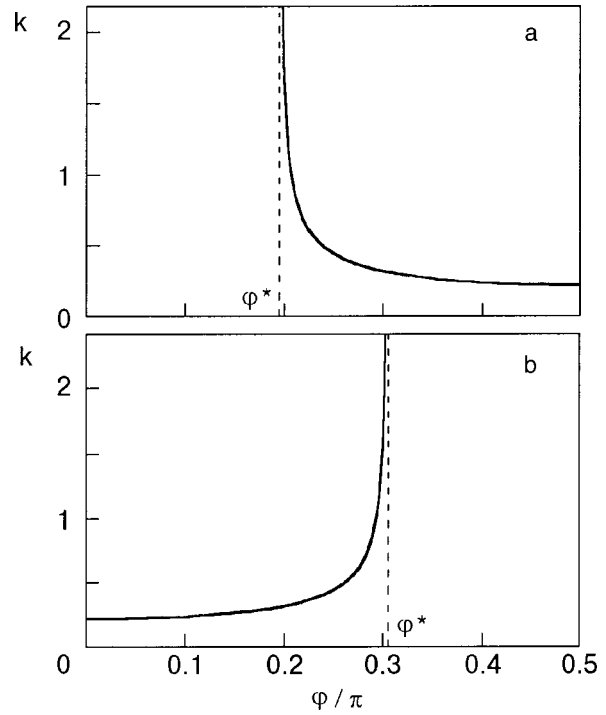

FIG. 3. Modulus of the wave vector k versus the angle φ for $h=20$, $\alpha_2 = -1$, $\varepsilon_0 = 0.5$, $m_2 = 1$, $n=0$: $m_1 = 1.5$, $m_3 = 2$ (a), $m_1 = 0.75$, $m_3 = 0.5$ (b). $\varphi^* = \arccos[m_3(m_1 - m_2)/m_1(m_3 - m_2)]^{1/2}$.

For other relationships among the parameters, waveguiding properties will not arise in the system.

2. The other limiting case is $m_2 = m_3$, $k_0 \neq 0$. Then

$$k(\varphi) = \frac{m_1}{m_1 - m_2}\left\{k_0\cos\varphi \pm \left[k_0^2\cos^2\varphi - \left(1 - \frac{m_2}{m_1}\right)\right.\right.$$

$$\left.\left.\times(2m_2\varepsilon_0 - (m_2/m_1)q^2(n) + k_0^2 - \kappa^2)\right]^{1/2}\right\}. \quad (15)$$

a) Let $m_1 = m_2$. Under this condition it follows directly from Eq. (13) that

$$k(\varphi) = \frac{2m_2\varepsilon_0 - q^2(n) + k_0^2 - \kappa^2}{2k_0\cos\varphi}. \quad (16)$$

Depending on the value of φ, formula (16) has meaning for $\cos\varphi > 0$ if $q^2(n) + \kappa^2 < 2m_2\varepsilon_0 + k_0^2$, and for $\cos\varphi < 0$ if $q^2(n) + \kappa^2 > 2m_2\varepsilon_0 + k_0^2$.

b) For $m_1 > m_2$ it is necessary to satisfy the condition

$$q^2(n) > \frac{m_1}{m_2}\left(2m_2\varepsilon_0 + k_0^2 - \kappa^2 - \frac{m_1k_0^2}{m_1 - m_2}\right),$$

and then there are two possible cases:

1) If $q^2(n) < (m_1/m_2)(2m_2\varepsilon_0 + k_0^2 - \kappa^2)$, then for any $\cos\varphi > 0$ there exist two solutions $k(\varphi)$, while for $\cos\varphi < 0$ there are no solutions.

2) If $q^2(n) > (m_1/m_2)(2m_2\varepsilon_0 + k_0^2 - \kappa^2)$, then for any φ there is one solution $k(\varphi)$.

c) For $m_1 < m_2$ the condition $q^2(n) < (m_1/m_2)[2m_2\varepsilon_0 + k_0^2 - \kappa^2 - m_1k_0^2/(m_1 - m_2)]$, and again there are two possible cases:

1) If $q^2(n) < (m_1/m_2)(2m_2\varepsilon_0 + k_0^2 - \kappa^2)$, then for any φ there is one solution $k(\varphi)$.

2) If $q^2(n) > (m_1/m_2)(2m_2\varepsilon_0 + k_0^2 - \kappa^2)$, then for any $\cos \varphi < 0$ there exist two solutions $k(\varphi)$, while for $\cos \varphi > 0$ there are no solutions.

Analysis of the case $\varphi = 0$ is of special interest, since it corresponds to treating the effect in a 2D system.

We rewrite (13) in the more convenient form

$$k^2 \frac{m_1 - m_3}{m_1} - 2kk_0 + 2\varepsilon_0 m_3 - \frac{m_3}{m_1} q^2(n)$$

$$- \frac{m_3}{m_2} \kappa^2 + k_0^2 = 0. \tag{17}$$

a) If $m_1 = m_3$, then there always exists a k such that Eq. (17) will hold (from here on we are doing the analysis for fixed n).

b) For $m_1 < m_3$ and

$$h^2 > h_1^2 = \frac{\pi^2}{m_1}(1 + 2n)^2 \frac{m_3 - m_1}{k_0^2 + (m_3 - m_1)(2\varepsilon_0 - \kappa^2/m_1)}$$

there are two solutions. If $h^2 < h_1^2$, then there are no solutions.

c) The case $m_1 > m_3$ and $m_1 - m_3 > k_0^2/2\varepsilon_0$. If

$$h^2 \leq h_2^2 = \frac{\pi^2}{m_1}(1 + 2n)^2 \frac{m_1 - m_3}{2(m_1 - m_3)\varepsilon_0 - k_0^2},$$

then there are two values of k that satisfy Eq. (17).

If $h^2 > h_2^2$, then for small $|\alpha_2|$ there are no solutions.

d) For $m_1 > m_3$ and $m_1 - m_3 < k_0^2/2\varepsilon_0$ there are always two solutions.

2. Let us now consider the solution that is antisymmetric in z:

$$\psi_1 = \begin{cases} A \sin(k_z z) e^{i(k_x x + k_y y)} & |z| < h/2, \\ 0 & |z| > h/2; \end{cases}$$

$$\psi_2 = \begin{cases} B \ e^{-\kappa(z - h/2)} e^{i(k_x x + k_y y)} & z > h/2, \\ D \sinh \kappa z \ e^{i(k_x x + k_y y)} & |z| < h/2, \\ -B \ e^{\kappa(z + h/2)} e^{i(k_x x + k_y y)} & z < -h/2. \end{cases} \tag{18}$$

Substituting (18) into the boundary conditions (6), we obtain

$$k_z = \tilde{q}(n) \equiv \frac{2\pi n}{h}, \quad n = 0, 1, 2, \dots \tag{19}$$

$$A \frac{(-1)^{n+1} \pi n}{2m_1 h} = D\beta \sinh\left(\kappa \frac{h}{2}\right), \tag{20}$$

$$1 + \coth\left(\kappa \frac{h}{2}\right) = -\frac{2m_2\alpha_2}{\kappa}. \tag{21}$$

Relations (19)–(21) are analogous in meaning to relations (10)–(12). Equation (21) has solutions for $\alpha_2 < 0$ and for $|\alpha_2| m_2 h > 1$. The rest of the analysis of the antisymmetric case is similar to that for the symmetric case.

If $\varepsilon_2 < \varepsilon_1$ it is straightforward to consider the energy region $\varepsilon_2 < \varepsilon < \varepsilon_1$, in which the waves of the first type are localized and the waves of the second type are freely propagating (ε_1 can be greater than ε_2, e.g., for $m_1 \ll m_2, m_3$). In this energy interval two planar defects will also have waveguiding properties.

Thus we have shown that two parallel planar defects can have waveguiding properties in respect to a wave having a dispersion relation with two branches, if its energy corresponds to freely propagating states of one branch and localized states of the other branch. Depending on the orientation of the wave vector of this wave with respect to the preferred directions of the isoenergy surface, waves with energies lying in a wide interval will be confined between the defects. In the two-dimensional case, waves with a discrete set of energies, depending on the relationships among the parameters of the dispersion relation, will be localized between the defects.

*E-mail: kosevich@ilt.kharkov.ua

[1] A. M. Kosevich and S. E. Savotchenko, Fiz. Nizk. Temp. **25**, 737 (1999) [Low Temp. Phys. **25**, 550 (1999)].

[2] C. S. Chu and R. S. Sorbello, Phys. Rev. B **40**, 5941 (1989).

[3] Y. B. Levinson, M. I. Lubin, and E. V. Sukhorukov, JETP Lett. **54**, 401 (1991).

[4] C. T. Liang, I. M. Castelton, J. E. F. Frost, C. H. W. Barnes, C. G. Smith, C. J. B. Ford, D. A. Ritchie, and M. Pepper, Phys. Rev. B **55**, 6723 (1997).

[5] M. W. Dellow, P. H. Beton, C. J. G. M. Langerak, T. J. Foster, P. C. Main, L. Eaves, M. Henini, S. P. Beaumont, and C. D. W. Wilkinson, Phys. Rev. Lett. **68**, 1754 (1992).

[6] A. M. Kosevich, Zh. Éksp. Teor. Fiz. **115**, 306 (1999) [JETP **88**, 168 (1999)].

[7] Ch. S. Kim and A. M. Satanin, Zh. Éksp. Teor. Fiz. **115**, 211 (1999) [JETP **88**, 118 (1999)].

Translated by Steve Torstveit

Some properties of dynamic solitons of nonlinear systems that are determined by the linearized equation

A. M. Kosevich*

B. Verkin Institute for Low Temperature Physics and Engineering, National Academy of Sciences of Ukraine, pr. Lenina 47, 61164 Kharkov, Ukraine
(Submitted February 9, 2000)
Fiz. Nizk. Temp. **26**, 620–625 (June 2000)

The features of dynamic solitons in nonlinear systems described by differential equations with fourth-order spatial derivatives are discussed for systems of different dimensionalities. The existence conditions for a nonradiative soliton are formulated for the case when the internal frequency of the soliton lies in the continuous spectrum of harmonic oscillations of the system under study. These conditions are determined by the form of the dispersion relation of the linear oscillations. The use of the stated conditions for determining the parameters of two-dimensional solitons is demonstrated. © *2000 American Institute of Physics.*
[S1063-777X(00)01406-7]

INTRODUCTION

We shall discuss the properties of dynamic solitons in certain nonlinear systems from the standpoint of the linear dynamics of these systems. By dynamic soliton we mean a nonlinear spatially localized disturbance whose stability is ensured by the presence of simple additive integrals of the motion. Examples of such solitons are the nonlinear Schrödinger equation (NSE) soliton and the magnetic soliton.[1]

A dynamic soliton is ordinarily characterized by an internal frequency, the value of which is one of the main parameters of the soliton. Traditionally dynamic solitons in condensed-matter physics have been studied on the basis of nonlinear differential equations with spatial derivatives of the second order. In the case of a scalar field the dynamical operator has local-state frequencies that must necessarily lie outside the continuous spectrum. Therefore the eigenfrequency of a dynamic soliton of such a physical field, like the frequency of any localized excitation, must lie outside the spectrum (in the case of an NSE or magnetic soliton, they lie below the continuum).

The situation is different if one is studying the dynamics of a discrete system or the dynamics of a continuous system described by differential equations of higher (then second) order in the spatial derivatives.[2] In that case it can happen that the soliton frequency lie in the continuous spectrum of harmonic oscillations, and there arises the problem of the existence of a soliton in the presence of radiation of linear waves and the problem of the radiational interaction of solitons (see, e.g., Refs. 3 and 4). In Ref. 5 such solitons were constructed in model 1D systems and their properties were discussed. We wish to show that the majority of the effects that arise here are connected with the properties of the linearized equations describing the harmonic oscillations of the system under study—in particular, the dispersion relation for small oscillations. These equations determine the asymptotic behavior of the field at large distances from the soliton and contain rich information about the possible soliton solutions of nonlinear equations.

1. ONE-DIMENSIONAL NONLINEAR SYSTEMS

Let us restrict discussion to a simple nonlinear model which takes the higher dispersion into account and is capable of describing the diverse situations that arise in soliton dynamics:

$$i\frac{\partial\psi}{\partial t}+\frac{\partial^2\psi}{\partial x^2}+\frac{\partial^4\psi}{\partial x^4}+F(\psi)=0,$$

$$F(\psi)=|\psi|^2\psi+\gamma_1\left|\frac{\partial\psi}{\partial x}\right|^2\psi+\gamma_2|\psi|^2\frac{\partial^2\psi}{\partial x^2}-\gamma_3|\psi|^4\psi. \quad (1)$$

We will be interested only in the stationary states $\psi(x,t)_\varphi(x)e^{i\omega t}$, i.e., the properties of the nonlinear equation

$$\omega\varphi=\varphi_{xx}+\varphi_{xxxx}+F(\varphi). \quad (2)$$

The linearized equation obtained by dropping the term $F(\varphi)$ in (2) has the dispersion relation (see Fig. 1)

$$\omega=-k^2+k^4. \quad (3)$$

At the point where $k^2=k_m^2=1/2$, the frequency ω reaches its lowest value $\omega_m=-1/4$. Consequently, we have a continuous spectrum of eigenfrequencies of harmonic oscillations $\omega_m<\omega<\infty$.

For the linearized equation it is easy to calculate the Green function corresponding to stationary oscillations at a definite frequency ω and describing a wave that is outgoing at infinity. In the frequency interval $0<\omega<\infty$ it has the form

$$G_\omega(x)=\frac{1}{4\sqrt{\omega-\omega_m}}\left(\frac{i}{k}e^{-ik|x|}+\frac{1}{\kappa}e^{-\kappa|x|}\right), \quad (4)$$

where

$$k^2=\frac{1}{2}(\sqrt{1+4\omega}+1), \quad \kappa^2=\frac{1}{2}(\sqrt{1+4\omega}-1). \quad (5)$$

In the frequency interval of the continuous spectrum, $\omega_m<\omega<0$, the Green function does not have exponentially decaying terms:
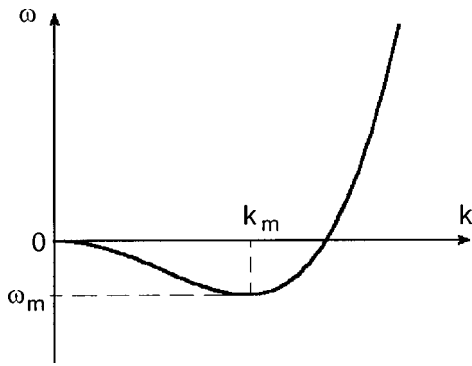
FIG. 1. A sketch of the dispersion relation of the linearized equation (frequency ω versus wave number k).

$$G_\omega(x) = \frac{1}{4\sqrt{\omega - \omega_m}}\left(\frac{e^{-ik_1|x|}}{k_1} + \frac{e^{-ik_2|x|}}{k_2}\right), \tag{6}$$

where

$$k_1^2 = \frac{1}{2}(1 + \sqrt{1+4\omega}), \quad k_2^2 = \frac{1}{2}(1 - \sqrt{1+4\omega}). \tag{7}$$

Finally, if the frequency lies below the continuum ($\omega < -1/4$), then the Green function takes a different form:

$$G_\omega(x) = \frac{1}{4\kappa k}e^{-\kappa x}\sin(kx + \varphi), \tag{8}$$

where

$$k^2 - \kappa^2 = 1, \quad 2\kappa k = \sqrt{\omega_m + \omega}. \tag{9}$$

Analysis of the form of the Green functions (4), (6), and (8), independently of the structure of the nonlinear term in Eq. (1), allows one to draw the following obvious conclusions about the possible soliton solutions of this equation and others like it.

1. Dynamic solitons with frequencies $\omega < \omega_m$ have exponentially decaying oscillatory "tails," and if they are exact solutions of equation (1), then they can radiate linear waves. The presence of nonmonotonically decaying "tails" has important significance for the study of the interaction of solitons and was apparently first discussed in Refs. 6 and 7.

2. Frequencies $\omega_m < \omega < 0$ cannot in principle correspond to soliton solutions, since there are no decaying asymptotic solutions for the corresponding stationary states.

3. A typical linear stationary state in the frequency interval $\omega > 0$ is a quasilocalized oscillation, with one of its components localized in space and the other being a standing wave of constant amplitude. The features of the scattering processes in the presence of such states are discussed in Ref. 8.

The presence of the asymptotic behavior indicated means that the possible soliton solutions of equation (1) with frequencies $\omega > 0$, as a rule, are accompanied by the radiation of harmonic waves. There have been various explanations as to the physical reasons and necessary conditions for the existence of nonradiative solitons in this frequency interval.

To elucidate the necessary conditions under which radiation will be absent, let us consider the forced solution of the linearized equation excited by a distributed force $f(x)$ concentrated in a small interval of x around $x = 0$. Suppose that $f(x)$ falls off with distance faster than $\exp(-\kappa|x|)$. Then the solution outside the region of the applied force is

$$\varphi(x) = \int G(x - x')f(x')dx'$$

$$= \frac{1}{2\sqrt{1 + 4\omega}}(iQ(k)e^{-ik|x|} + P(\kappa)e^{-\kappa|x|}), \tag{10}$$

where

$$kQ(k) = \int f(x)e^{ikx}dx, \quad \kappa P(\kappa) = \int f(x)e^{\kappa x}dx. \tag{11}$$

If the Fourier component of the distributed force vanishes at some value $k = k_0$ ($Q(k_0) = 0$), then the forced oscillations with frequency $\omega = \omega(k_0)$ will not excite radiation at infinity. There is completely quenching of the linear oscillations far from the source on account of wave interference. In the case of a symmetric force distribution ($f(x) - f(-x)$) the indicated solution has the form

$$\int f(x)\cos kx \, dx = 0, \tag{12}$$

and for an antisymmetric distribution ($f(-x) = -f(x)$)

$$\int f(x)\sin kx \, dx = 0. \tag{13}$$

It should be noted, however, that since the frequencies of such an oscillation lie in the quasicontinuous spectrum, its weight in the linear dynamics is very small, of the order of $1/\sqrt{N}$, where N is the number of atoms in the 1D chain under study. It is known, however, that in nonlinear dynamics the weight of such preferred stationary states can turn out to be altogether different.

The obvious mathematical condition (12) or (13) for solvability of the inhomogeneous differential equation lets one obtain the parameters of the stationary dynamic solitons which are unaccompanied by radiation.

Analyzing the structure of Eq. (2), one expects that it has a soliton solution of the form

$$\varphi_s(x) = \frac{A}{\cosh \kappa x}, \quad \omega = \text{const}, \tag{14}$$

where κ is related to the frequency ω by expression (5).

Substituting solution (14) into the nonlinear term of Eq. (1), we can treat it as an external force $f(x) = f(-x)$. According to (12), the soliton (14) will be unaccompanied by radiation under the condition

$$\int F(\varphi_s(x))\cos kx \, dx = 0. \tag{15}$$

To eliminate awkward manipulations, let us do the calculation separately for several cases: (1) $\gamma_1 \neq 0$, $\gamma_2 = \gamma_3 = 0$, (2) $\gamma_2 \neq 0$, $\gamma_1 = \gamma_3 = 0$, and (3) $\gamma_3 \neq 0$, $\gamma_1 = \gamma_2 = 0$.

In the first case it follows from (5) and (15) that

$$k^2 = \frac{3\gamma_1 - 12}{2\gamma_1}, \quad \kappa^2 = \frac{\gamma_1 - 42}{2\gamma_1}; \quad \omega = \left(\frac{\gamma_1 - 6}{\gamma_1}\right)^2 - \frac{1}{4}. \tag{16}$$

We see that for $\gamma_1 > 12$ there always exists a single soliton of type (14) which does not radiate linear waves. All the amplitude parameters of this soliton except the amplitude A can be obtained from an analysis of the linearized equation. It is easy to see that the exact solution of equation (2) corresponds to

$$A^2 = \frac{24}{\gamma_1} \kappa^2 = \frac{12(\gamma_1 - 12)}{\gamma_1^2}.$$

In the second case ($\gamma_1 = \gamma_3 = 0$) we have

$$k^2 = 3\frac{\gamma_2 - 4}{2\gamma_2}, \quad x^2 = \frac{\gamma_2 - 12}{2\gamma_2},$$

$$\omega = \frac{3}{4}\frac{(\gamma_2 - 4)(\gamma_2 - 12)}{\gamma_2^2}. \tag{17}$$

It follows from Eq. (2) that the amplitude obeys

$$A^2 = \frac{24\kappa^2}{\gamma_2} = \frac{2}{\gamma_2^2}(\gamma_2 - 12).$$

Thus soliton (14) exists in a system with $\gamma_2 > 12$.

Finally, in the case $\gamma_3 \neq 0$, $\gamma_1 = \gamma_2 = 0$ it follows from (5) and (15) that

$$\kappa^2 = \frac{\gamma_3}{2(6 - 5\gamma_3)}, \quad k^2 = \frac{3(4 - 3\gamma_3)}{2(6 - 5\gamma_3)},$$

$$\omega = \frac{3\gamma_3(4 - 3\gamma_3)}{4(6 - 5\gamma_3)^2}. \tag{18}$$

The soliton amplitude is obtained from (2):

$$A^2 = \frac{24\kappa^2}{\gamma_3} = \frac{12}{6 - 5\gamma_3}.$$

Interestingly, the soliton can exist only for $0 < \gamma_3 < 6/5 = 1.2$.

Let us apply these findings to the analysis of the more complicated soliton solution of a simplified equation (2) for $\gamma_1 = \gamma_2 = \gamma_3 = 0$. In this case one should expect a soliton of the type

$$\varphi(x) = A\frac{\sinh \kappa x}{\cosh^2 \kappa x}. \tag{19}$$

Since $\varphi(-x) = -\varphi(x)$ in this case, one should use condition (13):

$$\int \left(\frac{\sinh \kappa x \, dx}{\cosh^2 \kappa x}\right)^3 \sin \kappa x \, dx = 0. \tag{20}$$

The requirement (20) yields the relation $k^2 = k_0^2 \equiv 11\kappa^2$. Using Eq. (5), we find that $\kappa^2 = 0.1$ and $\omega = 0.11$. These parameters correspond to the only solution of the type (19) that does not give radiation. In the exact solution, which is presented in Ref. 9, one has $A = \sqrt{6/5}$.

It is clear that the stated conditions for the existence of a nonradiative dynamic soliton and their demonstration in specific cases do not constitute constructive recommendations for seeking an analytical soliton solution. However, they do show that the structure of the dynamic soliton is determined
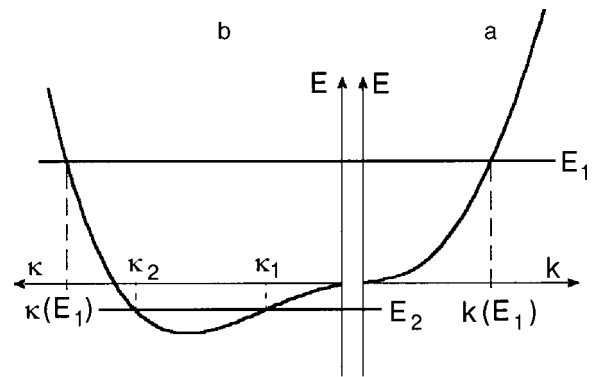

FIG. 2. Dispersion of the energy E of elementary excitations for a real wave vector (k) (a) and for a purely imaginary wave vector ($k = i\kappa$) (b).

as much by the properties of the dispersion relation of the linearized equation as by the form of the nonlinear terms in the dynamical equations.

2. TWO-DIMENSIONAL NONLINEAR EQUATIONS

Turning now to an analysis of the 2D situation, let us alter the relationship between the signs in front of the second and fourth spatial derivatives to point up how the general conclusions are independent of this relationship. Working from the nonlinear Schrödinger equation, we denote the energy eigenvalue by the letter E:

$$E\Psi = \frac{1}{2}\Delta\Psi - \frac{1}{2}\beta\Delta\,\Delta\Psi = F(\Psi), \tag{21}$$

where Δ is the 2D Laplacian operator,

$$\Delta = \frac{\partial^2}{\partial r^2} + \frac{1}{r}\frac{\partial}{\partial r} + \frac{1}{r^2}\frac{\partial^2}{\partial^2\theta}.$$

and $F\{\Psi\}$ is a regular function of Ψ and the spatial derivatives $\Delta\Psi$, of the form

$$F(\Psi) = \alpha|\Psi|^2\Psi + \gamma|\nabla\Psi|^2\Psi + \ldots. \tag{22}$$

The linearized equation describes the elementary excitations of the system, $\Psi = \exp(ikx - iEt)$, with the dispersion relation ($E > 0$)

$$E = \frac{1}{2}k^2 + \frac{1}{2}\beta k^4, \tag{23}$$

a graph of which is sketched in Fig. 2(a). The linearized equation for positive values of E also has another type of solutions: $\Psi(x) = \exp(\pm\kappa x)$, which correspond to purely imaginary $k = i\kappa$. The ''dispersion relation'' of these localized solutions has the form

$$E = \frac{1}{2}\beta\kappa^4 - \frac{1}{2}\kappa^2, \tag{24}$$

and a graph is sketched in Fig. 2(b).

Solutions of the linearized equation that depend exponentially (and monotonically) on the distance also exist in the interval $E_m < E < 0$, where there are two values of the parameter κ:

$$\kappa_{1,2}^2 = \frac{1}{2\beta}(1 \pm \sqrt{1 - 8|E|}). \tag{25}$$

Following the scheme proposed in Sec. 1, we construct the Green functions of the linearized equation for $E>0$:

$$G(r)=i\pi H_0^{(1)}(kr)-2K_0(\kappa r), \qquad (26)$$

where $H_0^{(1)}(kr)$, $K_0(\kappa r)$ are the standard Hankel functions of real and imaginary argument, and the parameters k and κ are determined by relations analogous to (5):

$$k^2=\frac{1}{2\beta}(\sqrt{1+8E}-1),$$

$$\kappa^2=\frac{1}{2\beta}(\sqrt{1+8E}+1). \qquad (27)$$

The asymptotic form of the Green function at large distances describes an outgoing cylindrical wave and an exponentially damped amplitude of the localized component. This sort of asymptotic behavior of the Green function means that the soliton of the nonlinear equation with $E>0$, as a rule, is accompanied by radiation. It is only for $E<0$ that the soliton solutions, if they exist, do not generate radiation. For example, in the interval $E_m<E<0$ the Green function has the form

$$G(r)=K_0(\kappa_1 r)-K_0(\kappa_2 r), \qquad (28)$$

where the definition of the parameters κ_1 and κ_2 is obvious (see Fig. 2). Consequently, a soliton with such values of E is stable against its radiative process.

However, for $E>0$ there can also exist stable solitons at discrete values of E determined by special equations of the type discussed in Sec. 1 in connection with the 1D case.

It is helpful to follow the derivation of these special conditions in the 2D case. Let us consider the forced solution of the linearized equation under the influence of a cylindrically symmetric external oscillatory force $f(\rho)e^{-iEt}$ concentrated near the origin of coordinates in a small region of radius $r\sim\rho_0\lesssim 1/\kappa(E)$, under the condition that E lies in the continuous spectrum ($E>0$):

$$E\Psi+\frac{1}{2}\Delta\Psi-\frac{1}{3}\beta\Delta\Delta\Psi=f(\rho). \qquad (29)$$

Having the Green function (26), we can immediately write the oscillatory part of the forced solution:

$$\Psi_{osc}-\int H_0^{(1)}[k(r-\rho\cos\theta)]f(\rho)\rho d\rho d\theta. \qquad (30)$$

The asymptotic form of (30) at large distances ($r\kappa(E)\gg 1$) has the form

$$\Psi_{osc}\sim\frac{e^{ikr}}{2\tau\sqrt{r}}\int f(\rho)\exp(-i\kappa\rho\cos\theta)\rho d\rho d\theta$$

$$=\frac{e^{ikr}}{r}\int_0^\infty f(\rho)J_0(\rho)\rho d\rho, \qquad (31)$$

where $J_0(k\rho)$ is the zero-order Bessel function.

It is obvious that the oscillations vanish under the condition

$$\int_0^\infty f(\rho)J_0(k\rho)\rho d\rho=0. \qquad (32)$$

Clearly condition (32) can be satisfied only for a certain discrete set of k (or E).

Let us now assume that the initial nonlinear equation (21) admits a soliton solution

$$\Psi_s=\Phi_s(\rho)e^{-iEt}, \qquad (33)$$

for which E lies in the continuum but which does not radiate linear outgoing waves.

We substitute (33) into the right-hand side of Eq. (21). Then at large distances ($\kappa r\gg 1$) we can write the following representation with the aid of the Green function:

$$\Phi_s(r)=\int G(r-\rho\cos\theta)F\{\Phi_s(\rho)\}\rho d\rho d\theta. \qquad (34)$$

It is now obvious that the radiation field far from the soliton vanishes if

$$\int_0^\infty F\{\Phi_s(\rho)\}J_0(\kappa\rho)\rho d\rho=0. \qquad (35)$$

Relation (35), as in the 1D case, can be satisfied only for a discrete set of possible k or E.

Unfortunately, we know of no exact analytical solution for a soliton in any 2D model described by an equation of the type (21), and we therefore cannot illustrate the use of relation (35) as we did for the 1D case in Sec. 1.

3. THREE-DIMENSIONAL NONLINEAR EQUATIONS

After the discussion of the 2D situation the analysis of the 3D case is obvious. Let us therefore draw some conclusions as to the possible existence of a nonradiative dynamic soliton of an equation of the type (21), where Δ is the 3D Laplacian.

The dispersion relation for linear oscillations is given as before by formula (23), and the Green function corresponding to positive energies ($E>0$) is obvious (it is given in the Appendix of Ref. 2):

$$G(r)=\frac{1}{4\pi\beta}\frac{e^{ikr}-e^{-\kappa r}}{(k^2+\kappa^2)r}, \qquad (36)$$

where the parameters k and κ are specified by expressions (27).

We assume that Eq. (21) has a soliton solution of the form ($E>0$)

$$\Psi_s=\Phi_s(r)e^{-iEt}, \qquad (37)$$

which is localized in a volume with a radius of the order of $1/\kappa(E)$. Then at large distances ($\kappa r\gg 1$) we have a representation analogous to (34), viz.,

$$\Phi_s(r)=\int G(r-\rho\cos\theta)F\{\Phi_s(\rho)\}\sin\theta\,d\theta d\varphi\rho^2 d\rho. \qquad (38)$$

Keeping only the oscillatory part of the Green function, we obtain the conditions for the absence of a radiation field far from the soliton:

$$\int_0^\infty F\{\Phi_s(\rho)\}\frac{\sin(k\rho)}{k\rho}\rho^2 d\rho=0. \qquad (39)$$

Relation (39) can hold only for a select discrete set of values of the modulus of the wave vector (or values of E).

In closing let us emphasize once again that the dynamic solitons with frequencies (or energies E) lying in the continuous spectrum of elementary excitations of a system can exist only as solutions of dynamical equations that effectively include higher dispersion in the linearized part of the equations. The term ''effectively'' means that formally the individual branches of the dispersion relation for E can be quadratic, but the field in question is multicomponent (similar to how the elastic field has independent longitudinal and transverse components). In this case the system effectively behaves, from the standpoint of the problem under discussion, as a one-component field but with additional allowance for the higher dispersion.

The author thanks M. M. Bogdan and A. S. Kovalev for helpful discussions.

[*]E-mail: kosevich@ilt.kharkov.ua

[1] A. M. Kosevich, B. A. Ivanov, and A. S. Kovalev, *Nonlinear Waves of Magnetization. Dynamic and Topological Solitons* [in Russian], Naukova Dumka, Kiev (1983); A. M. Kosevich, B. A. Ivanov, and A. S. Kovalev, Sov. Sci. Rev. A, Phys. **6**, 161 (1985).
[2] A. M. Kosevich and S. E. Savotchenko, Fiz. Nizk. Temp. **25**, 737 (1999) [Low Temp. Phys. **25**, 550 (1999)].
[3] A. V. Buryak and N. N. Akhmediev, Phys. Rev. E **52**, 3572 (1995).
[4] A. V. Buryak, Phys. Rev. E **52**, 1156 (1995).
[5] J. Yang, B. A. Malomed, and D. J. Kaup, Phys. Rev. Lett. **83**, 1958 (1999).
[6] K. A. Gorshkov, L. A. Ostrovskiĭ, and V. V. Papko, Zh. Éksp. Teor. Fiz. **71**, 586 (1976) [Sov. Phys. JETP **44**, 306 (1976)]; K. A. Gorshkov, L. A. Ostrovsky, and V. V. Papko, Phys. Lett. A **74**, 177 (1979).
[7] K. A. Gorshkov and L. A. Ostrovsky, Physica D **3**, 428 (1981).
[8] A. M. Kosevich, Zh. Éksp. Teor. Fiz. **115**, 306 (1999) [JETP **88**, 168 (1999)].
[9] A. Höök and M. Karlsson, Opt. Lett. **18**, 1390 (1993).

Translated by Steve Torstveit